

2021

Rare metal resources in polymetallic nodules from the Eastern Equatorial Pacific Ocean

Tupiti, Wycliff

<http://hdl.handle.net/10026.1/16922>

<http://dx.doi.org/10.24382/556>

University of Plymouth

All content in PEARL is protected by copyright law. Author manuscripts are made available in accordance with publisher policies. Please cite only the published version using the details provided on the item record or document. In the absence of an open licence (e.g. Creative Commons), permissions for further reuse of content should be sought from the publisher or author.



**UNIVERSITY OF
PLYMOUTH**

**RARE METAL RESOURCES IN POLYMETALLIC NODULES FROM THE
EASTERN EQUATORIAL PACIFIC OCEAN**

by

WYCLIFF TUPITI

A thesis submitted to the University of Plymouth

in partial fulfilment for the degree of

DOCTOR OF PHILOSOPHY

School of Geography, Earth and Environmental Sciences

February 2021

Copyright statement

This copy of the thesis has been supplied on condition that anyone who consults it is understood to recognise that its copyright rests with its author and that no quotation from the thesis and no information derived from it may be published without the author's prior consent.

ACKNOWLEDGEMENT

The successful completion of this PhD project may not have been possible without the tremendous support from many people. To start with, I would like to thank my former Director of Studies, Arjan Dijkstra for his supervision and continuous guidance and support, from the conception of the project to the hours spent in the lab with me, to the final write-up of the thesis.

Second, a massive thank you to Colin Wilkins who is currently my Director of Studies. Colin has always been a constant source of support throughout my PhD study especially in project planning and guidance, and reviewing of the thesis, and together with Arjan have followed my PhD journey from the start to the end. I would also like to thank my third supervisor, Gregory Price for his contributions in project meetings and also for his valuable comments on the thesis. I wish to extend my thanks to my RDC2 expert commentators, Michelle Harris, Stephen Grimes and Luca Menegon for their valuable comments that helped to steer the project forward after the RDC2 stage.

This PhD was funded by the UK Seabed Resources Ltd (UKSRL), therefore, I am grateful to UKSRL for providing me with a scholarship to pursue this study at the University of Plymouth, and for also allowing me to participate on a nodule sampling cruise to the Clarion-Clipperton Fracture Zone as part of my training programme. I would also like to extend my thanks to the International Seabed Authority (ISA) for its training programmes (of which this training is part of), to train trainees from developing countries for capacity building in the area of deep-sea minerals.

This project would not have been possible without the valuable technical support and assistance provided by many individuals. I would like to acknowledge the support

provided to me by the Earth Sciences technical staff: Jodie Fisher, Rob Hall, and Ian King, from lab trainings, access to lab facilities and equipment to ordering supplies. I would also like to thank Marc Davies for teaching me some proper and useful lab techniques and for always willing to assist when I consult him. I would like to thank Rob Clough and Andrew Fisher for their technical support with all my ICP-MS and ICP-OES analyses and for their patience at times waiting for me in the lab to complete my measurements after working hours. Furthermore, I greatly appreciate the support from the chemistry technical staff, in particular: Andrew Tonkin, Andy Arnold, Billy Simmonds and Jeremy Clarke for providing lab wares, equipment and chemicals for some of my experiments, as well as Deborah Bauckham and Claire Williams for ordering lab supplies including chemicals. I am grateful for the support provided by Alex Taylor and Geoff Millward of the Consolidated Radio-isotope Facility (CoRIF) for helping me with my XRF analyses. I would also like to thank Natasha Stephen, Roy Moate, Peter Bond, Glen Harper, Dan Haspel, Alex Strachan and Lorelei Robertson from the Plymouth Electron Microscopy Centre (PEMC) for their support with my electron microscopy work. In addition, I wish to thank Julia Parker of Diamond Light Source for carrying out a micro-synchrotron XRF pilot test study on my samples. A special thanks to Richard Pearce of the National Oceanographic Centre (NOC), University of Southampton, for carrying out XRD analyses as well as to Andy Milton of NOC for carrying out Nd and Sr isotopic measurements on my nodule samples.

I owe a lot of thanks to all my PhD friends with whom I have shared many good moments with that I will long cherish. Therefore, a dedicated thanks to all of you for being great office mates, for the good times spent together and the laughter and humour shared whether in the campus, outdoors or in the pub. Thanks to Christian (also for his help in

the lab), Maarten, and Tom for the pool games in JSV. Thanks to Camille and Max for sharing dinner and amazing music sessions. Thanks to Kilian, Josh and Jesse (for all the outdoor fun), Giulia, Fran, Grant, Louise, Francesca, Israel, Mohammed, Fabio, Luca, Simeon, Bugra and Felipe.

I would also like to say a big thank you to all the SoGEES staff at the University of Plymouth for their support in various ways in both academic and non-academic form during my time in Plymouth, from exchanging of ideas along the corridor in Davy building or in JSV, to demonstrating in practical classes.

Last but not the least, a dedicated thank you to Uwe Balthasar (University of Plymouth) and Richard Herrington (Natural History Museum, London) for examining this thesis, as well as Martin Attrill (viva chairperson) for the engaging viva discussion which I greatly enjoyed.

Finally, I will be forever grateful to my loving wife, Melissa and our two boys, Bunisoloso and Makare, as well as mum and dad for their patience, never ending support, encouragement and their belief in me during the course of the four years I was away from them to complete this PhD. This work is dedicated to you.

AUTHOR'S DECLARATION

At no time during the registration for the degree of Doctor of Philosophy has the author been registered for any other University award without prior agreement of the Doctoral College Quality Sub-Committee.

Work submitted for this research degree at the University of Plymouth has not formed part of any other degree either at the University of Plymouth or at another establishment.

This study was financed with the aid of a studentship from the University of Plymouth and grant from the UK Seabed Resources Ltd.

Presentations at conferences

University of Plymouth Earth Science Research Seminar, 2016, Plymouth, UK. 'A new look at the critical material potential of polymetallic nodules using advanced imaging techniques' (oral presentation).

Plymouth Imaging Network, 2017, Plymouth, UK. 'Role of imaging in Earth Sciences – The hunt for Rare Earth Elements' (oral presentation)

University of Plymouth Earth Science Research Seminar, 2018, Plymouth, UK.
'Polymetallic nodules as a source for critical metals' (poster presentation).

Resources for Future Generations, 2018, Vancouver, Canada. Polymetallic nodules as a source for critical metals (REYs, Co) (oral presentation).

Geological Society of London: Minerals at the frontier, 2018, London, UK. 'Distribution of critical metals (REYs) in polymetallic nodules' (oral presentation).

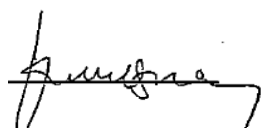
The Geological Society: Marine minerals, London, UK, 2018. 'Critical metals (REYs) in polymetallic nodules from the Clarion-Clipperton Fracture Zone' (oral presentation).

Goldschmidt, 2019, Barcelona, Spain. 'Critical metals in polymetallic nodules from the eastern equatorial Pacific (poster presentation).

University of Plymouth Earth Science Research Seminar, 2019, Plymouth, UK. 'Critical metals in deep-sea nodules' (oral presentation).

University of Plymouth Earth Science Research Seminar, 2019, Plymouth, UK. 'Mineral host phases of Rare Earth Elements and Yttrium in deep-sea nodules' (oral presentation).

Word count of main body of thesis: 47340

A handwritten signature in black ink, appearing to be 'F. M. Jones', written over a horizontal dotted line.

Signed.....

Date.....09/02/2021.....

RARE METAL RESOURCES IN POLYMETALLIC NODULES FROM THE EASTERN EQUATORIAL PACIFIC OCEAN

Wycliff Tupiti

ABSTRACT

The Clarion-Clipperton fracture zone (CCFZ) in the eastern equatorial Pacific is the area with the greatest interest in terms of metal resources in polymetallic nodules. The nodules are enriched (relative to crustal composition) in economically important metals such as Mn, Ni, Cu, Zn, and so-called critical metals such as Co, Rare Earth Elements and Y (REYs).

This project involves the geochemical and mineralogical investigation of nodules from five box cores from the UK claim area in the CCFZ. Bulk geochemical analysis shows that the nodules formed from both hydrogenetic (precipitation from bottom oxic seawater) and diagenetic (precipitation from oxic/suboxic sediment porewaters) processes. Bulk analysis revealed high contents of Mn (29%), Ni (1.3%), Cu (1.0%), Co (0.17%) and REY (700 – 800 ppm). Analysis of (micro-drilled) individual layers in two nodule samples using ICP-MS shows that REYs are more enriched in the hydrogenetic layers (up to 1200 ppm) compared to the diagenetic layers (up to 600 ppm). Similarly, Co is also concentrated in the hydrogenetic layers, while Ni and Cu are enriched in the diagenetic layers. Mineralogical analysis using XRD shows the 10 Å and 7 Å phyllosulfates as the dominant mineral phases in the nodules. Sequential leaching experiments using dilute acetic acid, HCl, oxalic acid and concentrated nitric acid revealed that ~60% of REYs are hosted in the interlayer spacings of the phyllosulfates while less than 7% are hosted

in the amorphous FeOOH phase compared to 30% of Co that is associated with the FeOOH phase. The association of the REYs with the phyllosilicates was further investigated using mineral synthesis approaches which shows that REY can occupy interlayer spacings. The Nd and Sr isotopic compositions of the individual growth layers of a nodule sample revealed that the hydrogenetic and diagenetic layers source their metals from different sources, with North American and east Asian dust the likely source for hydrogenetic layers while seamounts and oceanic basalt as the source for diagenetic layers.

Table of contents

1	General introduction	1
1.1	Mineral resources from the deep sea	1
1.2	History of deep-sea mineral exploration	2
1.3	Types of deep-sea ferromanganese deposits	3
1.3.1	Polymetallic nodules	3
1.3.2	Occurrence and distribution	4
1.3.2.1	The Clarion-Clipperton Fracture Zone	6
1.3.3	Ferromanganese crusts	9
1.4	Drivers for deep-sea minerals extraction	10
1.4.1	Rare earth elements plus Yttrium (REYs)	12
1.4.1.1	Global production, reserves and demand for REYs	13
1.4.2	Cobalt	15
1.5	Aims and objectives	16
2	Bulk chemical composition of polymetallic nodules from the UK Claim Area, UK1 in the Clarion-Clipperton Fracture Zone and an evaluation of the sodium peroxide sintering digestion method for REY analysis	18
2.1	Introduction	18
2.2	Method	22
2.2.1	Sample collection and sample sites	22

2.2.2	X-Ray Fluorescence Spectrometry (XRF) analysis for major oxides and minor elements.....	25
2.2.2.1	Measurement accuracy and repeatability (precision).....	26
2.2.3	Trace elements – Sodium peroxide sintering and ICP-MS measurements	26
2.2.3.1	Digestion procedure	28
2.2.3.2	Calibration standards.....	29
2.2.3.2.1	Drift correction	29
2.2.3.3	Polyatomic Interference corrections	30
2.2.3.4	Detection limits and blanks	31
2.2.3.5	Measurement accuracy and repeatability (precision).....	32
2.2.3.6	Assessment of the recoveries of trace metals after sintering.....	34
2.3	Results	36
2.3.1	Sample description.....	36
2.3.2	Bulk compositions	41
2.4	Discussion.....	45
2.4.1	Composition of nodules from the UK claim area.....	45
2.4.2	Comparison of nodule occurrence between box cores.....	51
2.4.3	Resource potential of polymetallic nodules	54
2.4.3.1.1	Rare earth elements and Yttrium.....	54

2.4.3.1.2	Cobalt	60
2.4.3.1.3	Nickel and copper.....	61
2.5	Conclusion.....	64
3	Structure and composition of individual nodule layers using electron microscopy and wet chemistry analyses.....	66
3.1	Introduction	66
3.2	Method.....	78
3.2.1	Scanning electron microscopy (SEM).....	78
3.2.1.1	Sample preparation	78
3.2.1.2	Instrumentation.....	79
3.2.1.3	Large area mapping	80
3.2.1.4	SEM-EDS mapping analysis using energy peak deconvolution	81
3.2.2	Chemical analysis of individual nodule layers.....	81
3.3	Results	82
3.3.1	Nodule morphology, texture, internal growth structures and composition of individual layers using SEM	82
3.3.1.1	The problem of mapping the distribution of REY and Co using EDS-SEM	96
3.3.2	Biogenic structures in polymetallic nodules	100
3.3.3	Chemical composition of REY in individual layers using ICP-MS/-OES ...	101
3.4	Discussion.....	109

3.4.1	Internal growth structures	109
3.4.2	Composition and elemental distribution	117
3.4.3	REY patterns	122
3.5	Conclusion	127
4	Determination of the host phases of rare earth elements in deep-sea nodules from the Eastern Equatorial Pacific using sequential leaching experiments and x-ray diffraction analyses	130
4.1	Introduction	130
4.2	Materials and method.....	135
4.2.1	Reagents.....	135
4.2.2	Simple leaching experiments	135
4.2.3	Sequential leaching experiments.....	138
4.2.4	Mineralogical analysis of nodules	140
4.2.4.1	Mineralogy of diagenetic vs hydrogenetic layers.....	140
4.2.4.2	Mineralogy before and after sequential leaching	141
4.2.5	X-ray diffraction analysis for mineralogy	142
4.3	Results	142
4.3.1	Sequential leaching	142
4.3.2	Mineralogy	147
4.3.2.1	Mineralogy of diagenetic versus hydrogenetic layers.....	147

4.3.2.2	Mineralogy before and after leaching	150
4.4	Discussion.....	153
4.4.1	Metal associations with different mineral phases.....	153
4.4.2	Mineralogy	161
4.5	Conclusion	163
5	Interlayer cationic exchange of Mg(II), Ca(II), Cu(II), Co(II), La(III), Nd(III) and Yb(III) for Na in synthetic birnessite	164
5.1	Introduction	164
5.2	Materials and method.....	165
5.2.1	Synthesis of Na-birnessite.....	165
5.2.2	Cation hydration experiments	166
5.2.3	Analytical techniques	166
5.2.3.1	XRD.....	166
5.2.3.2	SEM	167
5.3	Results	167
5.3.1	Na-birnessite	167
5.4	Discussion.....	175
5.5	Conclusion	182
6	Nd and Sr isotopic composition in the individual layers of a nodule sample	184
6.1	Introduction	184

6.2	Method.....	189
6.2.1	Sample preparation.....	189
6.2.2	Sequential leaching	189
6.2.3	Scanning Electron Microscopy	190
6.2.4	Nd and Sr isotope analysis	191
6.3	Results	192
6.3.1	Sample description.....	192
6.3.2	Nd and Sr Isotopic composition	193
6.4	Discussion.....	198
6.5	Conclusion	204
7	Final conclusions and future work.....	205
7.1	Final conclusions	205
7.2	Future work.....	214
	Appendix I. Sample preparation for SEM.....	237
	Appendix II. Sequential leachate concentrations for nodule samples: AB02 BC06 N5, AB02 BC19 N3, AB02 BC02 rubbles and FeMn CRM. All measurements for each element carried out in triplicates.	239
	Appendix III. Na-birnessite synthesis experimental set-up	247

TABLE OF FIGURES

Figure 1.1. Estimates of average nodule abundance in the four major locations in 2013 (Hein & Petersen, 2013).....	6
Figure 1.2. Location of the Clarion-Clipperton Fracture Zone (CCFZ) in the Eastern Equatorial Pacific and the UK claim area shown inset as UK1.....	7
Figure 1.3. Exploration areas in the CCFZ, colour-coded for the different contracting parties (ISA, 2015). The UK Claim Area, which is where samples in this study come from, is marked with a thicker outline in the map. The map also shows the areas of particular environmental interest (APEI) designated as part of the environmental management plan as areas unaffected by commercial extraction of nodules in order to preserve marine ecosystem health and function.	8
Figure 1.4. REY reserves worldwide by country (in 1,000 metric tons of REY oxides). Source: USGS (2020a).	14
Figure 1.5. Predicted growth of global REE demand (2010-2035), note; data does not include Y. Source: Yang et al. (2017).....	14
Figure 1.6. Industrial uses of cobalt (Battery University, 2018). Co has a range of industrial applications, the battery industry is currently the largest consumer of Co...	15
Figure 1.7. Cobalt reserves worldwide by country in tonnes. Source: (USGS, 2020b). At 3.6 million tonnes, the Democratic Republic of Congo (DRC) has the largest reserve of Co.	16
Figure 2.1. Study locations in the eastern equatorial Pacific Ocean in the area known as the Clarion-Clipperton Fracture Zone. Area A (AB01) and Area B (AB02) in UK1 are shown	

inset (Source: UKSR (2015)). Both areas were visited in two separate environmental baseline cruises, AB01 was visited in October 2013 while AB02 was visited in March – February 2015. Polymetallic nodules from five box-cores were used in this study, one box core was collected from AB01 while four box cores were collected in AB02, the locations and seafloor bathymetry for these are shown in the next two figures (Figure 2.2 and Figure 2.3).23

Figure 2.2. Seafloor bathymetry and box core site UK1-AB01- BC07 (Source: UKSR (2015)). Box core sampling depth is 4054 m, seafloor is mostly plain and flat with. Further site and nodule description, etc. are shown in Table 2.4 in the results section.24

Figure 2.3. Seafloor bathymetry and box core locations at UK1-AB02 (Source: UKSR (2015)). Samples studied are from four box cores as shown. Depths range from 4200 – 4400 m, bottom seafloor is mostly flat and plan with gentle slopes of less than 3°. This area is also characterised by several seamounts ranging in height from 100 – 700 m. Further site and nodule descriptions etc. are shown in Table 2.4 in the results section.25

Figure 2.4. Flow chart of preparation of digested sample solution using sodium peroxide sintering method for ICP-MS measurement.29

Figure 2.5. Recoveries of trace metals expressed as the percentage of the mean experimental value of six replicate measurements over the theoretical value of the FeMn-1 certified reference material.35

Figure 2.6. Images of nodules from each of the five box core. Nodules from AB01 BC07, AB02 BC06 and AB02 BC19 are similar in morphology (ellipsoidal to botryoidal), texture (smooth-rough) and size (up to 12 cm diameter). Nodules from AB02 BC04 also have

similar morphology to the ones described previously but are much smaller in size (not more than 8 cm diameter). Nodules from these four box cores are easily fragmented as can be seen in the images. Nodules from AB02 BC02 in contrast have a discoidal morphology, smooth texture and are generally small (1 – 3 cm diameter). Nodules from this box core are compacted and are not easily fragmented.....36

Figure 2.7. A typical nodule from the UK1 claim area. Nodules have a smooth top surface (A) where the nodule was recently in contact with seawater and a coarse, rough underside (B) where the nodule sat on the sediment. The rim (C, D) shows the flattened shape of the nodules and marks the seawater/sediment boundary, the rim is botryoidal in most of the nodules.40

Figure 2.8. Whilst most nodules show morphological characteristics shown in Figure 2.7, nodules from box core AB02 BC02 have slightly different characteristics. Nodules have ellipsoid shape and are generally small in size (1 – 3 cm), and well-rounded with smooth surfaces (A) on either side of the rim (B).....41

Figure 2.9. Proportions of Fe, Mn and (Ni+Cu)*10 (by weight) of studied samples plotting in the ternary discrimination diagram of Bonatti, Kraemer and Rydell (1972). Black lines border the different nodule genetic types. A genetic type ‘hydrothermal’ was added for comparison purposes, however, samples used in this study all plot in the mixed-type category.....46

Figure 2.10. REYs bivariate diagrams of bulk nodule samples in graphs of (A) Ce_{SN}/Ce_{SN^*} ratio vs Nd concentration and (B) Ce_{SN}/Ce_{SN^*} ratio vs Y_{SN}/Ho_{SN} (Note: the ratios are plotted based on weight proportions, mg/kg). The diagrams show the geochemical relationship between different genetic types of polymetallic nodules and the distinctive

areas they scatter (Bau et al., 1996; Bau et al., 2014). The formula inset for Ce_{SN}^* indicates the magnitude of the Ce anomaly which is obtained by comparing it to its neighbouring REEs.....46

Figure 2.11. PAAS-normalized REY plots for bulk nodules studied (combined rubble material and individual nodules). The FeMn-1 sample is a certified reference material (CRM) of diagenetic nodules from the Peru Basin and is included for comparison purposes. The PAAS data used is according to Rudnick and Gao (2003). 49

Figure 2.12. TREO grade vs ore tonnage of selected terrestrial REY deposits with a preliminary resource estimation of polymetallic nodules from the CCFZ. The data for the terrestrial deposits were sourced from (Pak et al., 2019), nodule grade data is based on this study while tonnage data was obtained from (ISA, 2010).....59

Figure 2.13. Cobalt grade vs ore tonnage modified after Petavratzi, Gunn and Kresse (2019), of selected terrestrial REY deposits with a preliminary resource estimation of polymetallic nodules from the CCFZ. The CCFZ data plotted by Petavratzi, Gunn and Kresse (2019) was based on data from Hein et al. (2013), which is slightly of higher grade than the one determined in this study (UK1 nodules). However, both show that Co in CCFZ nodules plots in the medium grade and high tonnage category..... 61

Figure 2.14. Nickel grade versus tonnage, modified after Lu, Leshner and Deng (2019) of some known deposits. The CCFZ grade of 1.3% was determined in this work and plots in the intermediate to high grade and high tonnage area. Other data source; Sorowako: Mining Data Solutions (2018); Goro: Mining Technology (2009); Murrin Murrin: Mining Technology (2005)..... 63

Figure 2.15. Copper grade versus ore tonnage, modified from Ero Copper (2019). The CCFZ grade of 0.98% was determined in this work and plots in the medium grade and high tonnage area. Note, some the world’s largest porphyry Cu deposits, which are the primary source of Cu mined today are denoted by the grey triangles..... 64

Figure 3.1. Formation model for hydrogenetic crusts on seamounts (Koschinsky & Halbach, 1995). The process begins with the formation of colloidal phases and scavenging of trace metals. The colloidal phases then precipitate as oxide/oxyhydroxide encrustations on hard substrate rocks of the seamounts. 68

Figure 3.2. Oxidative scavenging mechanism. It begins with the sorption of cations from the seawater by colloidal MnO₂ (step 1) followed by their oxidation on the surface of MnO₂ (step 2) and precipitation on a hard substrate rock or an existing nodule (Takahashi et al., 2007). 69

Figure 3.3. Schematic representation of trends in pore water profile and diagenetic zones in deep sea sediment, adapted from (Froelich et al., 1979). In Zone 1, organic carbon is oxidized by oxygen via aerobic respiration until oxygen is depleted. Oxidation of organic carbon continues in Zones 2 -5 by nitrate and Mn(IV), the oxidation pathway involving Mn(IV) results in its reduction to the soluble Mn(II) which is released into the porewaters and diffuses upward to Zone 3 where it is re-oxidized. In Zones 6 and 7, organic carbon is oxidized by ferric oxides, this results in the reduction of Fe(III) to Fe(II), the latter is then released into the porewater. 71

Figure 3.4. Formation environment of hydrogenetic, diagenetic and mixed-type nodules (ISA, 2010). Nodules grow by precipitation of oxides and oxyhydroxides from bottom

seawater (hydrogenetic), sediment porewaters (diagenetic) and from a combination of both sources (mixed-type). 75

Figure 3.5. General growth model of a mixed-type polymetallic nodule that forms from both hydrogenetic and diagenetic processes [modified from Kuhn et al. (2017)]..... 77

Figure 3.6. SEM backscattered images of five nodules from four box cores (see sample IDs inset) showing concentric layering. Nodules have similar but also varying morphologies, most nodules sit on the sediment surface with part of them buried in the sediment while the top part is exposed as can be seen in A and B where the tops are smoother than the bottoms. Some nodules (C) have a coarse, irregular surface all the way around and were likely completely buried so that the growth of the outer layer was controlled by rapid diagenetic precipitation. In contrast, all the nodules from one of the sampling area (box core AB02 BC02) were mostly smooth throughout with less porosity and were generally small in size (D) and their formation is interpreted as controlled by slow hydrogenetic precipitation while completely exposed (not buried on the seafloor). Hiatuses or growth discontinuities are common in nodules as can be seen in E where the older layers (marked by blue lines) are truncated by more recent layers, with the main hiatus marked in red. 84

Figure 3.7. Typical nodule morphologies of mixed type nodules from the UK claim area (nodule sample: AB02 BC04 N2). The EDS image (A) shows the distribution of the Fe-rich hydrogenetic and Mn-rich diagenetic layers, BSE image (B) shows the morphologies associated with the individual layers with 'H' denoting a predominantly hydrogenetic layer and 'D' a diagenetic layer. 86

Figure 3.8. Nodule sample: AB01 BC07 N1 prior to cutting for SEM analysis with a smooth top (A) and a much coarser underside (B). The sample was fragmented, and the half (marked as 'sample analysed') was the one prepared by cutting from top to bottom for SEM imaging analyses.87

Figure 3.9. SEM-derived textures and distribution of some elements in nodule sample AB01 BC07 N1. The BSE map of the nodule is shown in A while the EDS map is shown in B. More detailed maps of an 8 mm x 3.5 mm nodule area (marked as inset in A) are shown with the distributions of Fe, Mn, Ni, Cu, Al, Si, Ca and P. Note the EDS maps are image mosaics of two or three 'colour-coded' elemental maps overlain on each other and are not individual maps.....88

Figure 3.10. Nodule sample: AB02 BC02 N8b prior to cutting for SEM analysis. Nodule is discoidal to ellipsoidal and well-rounded throughout, is smooth on both sides (images A and B) including rim (C). A broken-off bit of the sample exposes the coarse interior texture (D).89

Figure 3.11. SEM micro-textures and distribution of some elements in nodule sample AB02 BC02 N8b. The BSE image in A shows the internal structures of the nodule sample with concentric layers. The distribution of Fe and Mn are shown in B while the Ca-phosphate and Al-silicate distribution are shown in C and D. Both phases are distributed as discrete phases where they occupy pore spaces, the Ca-phosphate phases can be seen in the diagenetic regions and are less abundant than the Al-silicates.....90

Figure 3.12. Nodule sample: AB02 BC06 N6 prior to cutting for SEM analysis with a smooth top (a) and a much coarser underside (b). The sample was fragmented in two

halves, and the half (marked with arrow and top shown) in image A is the one prepared for SEM where it was cut top to bottom.91

Figure 3.13. SEM microtextures and distribution of some elements in nodule sample AB02 BC06 N4 with the large area BSE (A) and EDS (B) maps shown. Detailed maps of the nodule (marked as inset in A and B) are shown with the distribution of Fe, Mn, Ni, Cu, Al, Si, Ca and P. An obvious hiatus is marked in the detailed map as well as the predominantly diagenetic (D) and hydrogenetic (H) regions.92

Figure 3.14. Large area BSE (A) and EDS (B) maps of nodule sample AB02 BC06 N3. The EDS map shows the distribution of the Fe-rich hydrogenetic and Mn-rich diagenetic layers as well as the 'area mapped' shown inset where detailed mapping by deconvolution of energy peaks was performed, the images of which are presented in the next figure (Figure 3.15).94

Figure 3.15. SEM photomicrographs of the hydrogenetic and diagenetic regions of a typical mixed type nodule from the UK claim area (AB02 BC06 N3) with the distribution patterns of different metals. The Fe-rich layer in A shows the hydrogenetic regions while the diagenetic regions are represented by the Mn-rich regions. Images B – E show the distribution of Ni, Cu, Co and Pb while F – H show the distribution patterns of the Al-silicate, Ca-phosphate and Ba-sulphate phases.....95

Figure 3.16. A fitted EDS spectrum obtained by SEM analysis on a nodule hydrogenetic layer showing only the energy window of where Ce peaks occur. The yellow banded region is the overall spectrum of the sample area analysed with the fitted spectrum shown in pink. The brown region is the Ce profile with three peaks (labelled inset), the

peaks (marked by green lines) show the emission lines of Ce which all appear below background levels.96

Figure 3.17. Imaging analysis of a nodule sample (AB02 BC04 N2) with the SEM EDS map of Fe and Mn is shown in A. A 25x25 µm section (inset in A) of the sample showing both layer types is shown in B with maps of Fe, Mn, Ce and Ba using µXRF. The spectrum of the hydrogenetic layer is shown in C with the emission lines of Ce indicating that it is distributed in the hydrogenetic layer.98

Figure 3.18. Fitted EDS spectrum obtained by SEM-EDS analysis on a nodule hydrogenetic layer showing only the energy window of where Co peaks occur. The yellow banded region is the overall spectrum of the sample area analysed with the fitted spectrum shown in pink. The brown region is the Co profile and shows the location of the $K\alpha_1$ and $K\alpha_2$ emission lines of Co (in red). The two Co emission lines confirm that the 'deconvolution of peaks' method used here is capable of separating out the Co and Fe peaks, which can be seen in image B where it appears above the background fitted spectrum as tail on the Fe $K\beta_1$99

Figure 3.19. A broken-off chip of nodule sample AB02 BC06 N1 mounted on a stub. Sample area imaged by detailed SEM analysis is marked as 'area imaged'.100

Figure 3.20. SEM secondary electron images (nodule sample AB02 BC06 N1) of platform-like support structures with holes filled by fibrous rosette-like structures. The structures are overgrown by platy phyllosulfates (shown inset in A). The images were acquired by scanning the surface of an area (marked in Figure 3.19) on a broken-off chip of the nodule sample.101

Figure 3.21. Nodule sample AB02 BC06 N4 with the Fe-rich hydrogenetic and the Mn-rich diagenetic layers (left) and the twelve regions marked in red sampled using a micro-drill (right). The numbers indicate layer number, some regions are thin strips and the number is placed beside the marked strip. Some regions cover an area and the number is placed in the area sampled. Layer 12 covers both an area plus a thin strip. 102

Figure 3.22. Nodule sample AB01 BC07 N1 with the Fe-rich hydrogenetic and the Mn-rich diagenetic layers (left) and the twelve regions marked in red sampled using a micro-drill (right). The numbers indicate layer number, some regions are thin strips and the number is placed beside the marked strip. Some regions cover an area and the layer number is placed in the area sampled. Layer 5 covers both an area plus a thin strip. 103

Figure 3.23. Typical nodule morphologies of mixed type nodules from the UK claim area (nodule sample: AB02 BC06 N1). The EDS image (A) shows the distribution of the Fe-rich hydrogenetic and Mn-rich diagenetic layers, BSE image (B) shows the morphologies associated with the individual layers as well as their Mn/Fe ratios. Diagenetic layers typically have Mn/Fe values of more than 3 while hydrogenetic layers have values less than 3. 113

Figure 3.24. SEM secondary electron images (nodule sample AB02 BC06 N1) of biogenic structures with holes filled by fibrous rosette-like structures. The structures are overgrown by platy phyllo-manganates. 115

Figure 3.25. Composition of biogenic material based on SEM-EDS which shows that they are comprised of calcareous and siliceous material. 116

Figure 3.26. SEM-EDS composition of Mn oxides overgrowth (spectrum 44) and rosette-like spheres (spectrum 47) infilling holes on the surface of the biogenic structures. The

compositions show that the rosette-like structures and the overgrowths are not Mn-oxides.	117
Figure 3.27. SEM-EDS map of an area of nodule AB02 BC19 N3 showing discrete CaP phases in the diagenetic and sediment-rich regions.	121
Figure 3.28. REY patterns normalised to PAAS abundances of the twelve individual layers of nodule sample AB02 BC06 N4. The growth layer type for each individual layer are shown inset.	125
Figure 3.29. REY patterns normalised to PAAS abundances of the twelve individual layers of nodule sample AB01 BC07 N1. The growth layer type for each individual layer are shown inset.	126
Figure 3.30. REY distribution patterns of North Pacific (NW) seawater (Alibo & Nozaki, 1999), North Pacific crusts, diagenetic nodules of Peru Basin and hydrogenetic nodules from Cook Islands (Hein et al., 2013), porewaters from CCFZ (Paul et al., 2019b) and bulk nodules: AB02 BC06 N4 and AB01 BC07 N1 from this study which were used for the layer chemical analyses. The REY patterns are normalised to PAAS abundances.	127
Figure 4.1. Schematic representations of the microstructures of the phylломanganates: 7 Å phylломanganate (Na-birnessite) and 10 Å phylломanganate (Mg-buserite), and the tectomanganate todorokite, modified after Hao-Jie et al. (2011).	132
Figure 4.2. Simple leaching recoveries of major and trace metals carried out on nodule sample AB02 BC06 N4 for method development purposes. Leaching was carried out using three leaching agents; (A) 0.1 M acetic acid buffered to pH 5 using Na acetate targets the exchangeable cations and the carbonates; (B) 0.5 M HCl dissolves the easily reducible fraction; (C) 0.2 M oxalic acid (pH3)/ammonium oxalate attacks the	

moderately reducible fraction. The leaching experiments were carried out at room temperature at various leaching times, (A) was done at 5 hours while (B) and (C) were performed at the times shown inset in the respective graphs.....138

Figure 4.3. Major and trace metal leaching recoveries of three nodules from the Eastern Equatorial Pacific and one from the Peru Basin (FeMn CRM) with (1) 0.1 M acetic acid/Na acetate pH 5, (2) 0.5 M HCl, (3) 0.2 M oxalic acid/ammonium oxalate pH 3.5 and (4) concentrated nitric acid.144

Figure 4.4. Total fraction not recovered by sequential leaching with the four leaching agents, expressed in percentage for each element in the four samples studied. The values were obtained by subtracting the combined recovery (of the four leaching steps – Figure 4.3) from 100%.....145

Figure 4.5. XRD patterns of the diagenetic versus hydrogenetic layers of nodule sample AB02 BC06 N4 before (40°C) and after heating (105°C). The d-spacing on the x-axis were obtained by converting from 2 theta using Bragg's law ($\sin \Theta = n\lambda/2d$; where $n = 1$ and λ for a Cu source = 1.5418 Å. Corrections were done on the curves to remove background signal and plotted using the same intensity scale, but the scale only applies to the lower curve, and the curves are stacked by using a y-axis off-set for the upper three patterns. XRD plots of the same samples without background subtraction are shown in the next figure (Figure 4.6).....149

Figure 4.6. XRD patterns of the diagenetic versus hydrogenetic layers of nodule sample AB02 BC06 N4 before (40°C) and after heating (105°C) without background subtraction. All four patterns were plotted using the same intensity scale, but the scale only applies to the lower curve, and the curves are stacked by using a y-axis off-set for the upper

three patterns. A comparison between the hydrogenetic versus diagenetic layers' patterns shows that the former have weaker intensity peaks compared to the latter.150

Figure 4.7. XRD patterns of nodule sample AB02 BC06 N4 before and after sequential leaching with 0.1 M acetic acid/Na acetate pH 5 and 0.5 M HCl, before (40°C) and after heating (105°C). The d-spacings on the x-axis were obtained by converting from 2θ using Bragg's law ($\sin \Theta = n\lambda/2d$; where $n = 1$ and λ for a Cu source = 1.5418 Å. Corrections were done on the curves to remove the background signal and plotted using the same intensity scale, but the scale only applies to the lower curve, and the curves are stacked by using a y-axis off-set for the upper three patterns. XRD plots of the same samples without background subtraction are shown in the next figure (Figure 4.8).151

Figure 4.8. XRD patterns (without background correction and plotted against angle 2 theta) of nodule sample AB02 BC06 N4 before and after sequential leaching with 0.1 M acetic acid/Na acetate pH 5 and 0.5 M HCl, before (40°C) and after heating (105°C). The curves are plotted using the same intensity scale, but the scale only applies to the lower curve, and the curves are stacked by using a y-axis off-set for the upper three patterns.152

Figure 4.9. REY distribution patterns of the three nodule samples plus the FeMn CRM from the Peru Basin normalised to PAAS for their HCl, buffered oxalic acid and concentrated nitric acid leaches. The REY distribution pattern for North Pacific (NW) seawater (Alibo & Nozaki, 1999) and North Pacific crusts (Hein et al., 2013) are included in the plots for AB02 BC06 N5.....160

Figure 5.1. SEM-EDS image of synthetic Na-birnessite (image a). The synthesised phyllosilicate is crystalline and has platy morphology with rosettes of hexagonal shaped crystals. The composition of the Na-birnessite is confirmed by SEM-EDS point analysis (area shown inset in image a), spectrum is shown in image b.168

Figure 5.2. SEM-EDS image of synthetic La+Nd+Yb doped birnessite (image a). The synthesised phyllosilicate is crystalline and has platy morphology with rosettes of hexagonal shaped crystals. The composition of the REY-birnessite is confirmed by SEM-EDS point analysis (area shown inset in image a), spectrum is shown in image b. The EDS spectrum shows that some of the Na still remain after the exchange and the La+Nd+Yb exchanged birnessite shows exchange capacity in the order: Yb>Nd>La.169

Figure 5.3. EDS images and spectra of Na-birnessite before cation exchange (a) and after exchange with Cu (b), Nd and La+Nd+Yb cations (c and d). Note that the platy birnessites are less crystalline after the exchanges compared to the Na-birnessite precursor mineral.170

Figure 5.4. La+Nd+Yb birnessite after cation exchange. Note that the platy birnessite crystals are slightly rounded and twisted on the edges compared to the original Na-birnessite (Figure 5.1).170

Figure 5.5. XRD patterns for Na-birnessite before cation exchange and after exchange with Ca, Mg, Cu and Co. Patterns shown with background subtracted and with regular vertical offsets for clarity.172

Figure 5.6. XRD patterns for Na birnessite before cation exchange and after exchange with the rare earth elements (Note: REE-doped = La+Nd+Yb combined). Patterns shown with background subtracted and with regular vertical offsets for clarity.173

Figure 5.7. XRD patterns (without background correction) for Na birnessite before and after cation exchange and plotted against 2 theta angle. The curves are plotted using the same intensity scale, but the scale only applies to the lower curve, and the curves are stacked by using a y-axis off-set for the upper spectra. 174

Figure 5.8. Schematic of the structural models of the two types of 10 Å buserite. The thermally unstable buserite-I loses one layer of water and collapses to 7 Å birnessite in air, upon heating to 105°C or in vacuum. The thermally stable buserite-II contains high proportions of interlayer cations above vacancy sites which prevent it from collapsing to birnessite. The models are adapted from Pal'chik, Grigor'eva and Moroz (2013). 180

Figure 5.9. Comparison between the XRD patterns of a natural nodule sample (dried at 40°C) and that of a combined Mg-doped and Ca-doped synthetic phyllosilicate (Mg-Ca mix). The individual patterns of both Mg- and Ca-doped phyllosilicates (shown in graph) were combined in the ratio 5:1 based on their ratio in seawater. Note that the samples (natural and synthetic) were dried in the same way (40°C for 48 hours) so that they are directly comparable. The curves are plotted using the same intensity scale, but the scale only applies to the lower curve, and the curves are stacked by using a y-axis off-set for the upper three patterns. 181

Figure 6.1. Image of nodule sample AB02 BC06 N3 before cutting and sampling of the individual layers. 193

Figure 6.2. Mosaics of SEM backscatter images (A) and EDS chemical maps for Fe and Mn (B) of nodule sample AB02 BC06 N3. The individual layers sampled shown by their sample numbers..... 194

Figure 6.3. SEM-EDS image of nodule sample showing the predominantly Fe-rich hydrogenetic (yellow) and Mn-rich diagenetic (blue) layers and the vertical profile with the individual layers sampled. The Nd and Sr concentrations and isotopic compositions based on ϵ_{Nd} values and $^{87}Sr/^{86}Sr$ ratios for the eleven layers sampled are also shown as well as the ϵ_{Nd} values of the North Pacific Deep Water (Abbott, Haley & McManus, 2015; Piepgras & Jacobsen, 1988) and the $^{87}Sr/^{86}Sr$ value of the present-day seawater (McArthur, Howarth & Shields, 2012) (both marked in grey). In the graphical diagram, the hydrogenetic layers are colour-coded yellow while the diagenetic layers are colourless.197

Figure 6.4. Nd isotopic composition based on ϵ_{Nd} values of the individual layers and compared to that of NPDW. Also included are the ϵ_{Nd} values of the North American-derived sediments and East Asian dust (both have lower ϵ_{Nd} values compared to NPDW) and sediments derived from basaltic Pacific Ocean crust and seamounts which have higher ϵ_{Nd} values when compared to NPDW. The two arrows show the younger region of the nodule (layers 1 -3) with generally lower ϵ_{Nd} values and the older regions (layers 4 -11) with higher ϵ_{Nd} values.202

Figure 6.5. Seawater Sr evolution in the past ~1.2 Ma based on data from Hodell, Mead and Mueller (1990) of $^{87}Sr/^{86}Sr$ ratios measured in planktonic foraminifera in sediments cores from the southwest Pacific. The grey region shows the range of $^{87}Sr/^{86}Sr$ ratios measured in the nodule sample studied which corresponds to seawater values up to 230 ka.203

Figure 7.1. Schematic of the proposed growth model of mixed-type nodules from the CCFZ. Nodules grow by both diagenetic and hydrogenetic precipitation. Hydrogenetic growth begins with the formation of colloidal FeOOH and MnO₂ phases in oxic seawater,

these phases possess surface charges, thereby enabling the adsorption of dissolved cations and anionic complexes. The colloidal oxide/oxyhydroxide phases then precipitate onto a hard rock substrate or an existing nodule and hence forming a hydrogenetic growth layer. In contrast, diagenetic reactions in porewaters starting with the oxidation of organic matter by aerobic bacteria and then by MnO_2 results in the mobilization and upward diffusion of Mn to the sediment where it precipitates as MnO_2 and hence forming a diagenetic growth layer. Both growth processes are associated with metal enrichment with MnO_2 as vernadite intergrown with FeOOH as the main host phases in hydrogenetic layers and MnO_2 as 10 \AA phyllo-manganate in diagenetic layers. Another source of cations for diagenetic growth is from dissolved nodules, cations released are mobilized in porewaters and diffuse to the oxic layer where they are incorporated into the phyllo-manganate structure. Neodymium in the nodules is sourced from two different sources, with Nd in hydrogenetic layers from terrigenous and aeolian sources while basaltic crust as the main source for diagenetic layers.212

TABLE OF TABLES

Table 2.1. Major interferences and their respective percentage corrections.	31
Table 2.2. Blanks and detection limits of trace metals from ICP-MS measurements. The blank concentrations are as-measured values and dilutions are not taken into account.	32
Table 2.3. Accuracy and repeatability data using FeMn-1 CRM. Note; n = number of measurements. Note; the uncertainty and RSD values are based on a 95% confidence interval.	33
Table 2.4. Box core geographical positions, water depths and descriptions of box core locations and nodules. Box core sample densities in kg/m ² are given including information on whether the nodules are exposed or covered by sediments (note; nodule densities at different sediment depths are shown in the next table) (Source: UKSR). ..	38
Table 2.5. Nodule abundance (in percentage) at different sediment depths from the surface to below 10 cm in each of the box cores. Most nodules were collected from the surface (0 – 2 cm) of the sediments except for box core AB02 BC06 and AB02 BC19 where varying proportions were collected at different depths (Source: UKSR).	39
Table 2.6. Shear strengths measurements in kilopascal (kPa) of the box core sediments at three depths.....	39
Table 2.7. Bulk chemical compositions of polymetallic nodules from rubbles of five box cores and four individual nodule samples. Note; LREYs = Light REYs, TLREYs = Total Light REYs, HREYs = Heavy REYs, THREYs = Total Heavy REYs, TREYs = Total REYs. The major oxides (including BaO) were analysed on a fused lithium tetraborate bead by XRF, minor and some trace metals (Co, Ni, Cu, Zn, Sr, Zr, Nb, Mo, Sb, W) were analysed on a pressed	

powder by XRF. The REYs, Pb, Th and U were determined by ICP-MS after sample decomposition by sodium peroxide sintering. The relative standard deviation expressed in percentage (RSD%) of the mean of the combined rubble material for each of the five box cores is based on a 95% confidence interval.42

Table 2.8. Total REYs and the percentage of HREYs from known areas with high nodule abundance and exploitation interests. Data from: 1 = (Rudnick & Gao, 2003); 2 = (Pattan & Parthiban, 2011), (Pattan et al., 2001), (Baturin & Dubinchuk, 2010); 3= (Hein et al., 2015); 4 = (Hein et al., 2013); 5 = (Kato et al., 2011); 6 = (Yang et al., 2011).56

Table 2.9. Marine deposits (Co-rich crusts, polymetallic nodules) with their Co concentrations. Two terrestrial Co deposits from the Democratic Republic of Congo (DRC) and Kalgoorlie, Australia are included for comparison. Data from: [1] (Rudnick & Gao, 2003); [2, 4] (Hein et al., 2013); [3] (Hein et al., 2015); [5] (Slack, Kimball & Shedd, 2017); [6] (Petavratzi, Gunn & Kresse, 2019).60

Table 3.1. Typical set-up conditions for a large area mapping analysis.81

Table 3.2. REY content in the individual layers of nodule sample AB02 BC06 N4. The columns are coloured to show the different layer types, yellow = hydrogenetic, blue = diagenetic, orange = mixed. The SEM image showing the different layers (1 – 12) sampled is shown in Figure 3.21. Note: LREE = Light REE, HREY = Heavy REY. The bulk nodule REYs composition for this nodule sample and the crustal abundance (Rudnick & Gao, 2003) of the REYs are also shown. Sample mass analysed depends on layer thickness and the amount of material that can be obtained from drilling the layer (typically 10 – 100 mg), approximate dilutions (500 – 4500x) were then carried out to determine final concentrations for each layer.106

Table 3.3. REY content in the individual layers of nodule sample AB01 BC07 N1. The columns are coloured to show the different layer types, yellow = hydrogenetic, blue = diagenetic, orange = mixed. The SEM image showing the different layers (1 – 10) sampled is shown in Figure 3.22. Note: LREE = Light REE, HREY = Heavy REY, LOD = Limit of detection, n/a = measurement not carried out. The bulk nodule REYs composition for this nodule sample and the crustal abundance (Rudnick & Gao, 2003) of the REYs are also shown. Note: the crustal abundance values for Co, Ni, Cu and Zn are in ppm. . Sample mass analysed depends on layer thickness and the amount of material that can be obtained from drilling the layer (typically 10 – 100 mg), approximate dilutions (500 – 4500x) were then carried out to determine final concentrations for each layer. The growth rate (GR) of individual layers determined for this sample is based on the Co, Fe and Mn content using the Co chronometry of Manheim and Lane-Bostwick (1988); $GR = 0.68 / (Co_n)^{1.67}$ where $Co_n = Co \times 50 / Fe + Mn$ with Co, Mn and Fe concentrations in wt%, note SD = standard deviation.....107

Table 3.4. Percentage total REY by mass in hydrogenetic layers of nodules AB02 BC06 N4 and AB01 BC07 N1. The values were obtained based on the total REY in hydrogenetic layers as a percentage of the relative hydrogenetic layer thickness of 20%.....111

Table 3.5. Growth rate and metal enrichment relationship between hydrogenetic and diagenetic layers in mixed-type nodules. The growth rates presented are for nodule sample AB01 BC07 N1 (Table 3.3).....118

Table 4.1. Compositions of Ca and P in wt% and converted to atomic proportions, before and after sequential leaching with 0.1 M acetic acid, 0.5 M HCl, 0.2 M oxalic acid and concentrated nitric acid of three samples. The before-compositions were obtained by XRF while the after-compositions were determined by SEM-EDS.147

Table 5.1. The interlayer spacings of the exchanged phyllosulfates. (Note: nd = not determined)	172
Table 5.2. Ionic radii and hydration energy values for REE and other cations [values for monovalent and divalent cations are obtained from Rosseinsky (1965), values for REEs are obtained from Moldoveanu and Papangelakis (2013)]. The interlayer spacings by previous workers from cation exchange experiments of air-dried exchanged synthetic birnessite/buserite are also included for comparison. (Note: nd = means no data). ..	176
Table 6.1. Location and description of nodule sample (AB02 BC06 N3) used in this study. Note, the bathymetry map of the box core location for this nodule sample can be seen in Figure 2.3 in chapter 2.	192
Table 6.2. Results table showing the Nd and Sr isotope ratios of the individual nodule layers.	195

Chapter 1

1 General introduction

1.1 Mineral resources from the deep sea

The Earth's oceans cover more than two thirds of planet and store 97% of its water. They regulate global climate and provides natural resources such as food, materials, medicine and energy for humans (Visbeck *et al.*, 2014). The oceans are essential for international trade, recreational and cultural activities and are home to the world's largest connected ecosystem (Chesters & Jickells, 2012).

The ocean has an average depth of 3700 m and extends from the continental margins to the deepest regions (Charette & Smith, 2010). It can be divided into two categories: the continental margin and the abyssal plain or the deep-sea. The continental margin which extends from the continents can be further divided into two categories: the continental shelf where water depths are generally less than 200 m and the continental slope. The deep-sea is the region beyond 200 m depth where there is very little or no sunlight penetration. The deep-sea consists of the abyssal floor, oceanic rise, oceanic ridge, and deep-sea trench provinces. These geological settings and geomorphological features and the many diverse range of processes associated with their evolution result in the deep seafloor hosting different types of mineral deposits. The ocean is also a major sink for much of the material mobilized during both natural crustal weathering and anthropogenic activities (Chesters & Jickells, 2012; Jones *et al.*, 2012; Zhu *et al.*, 2013). This material, which includes dissolved and particulate components, can be transported to the oceans by rivers or directly from the continents and over geological time scales can end up enriched in a range of deep-sea mineral deposits (ISA, 2010).

1.2 History of deep-sea mineral exploration

The first known discovery of deep sea minerals, in the form of polymetallic nodules (also known as manganese nodules or ferromanganese nodules), was made during the Challenger expedition (1872 – 1876) where their economic potential was also acknowledged (Murray & Renard, 1891b). Initial chemical analysis carried out on these nodules showed that they were composed of almost entirely Mn oxides and thus, the name 'manganese nodule' was used thereafter. Subsequently John Mero, after finishing his PhD on this subject, published his findings in the journal *Economic Geology* (Mero, 1962) and later as a book (Mero, 1965) unravelled the economic potential of polymetallic nodules based on their Mn, Ni, Cu and Co contents. Based on his findings, Mero predicted that mining of polymetallic nodules would commence in 20 years time. This prediction, plus the increasing prices of metals such as Ni, led private companies and governments to fund efforts to develop these resources from the 1970s to 1990s in the north-eastern Pacific between the Clarion and Clipperton Fracture Zones (CCFZ). Due to falling global metal prices coupled with the need for proper environmental considerations and legal implications, mining of polymetallic nodules never happened. However, the exploration of polymetallic nodules still continues, which has led to a better understanding of these deposits today, as well as increased commercial interest in mining them. Continued nodule research during the 1980s and 1990s also highlighted another type of deep sea Fe-Mn deposit type called Fe-Mn crusts which also have potential for exploitation (Lusty & Murton, 2018).

Warm saline waters in the Red Sea, later known as the Atlantis Deep II, were first discovered by the Swedish research vessel *Albatross* in 1948 (Bruneau, Jerlov & Koczy, 1953). Further investigations carried out in the 1960s led to the discovery of valuable

metals such as Zn, Cu, Ag and Au in sulphide-rich sediments underlying the warm saline waters (Danielsson, Dyrssen & Granéli, 1980; Degens & Ross, 2013). The potential source of the metals were of debate during that time and although volcanism had long been considered (Murray & Renard, 1891a), the discovery of submarine thermal vents later concluded sub-sea floor convective circulation of sea water and venting of hydrothermal fluids provides a major source of these metals (Corliss *et al.*, 1979). Further, investigations of valuable metals in hydrothermal vents were later recorded following the discovery of black smokers at the East Pacific Rise mid-oceanic ridge spreading centre in 1979 (Francheteau *et al.*, 1979; Spiess *et al.*, 1980). It is now widely recognized that hydrothermal vents are an important source for base metals (Zn, Cu, Pb, Sn), precious metals (Au, Ag) and a number of special metals (In, Ga, Ge) (Herzig, Petersen & Hannington, 2002).

1.3 Types of deep-sea ferromanganese deposits

1.3.1 Polymetallic nodules

Polymetallic nodules are concretions of manganese oxides and iron oxyhydroxides found on the seafloor and are mostly abundant on the abyssal plains at depths of 3500 – 6000 m. They generally range in size from 2 – 12 cm and come in various shapes including spherical, ellipsoidal and discoidal (Kuhn *et al.*, 2017). Nodules are classified based on the type of fluid they form from; nodules that form by precipitation from oxic/suboxic bottom seawater are known as hydrogenetic nodules, examples of nodules of this genetic type are nodules from the Cook Islands (Cronan & Hodkinson, 1993; Hein *et al.*, 2015) and the Blake Plateau (Hawkins, 1969; Pratt & McFarlin, 1966). Nodules that

form by precipitation from oxic/suboxic porewaters are known as diagenetic nodules, and the Peru Basin nodules are of this genetic type (Reyss *et al.*, 1985; Von Stackelberg, 1997). Nodules grow by accretion of oxide layers with different growth rates depending on the mechanism of formation. Hydrogenetic nodules grow at very slow rates of typically 1 – 10 mm/Ma (Hein *et al.*, 2015) due to the slow precipitation from the bottom seawater while diagenetic nodules grow at much faster rates (20 – 250 mm/Ma) due to rapid diagenetic precipitation (Von Stackelberg, 1997). Nodules from some ocean basins form from both mechanisms and are therefore known as mixed-type nodules, examples of mixed-type nodules are nodules from the Eastern Equatorial Pacific (ISA, 2010; Kuhn *et al.*, 2017; Wegorzewski & Kuhn, 2014) and the Central Indian Ocean Basin (Jauhari, 1987; Mukhopadhyay & Ghosh, 2010). Polymetallic nodules are mostly made up of Mn and Fe but are also enriched in some economically important metals such as Ni, Cu, and Co and there is also growing interest in their content of Rare Earth Elements plus yttrium (REY). The growing interest in their REY content is largely driven by their increasing usage in various technological applications, such as Nd and electromagnets (Haque *et al.*, 2014).

1.3.2 Occurrence and distribution

Polymetallic nodules are found in most oceans of the world. However, the seabed in the Pacific Ocean holds the highest abundance of nodules when compared to other ocean basins such as in the Indian and Atlantic Oceans (Valsangkar & Rebello, 2015).

Nodules can be found in various geological settings on the ocean floor. These include seamounts or knolls, oceanic plateaus, submerged calderas, fracture zones and abyssal

plains (Halbach, 1984; Hein *et al.*, 1997). Nodules of significant economic interest such as in the Pacific Ocean are found on abyssal plains. On the seabed, nodules are predominantly found on the surface of sediment-covered abyssal plains at depths of approximately 3500 to 6500 m (Hein *et al.*, 2013). At these depths, temperatures are just above freezing, pressures are high and sunlight is absent (Hein & Petersen, 2013). The occurrence of nodules on the ocean floor varies: they can be found in small to large quantities lying on the seabed, partly buried in the sediment or even completely buried (Hein *et al.*, 2013). Nodules are most abundant in oxygenated environments with low sedimentation rates and reach their greatest concentration at or below the calcium compensation depth (Glasby, 1986). Siliceous sediments are found to be the most favourable substratum for nodule growth, as their high porosity facilitates the upward diffusion of elements through the pore fluids in the sediment column (Mukhopadhyay & Ghosh, 2010).

The most extensive deposits have been found in the Pacific Ocean, especially between the Clarion and Clipperton Fracture Zones (CCFZ), the Peru Basin and the Penrhyn-Samoa Basins (Hein *et al.*, 2013). A large nodule field also occurs in the Central Indian Ocean Basin (CIOB) (Mukhopadhyay & Ghosh, 2010; Pattan & Parthiban, 2011). Fields may also occur in the Atlantic and Arctic Oceans, however, these areas are relatively poorly explored at present in terms of nodule abundance and distribution compared to the CCFZ and the CIOB (Hein *et al.*, 2017; Hein & Koschinsky, 2014a). The CCFZ, however, is the area of greatest economic interest, particularly because of high nodule abundances with high concentrations of Ni and Cu (ISA, 2010). The distribution of nodule abundance in areas of economic interest is shown in Figure 1.1.

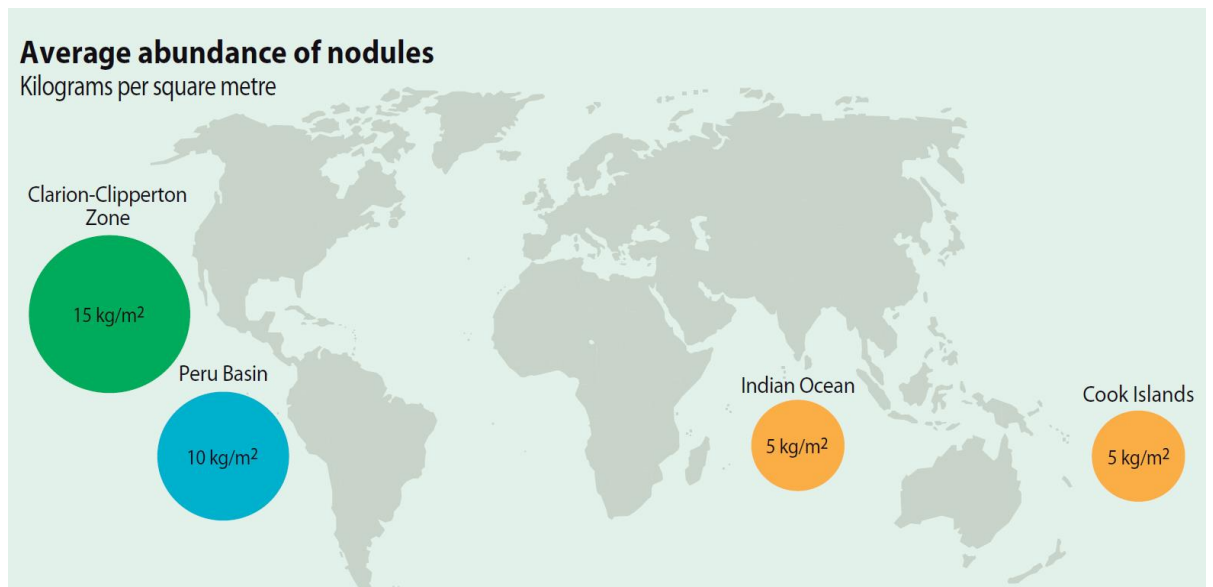


Figure 1.1. Estimates of average nodule abundance in the four major locations in 2013 (Hein & Petersen, 2013).

Although global nodule abundance varies across ocean basins, abundances can also vary over a small area. For example nodule coverage can be as high as more than 75% at a particular area and just a few hundred meters away can go down to almost zero (Glasby, 1986). The shape and size of nodules can also vary over the same distance. Such variability of nodule distribution can be due to local environmental factors at the deposition site. For example, the presence of small scale topographic variations can cause channelling by bottom water currents which can prevent sediment accumulation and thus leads to a localized high nodule abundance at the sediment surface (Cronan, 1977).

1.3.2.1 The Clarion-Clipperton Fracture Zone

The CCFZ is the area bound by the Clarion Fracture Zone in the north, the Clipperton Fracture Zone in the south, the East Pacific rise in the East and the Line Islands (of Kiribati

and the United States territories) in the West (Figure 1.2). This area is of greatest commercial interest in terms of polymetallic nodules beyond national jurisdictions. The CCFZ falls under the jurisdiction of the International Seabed Authority (ISA), an organisation established under the 1982 United Nations Convention on the Law of the Sea in which all parties subscribing to this convention take part. At present the Authority has already granted exploration licences to sixteen contractors who are currently carrying out exploration activities in the CCFZ (ISA, 2016). Similarly, the authority has granted one exploration licence to the Indian Government for exploration activities in the Indian Ocean (ISA, 2016). These are the only two areas of current polymetallic nodule exploration with the CCFZ obviously the one with more exploration activities occurring. The location of the CCFZ plus the different contractors carrying out exploration activities in the CCFZ are shown in Figure 1.3.

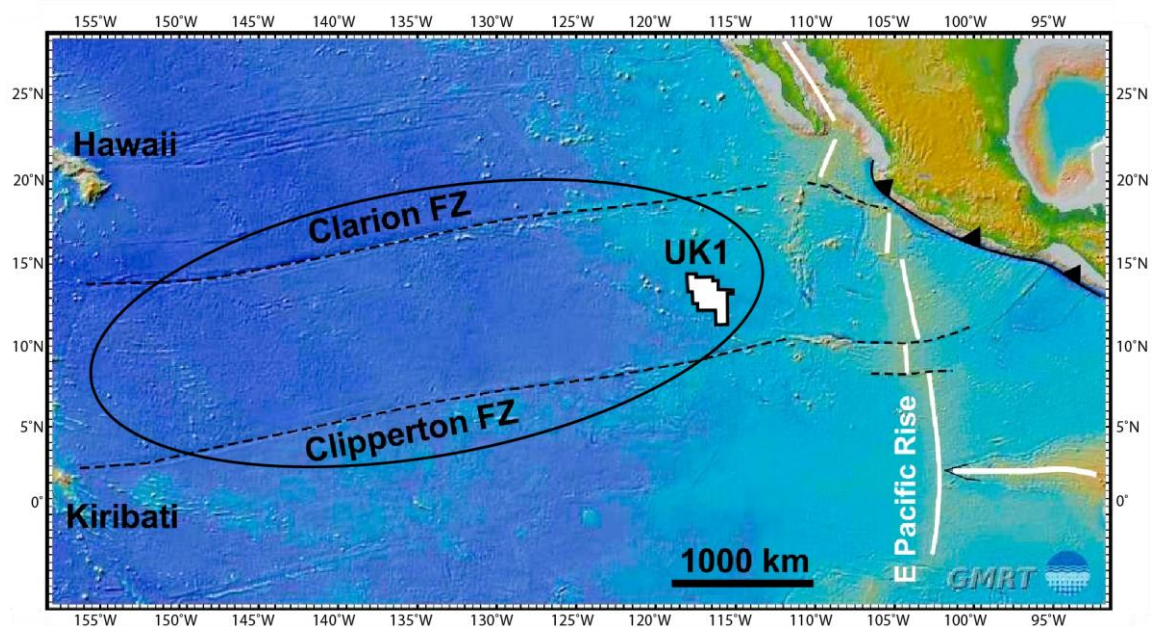


Figure 1.2. Location of the Clarion-Clipperton Fracture Zone (CCFZ) in the Eastern Equatorial Pacific and the UK claim area shown inset as UK1.

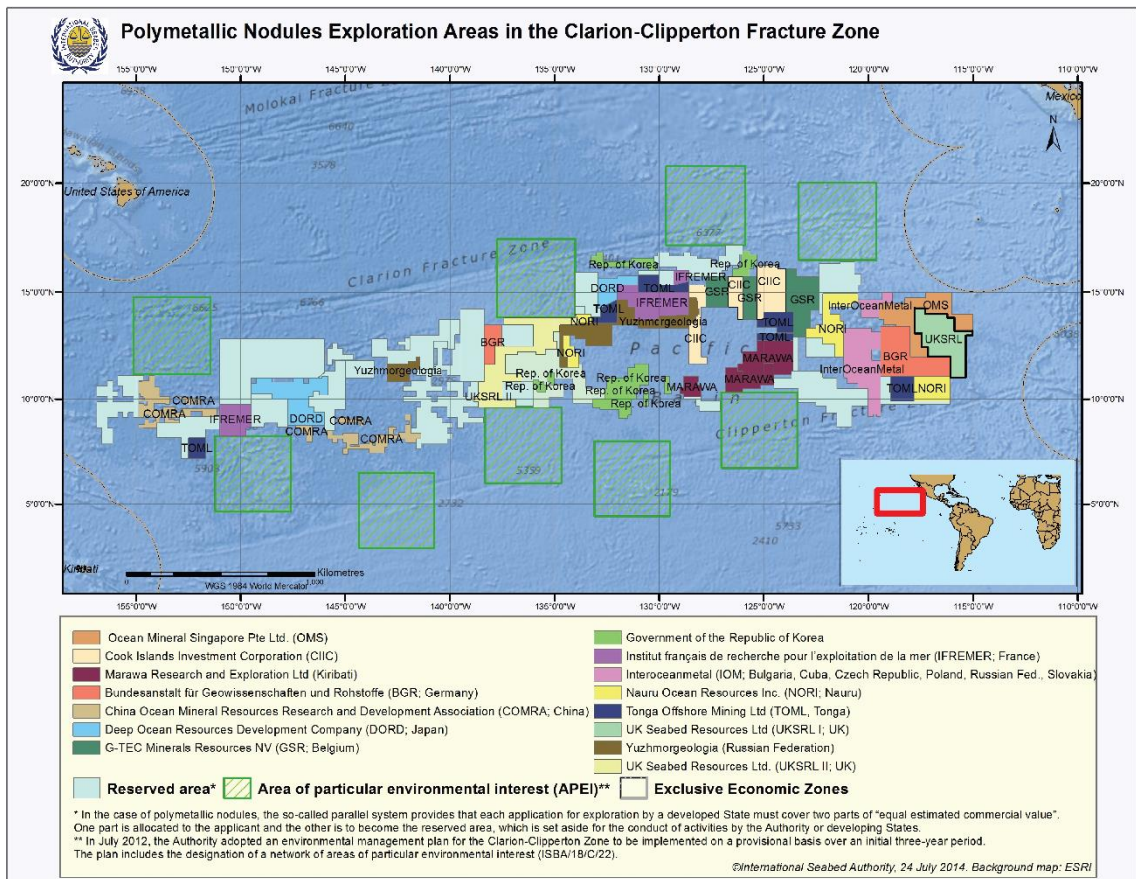


Figure 1.3. Exploration areas in the CCFZ, colour-coded for the different contracting parties (ISA, 2015). The UK Claim Area, which is where samples in this study come from, is marked with a thicker outline in the map. The map also shows the areas of particular environmental interest (APEI) designated as part of the environmental management plan as areas unaffected by commercial extraction of nodules in order to preserve marine ecosystem health and function.

The CCFZ covers an area of 4.5 million km² including an area of 4.2 million km² of commercial interests (ISA, 2010). Average nodule densities in the CCFZ were reported to be 15 Kg wet weight per m² and rarely exceed 75 Kg wet weight per m² (Hein & Koschinsky, 2014a) and are highest between 12 and 16° N latitude at depths between 4100 – 4200 m (ISA, 2010).

The increasing commercial interest in CCFZ nodules is particularly due to their metal content. The CCFZ has been reported to have more metal (such as Mn, Te, Ni, Co and Y)

reserves (up to 6000 times) than the entire global terrestrial reserve base for those metals (Hein & Petersen, 2013). Apart from that, the nodules also contain significant amounts of other important metals such as Cu, Mo, W, Li, Nb, and rare earth oxides compared to the global land-based reserves (Hein *et al.*, 2013).

1.3.3 Ferromanganese crusts

Ferromanganese crusts (also known as cobalt-rich crusts) are deep-sea deposits with hydrated oxide layers with thicknesses ranging from less than 1 cm to 25 cm that occur as encrustations on the surface hard substrate rocks such as basalts, limestone rocks and consolidated clay deposits (Halbach, Jahn & Cherkashov, 2017b). They occur at depths of 1000 – 5000 m and form by (hydrogenetic) precipitation from the bottom oxic seawater although the crusts in the Atlantic Ocean are usually associated with hydrothermal activity at seafloor spreading centres. They are found in all global oceans and only occur in geomorphological settings where rock surfaces are free of sediments, such as on the terraces and flanks of seamounts, submerged volcanic mountain ranges and guyot platforms (Halbach, Jahn & Cherkashov, 2017b). The age of crusts can range from a few Ma up to 75 – 80 Ma (Li *et al.*, 2008), with the accretion of individual oxide layers at rates of 1 – 10 mm/Ma (Halbach, Jahn & Cherkashov, 2017a). The slow growth rates allow the incorporation of trace metals onto hydrated oxide and oxyhydroxide phases in the water column and at the crust surfaces.

Crusts are mostly made up of Mn, Fe and P (P mainly in older generation crusts), however, they also contain a range of minor metals such as Co, Ni, Ti, Cu, Zn, Ba, Pb, Sr, and trace elements including the REYs, Mo, V, W, Nb, Te, Ga, Pt and Pd) (Halbach, Jahn

& Cherkashov, 2017a). The richest crust deposits are found in the Western Pacific Ocean where there are more seamounts and submarine mountain ranges compared to other parts of the Pacific Ocean, Atlantic and Indian Oceans, and therefore, the Western Pacific has the most prospect in terms of resource potential.

1.4 Drivers for deep-sea minerals extraction

Metals have been used by humans since the Bronze Age for various purposes that contributed to the development of the human society. They are particularly important to modern society as they are found in most products we use every day from kitchen wares to cell phones and cars. Metals have been mined from ores and minerals available in the Earth's crust and processed for further use. Modern society has rapidly increased in technological complexity since the second half of the 20th century and hence our metal usage has become much more intensive (Graedel *et al.*, 2015; Herrington, 2013). At the same time more diverse and rarer metals have been sought for a much wider range of consumer goods and industrial equipment (e.g. REYs) as compared to the traditional metals used for manufacturing such as Cu and Fe. There are most often constraints involved in accessing rarer metals, for example, most of these metals are available almost entirely as by-products. Some metals such as Co and the REYs are geopolitically concentrated and/or are associated with countries that have political instabilities and poor environmental policies and are thus termed 'critical metals' (Graedel *et al.*, 2015). These issues coupled with continued challenges associated with land based mining increases the need to search for additional and/or alternative sources of mineral raw materials (Lusty & Murton, 2018).

Deep-sea ferromanganese deposits are enriched in some economically important metals such as Mn, Ni, Cu, Co, Zn and the REYs which makes them very attractive in terms of their resource potential. Some of these metals such as the REYs and Co are termed 'critical metals' because of their economic importance, the difficulty in finding appropriate substitutes in end-products, and the supply risks associated with mining and processing these scarce metals (Graedel *et al.*, 2015). Current technologies use a wide range of critical metals in various industrial and green energy applications from smartphones to wind turbines and hybrid electric cars (Grandell *et al.*, 2016). Hence, with increasing demand for critical metals, mineral resources from the seabed such as polymetallic nodules could potentially provide a secure supply for these elements in the future.

The main driver for increased Co demand is due to its key role in rechargeable Lithium-ion batteries, which are used in many applications from mobile phones to electric vehicles. On the other hand, REYs such as Nd, Dy and Tb are important components in permanent magnets which are used in wind turbines and other technological applications, including the induction motors in electric vehicles. These technologies are important in society's global energy transition from fuel based to a low or zero carbon economy to help strengthen global action to the threat of climate change. Recent models by the World Bank (Hund *et al.*, 2020), showed that the demand for minerals vital for a clean energy transition (wind, solar, geothermal and energy storage) is expected to increase substantially up to 2050 to limit global temperature rise to well below 2°C (UN, 2016), with that of Co to increase by nearly 500% (particularly for energy storage) from 2018 levels. Polymetallic nodules are therefore seen as potential sources

for some important metals that are essential in many technological applications, some of which are needed in the clean energy sector.

1.4.1 Rare earth elements plus Yttrium (REYs)

The REYs are a group of 17 elements in the periodic table which includes the 15 elements in the lanthanides group plus Sc and Y (Connelly, 2005). The latter are included as they have similar physical and chemical properties to the lanthanides series. Based on their atomic weights, the REYs are broadly classified into the light REEs (LREEs) and heavy REEs (HREYs). The LREEs include La through to Sm while Gd to Lu plus Y are known as the HREYs. The LREEs and HREEs are naturally occurring except Pm (Massari and Ruberti, 2013). The name rare earth elements dates back to the time when the abundances of these metals were thought to be extremely low. Today, geologists now know that these metals are actually more abundant than previously thought, but they rarely occur in concentrated deposits which is why they are mostly mined as by-products of other metals such as Fe (Kanazawa & Kamitani, 2006). The most abundant REY is Ce with a crustal abundance of 43 ppm; this is similar to the abundances of Ni (59 ppm) and Cu (27 ppm) (Rudnick & Gao, 2003). The least abundant REY is Lu with 0.5 ppm crustal abundance, which is still more abundant than metals such as Bi (0.18 ppm) and the platinum group elements (PGEs). The REYs have unique physical and chemical properties, this enables them to be used in a wide range of technological applications, ranging from the energy industries and consumer electronics to military technological applications.

1.4.1.1 Global production, reserves and demand for REYs

Most of the world's REY deposits occur, and are mined from land-based sources (Wall et al., 2017). The common REY deposits are those that formed from high temperature magmatic and processes associated with carbonatites, alkaline igneous rocks, and their hydrothermal processes (Goodenough, Wall & Merriman, 2018). Our current supply of REYs comes from these deposit types, particularly the carbonatites which are the primary source for light REEs. Another type of natural REY deposits are those that formed from low temperature processes (erosion and weathering) such as placers, bauxites, laterites and ion-adsorption clays, the latter being the main source for the heavy REYs (Goodenough, Wall & Merriman, 2018; Van Gosen *et al.*, 2017). The total world REYs production (~95%) is currently dominated by China (Petersen et al., 2016). Apart from providing most of the REYs global supply, REYs mining activities in China are also largely unregulated and occur at great social, environmental and economic cost (Wall et al., 2017). Other significant deposits are also found in Brazil, Vietnam, India, Australia, Russia, United States and Malaysia (Figure 1.4). The global demand for REYs has been increasing and forecasts have shown that this will continue for many years which again raises the need to search for alternative sources to sustain the global demand (Figure 1.5).

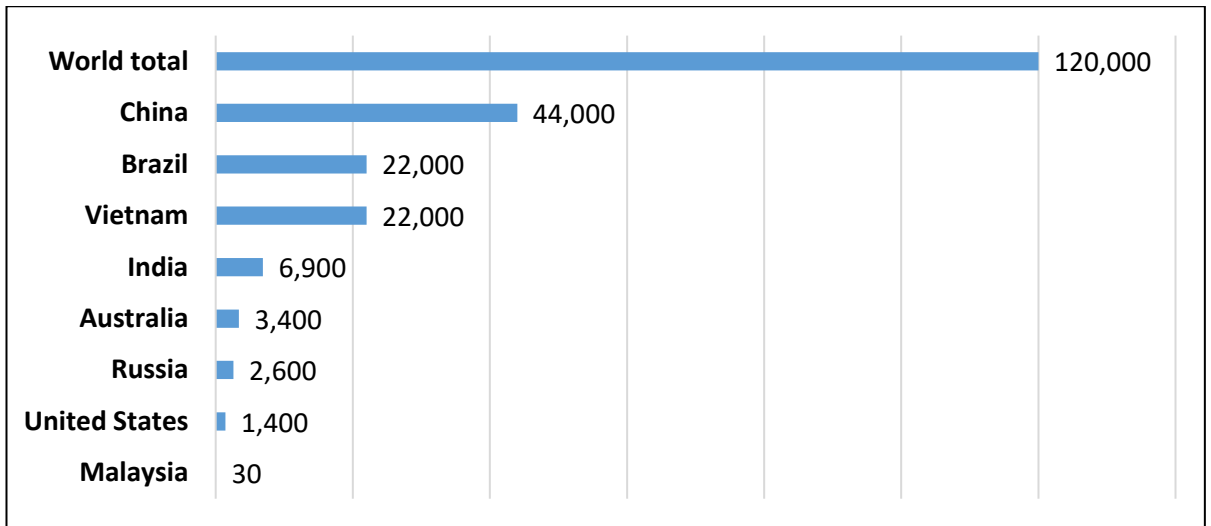


Figure 1.4. REY reserves worldwide by country (in 1,000 metric tons of REY oxides). Source: USGS (2020a).

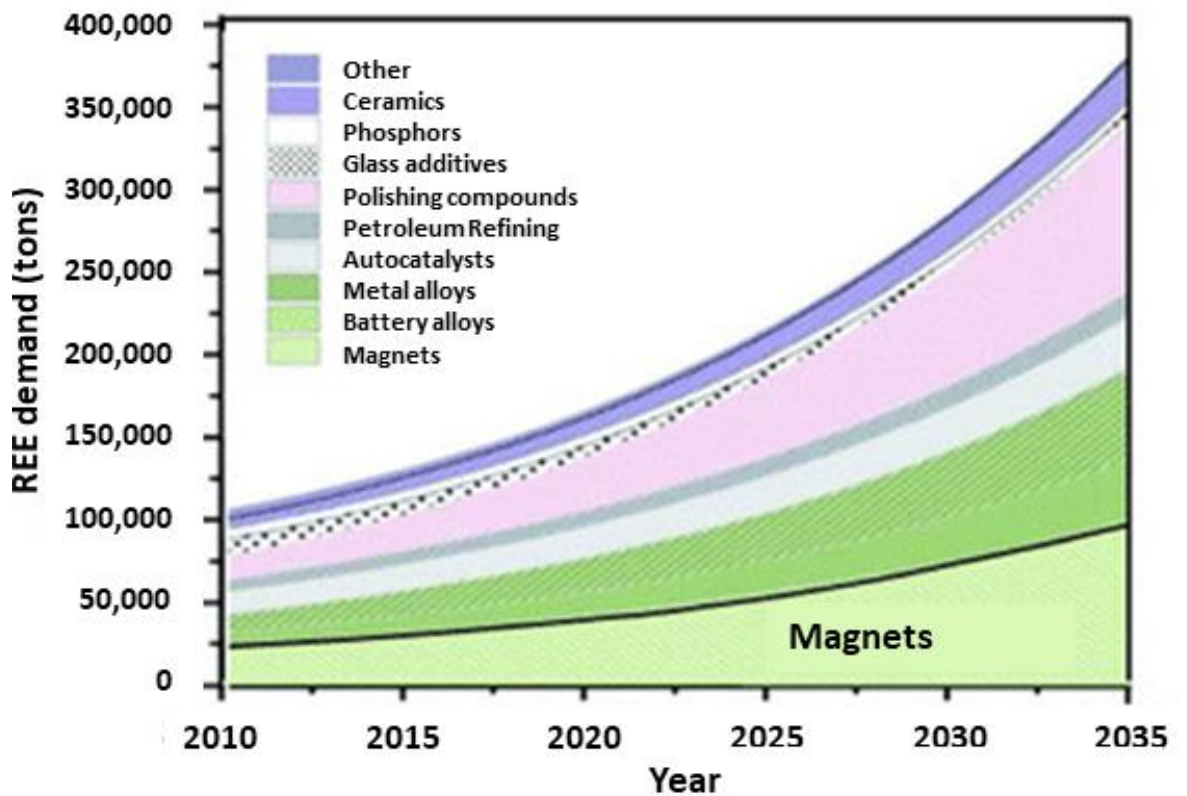


Figure 1.5. Predicted growth of global REE demand (2010-2035), note; data does not include Y. Source: Yang et al. (2017).

1.4.2 Cobalt

Cobalt (Co) is a chemical element with atomic number 27. Like the REYs, Co is a transition metal that is naturally occurring and relatively abundant (17.3 ppm) in the Earth's crust (Rudnick & Gao, 2003). Co has a range of applications in industry (Figure 1.6), however, the battery industry is the largest user of Co where it is currently considered having limited effective substitutes as a cathode material. Battery technologies are important in many applications from household appliances, to smart phones and electric vehicles, which are important for a sustainable energy future for the planet. Cobalt is recognised globally as a critical raw material due to its technological applications which are fundamental for economic growth, energy and environmental sustainability.

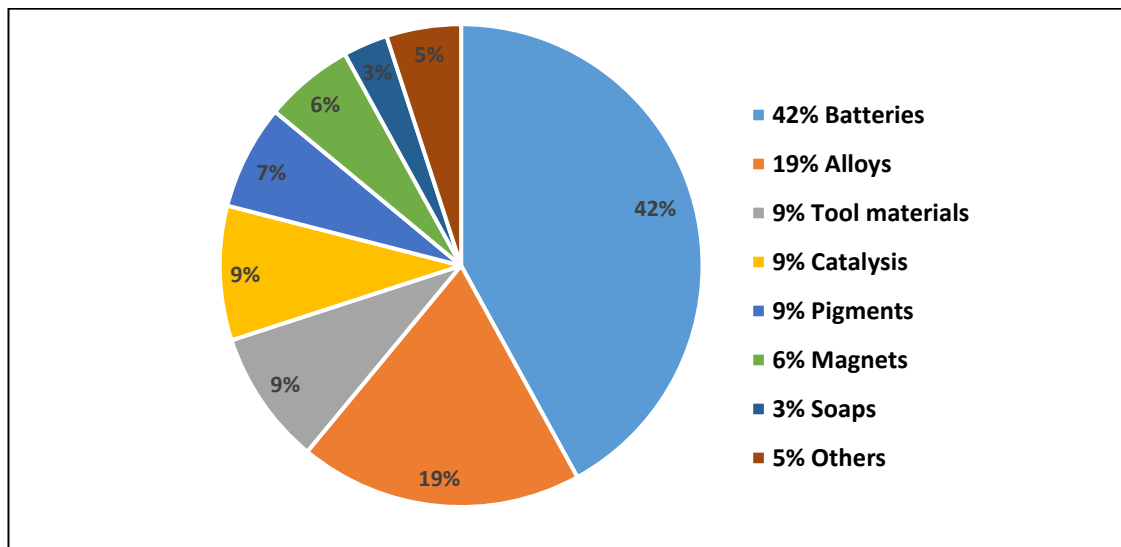


Figure 1.6. Industrial uses of cobalt (Battery University, 2018). Co has a range of industrial applications, the battery industry is currently the largest consumer of Co.

The Democratic Republic of Congo (DRC) has the largest Co reserves in the world at 3.6 million tonnes, which is around 50% of global reserves (Figure 1.7). However, the

extraction of Co in the DRC is also associated with social and human rights issues relating to unregulated mining such as child labour. With the projected increase in demand and usage for Co in the future, particularly in the battery industry, exploring for and understanding new Co deposits are important. Deep-sea mineral deposits such as Co-rich crusts and polymetallic nodules are estimated to be highly enriched in Co and could add significantly to the global supply.

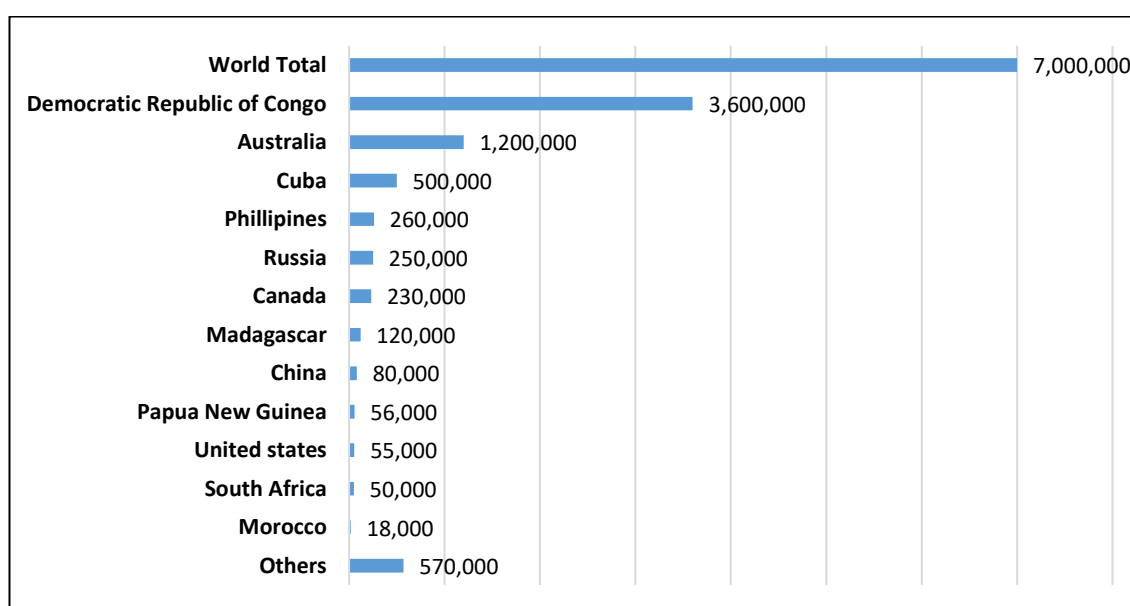


Figure 1.7. Cobalt reserves worldwide by country in tonnes. Source: (USGS, 2020b). At 3.6 million tonnes, the Democratic Republic of Congo (DRC) has the largest reserve of Co.

1.5 Aims and objectives

The growing interest in the exploitation of deep-sea polymetallic nodules particularly due to their high metal contents requires a better understanding of these deposits. The CCFZ is the area of greatest interest in terms of nodule abundance, and Ni and Cu contents. But the nodules also contain other so-called critical metals such as the REY and Co which are considered potential by-products when commercial extraction takes place. Therefore, understanding the geochemistry and mineralogy of these metals in the

nodules are important for resource estimation and nodule processing. Whilst several workers have studied REY in Pacific nodules (e.g. Hein and Koschinsky (2014b); Kuhn *et al.* (2017); Menendez *et al.* (2019)), detailed understanding of their distribution, mineral host phases and their sources are yet to be fully explored. This project resolves these issues and aims to carry out a detailed geochemical and mineralogical study of polymetallic nodules from the UK Claim Area in the CCFZ with a particular focus on REY. The goal is to develop a better and thorough understanding of REY in nodules from the UK Claim Area by integrating together several individual analytical approaches.

The following objectives were identified for this project, which are divided into individual chapters in the thesis.

1. To develop an effective and simple method for the determination of REY in polymetallic nodules (chapter 2).
2. To evaluate the chemical composition of polymetallic nodules from the UK Claim Area with high precision and accuracy (chapter 2).
3. To characterise textural and morphological features and develop a descriptive framework for the internal structure of nodules (chapter 3).
4. To constrain the distribution of critical metals in nodules (chapter 3).
5. To evaluate mineralogical composition of nodules and identify the mineral host phases of REY in nodules (chapter 4).
6. To further assess the host phases of REY in nodules using mineral synthesis approaches (chapter 5).
7. To constrain nodule growth processes using chemostratigraphic approaches (chapter 6)

Chapter 2

2 Bulk chemical composition of polymetallic nodules from the UK Claim Area, UK1 in the Clarion-Clipperton Fracture Zone and an evaluation of the sodium peroxide sintering digestion method for REY analysis

2.1 Introduction

Polymetallic nodules are mostly made up of Mn, Fe, Si and Al, but they also contain other metals of economic interest such as Ni, Cu, Co, Zn, Pb, Mo, Zr, Li and Rare Earth Elements plus Yttrium (REYs). These deposits have been previously regarded as a potential source for traditional metals of economic interest such as Ni, Cu and Zn (Mero, 1965). It was not until recently, with increasing efforts being put into understanding these deposits, that it was realised that there was potential for extracting critical metals such as the Rare Earth Elements plus Yttrium (REYs) and Co as by-products from nodules (Hein *et al.*, 2013).

Polymetallic nodules from the CCFZ are 'genetically' classified as mixed-type diagenetic-hydrogenetic nodules as they mostly formed from both diagenetic and hydrogenetic processes (Bau *et al.*, 2014) (Note that nodule formation processes are discussed in more detail in the introduction section of the next chapter (chapter 3)). As a result of these two processes, the internal structures of nodules is mostly made up of diagenetic and hydrogenetic layers. Hydrogenetic layers generally have low Mn/Fe ratios (<5) and low Ni + Cu (1.5 wt%) but are enriched in Co (~0.4 wt%) (Halbach, Friedrich & von Stackelberg, 1988). In contrast, diagenetic layers generally have high Mn/Fe ratios of >5,

high Ni + Cu (0.8 – 6.5 wt%) and low Co (0.07 wt%) (Halbach, Friedrich & von Stackelberg, 1988; Wegorzewski & Kuhn, 2014). Note that these values are based on mixed-type nodules from the German (BGR) Claim Area in the CCFZ, which shares part of the border with the UK Claim Area on the southwest end (Figure 1.3). The chemical composition of nodules of mixed-type origin fall between those of hydrogenetic and diagenetic nodules. The composition of metals in polymetallic nodules varies in different nodule fields, which is due to many factors such as formation mechanism and location of nodule field (Calvert & Price, 1977). Within a nodule field, metal content can be similar, however, variations of different scales also exist (Hein & Koschinsky, 2014a). The CCFZ is the area where most nodule exploration activities are taking place and, nodule bulk compositions in some nodules in the CCFZ have been documented e.g. (Hein *et al.*, 2013; Wegorzewski & Kuhn, 2014). Many aspects of nodules, however, are not fully understood, which raises the need for more work in this area.

The bulk chemical composition of nodules from the CCFZ has been documented in several studies particularly by Hein and co-workers (Hein & Koschinsky, 2014b; Hein *et al.*, 2013). The composition of nodules from the UK1 Claim area, in particular, have been documented by few authors (Menendez *et al.*, 2019; Reykhard & Shulga, 2019; Spickermann, 2012). Similarly, several authors (Kuhn *et al.*, 2017; Wegorzewski & Kuhn, 2014) have done work on nodules from the BGR Claim area which shares a border with the UK claim area to the west. These studies show that the composition of the nodules from this area of the CCFZ are generally similar: Fe 5.8%, Mn 29%, Cu 1.1%, Ni 1.2% and REYs 715 ppm.

The chemical composition of polymetallic nodules can be determined using several analytical techniques, the ones commonly used are: x-ray fluorescence (XRF), inductively

coupled plasma mass spectrometry (ICP-MS) and inductively coupled plasma optical emission spectrometry (ICP-OES). These techniques are multi-elemental, fully automated, have short sample turnover times and therefore, are the preferred choice at present. Prior to sample measurement, samples can be prepared by different methods depending on the analytical measurement technique used. For ICP-MS and ICP-OES, sample preparation normally involves wet chemical digestion and measurements are carried out on samples in solution. For other methods such as XRF, measurements are performed on samples in powdered (solid) form.

The most common approach for ICP-MS and ICP-OES is acid digestion using hydrofluoric acid (HF) and a mixture of several other inorganic acids. These include HNO₃, HCl, perchloric acid [(HClO₄)]⁻, hydrogen peroxide (H₂O₂) and aqua regia (Axelsson *et al.*, 2002; Balaram, 1999; Dubinin *et al.*, 2017; Menendez *et al.*, 2019; Wegorzewski & Kuhn, 2014). The resulting solution is normally then dried down and re-dissolved in diluted acid solution before elemental measurement. In some cases the drying down step is carried out again using a diluted acid before the final step of re-dissolution using another diluted acid such as 3 M HNO₃ and followed by elemental measurement (Menendez *et al.*, 2019). Using this approach, most of the relevant elements (major: Li, Na, Mg, Al, K, Ca, Ti, Mn, Fe and P; minor and trace: V, Cr, Co, Ni, Cu, Zn, Rb, Sr, Ba, Hf, Pb, Th, U and REY) in the nodules can be accurately determined as has been demonstrated by previous workers (Axelsson *et al.*, 2002; Menendez *et al.*, 2019; Wegorzewski & Kuhn, 2014). This sample preparation method typically ensures complete digestion of most elements of interest including the REYs. However, the method involves several highly corrosive acids including HF and therefore poses safety concerns when performing digestion work. In

addition, the digestion method can be time consuming as ensuring complete sample digestion is a lengthy process.

XRF is another method that is commonly used for nodule geochemistry (González *et al.*, 2010). This method has high precision and accuracy and does not need wet chemical digestion for sample preparation. The method is relatively straightforward and sample preparation is fast and simple. Since it is a dry chemical method, it does not use highly corrosive acids such as HF so is a much safer approach compared to wet chemical acid digestion sample preparation methods. This method works particularly well for the measurement of major and minor elements as well as some trace elements (Calvert, Cousens & Soon, 1985; Chubarov, Amosova & Finkelshtein, 2020; González *et al.*, 2010; Hein *et al.*, 2015). For REYs measurement however, the ICP-MS technique is considered the preferred method. XRF on the other hand, is not commonly used for REY measurements in nodules, which is probably due to lower recoveries compared to ICP-MS.

This study investigated the bulk composition of nodules in five box cores within the UK Claim Area, UK1. This was used to evaluate the distribution of different metals in the nodules in the five box cores, with a particular focus on the critical metals including Ni, Cu, Co and the REYs. The feasibility and effectiveness of polymetallic nodule decomposition by a sodium peroxide sintering method followed by Inductively Plasma Mass Spectrometry (ICP-MS) analysis was also investigated for the determination of trace metals including REYs.

2.2 Method

2.2.1 Sample collection and sample sites

Polymetallic nodule samples from five stations within one of the UK Seabed Resources (UKSR) licensed area (UK1) in the CCFZ in the equatorial Pacific were collected during two environmental baseline cruises in 2013 and 2015, and kindly provided to us by UK Seabed Resources. The 30 km x 30 km study areas are designated as UK1 AB01 and UK1 AB02.

Figure 2.1 shows the location of UK1 in the eastern equatorial Pacific. The samples were collected using a box core sampler which recovered samples from an area of 50 cm x 50 cm on the seabed. Area UK1-AB01 was visited and sampled in October 2013. This study area is characterized by a gently undulating surface, with depths ranging from 3600 to 4400 meters. The second area, (AB02) was sampled in March – February 2015, similarly, the majority of the UK1-AB02 is also characterized by a gently undulating surface, with depths ranging from 4200 to 4400 m. The seafloor bathymetry of both areas, including box core locations are shown in Figure 2.2 and Figure 2.3.

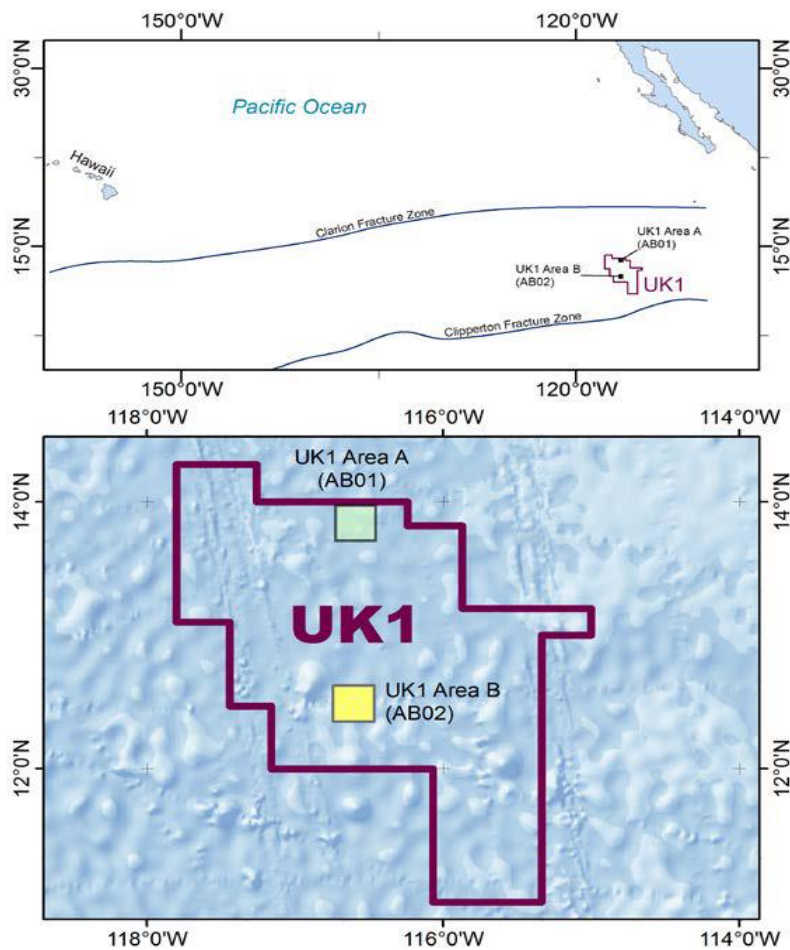


Figure 2.1. Study locations in the eastern equatorial Pacific Ocean in the area known as the Clarion-Clipperton Fracture Zone. Area A (AB01) and Area B (AB02) in UK1 are shown inset (Source: UKSR (2015)). Both areas were visited in two separate environmental baseline cruises, AB01 was visited in October 2013 while AB02 was visited in March – February 2015. Polymetallic nodules from five box-cores were used in this study, one box core was collected from AB01 while four box cores were collected in AB02, the locations and seafloor bathymetry for these are shown in the next two figures (Figure 2.2 and Figure 2.3).

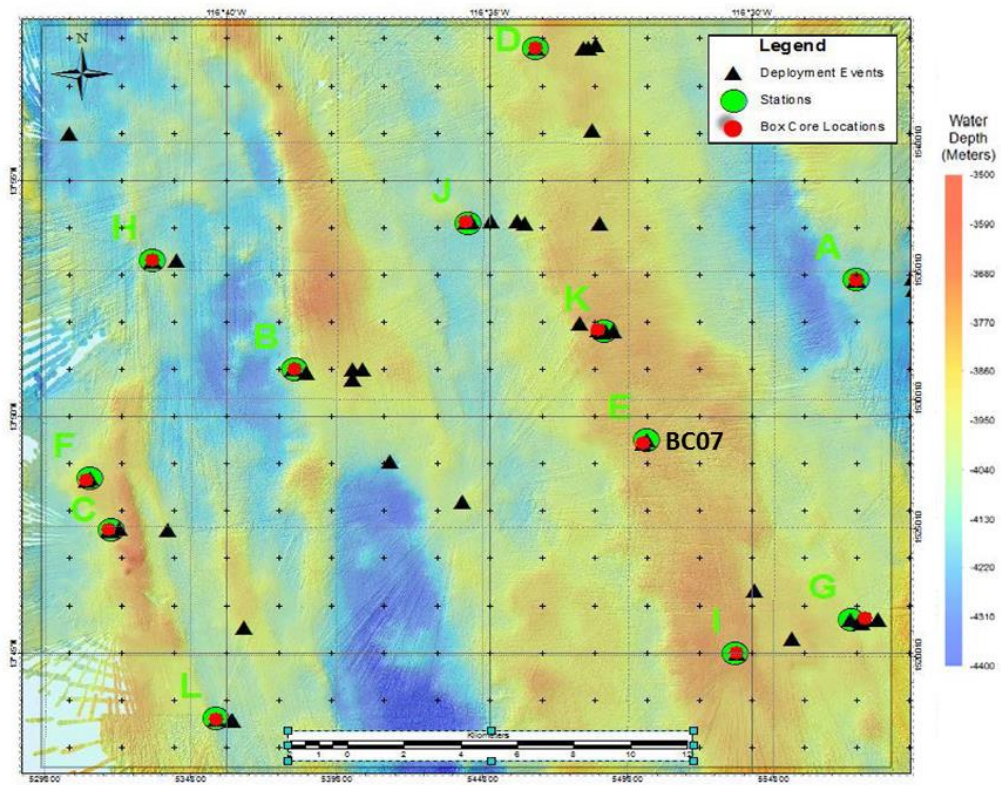


Figure 2.2. Seafloor bathymetry and box core site UK1-AB01- BC07 (Source: UKSR (2015)). Box core sampling depth is 4054 m, seafloor is mostly plain and flat with. Further site and nodule description, etc. are shown in Table 2.4 in the results section.

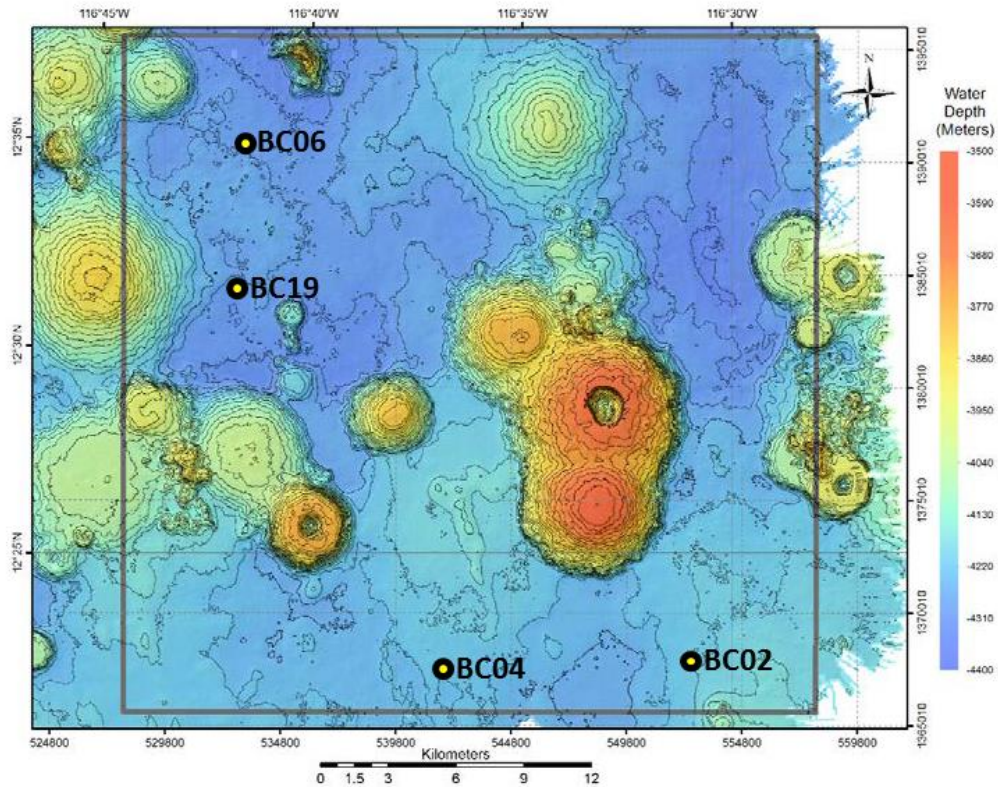


Figure 2.3. Seafloor bathymetry and box core locations at UK1-AB02 (Source: UKSR (2015)). Samples studied are from four box cores as shown. Depths range from 4200 – 4400 m, bottom seafloor is mostly flat and plan with gentle slopes of less than 3°. This area is also characterised by several seamounts ranging in height from 100 – 700 m. Further site and nodule descriptions etc. are shown in Table 2.4 in the results section.

2.2.2 X-Ray Fluorescence Spectrometry (XRF) analysis for major oxides and minor elements

Oxides of major elements (Si, Ti, Al, Fe, Mn, Mg, Ca, Na, K, P, Ba) were measured on a fused lithium tetraborate bead by XRF. Samples were finely ground using an agate mill and oven dried at 105 °C for 48 hrs. 9.0000 g of lithium tetraborate sample material was weighed in a Pt crucible, 0.9000 g of sample powder was added into the crucible and the mixture was homogenized. The mixture in the crucible was placed in a furnace at 1200 °C where fusion takes place. After cooling to room temperature, the fused disc was removed and prepared for XRF measurement of major elements.

Minor elements (Co, Ni, Cu, Zn, Zr, Sr, Y, Zr, Nb, Mo, Sb, W, Tl) were measured on a pressed powder by XRF. For this, 8.000 g of finely grounded rock powder was added to 2.000 g of wax binding agent and mixed in a rotary mixer for one hour. After mixing, the mixture was pressed at 150 kN and the pressed pellet was removed and prepared for XRF measurement of minor elements. XRF measurements were carried out using a PANalytical Axios MAX Wavelength Dispersive XRF (WD-XRF) at the Consolidated Radio-Isotope Facility (CORIF) laboratories at the University of Plymouth.

2.2.2.1 Measurement accuracy and repeatability (precision)

Measurement accuracy and precision are important criteria for the validity of geochemical measurements. Accuracy is the nearness of the measured quantity value to the true quantity value of the analyte of interest while repeatability relates to the precision of the analysis (Potts, 2012). The accuracy and repeatability of XRF analyses were evaluated by a triplicate measurement of the GeoPT23 FeMn-1 Certified Reference Material (CRM), (Bundesanstalt für Geowissenschaften und Rohstoffe, Hannover). For major oxides, an accuracy better than RSD (relative standard deviation) 11% was obtained, while the repeatability was better than RSD 2%. For minor elements, accuracy was better than RSD 10%, while the repeatability was better than RSD 6%.

2.2.3 Trace elements – Sodium peroxide sintering and ICP-MS measurements

Trace elements including REYs were measured by ICPMS after decomposition using sodium peroxide sintering and typical dilutions of c. 500 times (precisely determined).

Complete sample dissolution of geological materials is an important aspect of geochemical analysis by ICPMS. Different types of dissolution techniques exist, digestion using HF being the most popular in most geological materials including polymetallic nodules. The sodium peroxide (Na_2O_2) sintering method has several advantages: it is simple and rapid, highly effective in attacking refractory minerals, and the resulting sinter residue is easy to dissolve (Longerich *et al.*, 1990). An important consideration is also that it is a relatively safe procedure compared to the conventional multi-acid digestion involving HF. Sodium peroxide decomposes to NaOH and O_2 and does not introduce elements that may cause significant instrument memory (Meisel *et al.*, 2002). This method has been mostly applied to rock samples containing refractory minerals such as zircon and chromite and has allowed accurate measurements of REEs (Bokhari & Meisel, 2017). The application of this method to polymetallic nodules is not common particularly because samples containing larger amounts of Mn tend to form MnO_2 precipitates through oxidation (Meisel *et al.*, 2002). However, in this study, the formation of precipitates was avoided by removal of the water-dissolved fraction (containing most if not all of the Na, and significant proportions of Fe and Mn), and analysis for trace metals was carried out on the water-insoluble residues. This had the additional advantage that the total dissolved mass in the solutions used for mass-spectrometry was relatively low despite the addition of 600 mg Na_2O_2 per 100 mg of sample.

2.2.3.1 Digestion procedure

The sintering procedure that was carried out in this study was adapted from Meisel *et al.* (2002). Since ferromanganese nodule samples are highly hygroscopic, samples were first dried at 105 °C for 48 hrs. Weighing of the sample and Na₂O₂ was done in the ratio 1:6. 100 mg of sample powder was weighed into a glassy carbon crucible, 600 mg of Na₂O₂ was added and the mixture was homogenized. Sintering was performed at 480 °C in a muffle furnace for one hour. After sintering, the crucibles were removed from the furnace oven and allowed to cool. After cooling, the outer walls of the crucibles were rinsed carefully with ultra-pure water to remove any contaminants from the furnace before placing each crucible in a 150 ml PFA (Teflon) beaker. Once in the beaker, ultra-pure water was added dropwise until effervescence stopped, indicating the reaction was complete. The beakers containing the crucibles were then placed on magnetic stirring plates (set at 250 rpm, 90 °C), the crucibles were knocked over and the beakers were covered with PFA lids. Stirring and heating was carried out for 20 – 30 mins. The contents of the beaker were transferred into 50 mL PP vials and the residue was collected on the bottom of the vials after centrifugation at 2500 rpm for 10 mins. The supernatant was separated and the remaining residues in the crucibles were dissolved by adding 1 mL each of concentrated HCl and HNO₃. A minimum amount of HNO₃ (1 mL) was also added into the crucible to dissolve any residues that might be still present. At this stage, no residues remained (visual observations) which indicates a total digestion. The solutions from the vial and the crucible were then combined and made up to 50 mL mark with 5% each of HCl and HNO₃. Trace metal measurement was carried out on a Thermo Scientific iCAP RQ ICP-MS instrument using external calibration. The schematic of the procedure is shown in Figure 2.4.

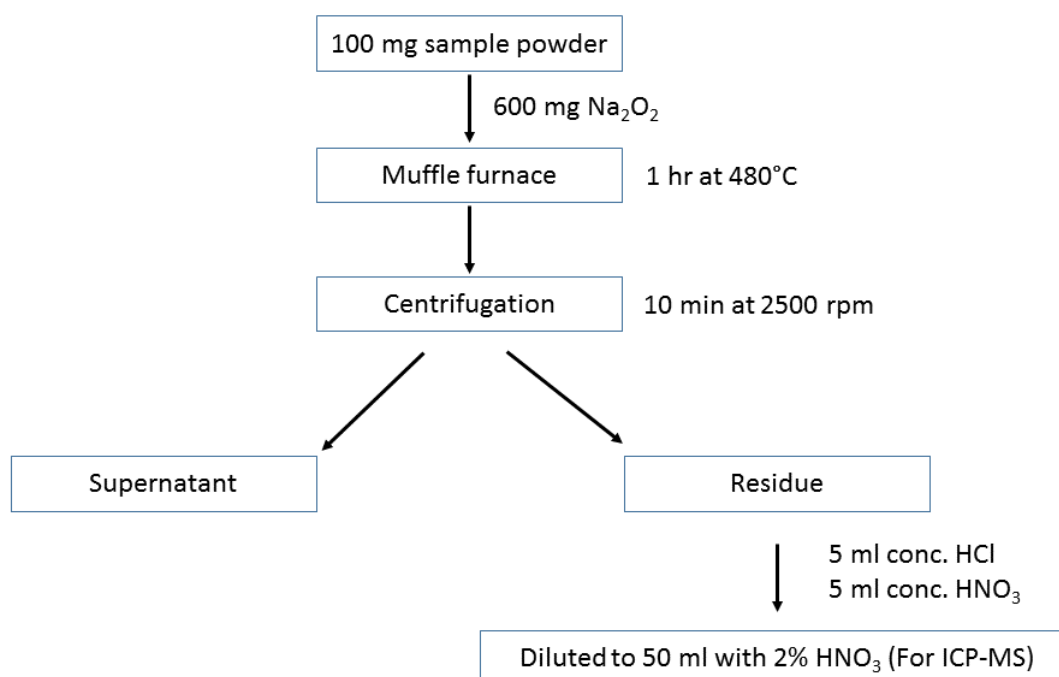


Figure 2.4. Flow chart of preparation of digested sample solution using sodium peroxide sintering method for ICP-MS measurement.

2.2.3.2 Calibration standards

2.2.3.2.1 Drift correction

Instrument signals obtained from modern ICP-MS instruments are relatively stable. However, signal drift, commonly a decrease in signal intensity over time is still inevitable. The likely cause for this is the accumulation of deposits on the ICP-MS cones (Bokhari & Meisel, 2017). In this study, signal drift was monitored using a calibration standard that sits somewhere in the calibration range. The check sample was analysed after every 10 runs and the signal was observed each time. The problem of signal drift can be addressed by using several internal standards that are spaced at several intervals across the mass spectrum and by frequent recalibration (Eggins *et al.*, 1997). This correction ensures normalisation of all data to a non-analyte isotope present in the sample or the calibrant (Bokhari & Meisel, 2017). The internal standardisation method was used in this study

using a solution containing 10 µg/L of ^{115}In and ^{193}Ir . This standard was selected as both isotopes are known to be nearly absent or present in very low levels in geological samples and theoretically should show least interference effects (Cotta & Enzweiler, 2012). Internal standards were selected in order to be close to the masses of the isotopes used for measurements. Thus, ^{115}In was used for the light trace elements while ^{193}Ir was used for the heavy trace elements.

2.2.3.3 Polyatomic Interference corrections

Polymetallic interferences in ICP-MS are spectroscopic interferences that are caused by atomic or molecular ions that have the same mass to charge ratio as isotopes of interest (May & Wiedmeyer, 1998). Their formation can be due to several sources such as sample matrix, reagents used for preparation, plasma gases and atmospheric gases. The Thermo Scientific iCAP RQ ICP-MS instrument is equipped with a collision cell that removes interference using pure He as the collision gas with Kinetic Energy Discrimination (KED) (Thermo Fisher Scientific, 2017). Unwanted polyatomic interferences are filtered out by He KED based on the difference in cross-sectional diameter of the analyte and polyatomic. While ICP-MS instrumentation can correct for all known atomic interferences or those of overlapping isotopes of different elements, most polyatomic interferences do exist. In this work, polyatomic interferences were minimised by selecting isotopes with least interferences on them. However, it is not always possible to avoid most interferences, some significant signal overlaps were still observed. To address these, an external calibration standardisation method was performed and empirical mathematical corrections were performed, these are shown in Table 2.1.

Table 2.1. Major interferences and their respective percentage corrections.

Isotope	Correction applied, interfering ions
¹⁵⁶ Gd	Applied 3.9% correction of ¹⁴⁰ CeO
¹⁵⁷ Gd	Applied 7.0% correction of ¹⁴¹ PrO
¹⁵⁹ Tb	Applied 0.2% correction of ¹⁴⁵ NdO

2.2.3.4 Detection limits and blanks

The detection limit is defined as the smallest quantity of an analyte that is significantly different from the background signal (Potts, 2012). This parameter depends on several factors such as isotopic abundance, instrumental sensitivity, memory effects, polyatomic interferences and contamination (Cotta & Enzweiler, 2012; Macholdt *et al.*, 2016). The detection limits and blank values of analytes measured by ICP-MS in this study are shown in Table 2.2. Detection limits were calculated as three times the standard deviation of three procedural blank measurements (Potts, 2012). Blanks presented are based on the mean of three procedural blank measurements.

Table 2.2. Blanks and detection limits of trace metals from ICP-MS measurements. The blank concentrations are as-measured values and dilutions are not taken into account.

Analyte	Procedural blank (pg ml ⁻¹)	Detection limit (pg ml ⁻¹)
Sc	48	9
Y	46	11
Zr	33	90
Nb	35	80
La	43	20
Ce	53	195
Pr	34	7
Nd	38	18
Sm	25	5
Eu	22	2
Gd	20	2
Tb	17	1
Dy	19	4
Ho	14	0.3
Er	11	1
Tm	10	1
Yb	11	1
Lu	8	1
Pb	104	313
Th	24	14
U	1.3	2.7

2.2.3.5 Measurement accuracy and repeatability (precision)

The quality control data is reported in Table 2.3 and shows the different quality control methods carried out for the three methods used for bulk chemistry. The repeatability and accuracy RSD values showed satisfactory results except for few elements that showed high values. The REYs showed satisfactory precision and accuracy. The HREYs

showed very good precision and accuracy. In general, high RSD% in accuracy for the elements can be due to absorption of moisture after oven drying adding unnecessary mass to the samples. This is because the samples are highly hygroscopic, but this effect has always been minimised at all possibilities. The limit of detection (LOD) values were determined for the trace elements.

Table 2.3. Accuracy and repeatability data using FeMn-1 CRM. Note; n = number of measurements. Note; the uncertainty and RSD values are based on a 95% confidence interval.

	Certified reference value (ppm)	Mean experimental value (ppm) (n = 6)	% RSD (n = 6) (Repeatability)	% RSD (n = 6) (Accuracy)
Sc	8.10 ± 0.25 (n = 36)	7.83 ± 0.726	9.27	4.55
V	469 ± 13 (n = 52)	133 ± 140	104	77.6
Y	69.1 ± 1.13 (n = 53)	58.4 ± 7.09	12.3	15.5
Zr	325 ± 5.22 (n = 53)	424 ± 76.2	18.0	31.4
La	68.2 ± 0.97 (n = 46)	64.3 ± 6.1	9.49	3.54
Nb	13.4 ± 0.33 (n = 46)	12.8 ± 5.99	46.7	4.16
Ce	110 ± 1.64 (n = 45)	109 ± 7.48	6.86	1.04
Pr	14.1 ± 0.20 (n = 35)	13.7 ± 1.13	8.26	0.79
Nd	63 ± 0.82 (n = 42)	62 ± 7.38	11.9	1.51
Sm	14 ± 0.20 (n = 39)	13.5 ± 1.39	10.3	1.11
Eu	3.8 ± 0.06 (n = 36)	3.78 ± 0.328	8.66	0.12
Gd	15.6 ± 0.28 (n = 34)	16.0 ± 0.98	6.14	2.37
Tb	2.52 ± 0.05 (n = 35)	2.59 ± 0.23	8.99	3.19
Dy	15.8 ± 0.30 (n = 35)	15.7 ± 1.36	8.66	0.65
Ho	3.42 ± 0.06 (n = 35)	3.28 ± 0.20	6.17	3.52
Er	9.80 ± 0.14 (n = 34)	9.74 ± 0.90	9.19	0.34
Tm	1.49 ± 0.03 (n = 32)	1.53 ± 0.14	9.39	1.56
Yb	10 ± 0.14 (n = 38)	10.1 ± 0.69	6.82	1.48
Lu	1.59 ± 0.02 (n = 34)	1.64 ± 0.12	7.54	2.96
Pb	127 ± 2.48 (n = 56)	166 ± 45.7	27.6	23.9
Th	6.87 ± 0.17 (n = 43)	7.10 ± 0.97	13.6	45.8
U	4.39 ± 0.13 (n = 39)	3.24 ± 0.28	8.76	25.5

2.2.3.6 Assessment of the recoveries of trace metals after sintering

The recoveries, expressed as the percentage of the ratio of measured value to reference value of some trace elements are shown in Figure 2.5. The recoveries are based on the mean of six measurements of the FeMn-1 certified reference material, with the water-soluble fraction after sodium peroxide digestion discarded. The measurements are based on two separate digestions carried out on two separate dates. For each measurement, analysis was carried out in triplicates, the combined data is presented. The measure of the uncertainty for each element is indicated by the error bars based on a 95% confidence interval. Using the sintering method the metals measured showed variable recoveries. The REYs showed complete recovery of 96 – 103%, except Y which showed a recovery of 86%, while Sc displayed a recovery of 97%. Some elements that were included in the measurement showed incomplete recovery, these include V (28%) and U (74%). Low recoveries indicate that a significant proportion of these elements were water-soluble after sintering, and therefore discarded. In contrast, Zr and Pb showed surprisingly high recoveries at 130%. Nb displayed complete recovery of 96%, however, the reproducibility is poor (RSD 47%). The quality control data shows that the sodium peroxide method is an effective and efficient technique for the detection of trace elements, particularly the REYs, Sc and Th.

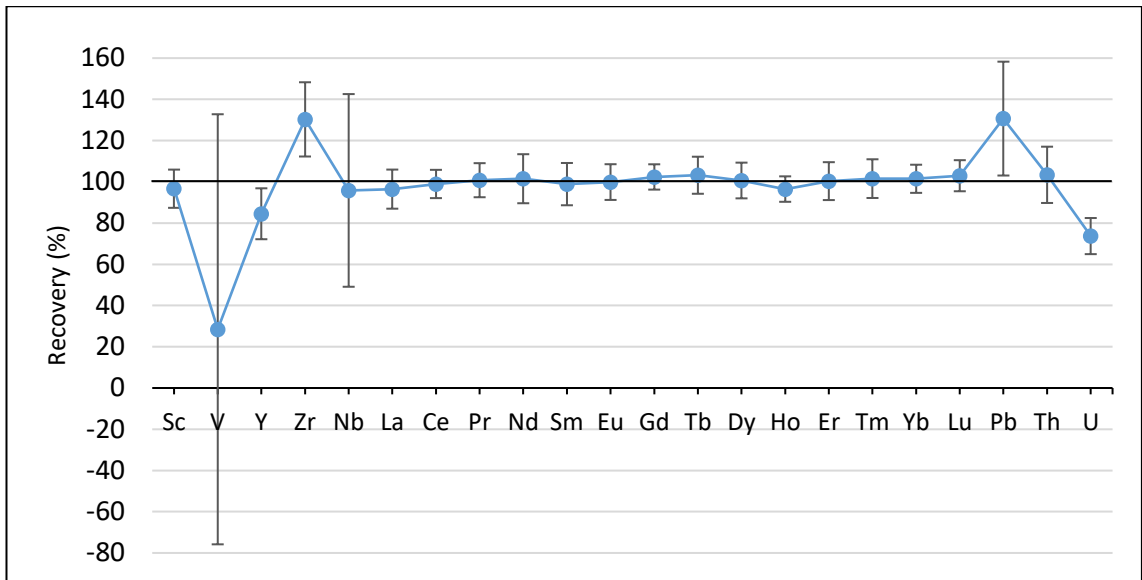


Figure 2.5. Recoveries of trace metals expressed as the percentage of the mean experimental value of six replicate measurements over the theoretical value of the FeMn-1 certified reference material.

2.3 Results

2.3.1 Sample description

Nodules analysed in this study mostly range in size from 2 – 12 cm. Nodules are dark grey to black in colour with granular to smooth textures. Images of nodules from each box cores are shown in Figure 2.6.

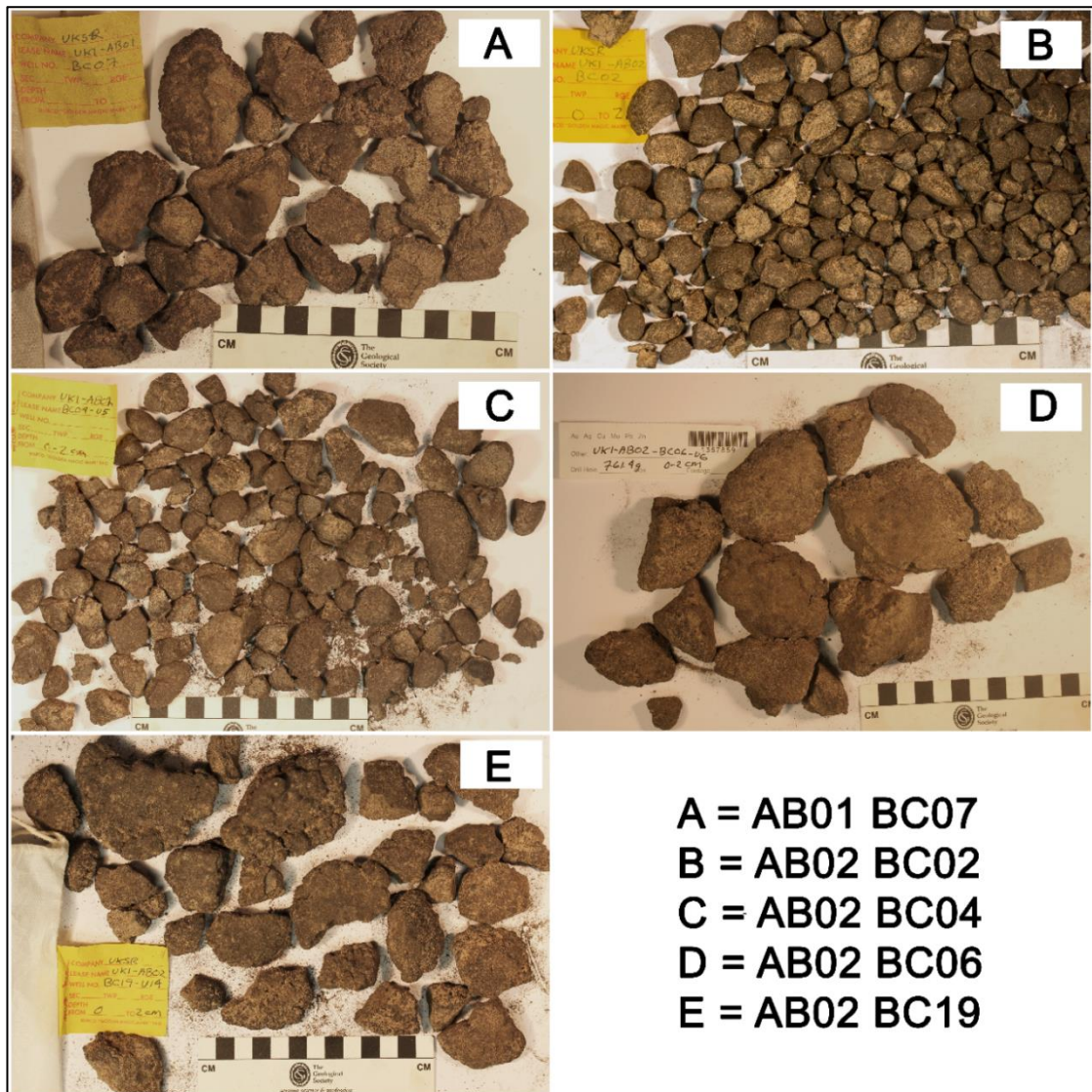


Figure 2.6. Images of nodules from each of the five box core. Nodules from AB01 BC07, AB02 BC06 and AB02 BC19 are similar in morphology (ellipsoidal to botryoidal), texture (smooth-rough) and size (up to 12 cm diameter). Nodules from AB02 BC04 also have similar morphology to the ones described previously but are much smaller in size (not more than 8 cm diameter). Nodules from these four box cores are easily fragmented as can be seen in the images. Nodules from AB02 BC02 in contrast have a discoidal morphology, smooth texture and are generally small (1 – 3 cm diameter). Nodules from this box core are compacted and are not easily fragmented.

The general descriptions of nodules and box core locations are given in Table 2.4. Nodule shapes are similar in most box cores, which show generally ellipsoidal to discoidal shape. Nodules have a smooth texture on the top where it was in contact with seawater, and a coarse botryoidal structure on the underside where it sat on or in the sediment (e.g. Figure 2.7). Nodules are marked by a botryoidal coarse rim which probably marks the seawater-sediment interface. Small nodules ranging in size from 1 – 3 cm are found in UK1-AB02 BC02. These are also ellipsoidal to discoidal in shape but are mostly well rounded, and smooth all round including the rim (Figure 2.8). Nodule abundances at different sediment depths are shown in Table 2.5 and shows that most of the nodules (>68%) were collected from the top 0 – 2 cm of the sediment. Zero nodule abundances were recorded for AB01 BC07, AB02 BC02 and AB02 BC04 at depths below 10 cm while abundances for AB02 BC06 and AB02 BC19 were 11.3 and 12.3% respectively at the same depth.

In addition, the *in-situ* shear strength of box core sediments was also determined during sampling. These were carried out at three depth intervals for each box core, the measurements give information about the magnitude of the shear stress of the sediment. The shear strength measurements of box core sediments at three different depth intervals are shown in Table 2.6 for each box core. Shear strength increases with sediment depth in each box core, at the sediment top (0 – 10cm) the values are generally similar while at depths below 15 cm to 40 cm the values are more variable. Based on the shear strength values, AB02 BC19 sediments were the least compacted at depths more than 15 cm while that of AB02 BC02 were the most compacted at the same depth intervals.

Table 2.4. Box core geographical positions, water depths and descriptions of box core locations and nodules. Box core sample densities in kg/m² are given including information on whether the nodules are exposed or covered by sediments (note; nodule densities at different sediment depths are shown in the next table) (Source: UKSR).

UKSR box core sample ID	Position	Water depth (m)	Topographical/geological description of box core location	Nodule sample descriptions	Nodule abundance (kg/m ²)		Presence/absence of sediment cover on nodules	
					Medium (10 - 20 kg/m ²)	High (20 - 30 kg/m ²)	Nodules covered	Nodules exposed
UK1-AB01 BC07	13° 49.446 N 116° 32.055 W	4054	Plain, flat and open	Size: 4 – 7 cm Smooth top and rough bottom		✓		✓
UK1-AB02 BC02	12° 22.01861 N 116° 31.02094 W	4159	Plain, flat, open, with average slopes <3°. Outcrops to the southeast (~2 km)	Size: 1 - 2 cm. Well-rounded and smooth all round	✓			✓
UK1-AB02 BC04	12° 22.25746 N 116° 36.81834 W	4160	Plain, flat, open, with average slopes <3°. No outcrops	Size: 2 - 6 cm Smooth top and rough on the bottom		✓		✓
UK1-AB02 BC06	12° 34.73770 N 116° 41.21773 W	4237	Plain, flat, open, with average slopes <3°. Outcrops to the west and northeast (~3 km)	Size: 6 - 12 cm. Smooth top and rough bottom		✓		✓
UK1-AB02 BC19	12° 31.26974 N 116° 41.88958 W	4237	Flat valley bottom between two seamounts, each approximately 2km away to the west and east.	Size 4 - 8 cm. Smooth top and rough bottom. Some nodules are rough on all sides		✓	✓	✓

Table 2.5. Nodule abundance (in percentage) at different sediment depths from the surface to below 10 cm in each of the box cores. Most nodules were collected from the surface (0 – 2 cm) of the sediments except for box core AB02 BC06 and AB02 BC19 where varying proportions were collected at different depths (Source: UKSR).

	AB01 BC07 (%)	AB02 BC02 (%)	AB02 BC04 (%)	AB02 BC06 (%)	AB02 BC19 (%)
0 – 2 cm depth	99.7	92.3	96.4	76.8	68.6
2 – 5 cm depth	0.3	5.1	2.8	5.3	0.5
5 – 10 cm depth	0	2.6	0.8	6.6	18.6
Below 10 cm	0	0	0	11.3	12.3

Table 2.6. Shear strengths measurements in kilopascal (kPa) of the box core sediments at three depths.

	AB01 BC07 (kPa)	AB02 BC02 (kPa)	AB02 BC04 (kPa)	AB02 BC06 (kPa)	AB02 BC19 (kPa)
0 – 10 cm depth	2.25	1.97	2.04	2.28	1.88
15 – 25 cm depth	6.00	7.03	4.98	5.22	4.28
30 – 40 cm depth	6.22	7.00	6.42	6.00	5.06

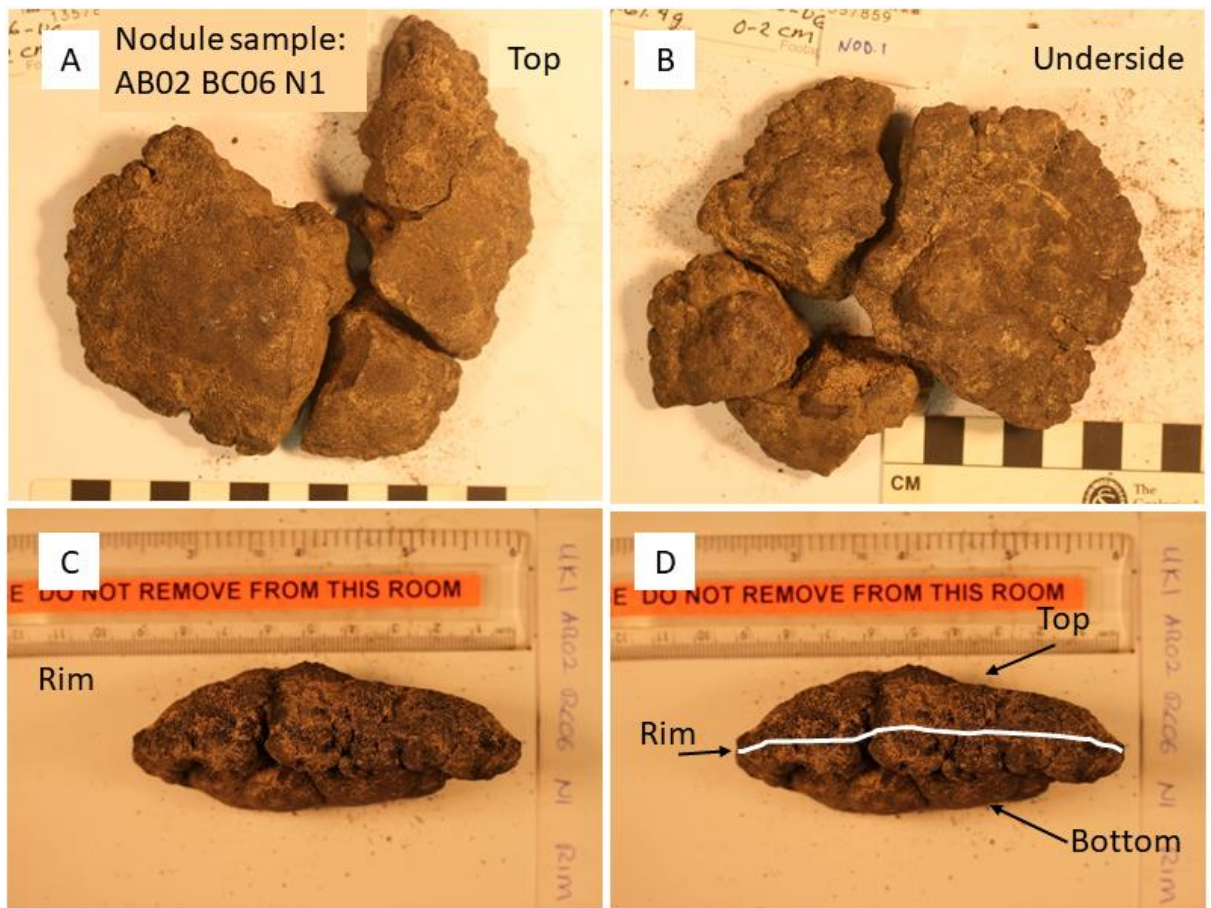


Figure 2.7. A typical nodule from the UK1 claim area. Nodules have a smooth top surface (A) where the nodule was recently in contact with seawater and a coarse, rough underside (B) where the nodule sat on the sediment. The rim (C, D) shows the flattened shape of the nodules and marks the seawater/sediment boundary, the rim is botryoidal in most of the nodules.

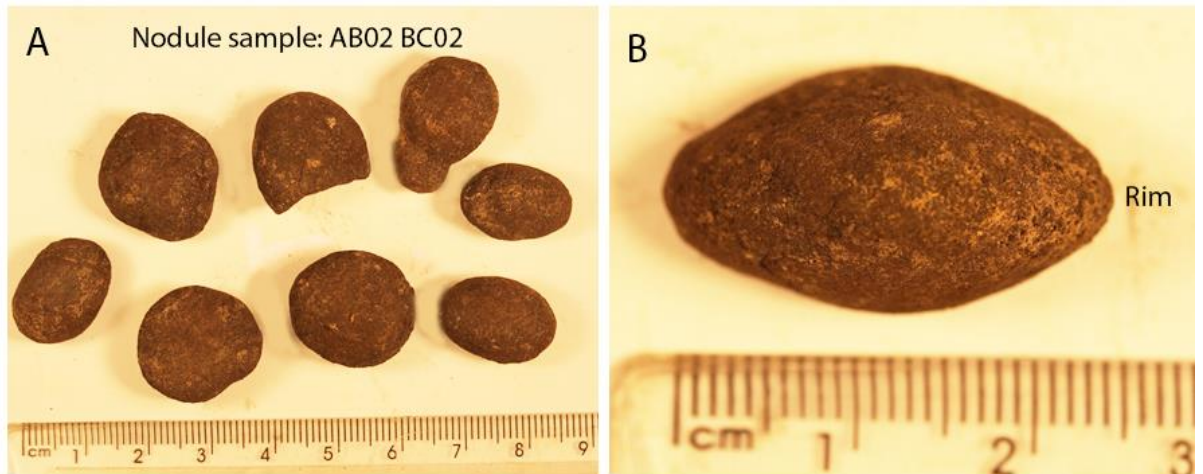


Figure 2.8. Whilst most nodules show morphological characteristics shown in Figure 2.7, nodules from box core AB02 BC02 have slightly different characteristics. Nodules have ellipsoid shape and are generally small in size (1 – 3 cm), and well-rounded with smooth surfaces (A) on either side of the rim (B).

2.3.2 Bulk compositions

The bulk chemical compositions of nodules from the five box cores determined in this study are given in Table 2.7. Bulk samples for each box core were obtained by combining the 'rubble', i.e., broken off chips, from the sample bags received and ground in an agate mill to obtain a bulk sample assumed to be approximately representative for the whole of the box core. Overall, compositions for most metals and oxides in each of the box core are similar. Analysis of the major oxides (by weight) shows that the nodules are mostly made up of Mn (28.7%), Fe (6.02%), SiO₂ (13.6%) and Al₂O₃ (4.44%). Other major oxides also show significant concentrations in nodules. These include MgO (2.95%), CaO (2.33%), Na₂O (2.91%), K₂O (1.17%) and P₂O₅ (0.45%). The Mn/Fe ratio (by weight) for the nodules in the five box cores range from 2.9 to 6.4. The concentrations of (Ni + Cu) range from 2.06 to 2.46 wt% while Co concentrations generally range from 0.1 – 0.2 wt%. The concentrations of REYs in the UK1 averages 770 ppm.

Table 2.7. Bulk chemical compositions of polymetallic nodules from rubbles of five box cores and four individual nodule samples. Note; LREYs = Light REYs, TLREYs = Total Light REYs, HREYs = Heavy REYs, THREYs = Total Heavy REYs, TREYs = Total REYs. The major oxides (including BaO) were analysed on a fused lithium tetraborate bead by XRF, minor and some trace metals (Co, Ni, Cu, Zn, Sr, Zr, Nb, Mo, Sb, W) were analysed on a pressed powder by XRF. The REYs, Pb, Th and U were determined by ICP-MS after sample decomposition by sodium peroxide sintering. The relative standard deviation expressed in percentage (RSD%) of the mean of the combined rubble material for each of the five box cores is based on a 95% confidence interval.

	Combined rubble material							Individual nodules			
	AB01 BC07	AB02 BC02	AB02 BC04	AB02 BC06	AB02 BC19	Mean	RSD%	AB02 BC06 N4	AB01 BC07 N3	AB02 BC06 N5	AB02 BC19 N3
Fe ₂ O ₃ (wt%)	7.68	12.2	8.80	8.25	6.17	8.62	25.6	7.87	7.92	8.6	8.68
Mn ₃ O ₄	43.6	34.4	40.3	40.2	38.5	39.4	8.58	42.3	43.5	41.4	40.3
Mn/Fe (wt%/wt%)	5.84	2.91	4.72	5.02	6.42	4.98	26.9	5.53	5.65	4.95	4.78
SiO ₂ (wt%)	11.1	14.6	12.6	13.0	16.7	13.6	15.8	11.8	10.9	12.5	13.2
Al ₂ O ₃	3.91	4.66	4.14	4.40	5.11	4.44	10.5	3.99	3.83	4.07	4.27
MgO	3.15	3.00	2.91	2.99	2.70	2.95	5.50	2.90	3.01	2.81	2.68
CaO	2.16	3.13	2.26	2.12	2.00	2.33	19.5	2.19	2.12	2.27	2.39
P ₂ O ₅	0.350	0.883	0.367	0.35	0.308	0.452	53.7	0.350	0.363	0.36	0.357
TiO ₂	0.391	0.796	0.462	0.46	0.366	0.495	35.2	0.420	0.424	0.435	0.432
BaO	0.467	0.370	0.464	0.560	0.698	0.511	24.2	0.539	0.438	0.515	0.597
Co	0.154	0.229	0.185	0.179	0.117	0.173	23.8	0.171	0.140	0.181	0.174
Ni	1.42	1.25	1.34	1.35	1.18	1.31	7.18	1.38	1.39	1.47	1.51
Cu	1.02	0.810	0.978	1.11	0.981	0.98	11.0	0.1	0.976	1.12	1.14

Zn	0.188	0.122	0.158	0.131	0.190	0.158	19.8	0.146	0.180	0.165	0.168
Rb (ppm)	25.9	25.4	27	27	39	28.9	19.8	26	23.1	23.2	23.6
Sr	618	728	651	622	550	634	10.1	617	645	638	677
Zr	278	434	331	302	202.8	310	27.2	282	294	293	304
Nb	16.9	28.4	19.9	17.4	13	19.1	30.1	16.5	17.8	17.8	18.1
Mo	657	541	617	638	627	616	7.22	640	628	690	713
Sb	62.6	44.4	57.1	56.8	58.3	55.8	12.2	63.2	60.9	57.6	61.6
W	60.4	66.9	60.1	62.1	47.7	59.4	12.0	54.2	59.7	70.5	70.7
LREYs											
La	106	148	117	110	78.4	112	22.2	108	94.3	98.9	91.4
Ce	244	375	278	264	185	269	25.6	253	262	274	243
Pr	29.2	39.2	32.3	32.0	24.8	31.5	16.6	30.4	27.1	28.2	25.9
Nd	127	168	140	138	109	136	15.7	131	117	121	112
Sm	30.3	39.1	33.1	33.4	26.4	32.5	14.4	31.6	28.4	28.9	26.6
Eu	7.43	9.45	8.06	8.20	6.56	7.94	13.4	7.77	7.15	7.29	6.78
TLREYs	544	779	608	586	430	589	21.4	562	536	558	506
HREYs											
Gd	27.4	35.3	30.0	29.5	23.2	29.0	15.0	28.4	30.0	30.1	27.8
Tb	4.51	5.72	4.87	4.94	3.82	4.77	14.5	4.69	4.50	4.53	4.19

Dy	25.6	32.3	27.5	27.8	21.5	26.9	14.5	26.5	25.0	24.8	23.2
Y	81.3	106	86.6	82.6	67.6	84.8	16.2	80.6	89.5	86.6	81.3
Ho	4.64	5.76	4.92	4.95	3.82	4.82	14.5	4.77	4.56	4.63	4.24
Er	13.0	16.2	13.8	13.9	10.7	13.5	14.4	13.3	12.6	13.0	11.8
Tm	1.84	2.25	1.94	1.96	1.51	1.9	13.9	1.88	1.88	1.87	1.73
Yb	12.8	15.6	13.5	13.6	10.5	13.2	14.0	13.1	12.5	12.8	11.7
Lu	1.93	2.35	2.03	2.06	1.61	2.00	13.7	1.99	1.95	1.90	1.79
THREYs	173	221	185	181	144	181	15.2	175	182	180	168
TREYs	717	1000	794	767	574	770	19.9	737	718	739	673
HREYs as % of TREYs	24.1	22.1	23.3	23.6	25.1	23.5	4.63	23.8	25.4	24.4	24.9
Pb (ppm)	285	432	328	307	212	313	25.5	300	264	316	289
Th	12.4	16.3	13.3	14.8	10.2	13.4	17.5	13.1	13.5	13.9	12.2
U	3.13	3.70	3.09	3.28	2.57	3.15	12.9	3.25	2.20	2.82	2.98

2.4 Discussion

2.4.1 Composition of nodules from the UK claim area

The bulk chemical compositions in each of the box cores are given in Table 2.7. The results show that the compositions are generally similar (with standard deviations <30% RSD for most elements). The compositions are also similar to ones reported in previous works carried out in the CCFZ e.g. (Hein & Koschinsky, 2014b; Menendez *et al.*, 2018; Wegorzewski & Kuhn, 2014). The nodules in the UK claim area are mostly made up of Mn, Fe and Al-silicates. The presence of Al-silicates within nodules is not unexpected as the nodules are mostly underlain by siliceous sediments which are incorporated in nodules as sediment particles (ISA, 2010); in the next chapter it is shown that Al-silicates form a coating on the pores within nodules, and are also concentrated along growth hiatus surfaces. The mean Mn/Fe ratio for the bulk rubble samples is 4.98 indicating a mixed type origin according to Halbach, Friedrich and von Stackelberg (1988). A more robust classification of Fe-Mn deposits can be done using the Bonatti ternary diagram (Bonatti, Kraemer & Rydell, 1972) using Fe, Mn and Ni+Cu for discrimination of genetic types. Another commonly used and robust genetic classification is based on the geochemical relationships controlling the REYs in Fe-Mn deposits (Bau *et al.*, 2014). Both these classification schemes were applied in this work, both approaches showed that the studied samples scatter in the mixed-type zone (Figure 2.9 and Figure 2.10). These results are consistent with that of previous authors where they have shown that nodules from the CCFZ are typically classified as of mixed-type origin (Halbach, Friedrich & von Stackelberg, 1988; Wegorzewski & Kuhn, 2014).

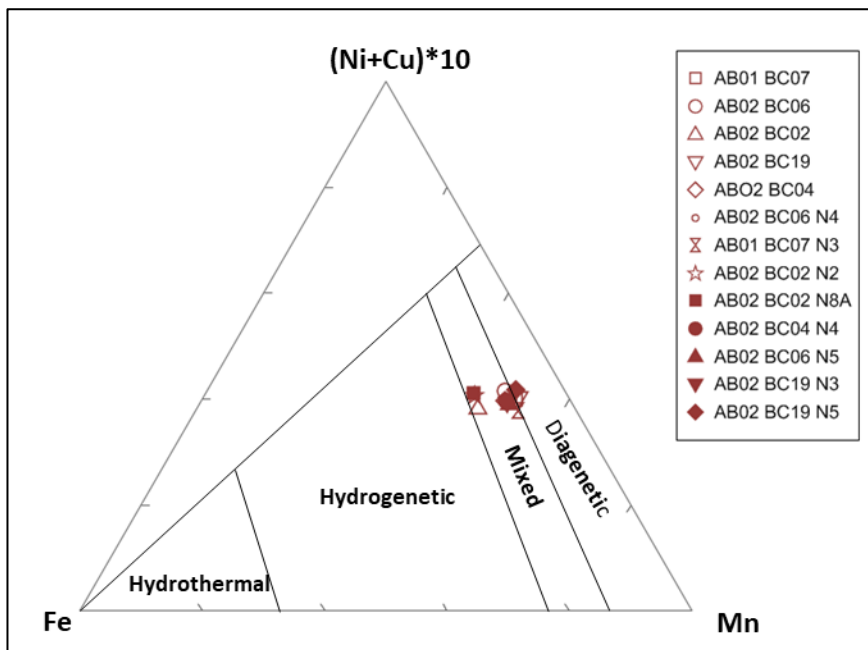


Figure 2.9. Proportions of Fe, Mn and (Ni+Cu)*10 (by weight) of studied samples plotting in the ternary discrimination diagram of Bonatti, Kraemer and Rydell (1972). Black lines border the different nodule genetic types. A genetic type ‘hydrothermal’ was added for comparison purposes, however, samples used in this study all plot in the mixed-type category.

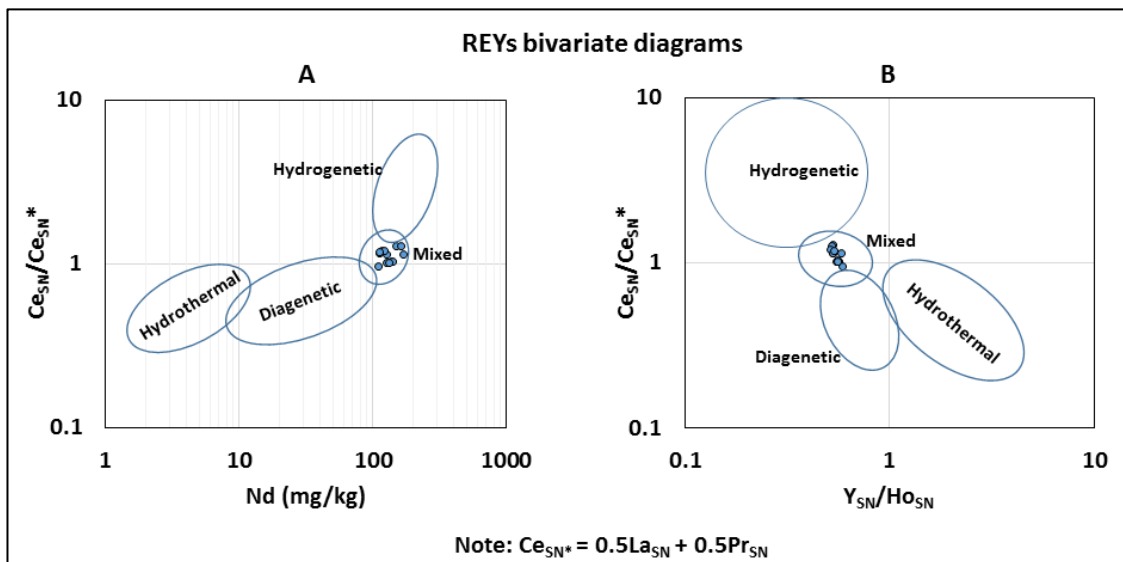


Figure 2.10. REYs bivariate diagrams of bulk nodule samples in graphs of (A) Ce_{SN}/Ce_{SN}^* ratio vs Nd concentration and (B) Ce_{SN}/Ce_{SN}^* ratio vs Y_{SN}/Ho_{SN} (Note: the ratios are plotted based on weight proportions, mg/kg). The diagrams show the geochemical relationship between different genetic types of polymetallic nodules and the distinctive areas they scatter (Bau et al., 1996; Bau et al., 2014). The formula inset for Ce_{SN}^* indicates the magnitude of the Ce anomaly which is obtained by comparing it to its neighbouring REEs.

The Post Archean Australian Shale (PAAS) normalized plots for the nodules are shown in Figure 2.11. The nodules show large negative Y anomalies (which exceed the 15% accuracy error determined for Y in our analytical method) which is characteristic of all nodules regardless of how they formed. The behaviour (positive or negative anomaly) of the redox-sensitive Ce anomaly is an important factor for distinguishing between nodule types. Diagenetic nodules typically show large negative Ce anomalies while hydrogenetic nodules show positive Ce anomalies (Hein et al., 2015). Previous work on hydrogenetic crusts showed that the size of the Ce anomaly varies, and appears to be related to crust growth rate: crusts with a slow growth rate show the largest positive Ce anomaly while those with high growth rates show the least (Kuhn *et al.*, 1998; Ohta *et al.*, 1999). Similarly, this can be applied to nodules as well. The positive Ce anomalies in marine ferromanganese deposits of hydrogenetic origin are due to oxidative scavenging, where Ce(III) is scavenged from seawater by MnO₂ and FeOOH followed by its subsequent oxidation to the less soluble Ce(IV) on the hydr(oxide) surface. This results in the decrease of Ce(III) concentration on the hydr(oxide) surface, thus scavenging of Ce(III) from seawater continues followed by its oxidation which then results in the enrichment of Ce as Ce(IV) in hydrogenetic nodules (Takahashi *et al.*, 2000). In contrast, this mechanism is probably less prominent in sub-oxic conditions which results in the negative Ce anomaly in diagenetic nodules. Another explanation for the negative Ce anomaly in diagenetic nodules as suggested by Bau *et al.* (2014) is due to sediment pore waters inability to reduce or transport Ce(IV). While Mn(II) and REYs(III) can mobilize in pore waters, Ce(IV) remain fixed in discrete phases resulting in negative Ce anomalies. Our PAAS normalized plots of bulk samples showed very little presence of Ce anomalies to slightly positive Ce anomalies, which is characteristic of nodules of mixed-type origin.

The AB02 BC02 nodules showed the distinct positive Ce anomalies, which shows that nodules from this site tend to show predominantly hydrogenetic characteristics and thus, increased oxidative scavenging of Ce from the oxic seawater compared to nodules from the other four box cores.

It is unlikely that the Ce anomalies observed in this work are influenced in part by the method used in this study. The Ce measured is expected to be in the oxidised form due to the Na₂O₂ sintering, and therefore, is water-insoluble, so we do not expect to have 'lost' Ce by discarding the water-based fraction. This is also reflected in the very good recovery of Ce for the FeMn-1 certified reference material.

The physical features of the nodules from this box core such as: their small size ranging from 1 – 2 cm (suggesting relatively slow growth rates compared to other sites) and their smoothness and well-roundedness, which means they probably sat on the sediment surface where hydrogenetic processes dominate for most of their growth history. In the ternary diagram in Figure 2.9, nodules from AB02 BC02 scatter in the mixed type zone but slightly towards the boundary with hydrogenetic type.

In general, neither of the two processes dominate in these nodules and hence the nodules formed from both hydrogenetic and diagenetic processes, which is typical of nodules from the CCFZ (Wegorzewski and Kuhn, 2014). The relative proportions of diagenetic layers versus hydrogenetic layers are estimated in the next chapter using scanning electron microscopy, for the nodules studied these are: 50% diagenetic, 20% hydrogenetic and 30% pore spaces. The plot for the FeMn-1 CRM, which represents diagenetic nodules from the Peru Basin is included for comparison, and shows a negative Ce anomaly on the PAAS-normalized plot which is characteristic of nodules of this

genetic type. This negative Ce anomaly shows that the bottom seafloor conditions in the Peru Basin are less oxic. Therefore, oxidative scavenging is less prominent when compared to the CCFZ. This results in the relatively low Ce concentrations in the Peru Basin nodules (110 ppm) compared to the CCFZ nodules from this study (185 – 375 ppm).

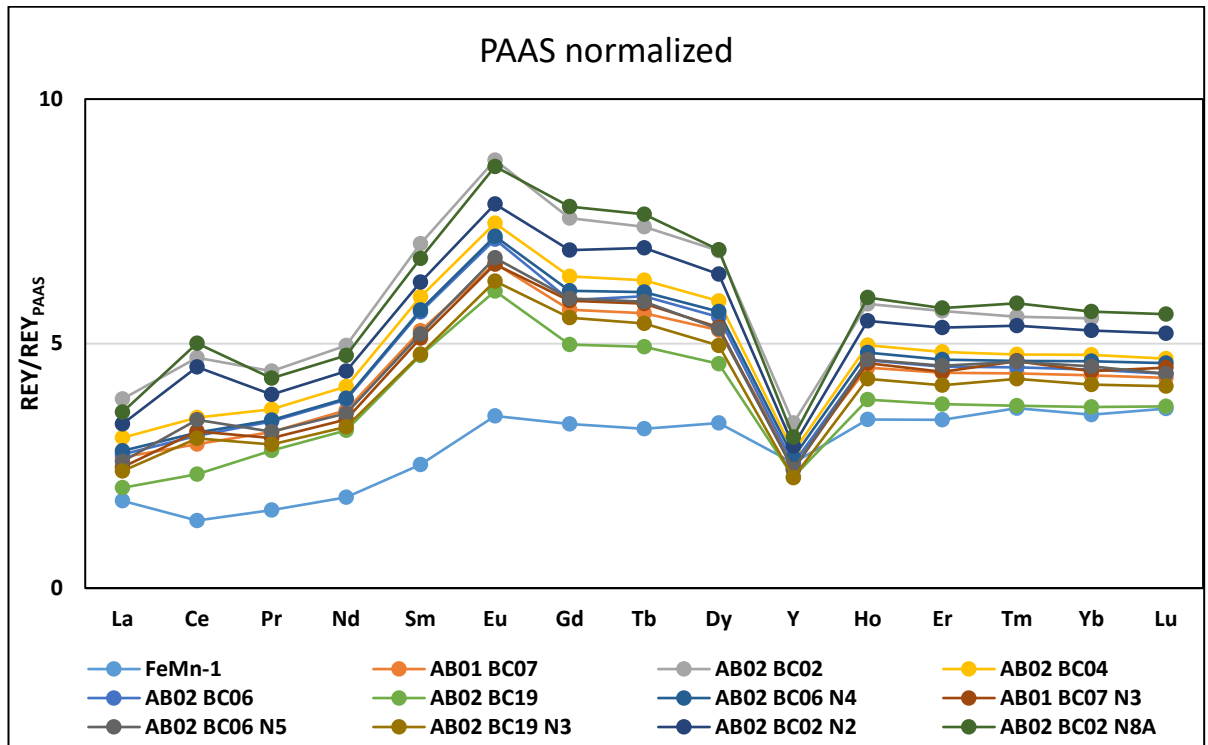


Figure 2.11. PAAS-normalized REY plots for bulk nodules studied (combined rubble material and individual nodules). The FeMn-1 sample is a certified reference material (CRM) of diagenetic nodules from the Peru Basin and is included for comparison purposes. The PAAS data used is according to Rudnick and Gao (2003).

Although nodules in the five box cores from UK1 showed similar bulk compositions, some variations do exist. Nodules from AB02 BC02 show the lowest Mn/Fe ratio at 2.91, highest REYs (1000 ppm) and Co (0.229%). Based on these compositions, their geochemical behaviour in the discriminating diagrams (Figure 2.9 and Figure 2.10), REYs normalized plots (Figure 2.11), and physical characteristics, these nodules show

predominantly hydrogenetic characteristics. This might explain the slight variation in their chemical composition inventory that sits somewhere between a mixed type and a hydrogenetic type but with still a predominately mixed type characteristic. These nodules are also small in size (1 – 3 cm) and are well-rounded with smooth surfaces (Figure 2.8) which indicate that they were predominately sitting exposed on the surface throughout most of their entire life, where their growth was controlled by slow hydrogenetic precipitation. In contrast, nodules from AB02 BC19 showed the strongest diagenetic characteristics. Their bulk Mn/Fe ratio is the highest at 6.42, and they contain the lowest Co (0.117%) and REYs (574 ppm). The nodules from this box core were mostly buried or partially buried when collected from the seabed. Nodules in the other three box cores show chemical and physical characteristics typical of mixed-type nodules and their bulk composition inventory sit somewhere between those of AB02 BC02 and AB02 BC19.

The concentrations of Co in the five box cores range from 0.117 to 0.229% with an average value of 0.173%. In terms of the bulk composition in each box core, they behave just like the REYs where the highest concentrations are found in AB02 BC02, while the lowest concentration is found in AB02 BC19. Similarly, the highest concentrations of Ti and P are also found in AB02 BC02 while their concentrations are the lowest in AB02 BC19. The genetic processes that control growth of nodules from AB02 BC02 are more towards the hydrogenetic-type. Therefore, this will be also reflected in their composition. Hydrogenetic deposits source their metals from the oxic seawater and are dominated by mineral phases of vernadite (a phyllosulfate) intergrown with FeOOH. The metals enriched in AB02 BC02 nodules hence, are associated with these mineral phases. This will be discussed in more detail in the next two chapters.

2.4.2 Comparison of nodule occurrence between box cores

Nodule abundances at different sediment depths are given in Table 2.5, and it can be seen that most nodules (>90%) in three box cores (AB01 BC07, AB02 BC02 and AB02 BC04) were collected from the top of the sediment surface (0 – 2 cm). Nodule abundances in the other two box cores, AB02 BC06 and AB02 BC19 were much lower at this same depth (0 – 2 cm) while at increasing depths, nodules were still present and were more abundant than the other three box cores at the same depths. These two box cores also contain the largest nodules (6 –12 cm) which is likely to indicate that rapid diagenetic precipitation was much more predominant at these locations, which resulted in the larger nodule size. Furthermore, the presence of nodules at sediment depths below 10 cm were recorded in these two box cores only. This means that sub-oxic diagenetic precipitation at depths below 10 cm was only occurring at these sites. The shear strength data Table 2.6) shows that sediments from these two box cores were the least compacted at depths below 10 cm. This suggests that the soft and less compacted sediments allow more sub-oxic diagenetic precipitation than in more compacted sediments. It is likely that the soft sediments allow mobilization of Mn in the sediment pore waters and hence diagenetic precipitation at depth. In contrast AB02 BC02 sediments were the most compacted, whilst some nodules were found at depths 2 – 10 cm, the much more compacted sediments beneath the nodules suggests that nodule burial and hence diagenetic growth mechanism were minimal. Therefore, the nodules from this box core generally remain at the sediment top for most of their growth history where slow hydrogenetic precipitation prevails. This resulted in their physically small size, and their well-rounded and smooth surface texture. The internal structures of nodules in this study are shown in the next chapter (chapter 3). The results show that

nodules from this box core are less porous, contain more hydrogenetic layers and are compacted. All these features resulted from the predominantly slow hydrogenetic precipitation from their bottom sea environment.

Nodule occurrence at depth might be also influenced by the redox conditions in the sub-seafloor environment. Typical oxygen penetration depths (OPD) in CCFZ sediments have been reported to be 0.5 – 7.5 m (Mewes *et al.*, 2014; Mogollón, Mewes & Kasten, 2016; Rühlemann *et al.*, 2011; Volz *et al.*, 2020; Volz *et al.*, 2018), similarly the OPD in the UK contract area is reported to be 1.5 m (Menendez *et al.*, 2019). With increasing depths, the redox conditions are more reducing, which will lead to the dissolution of Mn(IV)O₂ in ferromanganese oxides into porewater as soluble Mn(II). The dissolved Mn in the porewaters then diffuses upward to the oxic layer where it gets oxidized and re-precipitates as MnO₂. This might explain the low occurrence of nodules with increasing depth, and the occurrence of ‘ghost’ outlines of dissolved nodules at depth in the sediment column (personal observation during 2020 research cruise to the UK Claim Area).

The observations discussed above show that the occurrence of nodules in the sediments depends on the depth whereby oxic conditions exist. The occurrence of nodules at increasing depths at some sites compared to their absence at the same depths at other sites indicates that the OPD is quite variable in the CCFZ. This is consistent with the OPD determined in several studies ranging from 0.5 – 7.5 m for the CCFZ as mentioned earlier. Therefore, in areas where the OPD is greater, sub-oxic conditions still prevail at depth and nodules can occur at depth (though in low abundance). In contrast, in areas where the OPD is shallower, sub-oxic conditions only prevail at the top few centimetres of the sediment only. In this case, the occurrence of nodules at depth is minimal as can

be seen in some of the box cores studied. As shown earlier, this is also linked to the compactness of the sediments. At sites where the sediment is soft and less compacted, the depth where sub-oxic conditions prevail are deeper and hence, nodules can occur at increasing depths (e.g. AB02 BC06 and AB02 BC19). Nodules from these sites are generally large in size and the nodules are dominated by bulbous botryoidal structures due to rapid diagenetic precipitation in sub-oxic conditions. In contrast, at sites where the sediment is compacted, the OPD is shallower, therefore sub-oxic conditions are less predominant and nodules dissolve at depth. The nodules at the seawater-sediment interface are therefore underlain by weaker sub-oxic diagenetic conditions, instead the predominant mechanisms shifts to a more hydrogenetic-type. As a result nodules have slightly hydrogenetic features which can be observed in the small compacted, well-rounded nodules in AB02 BC02.

Another feature that can influence nodule occurrence and morphology is bottom seafloor topography. The seafloor bathymetry information shows that AB02 BC19 was located on a flat valley bottom between two seamounts. This shows that the movement of bottom seawater at this site was restricted and there was not much flow. Such conditions can allow nodules to be buried by sediments due to less seawater flow to move nodules and keep them atop. Upon burial (or partial burial) nodule growth is predominantly diagenetic and if there is a high degree of Mn mobilization for sub-oxic diagenetic precipitation in the sediment pore waters, the nodules will be large in size with botryoidal rims. These features were observed in nodules from this box core. Similarly, the bottom seafloor topography for AB02 BC06 shows that it was located at the same depth as AB02 BC19, on a flat abyssal plain that appears to be more like an extensive flat valley bottom between two outcrops ~3km to the west and northeast.

These observations suggest that the bottom seawater movement is also restricted at this site, and therefore, the same explanation for the AB02 BC19 can be applied here.

The site for AB02 BC19 is located on a flat valley between two seamounts, with each approximately 2 km away to the west and east (see seafloor bathymetry in Figure 2.3 and site descriptions in Table 2.4). This location and topographical features indicate that the bottom water currents at this site are slow-flowing, this prevents sediment removal resulting in nodules being covered and eventually some nodules may be buried by sediments. In contrast, nodules from AB01 BC07, AB02 BC02 and AB02 BC04 were collected from flat plains where there is more rapidly flowing Bottom water currents that removes sediments from the surfaces of nodules and preventing them from being buried. These oceanographic conditions were the strongest at AB02 BC02 which is probably coupled with low sedimentation rates which results in the nodules being exposed for at least a few million years and there is continuous flow of bottom oxic water.

2.4.3 Resource potential of polymetallic nodules

2.4.3.1.1 Rare earth elements and Yttrium

Table 2.8 gives the REY concentrations in nodules from different ocean basins as well as those of other deep-sea deposits types from the Pacific Ocean and the Bayan Obo mining district, which is the world's main supplier of REYs. The mean total REYs concentration of nodules from the UK1 is 770 ppm. Comparing this value with total REYs concentrations from other known areas for nodules of commercial interests, nodules from the Cook Islands EEZ (hydrogenetic type) contain the highest concentrations of

REYs (1680 ppm), while Peru Basin nodules (diagenetic type) contain low concentration of 403 ppm. Nodules from the CCFZ and Indian Ocean (REYs = 1070 ppm) are of mixed-type origin and their REYs concentration falls between that of hydrogenetic and diagenetic nodules. Their total REYs are lower than that of the hydrogenetic nodules from the Cook Islands EEZ and higher than Peru Basin nodules. This comparison shows that hydrogenetic nodules contain more REYs than diagenetic nodules, while those with both hydrogenetic and diagenetic characteristics fall in between. The comparison of LREEs vs HREYs shows that LREEs dominate in the UK1 nodules (76.5%) while the HREYs make up 23.5%. HREYs are scarcer and therefore more expensive. While the value of 23.5% for HREYs is still comparable to those of nodules from other ocean basins, the value is significantly higher when compared to land based REYs deposits such as the Bayan Obo mine (1.3%) in China where most of the world's REYs supply is sourced (Yang *et al.*, 2011). The %HREY in CCFZ nodules is also higher than those of nodules from the Indian Ocean and Cook Islands and North Pacific crusts which shows why there is currently great interest in them. The %HREY is much higher in diagenetic nodules from the Peru Basin (32.3%), however, their total REYs is much lower than the CCFZ nodules. Another deep-sea mineral deposit type that has gained increasing interests recently particularly due to its high REY contents (>1000 ppm) are REE-rich muds from various regions in the Pacific Ocean, data for REE-rich muds from the Eastern South Pacific are shown in Table 2.6 (Iijima *et al.*, 2016; Kato *et al.*, 2011; Kon *et al.*, 2014; Takaya *et al.*, 2018). These deposits have even higher %HREY (52.1%), which makes them very attractive as a source for REYs and HREY in particular.

Table 2.8. Total REYs and the percentage of HREYs from known areas with high nodule abundance and exploitation interests. Data from: 1 = (Rudnick & Gao, 2003); 2 = (Pattan & Parthiban, 2011), (Pattan et al., 2001), (Baturin & Dubinchuk, 2010); 3= (Hein et al., 2015); 4 = (Hein et al., 2013); 5 = (Kato et al., 2011); 6 = (Yang et al., 2011).

	Crustal abundance	CCFZ nodule (mixed-type)	Central Indian Ocean nodules (mixed-type)	Cook Islands Nodules (hydrogenetic)	Peru Basin Nodules (diagenetic)	North Pacific Crusts	Eastern South Pacific REE-rich mud	Bayan Obo (Carbonatites, terrestrial deposit)
Reference	[1]	[This study]	[2]	[3]	[4]	[4]	[5]	[6]
LREE								
La (ppm)	20	112	129	173	68	338	158.8	9230
Ce	43	269	486	991	110	1311	80.8	16900
Pr	4.9	31.5	33	40.9	14.1	61	42.0	1620
Nd	20	136	146	160	63	255	187.1	4250
Sm	3.9	32.5	32	35	14	51.3	38.8	299
Eu	1.1	7.94	7.83	8.53	3.9	12.4	9.9	64.6
Total LREE	92.9	589	834	1410	273	203	517	32400
HREY								
Gd	3.7	29.0	32	36.1	15.6	55.8	47.6	198
Tb	0.60	4.77	5	6.09	2.52	8.73	7.2	20.9
Dy	3.6	26.9	26.5	34.9	15.8	59.2	47.5	63.3
Y	19	84.8	108	141	69.1	222	389	135
Ho	0.77	4.82	4.92	7.18	3.42	10.9	10.5	7.44

Er	2.1	13.5	12.9	19.1	9.8	30.9	30.9	12.2
Tm	0.28	1.9	2	3.02	1.49	4.54	4.3	1.02
Yb	1.9	13.2	11.8	19.8	10.3	28.5	26.9	3.86
Lu	0.30	2.00	1.93	2.98	1.61	4.3	4.2	0.43
Total HREY	32.3	181	205	270	130	425	568	442
Total REY	125	770	1070	1680	403	2450	1090	32800
%HREY	32.3	23.5	19.2	16.1	32.3	17.3	52.1	1.35

The resource potential of REYs in polymetallic nodules from the CCFZ is based on the consideration that they will be extracted as by-products of the economic drivers Ni (1.3%), Cu (0.98%), Co (0.17%) and Mn (28%). The ore tonnage of nodules in the CCFZ is estimated to be 21.1×10^9 tonnes (Hein *et al.*, 2013) covering an area of 4.2×10^6 km². Assuming that the TREO (total rare earth oxide) grade is generally similar across the entire area, we can use our data in this study to estimate their resource potential and compare them with that of terrestrial deposits. The TREO grade vs tonnage diagram of some major rare earth metal terrestrial deposits and CCFZ nodules is presented in Figure 2.12. The TREO grade in the UK1 is 0.09 wt%, this is considered as 'low grade' when compared to some terrestrial deposit types. However, the ore tonnage is large, even larger than the 'giant' Bayan Obo deposit in China which is the largest REE resource in the world. Therefore, CCFZ nodules can be classified as a low-grade mineral deposits with a large TREO tonnage. In this context, CCFZ nodules can be considered as important REE deposits for long-term investments with predictable ore grade and few challenges given minimal waste that will be generated during ore processing. The HREY composition of the CCFZ nodules compared to land based deposits is even more interesting. HREY are scarcer and therefore are more expensive compared to LREEs. In CCFZ nodules HREYs make up 24% of total REYs compared to less than 1% in land based deposits.

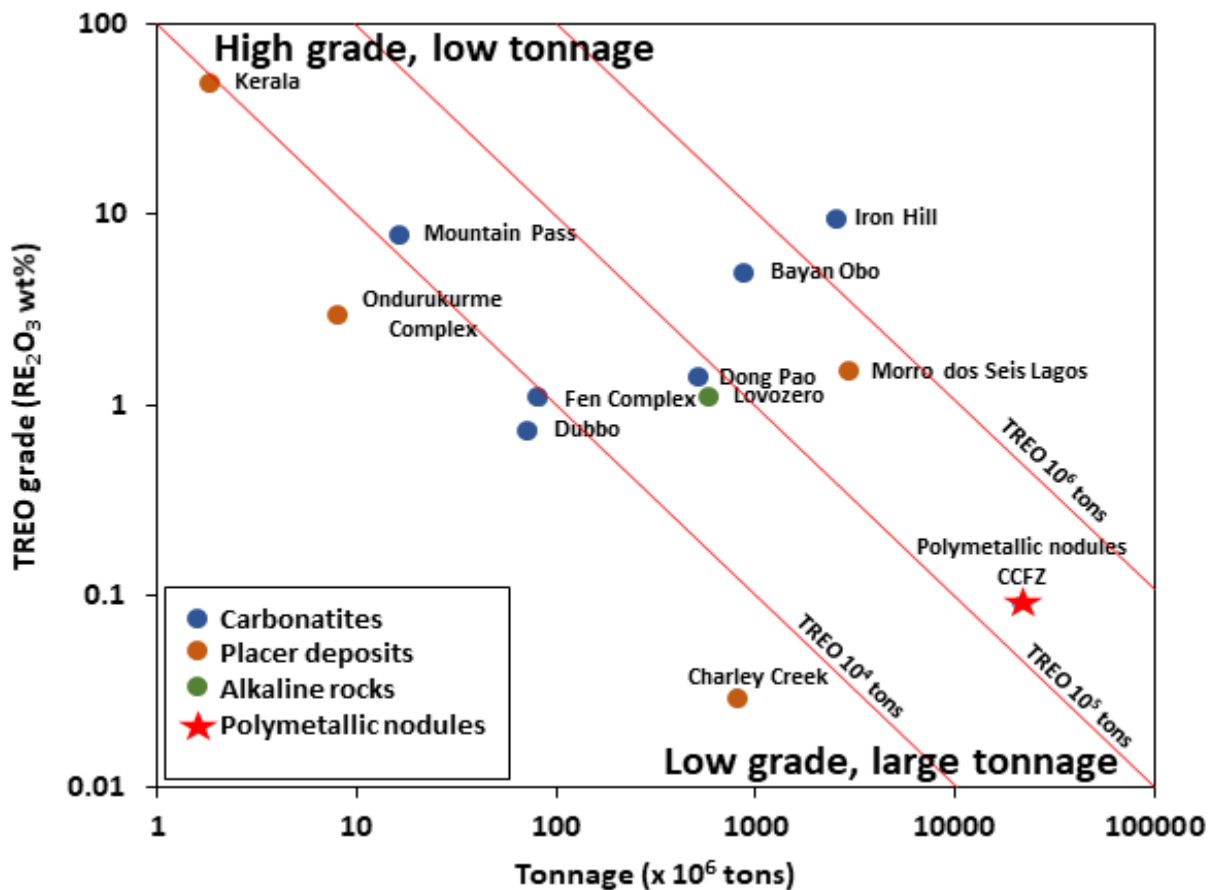


Figure 2.12. TREO grade vs ore tonnage of selected terrestrial REY deposits with a preliminary resource estimation of polymetallic nodules from the CCFZ. The data for the terrestrial deposits were sourced from (Pak et al., 2019), nodule grade data is based on this study while tonnage data was obtained from (ISA, 2010).

REYs deposits are characterised by several factors, one of which is the concentration of radioactive minerals. In carbonatite and alkaline rock deposits where REYs are mostly sourced from, Th levels are usually high (69.7 ppm) (Yang et al., 2011). High concentrations of such radioactive ‘penalty elements’ are of concern as they restrict shipping and processing of REYs ores and concentrates and can cause public fear (Wall et al., 2017). This is a major drawback for exploitation of REYs in land-based carbonatite/alkaline rock deposits. In polymetallic nodules, concentrations of

radioactive elements, particularly Th and U are relatively low (Th = 13.4 ppm, U = 3.99 ppm) (Table 2.7). This makes polymetallic nodules a potentially attractive REY resource.

2.4.3.1.2 Cobalt

Deep-sea deposits are potentially important source for Co, in particular ferromanganese crusts are estimated to be the most enriched in Co content (Table 2.9). In nodules, hydrogenetic nodules such as in the Cook Islands EEZ contain the most Co content followed by mixed type nodules such as CCFZ nodules. However, in terms of tonnage, the CCFZ contains the highest amount of Co metal which is estimated to be 44 million tonnes (Hein *et al.*, 2013) which far exceeds the global terrestrial reserves of 7 million tonnes (Figure 1.7, chapter 1). Plotting the UK1 nodule Co grade from this study in the grade-tonnage resource graph of the British Geological Survey (BGS) (Petavratzi, Gunn & Kresse, 2019) shows that the CCFZ nodules can be classified as medium grade, high tonnage deposits (Figure 2.13).

Table 2.9. Marine deposits (Co-rich crusts, polymetallic nodules) with their Co concentrations. Two terrestrial Co deposits from the Democratic Republic of Congo (DRC) and Kalgoorlie, Australia are included for comparison. Data from: [1] (Rudnick & Gao, 2003); [2, 4] (Hein *et al.*, 2013); [3] (Hein *et al.*, 2015); [5] (Slack, Kimball & Shedd, 2017); [6] (Petavratzi, Gunn & Kresse, 2019).

	Crustal abundance [1]	CCFZ Nodule (mixed-type) [This study]	Central Indian Ocean Nodules (mixed-type) [2]	Cook Islands Nodules (hydrogenetic) [3]	North Pacific Crust [4]	Tenke Fungurume (DRC) Sediment hosted Cu-Co deposits [5]	Kalgoorlie Nickel Project, Australia Ni-Co laterites [6]
Co (ppm)	17.3	1723	1111	3751	6655	2500	500

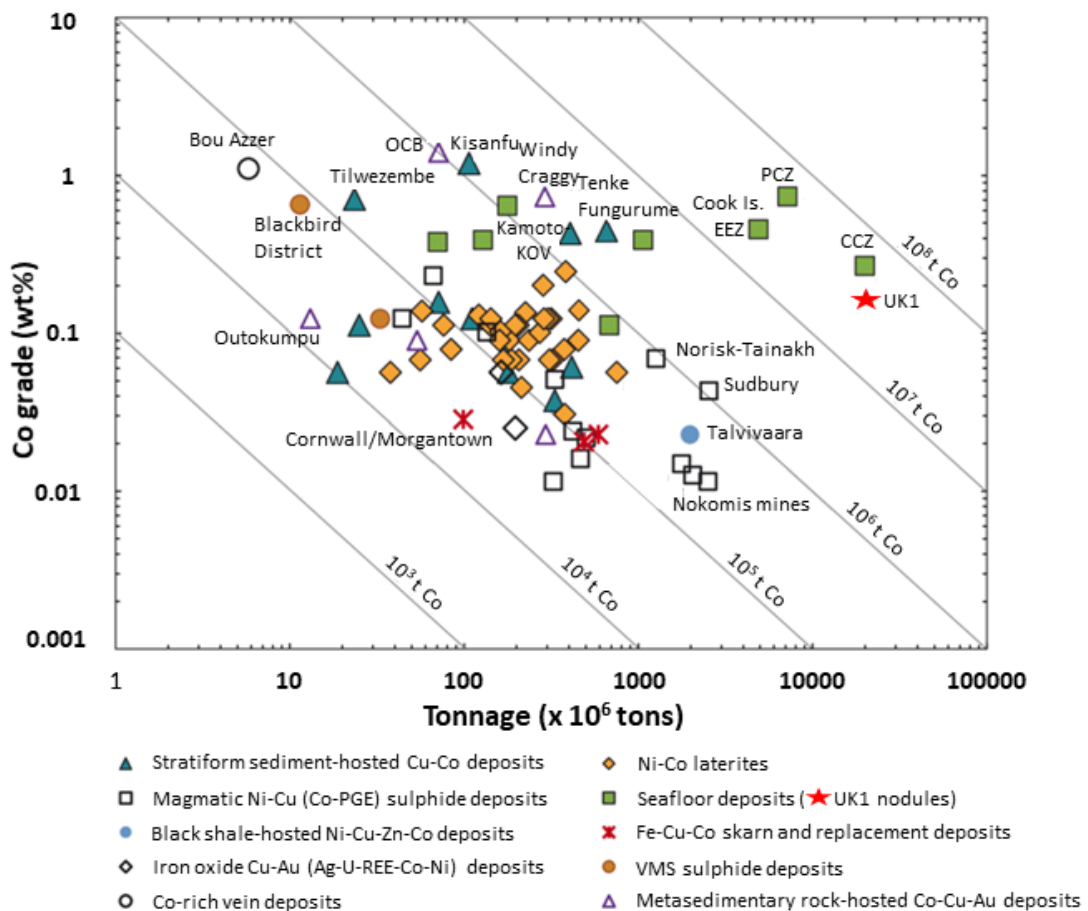


Figure 2.13. Cobalt grade vs ore tonnage modified after Petavratzi, Gunn and Kresse (2019), of selected terrestrial REY deposits with a preliminary resource estimation of polymetallic nodules from the CCFZ. The CCFZ data plotted by Petavratzi, Gunn and Kresse (2019) was based on data from Hein *et al.* (2013), which is slightly of higher grade than the one determined in this study (UK1 nodules). However, both show that Co in CCFZ nodules plots in the medium grade and high tonnage category.

2.4.3.1.3 Nickel and copper

The metals of traditional economic interest in polymetallic nodules are Ni and Cu. Although these two metals are known to be enriched in diagenetic nodules, the highest Ni and Cu concentrations in nodules are in CCFZ nodules. The high Ni content in the pore waters of siliceous deep sea sediments has been suggested as the probable cause for the high Ni content in CCFZ nodules (Kuhn *et al.*, 2017). The mean Ni concentration in

UK1 is 1.31% while Cu is 0.98%. The concentration of Ni does not vary much between the box cores, ranging from 1.18 – 1.42%. This small variation is also similar when a comparison is made between Ni content in the published literature in mixed type nodules from the eastern CCFZ (1.40%) versus diagenetic nodules (1.30%) (Hein *et al.*, 2013). Hydrogenetic nodules on the other hand, show relatively low levels of Ni, for instance as in the Cook Islands basin (0.38%). The concentrations of Cu in the five box cores show small variations similar to that of Ni, ranging from 0.810 to 1.11%. Nodules in AB02 BC02 showed the lowest concentrations of Cu (0.810%) while the concentrations in the rest of the box show little variation ranging from 0.978 – 1.11%. The geochemical relationships of the different types and their genetic origins are discussed in much more detail in the next chapters.

The CCFZ is the world's largest known deposit of Ni and Cu. In fact, early exploration work on polymetallic nodules in the CCFZ in the 1960s – 1970s was particularly due to their Ni and Cu contents (Glasby, 1977; Mero, 1962; Mero, 1965). They are used in a wide range of applications from kitchen-ware to medical equipment and uses in the military. For Ni, it is now increasingly being used in making rechargeable batteries that are important in green technology such as in electric vehicles. This has increased interests in the Ni deposits from the CCFZ, although there is less concern over its supply as Ni mines are currently distributed in many countries. Copper is largely used in electrical products and is also used in other industries such as in construction and a wide range of general consumer products. Deposits of Cu are found worldwide in a variety of geological deposits and similarly to Ni, there are currently less concern over its supply.

The Ni and Cu deposits in the CCFZ are estimated to contain 274 and 226 million tonnes of metal respectively (Hein *et al.*, 2013). The resource diagrams in Figure 2.14 and Figure

2.15 show the Ni and Cu grade-tonnage relationship of some known deposits with that of the CCFZ included, based on this work. The grades of Ni and Cu determined in this work for the UK1; 1.3% Ni and Cu 0.98% respectively, are included in the grade-tonnage diagrams for resource estimation. The plots show that at a grade of 1.3% for Ni and 0.98% for Cu and ore tonnage of 21.1 billion tonnes (ISA, 2010), both plot in the medium grade and high tonnage categories.

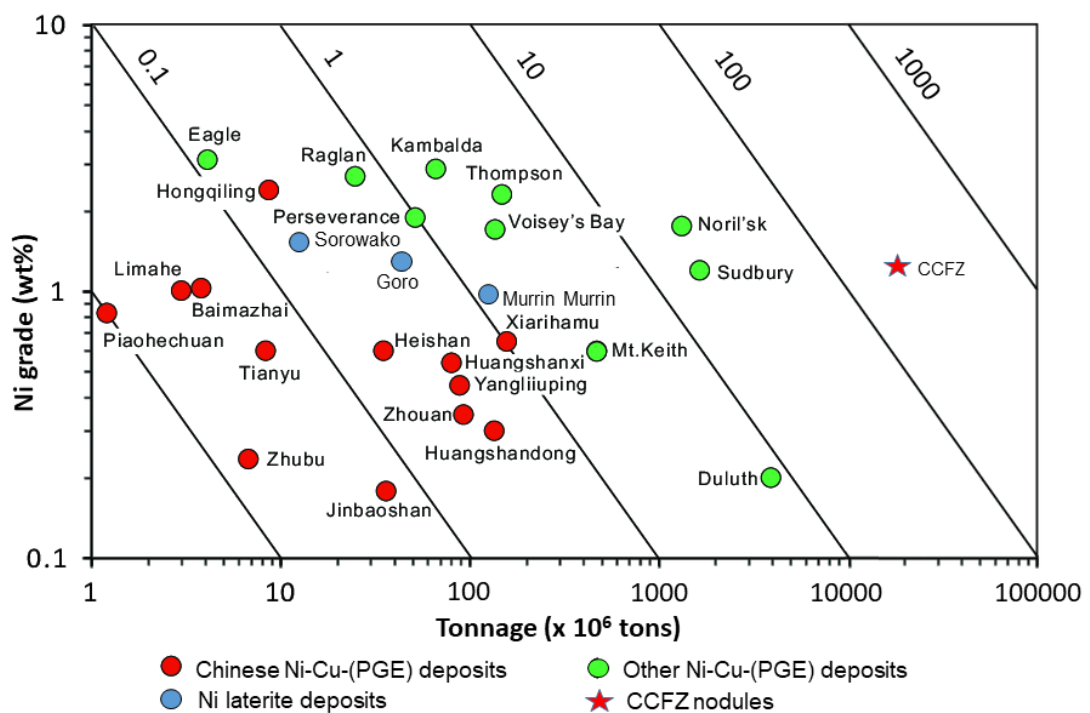


Figure 2.14. Nickel grade versus tonnage, modified after Lu, Lesher and Deng (2019) of some known deposits. The CCFZ grade of 1.3% was determined in this work and plots in the intermediate to high grade and high tonnage area. Other data source; Sorowako: Mining Data Solutions (2018); Goro: Mining Technology (2009); Murrin Murrin: Mining Technology (2005).

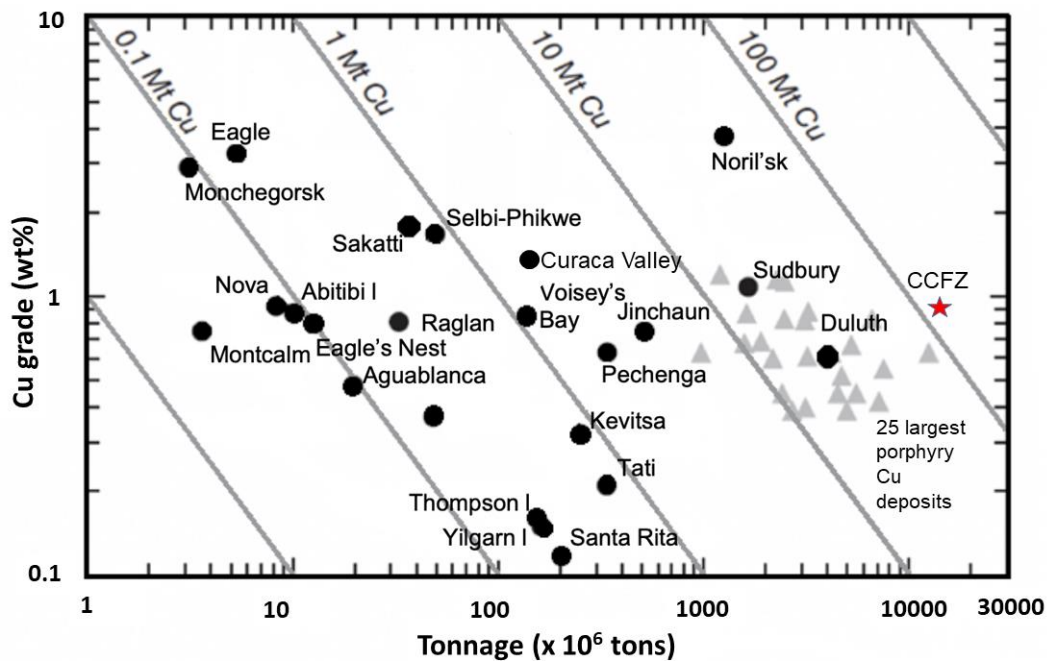


Figure 2.15. Copper grade versus ore tonnage, modified from Ero Copper (2019). The CCFZ grade of 0.98% was determined in this work and plots in the medium grade and high tonnage area. Note, some the world's largest porphyry Cu deposits, which are the primary source of Cu mined today are denoted by the grey triangles.

2.5 Conclusion

The nodules from the five box cores studied generally show features of mixed-type nodules. Nodules have a smooth top where they were in contact with slow hydrogenetic precipitation from the ambient seawater and a rough bottom where they were in contact with the more rapid diagenetic precipitation from sediment porewaters. In particular, nodules from AB02 BC02 showed more hydrogenetic features which is also reflected in their chemical composition i.e. low Mn/Fe ratios and high concentrations of Co and REY. Sample decomposition using sodium peroxide sintering proved to be a simple, safe and reliable method for the determination of trace metals including REYs in polymetallic nodules. The approach in which only the water-insoluble fraction of the sinter was dissolved and analysed yielded acceptable recoveries within the range 84 –

103% (96-103% for the REYs alone) and repeatability of $\leq 12\%$ RSD for certified reference material FeMn-1. The bulk composition of nodules in the five box cores are similar but variations exist. Compositionally, the nodules are mostly made up of Fe, Mn and Si and Al. Bulk compositions of some individual nodules analysed showed that their compositions are very similar to the combined or 'rubble' composition, which shows that the nodules in the same box core are similar in terms of their composition. In terms of their Mn and Fe composition, Mn/Fe ratios range from 2.91 to 6.42 and averages at 4.98 which is within the range for nodules of mixed-type origin. Average bulk composition of nodules in UK1 for some important metals are as follows: Mn = 28.4%, Ni = 1.3%, Cu = 1%, Co = 0.2% and REYs = 770 ppm. Nodules in all box cores generally show characteristics of a mixed type origin with nodules in AB02 BC02 showing some small hydrogenetic characteristics and nodules in AB02 BC19 showing some diagenetic characteristics. In terms of their resource potential, CCFZ nodules can be classified as large tonnage deposits for REY, Co, Ni and Cu. In terms of grade, the nodules can be classified as low grade TREY, and medium grade Co, Ni and Cu.

Chapter 3

3 Structure and composition of individual nodule layers using electron microscopy and wet chemistry analyses.

3.1 Introduction

In the Clarion-Clipperton Fracture Zone (CCFZ) area in the Pacific Ocean, polymetallic nodules form from both hydrogenetic and diagenetic processes (see Introduction section in chapter 2) and thus, are generally interpreted as mixed-type nodules (Bau *et al.*, 2014; Halbach, Friedrich & von Stackelberg, 1988; ISA, 2010; Wegorzewski *et al.*, 2015). This is in contrast to polymetallic nodules from other areas, which are often formed by a single process; for instance, the hydrogenetic nodules from the Blake Plateau in the Atlantic Ocean (Cronan, 1975; Cronan, 1977) and the diagenetic nodules from the Peru Basin (Paul *et al.*, 2019a; Von Stackelberg, 1997). In order to classify nodules and understand their environment and mechanism of formation, some studies have used chemical proxies such as Mn/Fe ratios and trace element concentrations, including rare earth contents (Bau *et al.*, 2014; Menendez *et al.*, 2019; Pattan & Parthiban, 2011; Takematsu, Sato & Okabe, 1989). Other useful methods of classification that have been used by others, sometimes in combination with chemical proxies, are based on morphological characteristics such as shape, size, surface texture and internal growth structures (Benites *et al.*, 2018; Halbach *et al.*, 1981; Vineesh *et al.*, 2009).

Polymetallic nodules form by growth accumulation of Mn and Fe oxides around a nucleus. Several theories have been proposed for the formation of polymetallic nodules. However, out of the several theories, the two main processes are hydrogenetic precipitation and diagenetic precipitation.

Hydrogenetic precipitation involves the slow precipitation of Mn and Fe oxides onto hard substrates on the seafloor (Bonatti, 1981; Halbach, Friedrich & von Stackelberg, 1988; Koschinsky & Halbach, 1995). This process is responsible for the formation of hydrogenetic crusts as well as hydrogenetic nodules (Koschinsky & Halbach, 1995). The process, as summarised from Kuhn *et al.* (2017) and references therein, begins with the formation of colloidal MnO₂ and FeOOH under normal seawater conditions (Eh > 0.5; pH ~8). The tendency of both phases to hydrolyze results in both possessing surface charges, with MnO₂ having a strong negative charge while FeOOH a slightly positive charge. As a result, cations such as Co(II), Ni(II), Cu(II), and Zn(II) are adsorbed onto MnO₂ while δ-FeOOH adsorbs ions that form anionic complexes such as (REE(CO₃)₂⁻) and (Hf(OH)₂⁻). The colloidal oxide phases then precipitate on sediment-free hard substrate rocks to form crusts and nodules. In crusts the substrate rocks occur as pavements, hence the crust occurrence covers an area of the seafloor while in nodules the oxides precipitate onto a 'nucleus' such as a rock substrate, fish tooth or an existing nodule. This formation model is summarised in Figure 3.1.

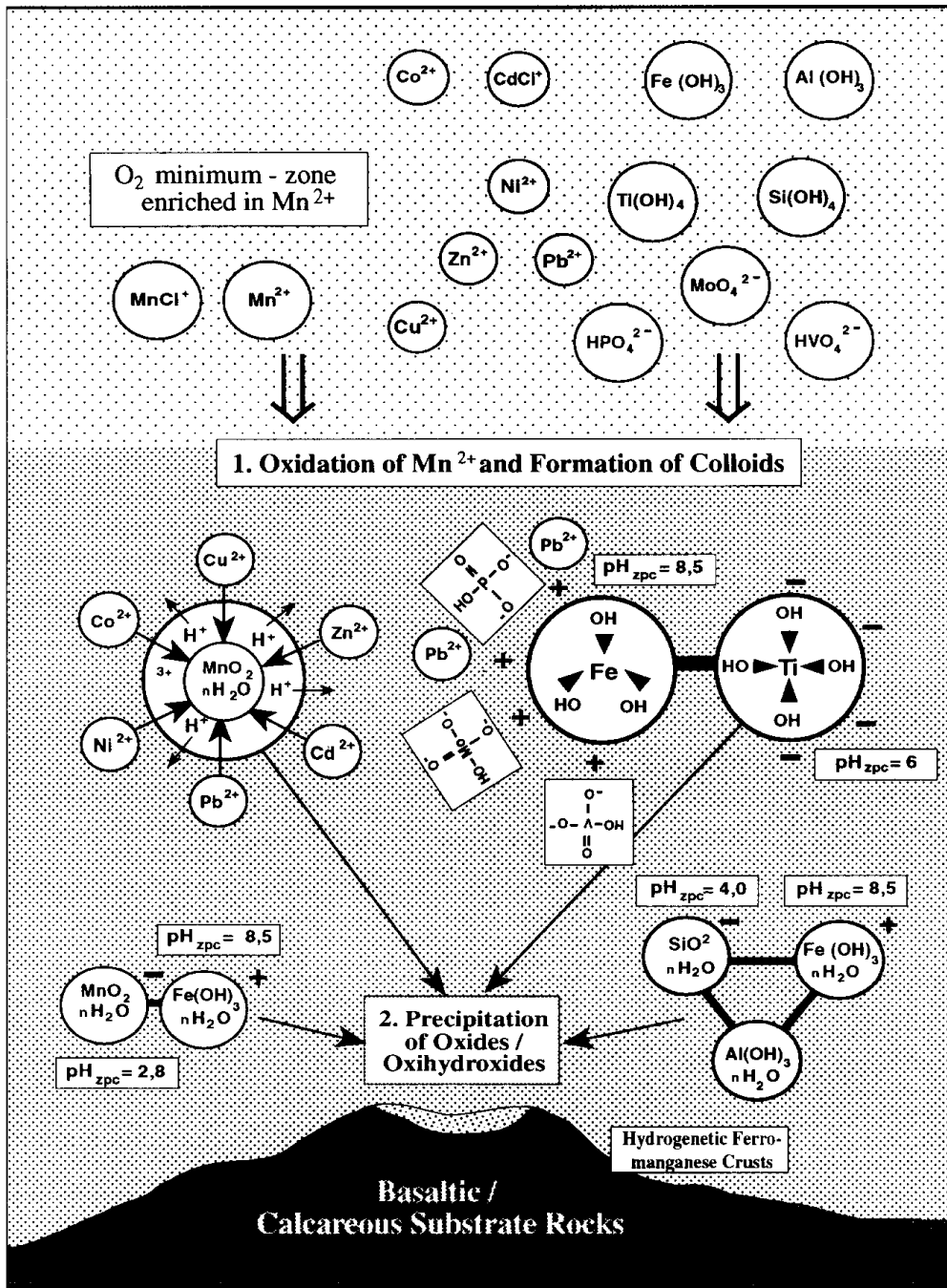


Figure 3.1. Formation model for hydrogenetic crusts on seamounts (Koschinsky & Halbach, 1995). The process begins with the formation of colloidal phases and scavenging of trace metals. The colloidal phases then precipitate as oxide/oxyhydroxide encrustations on hard substrate rocks of the seamounts.

Some elements that are enriched in ferromanganese nodules and associated with MnO_2 , can exist in several oxidation states in the marine environment. Examples include Ce, Co

and Pb, they exist as positively charged cations in their lower oxidation state as soluble ions in seawater. Once sorbed onto the surface of colloidal MnO_2 they are oxidized to their higher oxidation state [$\text{Ce(III)} \rightarrow \text{Ce(IV)}$, $\text{Co(III)} \rightarrow \text{Co(IV)}$, $\text{Pb(II)} \rightarrow \text{Pb(IV)}$] and then precipitate to a hard substrate that acts as a nucleus or an existing nodule surface (Figure 3.2). As oxidation proceeds on the MnO_2 surface, more of the metal is scavenged from seawater. This mechanism is known as oxidative scavenging and is said to be responsible for the enrichment of these metals in polymetallic nodules (Takahashi *et al.*, 2007; Takahashi *et al.*, 2000).

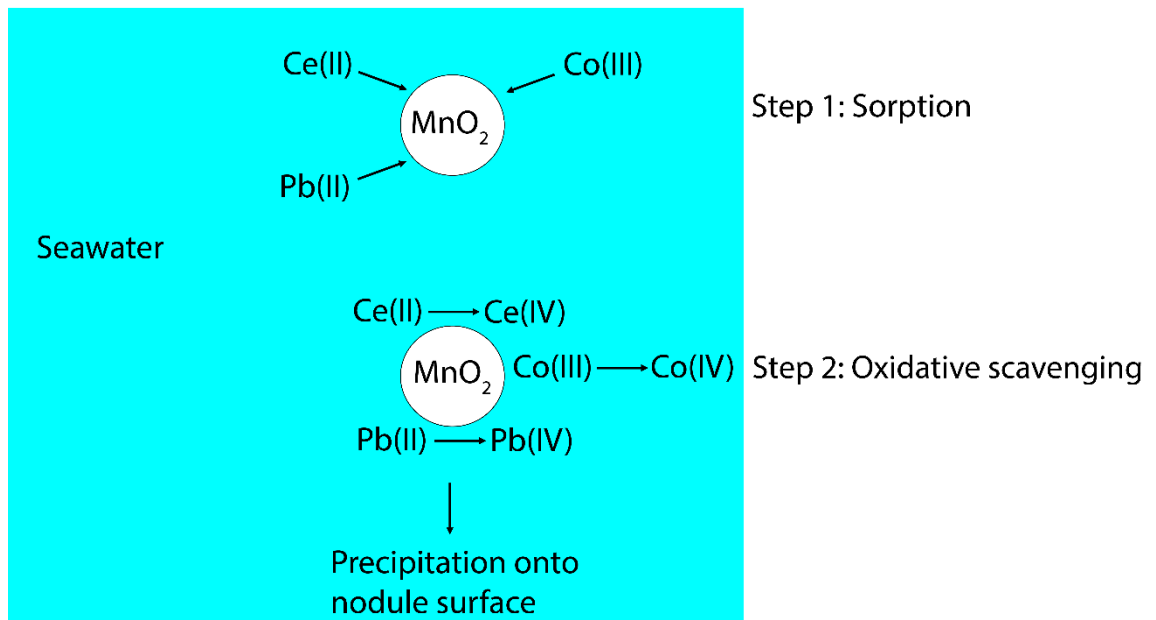


Figure 3.2. Oxidative scavenging mechanism. It begins with the sorption of cations from the seawater by colloidal MnO_2 (step 1) followed by their oxidation on the surface of MnO_2 (step 2) and precipitation on a hard substrate rock or an existing nodule (Takahashi *et al.*, 2007).

The process of nodule formation whereby elements precipitate from within sediment pore waters, under oxic or suboxic conditions is called diagenetic precipitation (Ku, 1977; Kuhn *et al.*, 2017; Reyss *et al.*, 1985). This process begins with the diagenesis of marine organic matter in sediments via a sequence of oxidation reaction pathways.

These reaction pathways as described by Froelich *et al.* (1979), and shown in Figure 3.3 are summarised as follows: Organic matter reaching the seafloor is first oxidised by aerobic organisms using dissolved oxygen (Zone 1). When all the oxygen is consumed, oxidation continues under anaerobic conditions as suboxic diagenesis utilizing the next most efficient (i.e. most energy producing) oxidant which in this case are nitrate and MnO_2 (Zones 2 – 5). The reaction sequence then continues after the consumption of these two oxidants using iron oxide and sulfate (Zone 6 -7). However, the step where this is important for nodule formation is the one involving MnO_2 . The oxidation of organic matter by MnO_2 in this step results in the subsequent reduction of Mn(IV) to Mn(II). The Mn(II) is soluble, therefore, it is released to the interstitial water and then diffuses upwards and is oxidized back to MnO_2 when it reaches Zone 3 in the sediment column and thereby significantly contributing to nodule growth (Chester & Jickells, 2012; Kuhn *et al.*, 2017).

In porewaters within sediments in the CCFZ, Ce concentration decreases with increasing depth while Mn and Fe concentrations in associated sediments show general increasing trends (Paul *et al.*, 2019b). The decreasing Ce concentration with increasing depth in porewaters is hence interpreted as due to the fact that most of the Ce is bound as Ce(IV) to Mn oxides and Fe oxyhydroxide phases in the associated sediments. This suggests that some of the Ce that remained in the porewaters at increasing depth is in the reduced state as Ce(III) since the probable mechanism of enrichment in both oxides phases is oxidative scavenging, and FeOOH is also an oxidative scavenger. Therefore, at increasing depths, Ce exists in the reduced form as Ce(III) in the porewaters.

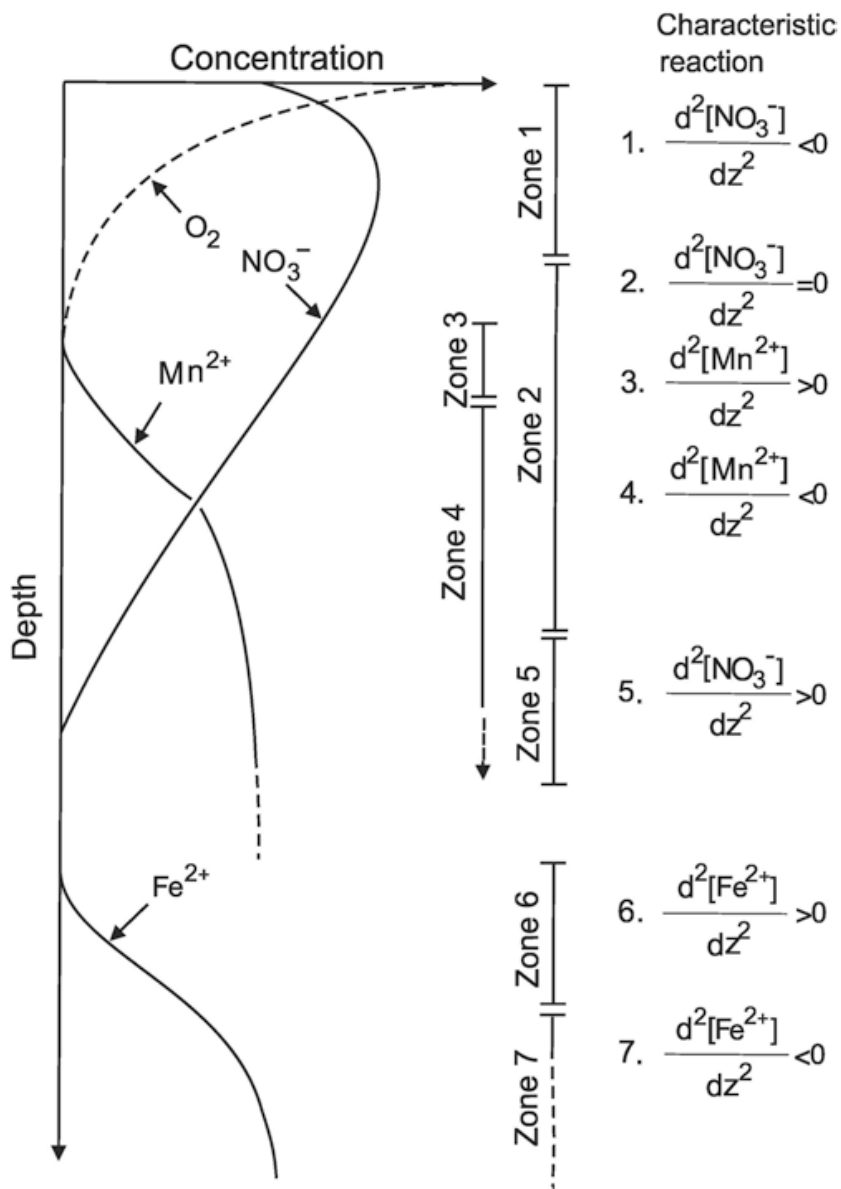


Figure 3.3. Schematic representation of trends in pore water profile and diagenetic zones in deep sea sediment, adapted from (Froelich et al., 1979). In Zone 1, organic carbon is oxidized by oxygen via aerobic respiration until oxygen is depleted. Oxidation of organic carbon continues in Zones 2 -5 by nitrate and Mn(IV), the oxidation pathway involving Mn(IV) results in its reduction to the soluble Mn(II) which is released into the porewaters and diffuses upward to Zone 3 where it is re-oxidized. In Zones 6 and 7, organic carbon is oxidized by ferric oxides, this results in the reduction of Fe(III) to Fe(II), the latter is then released into the porewater.

Whilst nodules can be purely hydrogenetic or diagenetic, nodules from some ocean basins such as those from the CCFZ form by a combination of both processes, and therefore are commonly known as 'mixed-type' nodules (Hein et al., 2013). As a result,

mixed-type nodules are composed of the characteristics (chemical composition, internal structures, growth rates) of both growth types. Nodule occurrence on the seabed are mostly on the seawater-sediment interface where they grow by hydrogenetic and/or diagenetic processes. Nodules can be also found within the sediments where they are buried particularly due to changing oceanographic conditions that result in slow-flowing bottom water currents and hence high sedimentation rates. Another scenario that can bury nodules is due to debris supply from above or more appropriately known as surface bio-productivity, whilst this debris is important for nodule growth (as it supplies materials for nodule growth), a high supply rate can result in the subsequent burial of nodules in the sediments (Kerr, 1984). On the other hand, if the supply stops or becomes limited, nodule growth can be inhibited and this can be also interpreted as a period of non-deposition. One geological event when this may happen and can be linked to growth discontinuities is during glacial periods, which also further suggests that deposition happens only (or mostly) during interglacial periods. For example, Pb isotopic measurements in sediment cores from the Pacific Ocean have shown greater aeolian dust fluxes from the Central American continent during interglacial periods (Abouchami *et al.*, 1997). Similarly, continental weathering is the main source of materials for nodule growth (ISA, 2010), therefore, it is possible that glacial events leading to decreased supply of materials to the ocean might also result in the discontinuities in nodules. Whilst the bulk of the current knowledge on surface nodule formation and growth processes, less is known about buried nodules. Previous works on buried nodules from the Central Indian Ocean Basin (CIOB) shows that nodule size decreases with sediment depth, and at depths of more than 1 m, nodules are absent (Pattan & Banakar, 1993; Pattan & Parthiban, 2007). Furthermore, the morphology and chemical composition of

buried nodules are similar to that of surface nodules and diagenetic remobilization of metals in the associated sediment column was not present. These observations led Pattan and Banakar (1993) and Pattan and Parthiban (2007) to conclude that nodules neither grow nor dissolved at depth. In contrast, recent work by Heller *et al.* (2018) on buried nodules from the German (BGR) Claim area in the CCFZ showed that when nodules become buried long enough that suboxic conditions begin to prevail, nodules undergo dissolution. The depth of burial in this case is 16 – 926 cm below sediment surface. The dissolution process is not straightforward whereby the whole nodule dissolves, but is rather selective where only the Mn oxide phase dissolves. This results in the metals bound to Mn oxides being released to the pore water while the Fe oxides react with the surrounding sediment and porewater to form an authigenic Fe-Si-Al-rich layer consisting of nontronite and goethite.

In addition to the two main nodule formation processes as discussed above, a number of other processes have also been proposed. These include hydrothermal process where the metals derive from hot springs associated with volcanic activity, and halmyrolithic processes where metals derive from the decomposition of basaltic debris by seawater (Bonatti, 1981; Pelleter *et al.*, 2017). Furthermore, the formation of polymetallic nodules by biogenic processes has also been proposed where free living and biofilm forming bacteria provide the matrix for manganese deposition (Wang & Müller, 2009).

The presence of biogenic structures in nodules have led some workers to interpret that nodule formation is to some extent influenced by biomineralization where organisms form minerals and the mineralized products comprised of both mineral and organic components (Lowenstam & Weiner, 1989; Weiner & Dove, 2003). The works of Wang and colleagues (Wang & Müller, 2009; Wang *et al.*, 2009) in particular on nodules from

the Eastern CCFZ have documented the presence of biogenic structures in ferromanganese deposits which they interpreted as microbial colonisations. They proposed that the microorganisms play a part in nodule formation where the structures (as biofilms) provide a medium where Mn is deposited due to the oxidation of Mn(II) to Mn(III)/(IV). Similarly, recent work by Yu and Leadbetter (2020) using synthetic manganese nodules showed that the mechanism of Mn deposition via microbial process is possible. Although these studies show the potential role microorganisms can play in nodule formation, this is not well understood at present. Polymetallic nodules have very slow growth rates which mean that bacterial activity may not be the main factor in their formation. However, bacteria play an active role in sediment diagenesis where some elements such as Mn, Ni and Cu are released into the pore fluids and then taken up during nodule formation and growth (Petersen *et al.*, 2016). In addition, feeding and burrowing animals present in and on the ocean floor can stir up sediments on the seafloor. When these sediment disturbance activities occur close to nodules and metals are desorbed from the sediment, they can then be adsorbed into the nodules (Kerr, 1984).

Most of the metals in nodules are from terrigenous and volcanic sources, which end up in the ocean by weathering or as river wash offs. The metals are then adsorbed onto the surfaces of fine grained sediments and are transported by the movement of currents away from continents. The sediments are consumed by marine organisms such as zooplanktons and were later converted to fecal matter that are large and heavy enough to sink to the bottom floor where they are subjected to hydrogenetic and diagenetic processes for nodule growth (ISA, 2010). The formation environment of hydrogenetic, diagenetic and mixed-type nodules is shown in Figure 3.4.

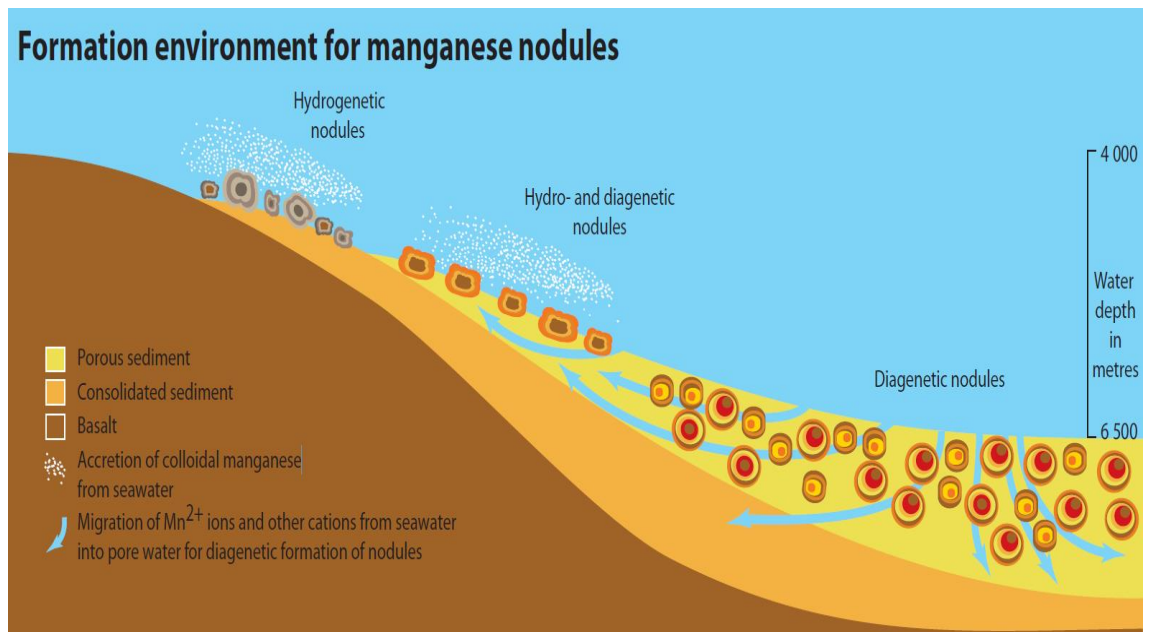


Figure 3.4. Formation environment of hydrogenetic, diagenetic and mixed-type nodules (ISA, 2010). Nodules grow by precipitation of oxides and oxyhydroxides from bottom seawater (hydrogenetic), sediment porewaters (diagenetic) and from a combination of both sources (mixed-type).

Polymetallic nodules grow at different rates depending on the mechanism of the growth process and therefore, is an important aspect governing their formation. On average, they grow at very slow rates of typically 10 – 20 mm/Ma based on ^{10}Be dating (Somayajulu, 1967). Determination of nodule growth rates (and age) can be done by radiometric and non-radiometric isotopic methods, although the former is the most common approach. Common radiometric isotopes that proved useful in growth rate and age determinations are ^{230}Th , ^{10}Be , ^{40}K and ^{238}U (Ku, 1977; Somayajulu, 2000; Somayajulu *et al.*, 1971; Vlasova, 1995). By comparing individual nodule types, hydrogenetic nodules grow at slow rates of 1 – 5 mm/Ma as a result of the slow hydrogenetic precipitation from the bottom seawater (Koschinsky & Hein, 2003). In contrast, diagenetic nodules grow at much faster rates, from 20 up to 250 mm/Ma as has been reported for Peru Basin nodules (Von Stackelberg, 1997). These fast growth

rates are due to rapid diagenetic precipitation from the underlying suboxic/oxic sediment pore waters. Mixed-type nodules are composed of both hydrogenetic and diagenetic layers, therefore, their average growth rates fall between those of the two end member types.

The type of internal growth structures in nodules, as well as their associations with different metals and mineral host phases are influenced by the environmental conditions in the deep sea. Generally, nodules consist of concentrically banded zones of microlayers around a nucleus Figure 3.5. The nucleus can be composed of indurated sediments, rock particles, biogenic fragments, or micro-nodules (von Stackelberg & Beiersdorf, 1988). Several types of internal growth structures have been observed in polymetallic nodules, these include: finely laminated, columnar, pillar-like, dendritic, and massive layers (von Stackelberg & Marchig, 1987). According to Wegorzewski and Kuhn (2014), hydrogenetic layers are typically composed of finely laminated to columnar structures, while diagenetic layers are characterized by dendritic layers and less frequently by dense massive layers. The formation of these structures is due to different formation mechanisms associated with nodule growth. The generation of finely laminated to columnar structures are due to the slow hydrogenetic precipitation from the ambient bottom seawater. In contrast, diagenetic processes originating from within the pore spaces of underlying sediments result in the dendritic structures.

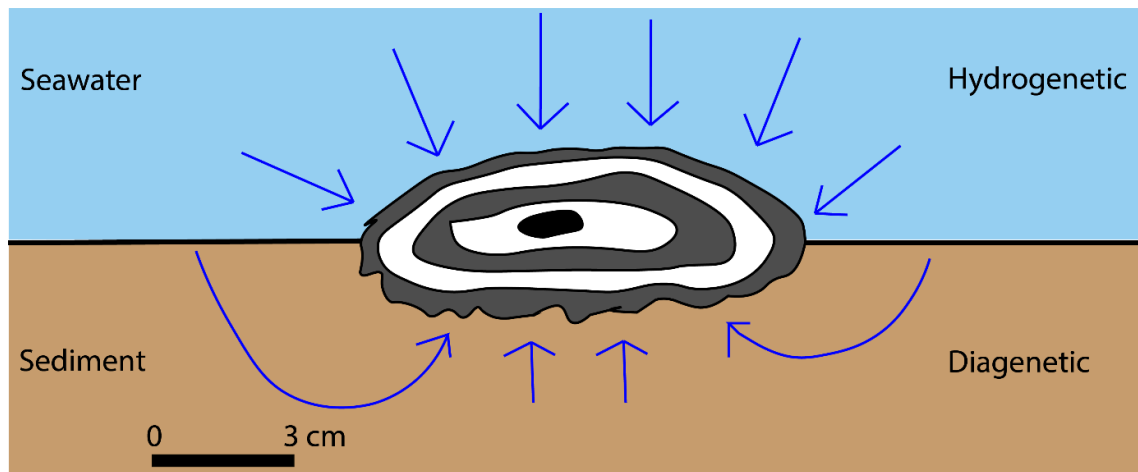


Figure 3.5. General growth model of a mixed-type polymetallic nodule that forms from both hydrogenetic and diagenetic processes [modified from Kuhn *et al.* (2017)].

The chemical composition of nodules depends on the type of formation mechanism (i.e. hydrogenetic or diagenetic). Hydrogenetic nodules are characterized by a Mn/Fe ratio of <3 and they are enriched in metals such as Co and REYs (Bau *et al.*, 2014; Hein *et al.*, 2013; Hein *et al.*, 2015). In contrast, diagenetic nodules show a Mn/Fe of >3 and high levels of metals such as Ni and Zn (Halbach *et al.*, 1981; Hein *et al.*, 2013). Nodules from the CCFZ are of mixed type origin, therefore, they show both types of layers, and each with its associated metal enrichments (Kuhn *et al.*, 2017; Wegorzewski *et al.*, 2015). Previous reports have demonstrated that REYs, Co and Pb are concentrated in the hydrogenetic regions while Ni and Cu are more enriched in the diagenetic layers of nodules (Manceau, Lanson & Takahashi, 2014; Menendez *et al.*, 2019).

The different types of growth structures and their associated metal enrichments are reported and discussed in this chapter. Analytical work was carried out by electron microscopy imaging analysis and spectroscopic measurements after wet chemistry digestions of individual layers. The aim of this work was to study the individual hydrogenetic and diagenetic layers and determine quantitatively the critical metal

(REYs, Co) compositions of the individual layers. This enables an improved understanding of their distribution in the nodules, with implications on the genesis of nodules in the deep sea and their resource potential.

3.2 Method

3.2.1 Scanning electron microscopy (SEM)

3.2.1.1 Sample preparation

Nodule samples were cut up using a diamond saw, oven dried at 105°C before impregnated with a mix of liquid resin (EPO Flo resin) and a liquid hardener (EPO Flo hardener) and left to cure overnight at 50 – 60°C. The samples were then polished down to a 1 µm grain size and analysed by SEM. Prior to analysis, polished sections were oven-dried overnight at 105°C to remove moisture to allow instrument to create vacuum conditions. For a more detailed description of sample preparation process, please refer to Appendix I.

A conducting surface is essential to prevent charging effects which can affect the quality of the SEM images and X-ray elemental analysis. This is because SEs have low energies and are very easily deflected by the presence of any charge present on the surface of the sample. For insulating surfaces, this can be done by coating with a conducting material. It is also important that coating is done carefully as the presence of dirt on the surface of the specimen can lead to a defective coating which can still cause charging effects. Coating of the polished section surface of the nodule samples was performed by applying a thin layer (c. 10 nm) of carbon, which is transparent for the electron beam, onto the surface of the sample by thermal evaporation of carbon from a high purity

carbon rod mounted between high-current electrodes under vacuum conditions. Prior to coating, the surface was air-sprayed to remove any possible presence of dirt to avoid defects.

For two nodule samples, electron microscopy analysis was combined with layer-by-layer wet chemical trace element analysis. Individual nodule samples were cut in half from top to bottom using a diamond saw, one half was prepared for SEM imaging while the other half was used for sampling of individual layers. Polished sections of the nodules were first imaged to identify the Fe-rich hydrogenetic and the Mn-rich diagenetic layers using the SEM. Based on the large area chemical maps obtained (method described in section 3.2.1.4), the individual layers on the other nodule halves were sampled using a micro-drill. The drilled sample layers (20 – 50 mg) were then ground using agate and mortar and digested using the sodium peroxide sintering method (method used is same as described in section 2.2.3.1 in chapter 2 for bulk nodule geochemistry).

3.2.1.2 Instrumentation

Detailed analysis for morphological, textural and mineralogical composition was carried out using Scanning Electron Microscopy (SEM) performed on a JEOL 7001 Field Emission Gun (FEG) SEM instrument at the University of Plymouth Electron Microscopy Centre. Polished sections were scanned using a focussed electron beam produced by a Schottky field emission gun at accelerating voltage of 15 – 20 kV, a probe current of 10 nA and a working distance of 10 mm. The microstructures of polished nodule sections were imaged using both a secondary detector and a backscatter electron detector. Major

element concentrations were determined using Energy Dispersive X-ray Spectroscopy (EDS; Oxford Instruments, Abington, UK) combined with Aztec Energy software.

3.2.1.3 Large area mapping

Large area mapping is a useful type of SEM-EDS technique that can be used to acquire information about the chemical composition of samples and the distribution of different elements in the sample. This analysis was carried out on all nodule samples studied using the SEM including those used for individual layer chemistry. This method uses an electron beam which scans a defined area (a whole nodule sample area or an area of interest in this case) and uses the Aztec software to acquire EDS spectra by mapping the intensity of the characteristic X-rays point after point to create an EDS map. This method is time consuming as samples are scanned 'frame by frame' and the images stitched together to create a high resolution image of the 'large area' mapped. Despite that, it is quite easy to set up and the process is fully automated so for most of the analyses, the mapping was carried out overnight (or over 2 -3 nights depending on number of samples and size of area to be mapped) and the images and spectra were processed the next day (or when the run was complete). Typical set-up conditions for large area mapping are shown in Table 3.1 for a sample with 100 – 400 frames (50 – 100x magnification).

Table 3.1. Typical set-up conditions for a large area mapping analysis.

	Detector mode	
	BSE	EDS
Number of scans for each frame	1	3
Image resolution (pixels)	1024 x 1024	512 x 512
Dwell time on each frame (μ s)	35	35

3.2.1.4 SEM-EDS mapping analysis using energy peak deconvolution

The standard mode for chemical mapping analysis using SEM-EDS is the one using an energy window which is ideal when there are no overlapping peaks. This approach is the one commonly used for mapping analyses using SEM-EDS, and is also the one used for most of the mapping analyses in this work. However, peak overlaps do exist due to the similarity of the emission lines of elements and thus, can give rise to a 'false signal'. In this work, this problem was resolved by peak deconvolution where the actual energy window of the emission line of the element of interest was selected and mapped. This was done using Aztec software and uses 'trumap' to generate the maps which require long counting times depending on the size of the area mapped and the image resolution. This technique was applied to the measurement of Co in the nodules as Co has similar emission lines to Fe which is highly concentrated in the nodules.

3.2.2 Chemical analysis of individual nodule layers

Analytical measurements of REY concentrations in individual growth layers were determined by ICP-MS, the instrumentation conditions are as described in section 2.2.3.1 in chapter 2. The concentrations of Al, Si, K, Ca, Mg, Ti, Mn, Fe, Co, Ni, Cu, Zn, Ba

and Pb were carried out using inductively coupled optical emission spectroscopy (ICP-OES). The accuracy and precision of the measurements were evaluated using the GeoPT23 FeMn-1 Certified Reference Material (CRM), (Bundesanstalt für Geowissenschaften und Rohstoffe, Hannover). For both measurements, the accuracy and repeatability were better than 10% and 6% respectively.

3.3 Results

3.3.1 Nodule morphology, texture, internal growth structures and composition of individual layers using SEM

The morphology of the studied nodules from the CCFZ is typical of mixed-type nodules. Most of the nodules have a smooth surface texture on the top and a coarse bottom texture. The smooth top is where the nodule was recently in contact with bottom seawater while the coarse bottom is the part of the nodule where it was in contact with the underlying sediments of the sea floor. The top and the bottom are separated by a rim which probably marks the seawater-sediment interface boundary (see images in Figure 2.7 and Figure 2.8, chapter 2).

The internal structure of nodules is made up of three distinct structural features: nucleus, concentric layers and unconformities (or hiatuses), some examples of these are shown in Figure 3.6. The nucleus is typically located at the centre or towards the centre of the nodule. In most nodules, the nucleus is not visible with the naked eye and it is best observed with an electron microscope. The common nucleus material in the studied nodules is indurated detrital sediments, mainly Al-silicate phases. Concentric bands of layers form around the nucleus and extend towards the outer rim. The nature

of the concentric layers varies in nodules. Small (1 – 2 cm diameter) well rounded nodules tend to show well-formed concentric patterns in a regular fashion. In contrast, larger nodules tend to display concentric layers from regular to irregular and complex patterns, with the irregular shaped nodules showing the most irregular patterns. Between concentric layers are hiatuses or discontinuities, they can be also found cutting off a whole sequence of concentric layers Figure 3.6e. Discontinuities are interpreted as periods of dissolution and non-deposition and they are common in all nodules. They are mostly composed of thin layers of sediment particles, quartz and clay minerals ranging in thickness from 10 – 200 μm .

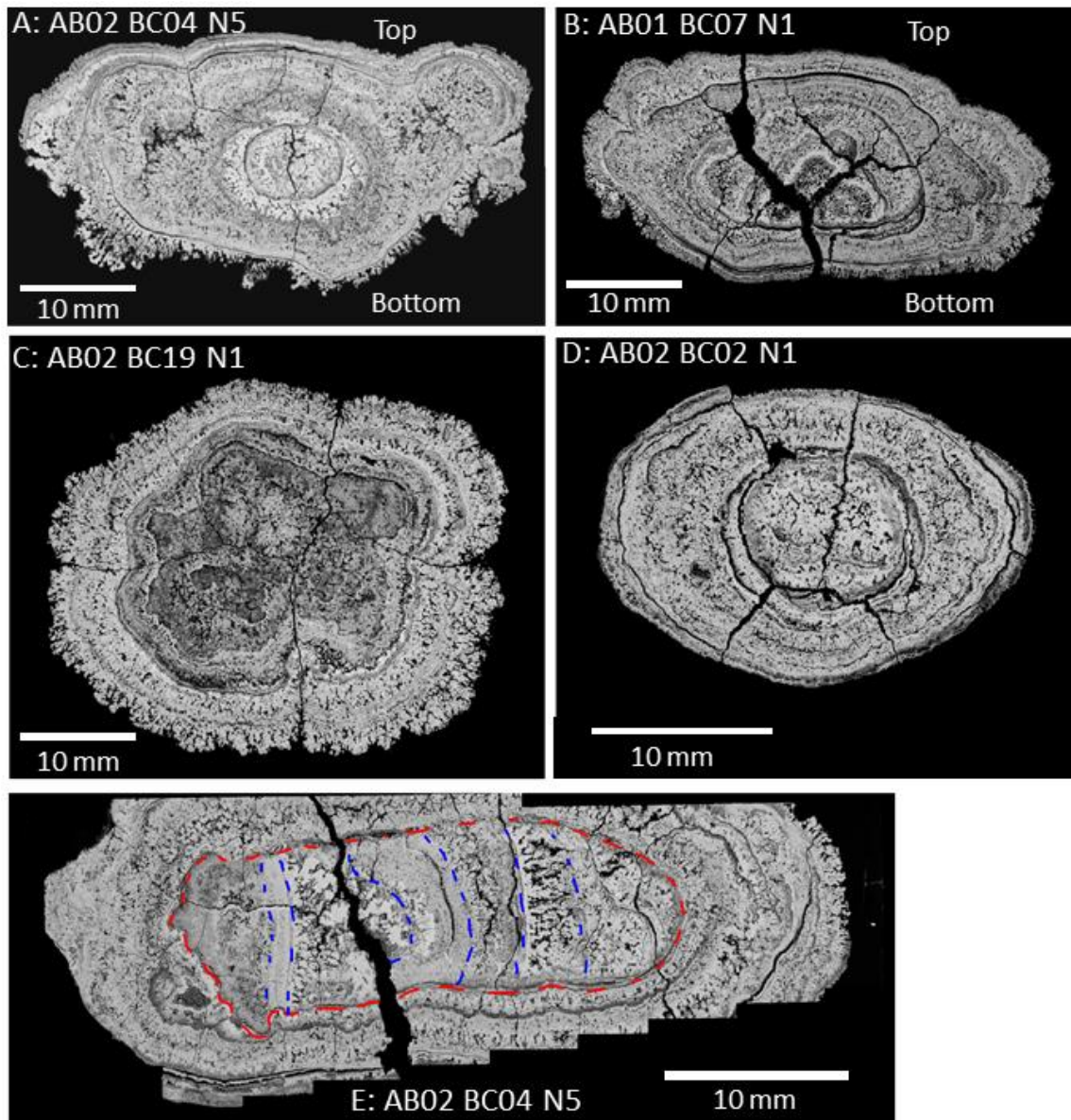


Figure 3.6. SEM backscattered images of five nodules from four box cores (see sample IDs inset) showing concentric layering. Nodules have similar but also varying morphologies, most nodules sit on the sediment surface with part of them buried in the sediment while the top part is exposed as can be seen in A and B where the tops are smoother than the bottoms. Some nodules (C) have a coarse, irregular surface all the way around and were likely completely buried so that the growth of the outer layer was controlled by rapid diagenetic precipitation. In contrast, all the nodules from one of the sampling area (box core AB02 BC02) were mostly smooth throughout with less porosity and were generally small in size (D) and their formation is interpreted as controlled by slow hydrogenetic precipitation while completely exposed (not buried on the seafloor). Hiatuses or growth discontinuities are common in nodules as can be seen in E where the older layers (marked by blue lines) are truncated by more recent layers, with the main hiatus marked in red.

The concentric layers in nodules are made up of several individual micro-growth layers which were imaged using the SEM (e.g. Figure 3.7). These layers can be grouped into three layer types, each with two to three micro-growth structures. These are: hydrogenetic, diagenetic and mixed type layers, Wegorzewski and Kuhn (2014) refer to these layer types as: *Layer type 1 with low Mn/Fe ratios; Layer type 2 with high Mn/Fe ratios; and mixed layer type 3* respectively. The hydrogenetic layers are mostly characterised by columnar to laminated growth structures (Glasby, 1977). The columnar structures are intricate curved laminae of Mn and Fe oxides that appear as layers of column-like structures stacking on top of each other. The laminated layers are similar to columnar structures but with well-formed superimposed colloform layering on a much larger scale (100 – 500 µm). They are denser and much thicker than columnar structures. Both layer types normally have small sized vein-like alternating bright (Mn-rich) and dark (Fe-rich) layers. Another very dense Fe-rich amorphous layer which is roughly conformable with fine laminated layers is the compact zone. These hydrogenetic layers have high reflectivity, appear bright and have low Mn/Fe ratios (<3) based on EDS point analysis and are characterized by FeMn-rich phases. They are found in most parts of the nodule alternating with diagenetic layers, from the outer to the inner parts. They are found in all nodules but in varying proportions. Small, dense and well-rounded nodules with low porosity are dominated by these growth structures.

Diagenetic layers are composed of two types of growth structures. The first type are the dendritic growth structures with high porosity, they have high reflectivity and appear bright with high Mn/Fe ratios (>3). These growth structures are the dominant diagenetic-type layers and are found in all parts of nodules. The second type of diagenetic growth structures are less commonly occurring, dense massive growth

structures. They have high Mn/Fe ratios (>3), high reflectivity, and appear bright and occur as thin laminated strips within hydrogenetic layers or between columnar growth structures and dendritic structures. These layers are characterized by Mn-rich phases. Diagenetic layers are accompanied with an enrichment of trace metals such as Ni and Cu.

A third type of layer is a mixture of hydrogenetic and diagenetic type structures, thus is termed as a 'mixed' layer. This layer is made up of a combination of dendritic to columnar structures with low reflectivity and small-sized veins (~10 – 100 µm thickness) with varying Mn/Fe ratios ranging from <3 to 25, based on spot analysis.

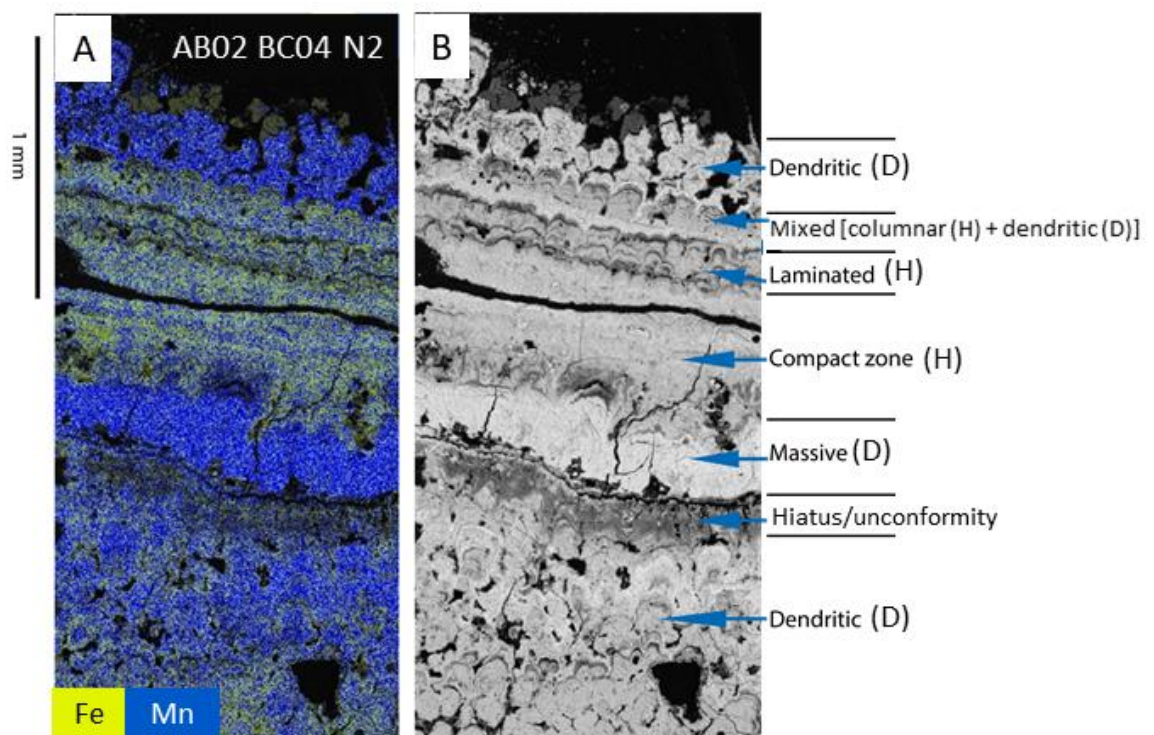


Figure 3.7. Typical nodule morphologies of mixed type nodules from the UK claim area (nodule sample: AB02 BC04 N2). The EDS image (A) shows the distribution of the Fe-rich hydrogenetic and Mn-rich diagenetic layers, BSE image (B) shows the morphologies associated with the individual layers with 'H' denoting a predominantly hydrogenetic layer and 'D' a diagenetic layer.

Descriptions and results of some individual nodule samples are presented in the following section:

Box core: AB01 BC07 (Nodule AB01 BC07 N1)

The nodule prior to cutting is shown in Figure 3.8. The nodule has a discoidal to ellipsoidal morphology. The top where it was in contact with seawater has a smooth texture (Figure 3.8a) while the underside where it was in contact with the sediments is rough (Figure 3.8b).

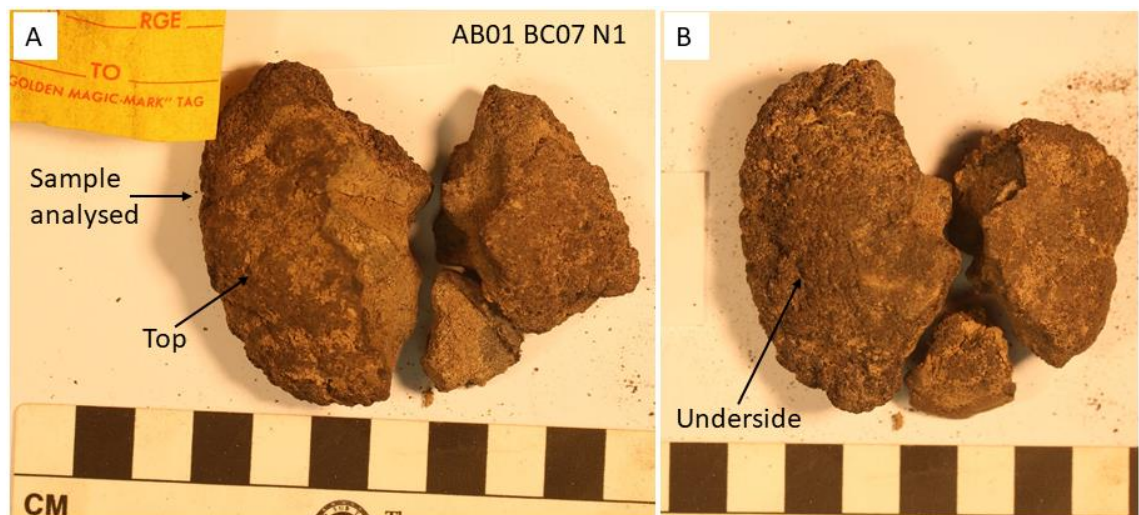


Figure 3.8. Nodule sample: AB01 BC07 N1 prior to cutting for SEM analysis with a smooth top (A) and a much coarser underside (B). The sample was fragmented, and the half (marked as 'sample analysed') was the one prepared by cutting from top to bottom for SEM imaging analyses.

The internal features of this nodule obtained using SEM are shown in Figure 3.9, and shows that the nodule is characterised by a non-distinct nucleus and is dominated by concentric banded Fe-rich hydrogenetic and Mn-rich diagenetic layers. The distribution of the two main (Fe-rich and Mn-rich) phases can be observed alternating with each

other. The distribution of some important minor metals can be also observed, Ni and Cu are distributed in the Mn-rich layers while Al-silicate phases are concentrated around the edges of pore spaces and in the unconformity (hiatus) layer. Tiny bright spots of Ca-phosphate rich phases can be observed. The distribution of Al does not follow either of the two main layer types, it is mostly observed filling up pore spaces. Pore spaces can be observed in both layer types but are more extensive in the diagenetic layers.

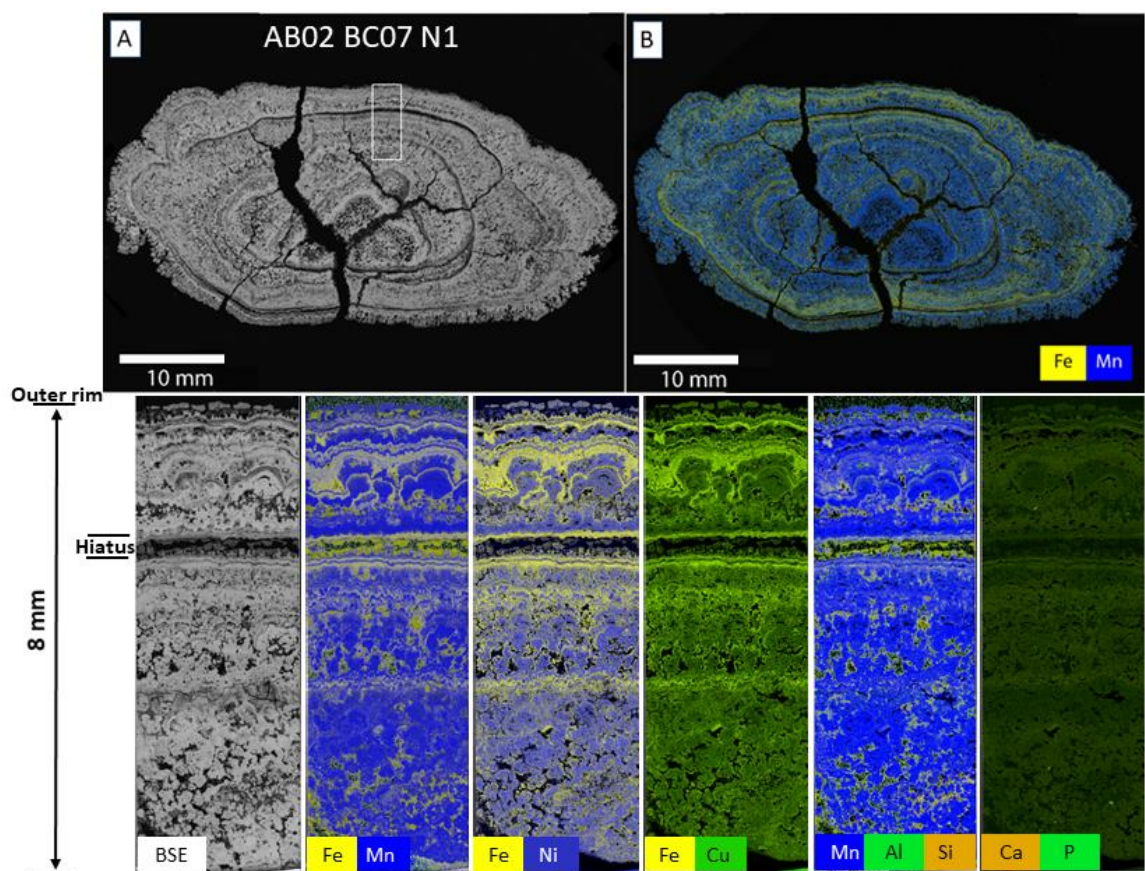


Figure 3.9. SEM-derived textures and distribution of some elements in nodule sample AB01 BC07 N1. The BSE map of the nodule is shown in A while the EDS map is shown in B. More detailed maps of an 8 mm x 3.5 mm nodule area (marked as inset in A) are shown with the distributions of Fe, Mn, Ni, Cu, Al, Si, Ca and P. Note the EDS maps are image mosaics of two or three 'colour-coded' elemental maps overlain on each other and are not individual maps.

Box core: AB02 BC02 (Nodule AB02 BC02 N8b)

The nodule prior to cutting is shown in Figure 3.10. This nodule sample has a discoidal morphology. The sample is small in size (~3cm), has a discoidal to spherical morphology and has a smooth texture all round including the rim. This sample's morphology, texture and size is representative of all the samples from this box core and is physically distinct from the nodules from the other four box cores.

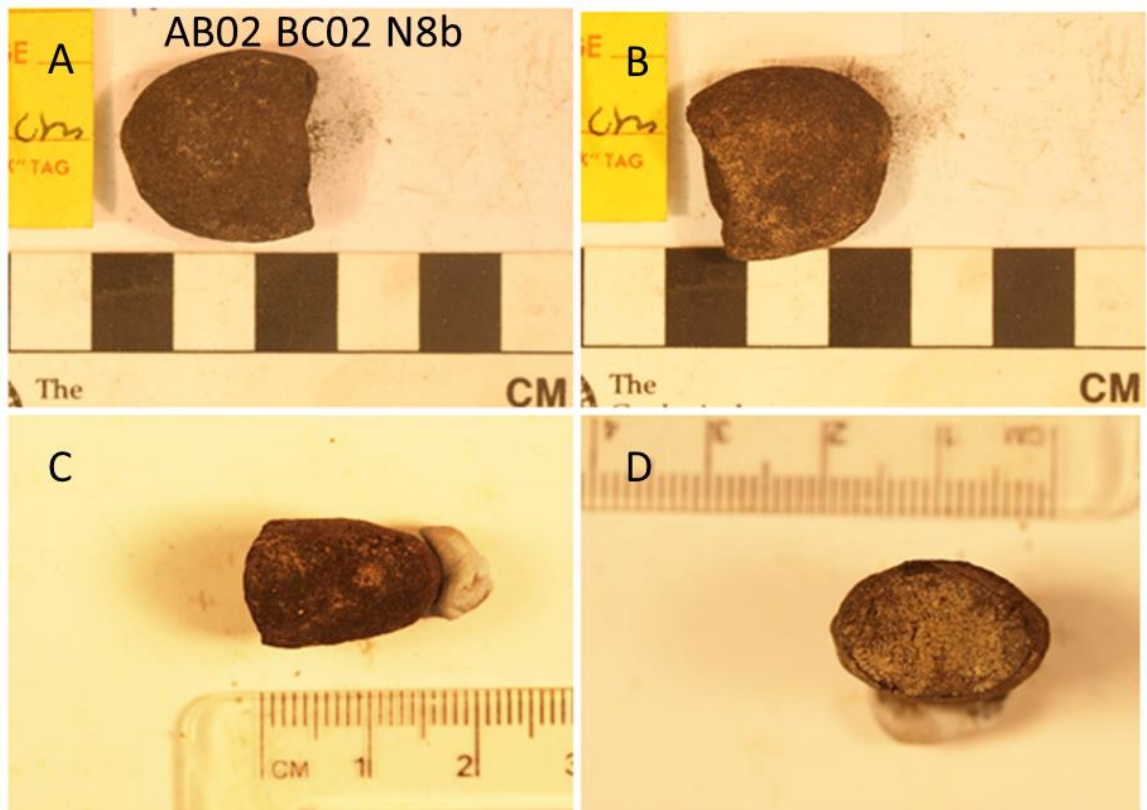


Figure 3.10. Nodule sample: AB02 BC02 N8b prior to cutting for SEM analysis. Nodule is discoidal to ellipsoidal and well-rounded throughout, is smooth on both sides (images A and B) including rim (C). A broken-off bit of the sample exposes the coarse interior texture (D).

The internal features of this nodule are shown in Figure 3.11. This nodule is characterised by a non-distinct nucleus. Concentric-banded Fe-rich hydrogenetic and

Mn-rich diagenetic layers dominate the nodule. The distribution of the two main (Fe-rich and Mn-rich) phases can be observed alternating with each other (Figure 3.11b). The distribution of Ca and P can be also observed in Figure 3.11c, they appear as discrete phases in the Mn-rich layers as well as on the edges of pore spaces. The distribution of Al and Si do not follow either of the two main layer types, they are mostly observed filling up pore spaces (Figure 3.11d).

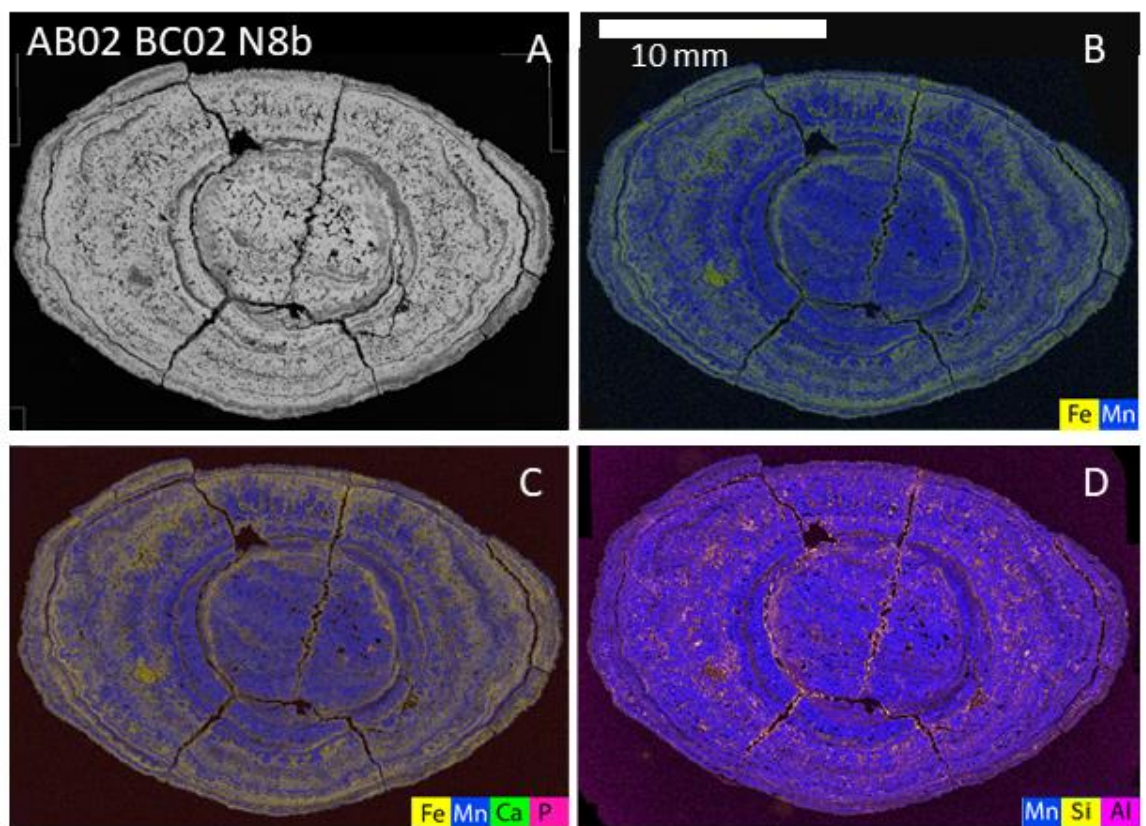


Figure 3.11. SEM micro-textures and distribution of some elements in nodule sample AB02 BC02 N8b. The BSE image in A shows the internal structures of the nodule sample with concentric layers. The distribution of Fe and Mn are shown in B while the Ca-phosphate and Al-silicate distribution are shown in C and D. Both phases are distributed as discrete phases where they occupy pore spaces, the Ca-phosphate phases can be seen in the diagenetic regions and are less abundant than the Al-silicates.

Box Core AB02 BC06: Nodule AB02 BC06 N4

The nodule prior to cutting is shown in Figure 3.12. The nodule has an irregular morphology, the top where it was contact with seawater has a smooth texture while the underside where it was in contact with the sediments is rough.

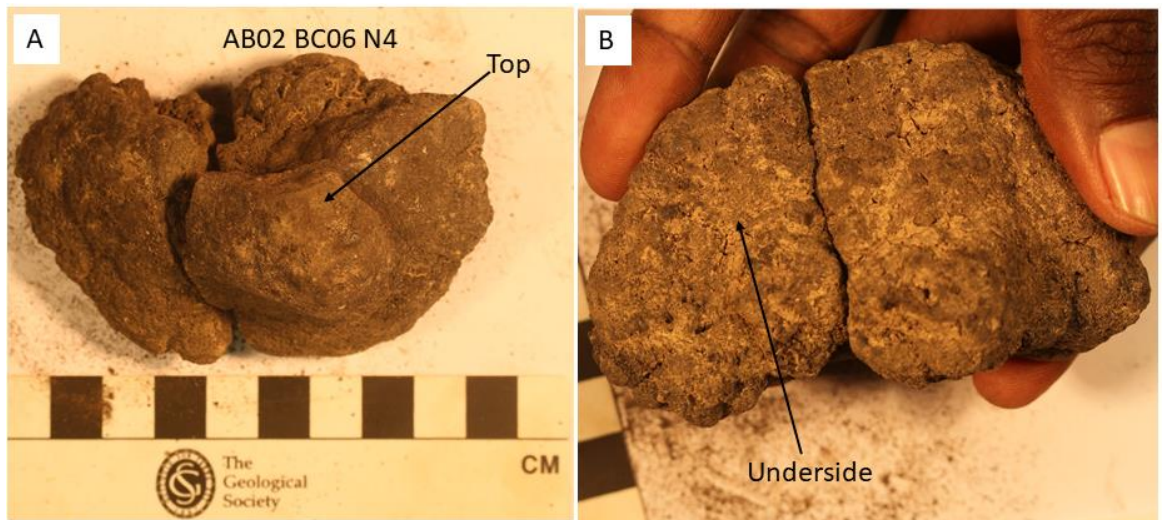


Figure 3.12. Nodule sample: AB02 BC06 N6 prior to cutting for SEM analysis with a smooth top (a) and a much coarser underside (b). The sample was fragmented in two halves, and the half (marked with arrow and top shown) in image A is the one prepared for SEM where it was cut top to bottom.

The internal features of this nodule are shown in Figure 3.13. Unlike most nodules, the nucleus is located towards the rim and is mostly made up of indurated sediment particles. Alternating banded Fe-rich hydrogenetic and Mn-rich diagenetic layers dominate the nodule. The EDS maps of a nodule area (10 mm x 2.5 mm) are shown in the figure and shows that Ni and Cu are concentrated in the diagenetic regions while Al-silicate rich phases dominate the pore spaces and hiatuses. Discrete Ca-phosphate rich phases can be observed which are mostly found on the edges of pore spaces and in the

hiatus. The maps also show that the Mn-rich diagenetic regions are more porous than the Fe-rich hydrogenetic regions.

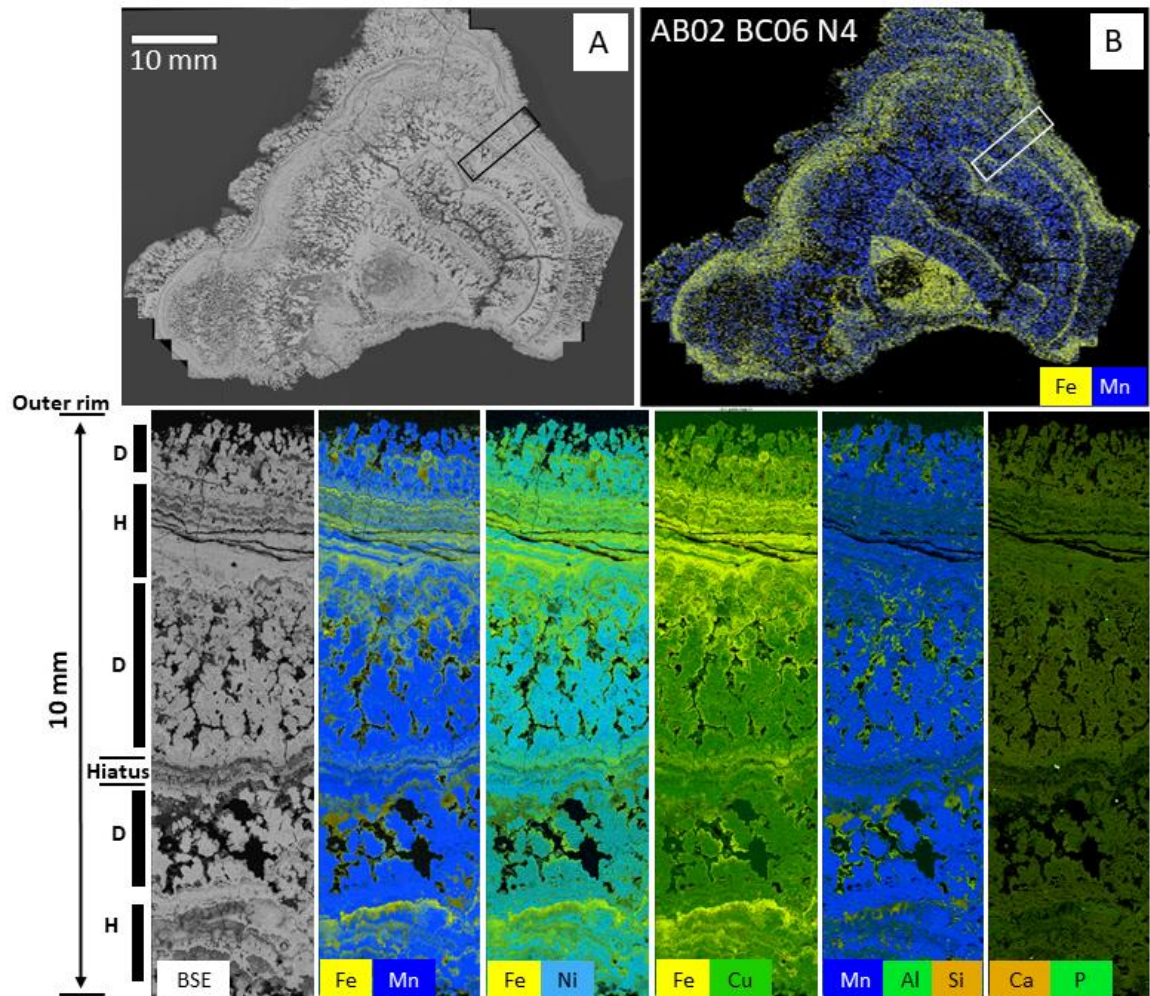


Figure 3.13. SEM microtextures and distribution of some elements in nodule sample AB02 BC06 N4 with the large area BSE (A) and EDS (B) maps shown. Detailed maps of the nodule (marked as inset in A and B) are shown with the distribution of Fe, Mn, Ni, Cu, Al, Si, Ca and P. An obvious hiatus is marked in the detailed map as well as the predominantly diagenetic (D) and hydrogenetic (H) regions.

Detailed SEM EDS mapping was performed on a nodule sample (AB02 BC06 N3) which represents a typical mixed type nodule from the eastern CCFZ. The BSE and EDS large area maps of the nodule are shown in Figure 3.14 with the distribution of the Fe-rich

hydrogenetic and Mn-rich diagenetic layers. Detailed maps of an area 220 μm x 160 μm (shown inset in Figure 3.14b as 'area mapped') are presented in Figure 3.15. These images were determined by deconvolution of the energy peaks in the EDS spectrum instead of a simple energy window approach used in Figure 3.9, Figure 3.11 and Figure 3.13. The distribution of cobalt can only be mapped accurately with this deconvolution approach, which requires long counting times (typically in the order of 1s per pixel). The photomicrograph in Figure 3.15a shows a region with both the Fe-rich (hydrogenetic) and Mn-rich (diagenetic) layers. Figure 3.15b shows Ni distribution in the diagenetic layers, which is the same distribution pattern to that of Cu (Figure 3.15c). The distribution of Co (Figure 3.15d) is similar to that of Pb (Figure 3.15e) which shows their enrichment in the hydrogenetic layers. The distribution patterns of the Al-silicate phases are shown in Figure 3.15f where they mostly occur as infillings in pore spaces. The distribution of the Ca-phosphate phase is shown by the distribution of Ca and P where they are seen to be distributed in the hydrogenetic regions as well as discrete phases in the diagenetic regions Figure 3.15g. Finally, the distribution of the discrete phases of Ba-sulphate are shown in Figure 3.15h.

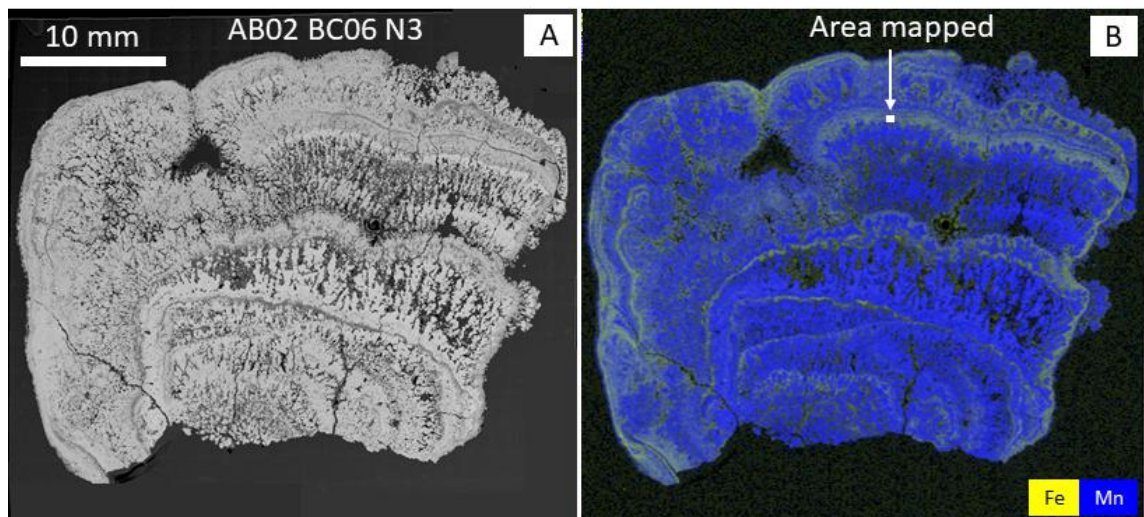


Figure 3.14. Large area BSE (A) and EDS (B) maps of nodule sample AB02 BC06 N3. The EDS map shows the distribution of the Fe-rich hydrogenetic and Mn-rich diagenetic layers as well as the 'area mapped' shown inset where detailed mapping by deconvolution of energy peaks was performed, the images of which are presented in the next figure (Figure 3.15).

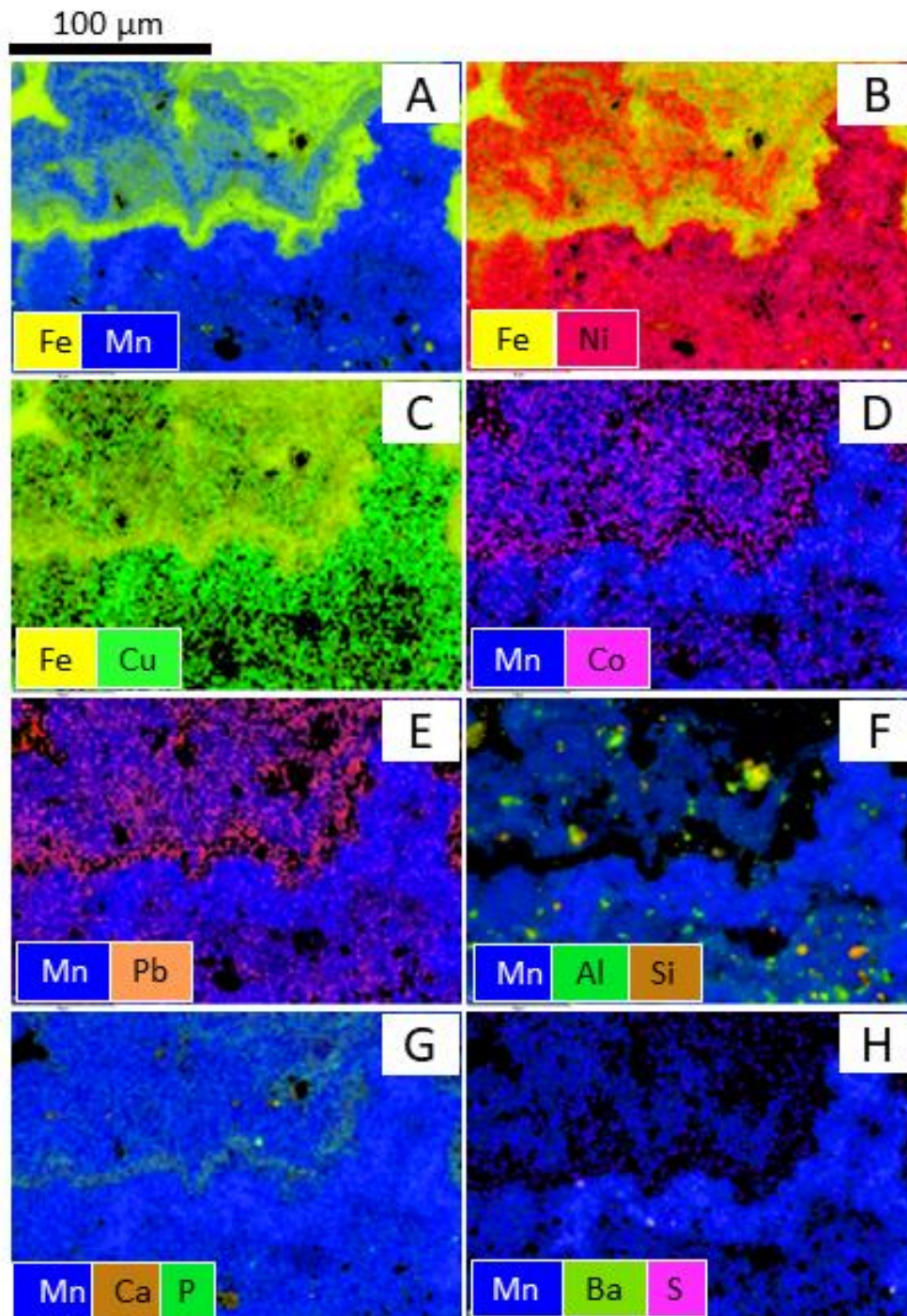


Figure 3.15. SEM photomicrographs of the hydrogenetic and diagenetic regions of a typical mixed type nodule from the UK claim area (AB02 BC06 N3) with the distribution patterns of different metals. The Fe-rich layer in A shows the hydrogenetic regions while the diagenetic regions are represented by the Mn-rich regions. Images B – E show the distribution of Ni, Cu, Co and Pb while F – H show the distribution patterns of the Al-silicate, Ca-phosphate and Ba-sulphate phases.

3.3.1.1 The problem of mapping the distribution of REY and Co using EDS-SEM

Whilst the distribution of some minor metals can be studied using the SEM, this was not possible for low abundance trace metals such as the REYs. To ascertain this, SEM-EDS analysis was carried out on Ce, the most abundant REY. The results showed that the energy intensities measured at the expected Ce x-ray emission line energies i.e., $L\alpha_1$ (4.84 keV), $L\beta_1$ (5.26 keV) and $L\beta_2$ (5.61 keV), were all below background intensities (Figure 3.16). This, therefore, limits the investigation of REY distribution in the nodules using SEM.

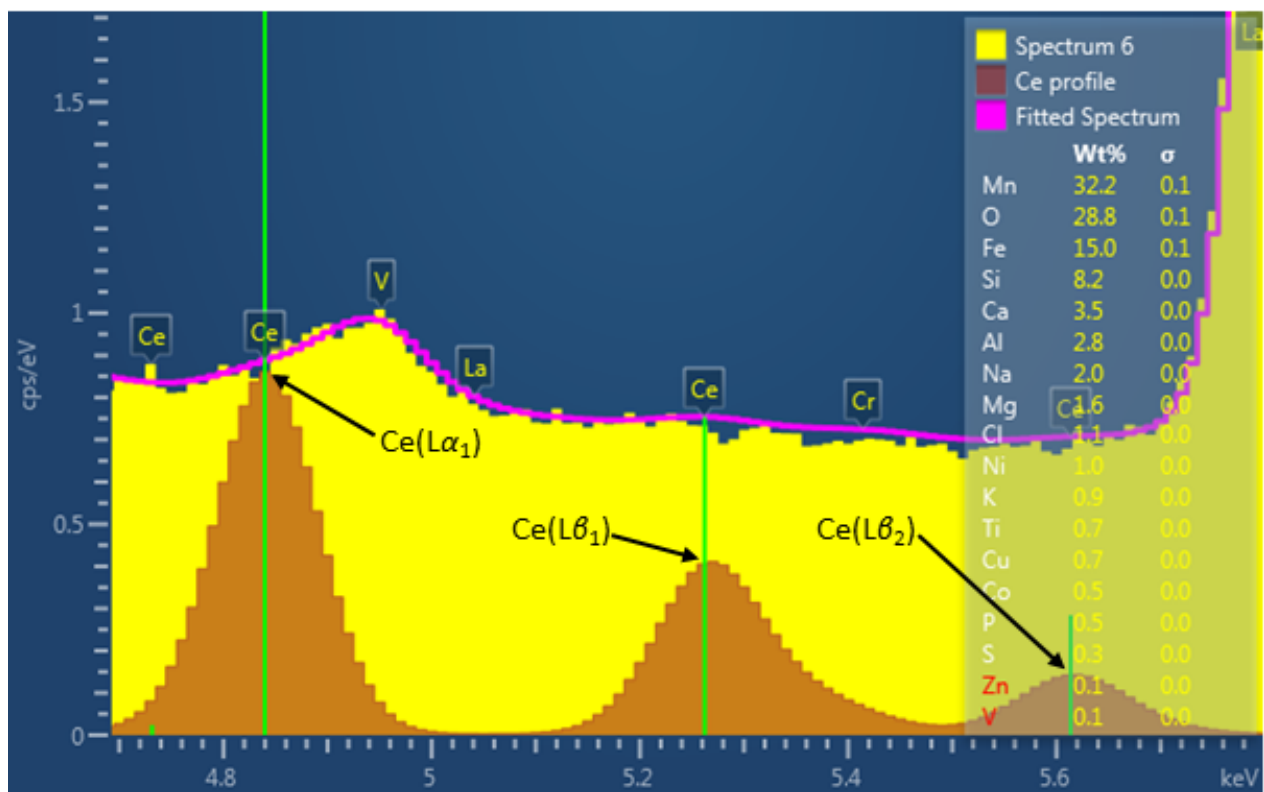


Figure 3.16. A fitted EDS spectrum obtained by SEM analysis on a nodule hydrogenetic layer showing only the energy window of where Ce peaks occur. The yellow banded region is the overall spectrum of the sample area analysed with the fitted spectrum shown in pink. The brown region is the Ce profile with three peaks (labelled inset), the peaks (marked by green lines) show the emission lines of Ce which all appear below background levels.

Whilst the imaging of Ce was not possible using SEM, imaging of a Fe-rich hydrogenetic layer carried out as part of a pilot study using μ SXRF at the Diamond Light Source Synchrotron (<https://www.diamond.ac.uk/Home.html>) by operator Julia Parker provided some insights on the distribution of Ce. Figure 3.17a shows the μ XRF image of a mixed type nodule with its diagenetic (blue = Mn) and hydrogenetic regions (Yellow = Fe). The spectrum in Figure 3.17b shows three of the x-ray energy peaks that very likely resemble those of Ce: $L\alpha_1$ (4.84 keV), $L\beta_1$ (5.26 keV) and $L\beta_2$ (5.61 keV) peaks were observed when a small region in a hydrogenetic region of a nodule from the study area was mapped. When Ce (red) is added, the hydrogenetic region slightly changes colour to mustard yellow from yellow which indicates that Ce is distributed in this region. The red spots seen on the diagenetic region are discrete phases of barite. Due to the overlaps of Ba and Ce emission lines, it is quite difficult to differentiate them by a simple energy window mapping approach. However, the SEM analyses have shown that Ba-sulphate rich phases normally occur as discrete phases in diagenetic regions which led to the conclusion that the spots are those of barite and not Ce. The spectrum in Figure 3.17c confirms the occurrence of Ce in the hydrogenetic region.

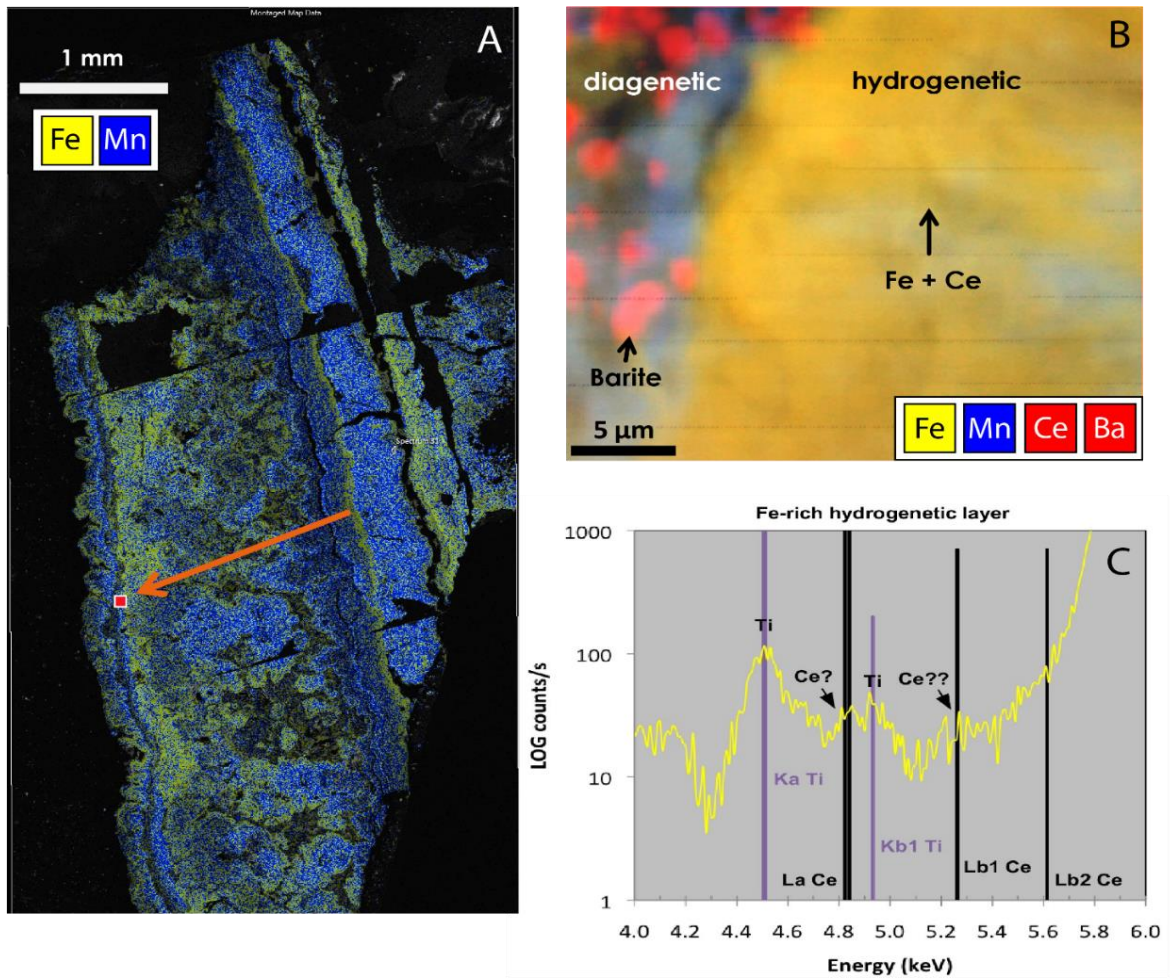


Figure 3.17. Imaging analysis of a nodule sample (AB02 BC04 N2) with the SEM EDS map of Fe and Mn is shown in A. A 25x25 μm section (inset in A) of the sample showing both layer types is shown in B with maps of Fe, Mn, Ce and Ba using μXRF. The spectrum of the hydrogenetic layer is shown in C with the emission lines of Ce indicating that it is distributed in the hydrogenetic layer.

Imaging of cobalt using SEM also suffers from similar problem as Ce. However, for Co, its $K\alpha_1$ and $K\alpha_2$ lines appear above the background in an energy spectrum obtained by a long (~30 minute) acquisition time. The $K\alpha$ emissions overlap strongly with the $K\beta_1$ of Fe (Figure 3.18), and peak deconvolution was required to separate the Co and Fe emission peaks. This technique was applied in a single experiment, as it required a very long acquisition time, and the Co distribution observed in the image obtained during this experiment is considered accurate. Note that in some published studies that report the

distribution of Co in polymetallic nodules based on EDS-SEM images, a simple energy window approach is carried out e.g. Wegorzewski *et al.* (2018). Maps thus produced for Co are unreliable, and in effect simply show the Fe distribution.

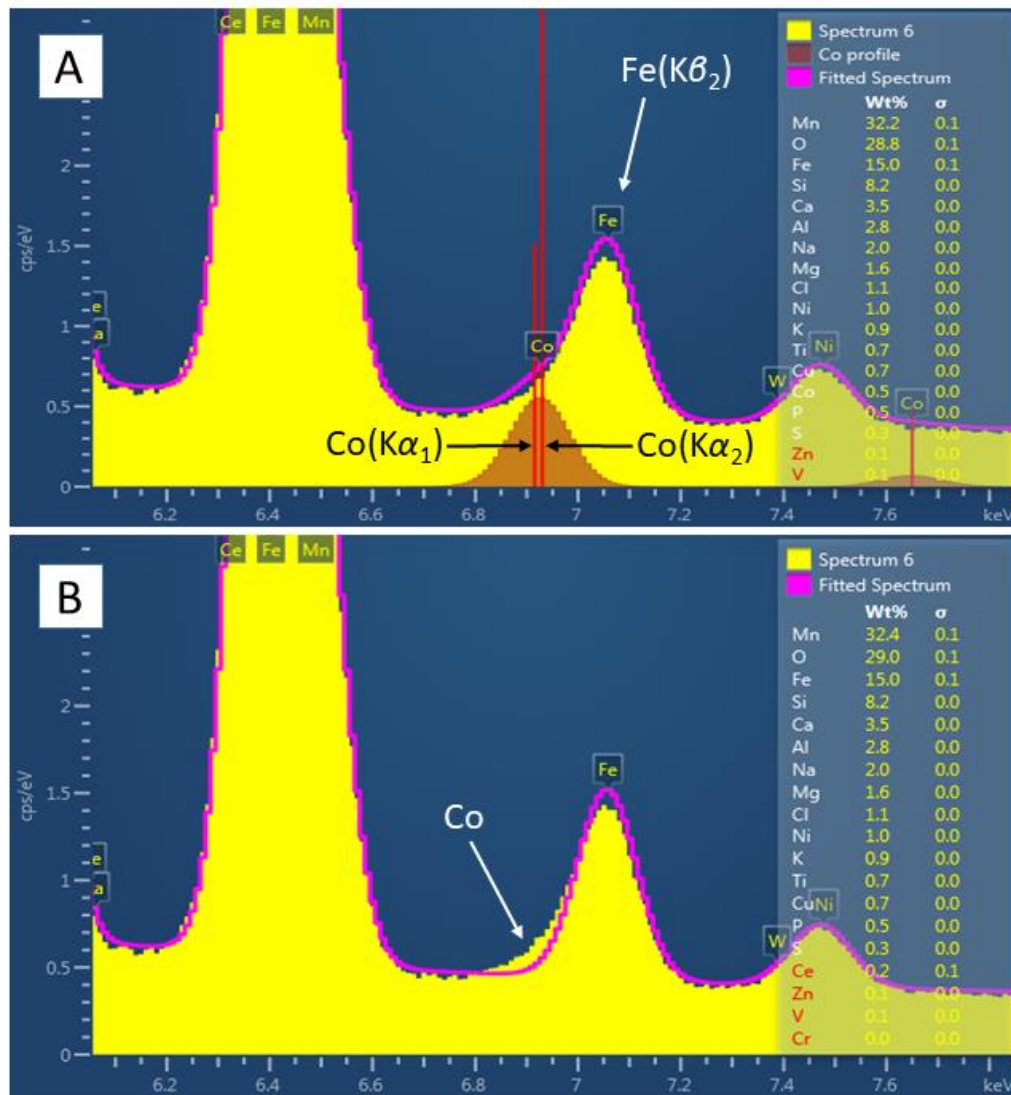


Figure 3.18. Fitted EDS spectrum obtained by SEM-EDS analysis on a nodule hydrogenetic layer showing only the energy window of where Co peaks occur. The yellow banded region is the overall spectrum of the sample area analysed with the fitted spectrum shown in pink. The brown region is the Co profile and shows the location of the $K\alpha_1$ and $K\alpha_2$ emission lines of Co (in red). The two Co emission lines confirm that the ‘deconvolution of peaks’ method used here is capable of separating out the Co and Fe peaks, which can be seen in image B where it appears above the background fitted spectrum as tail on the $Fe K\beta_1$.

3.3.2 Biogenic structures in polymetallic nodules

Another type of structure that was imaged by SEM on a broken-off piece from nodule sample AB02 BC06 N1 (Figure 3.19) was a systematic cluster arrangements with hollow features of diameters ranging in size of 1 -2 μm where some of the holes are filled by spherical fibrous structures (Figure 3.20). Some areas of these structures were exposed while in most regions they are overgrown by phylломanganates. These structures are further discussed in the discussion section.

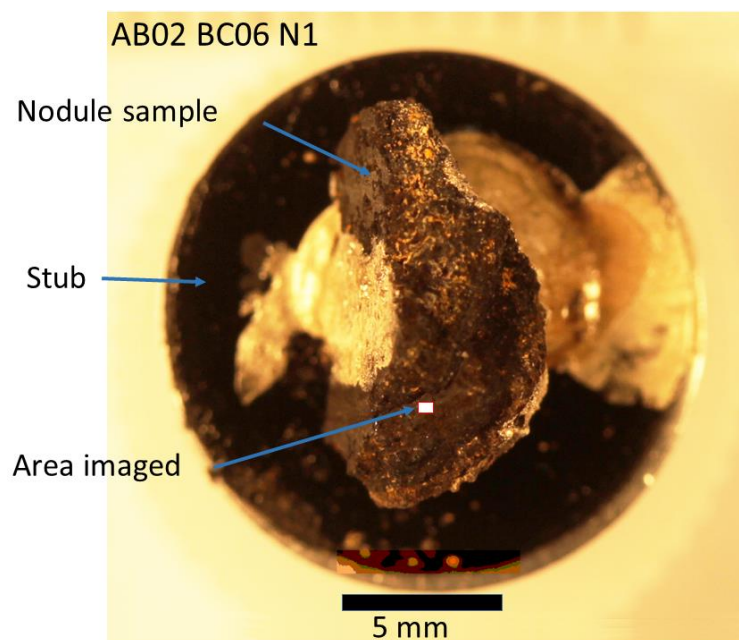


Figure 3.19. A broken-off chip of nodule sample AB02 BC06 N1 mounted on a stub. Sample area imaged by detailed SEM analysis is marked as 'area imaged'.

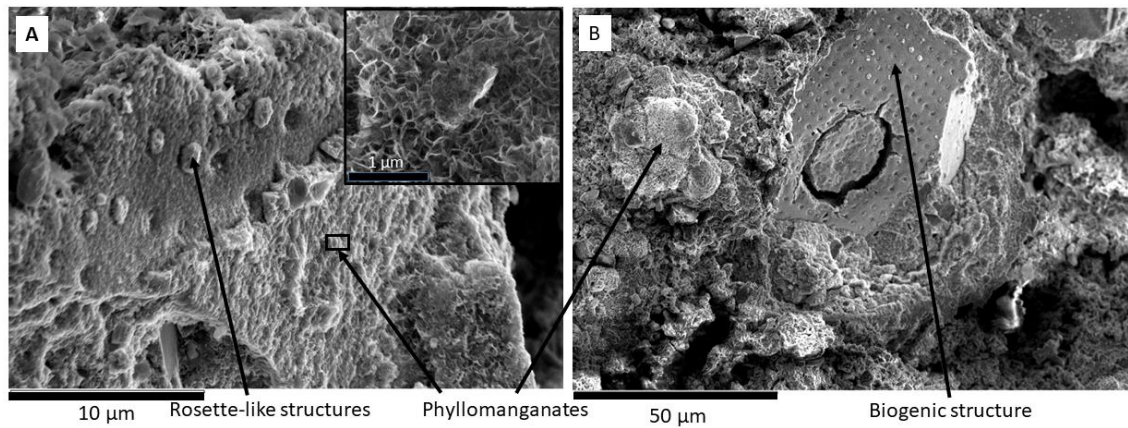


Figure 3.20. SEM secondary electron images (nodule sample AB02 BC06 N1) of platform-like support structures with holes filled by fibrous rosette-like structures. The structures are overgrown by platy phyllomanganates (shown inset in A). The images were acquired by scanning the surface of an area (marked in Figure 3.19) on a broken-off chip of the nodule sample.

3.3.3 Chemical composition of REY in individual layers using ICP-MS/-OES

Since determining the distribution of REY in layered polymetallic nodules is not possible using SEM, wet chemistry digestion followed by ICP-MS/-OES measurement of individual sample layers was carried out. This was carried out on two nodule samples. REY concentration measurements on individual layers were carried out on nodule sample AB02 BC06 N4 (Figure 3.21). The measurement of REY and other trace metals was carried out on nodule sample AB01 BC07 N1 (Figure 3.22).

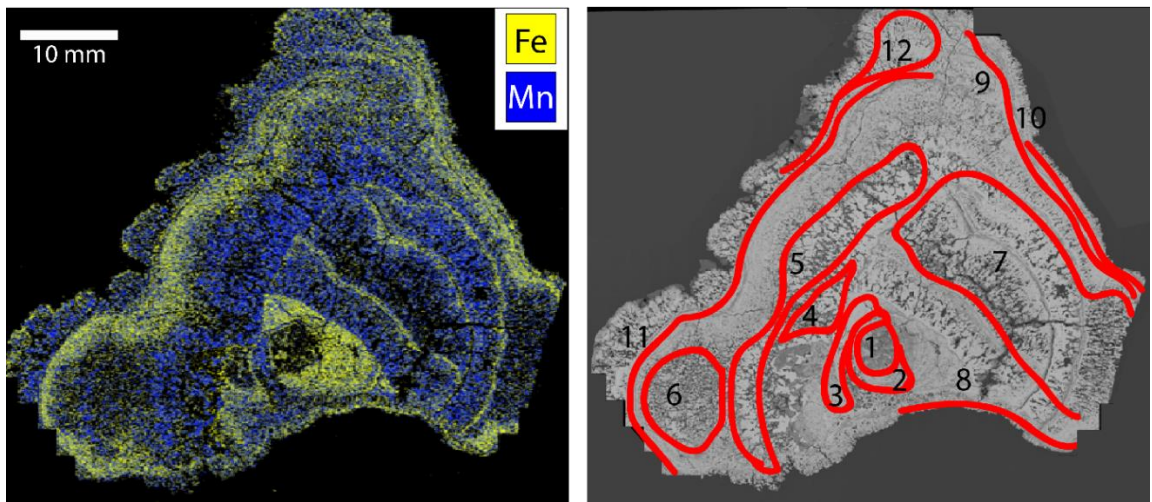


Figure 3.21. Nodule sample AB02 BC06 N4 with the Fe-rich hydrogenetic and the Mn-rich diagenetic layers (left) and the twelve regions marked in red sampled using a micro-drill (right). The numbers indicate layer number, some regions are thin strips and the number is placed beside the marked strip. Some regions cover an area and the number is place in the area sampled. Layer 12 covers both an area plus a thin strip.

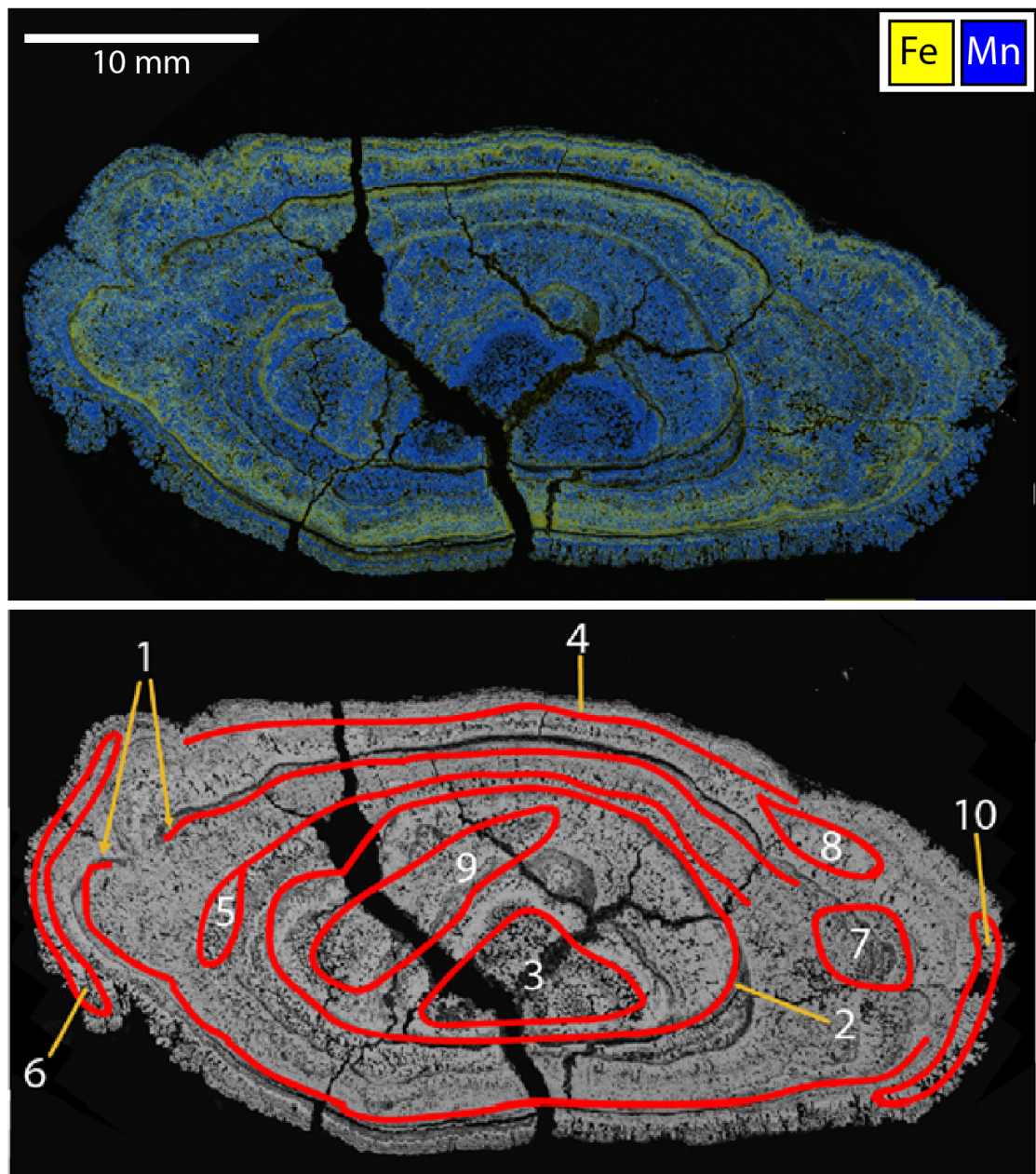


Figure 3.22. Nodule sample AB01 BC07 N1 with the Fe-rich hydrogenetic and the Mn-rich diagenetic layers (left) and the twelve regions marked in red sampled using a micro-drill (right). The numbers indicate layer number, some regions are thin strips and the number is placed beside the marked strip. Some regions cover an area and the layer number is placed in the area sampled. Layer 5 covers both an area plus a thin strip.

The individual layer chemical compositions of nodule sample AB02 BC06 N4 are shown in Table 3.2 while layer compositions of nodule AB01 BC07 N1 are shown in Table 3.3. Colour coding is used in both tables to differentiate between hydrogenetic (yellow),

diagenetic (blue) and mixed type (orange) layers. The results show that the chemical composition of individual layers vary between the layers. Nodule sample AB02 BC06 N4 was analysed for REYs only in twelve individual layers, the bulk total REY composition of this nodule is 728 ppm. The results show that the REYs are more enriched in the hydrogenetic layers, (542 - 1216 ppm) while the concentrations in the diagenetic layers range from 335 – 624 ppm. The concentrations in the mixed type layers fall between those of the hydrogenetic and diagenetic layers (523 – 564 ppm). For nodule sample AB01 BC07 N1, apart from the REYs, other metals (Al, Si, K, Ca, Mg, Ti, Mn, Fe, Co, Ni, Cu, Zn, Ba, Pb) were also included in the measurements. The REY distribution pattern in this nodule is similar to the nodule sample AB02 BC06 N4, the total REY composition is highest in the hydrogenetic layers (971 – 1131 ppm), lowest in diagenetic layers (561 – 748 ppm) and intermediate (401 - 801 ppm) in the mixed type layers. The distribution of Co is similar to that of the REYs in nodule sample AB01 BC07 N1 where its enrichment is higher in the hydrogenetic (0.12 – 0.21 wt%) compared to the diagenetic (0.06 – 0.11 wt%) and mixed type (0.07 – 0.165 wt%) layers. Individual layer growth rates (GR) were calculated for nodule sample AB01 BC07 N1 (Table 3.3) based on the Co, Fe and Mn content using the Co chronometry of Manheim and Lane-Bostwick (1988):

$$GR = 0.68/(Co_n)^{1.67},$$

Where $Co_n = Co \times 50/Fe + Mn$ with Co, Mn and Fe concentrations in wt%.

This method does not account for hiatuses during nodule growth, therefore, the rates calculated are minimum ages (Manheim & Lane-Bostwick, 1988). The values show that hydrogenetic layers grow at slower rates compared to diagenetic layers. The values are in agreement with the literature for diagenetic layers (Von Stackelberg, 2000), and

hydrogenetic layers (Koschinsky & Hein, 2003). The average growth rate for this sample is 13.5 mm/Ma which is also consistent with literature values of 10 – 20 mm/Ma (Kuhn *et al.*, 2017).

Table 3.2. REY content in the individual layers of nodule sample AB02 BC06 N4. The columns are coloured to show the different layer types, yellow = hydrogenetic, blue = diagenetic, orange = mixed. The SEM image showing the different layers (1 – 12) sampled is shown in Figure 3.21. Note: LREE = Light REE, HREY = Heavy REY. The bulk nodule REYs composition for this nodule sample and the crustal abundance (Rudnick & Gao, 2003) of the REYs are also shown. Sample mass analysed depends on layer thickness and the amount of material that can be obtained from drilling the layer (typically 10 – 100 mg), approximate dilutions (500 – 4500x) were then carried out to determine final concentrations for each layer.

	1	2	3	4	5	6	7	8	9	10	11	12	Bulk nodule	Crustal abundance
LREE														
La (mg/L)	125	188	99.9	60.5	85.5	44.8	72.2	89.5	157	76.1	140	79.9	107	20.0
Ce	352	409	178	116	135	114	177	200	469	181	426	202	253	43.0
Pr	38.1	53.1	28.4	21.1	24.3	13.8	22.1	24.2	49.5	22.9	40.5	23.0	30.4	4.90
Nd	156	229	124	91.9	107	59.6	95.5	98.9	202.9	98.6	173	101	131	20.0
Sm	36.9	53.3	29.9	22.4	25.2	14.9	23.7	23.7	49.1	24.4	39.6	24.4	31.6	3.90
Eu	8.47	13.0	7.43	5.53	6.35	3.61	6.02	6.21	11.9	5.94	9.55	6.06	7.77	1.10
HREY														
Gd	33.43	49.0	27.0	19.8	23.2	13.3	21.3	21.5	43.6	21.8	35.9	22.1	28.4	3.70
Tb	5.71	7.98	4.29	3.30	3.79	2.22	3.54	3.48	7.21	3.71	5.80	3.56	4.69	0.60
Dy	32.2	44.9	25.7	18.6	21.8	12.7	19.9	20.0	40.0	20.7	32.3	20.2	26.5	3.60
Y	84.2	111	66.7	53.3	66.9	38.6	55.7	57.1	93.2	59.1	88.5	55.2	72.2	19.0
Ho	5.77	7.96	4.55	3.35	4.01	2.28	3.53	3.60	6.92	3.71	5.75	3.59	4.77	0.77
Er	16.2	22.2	12.8	9.35	11.3	6.53	9.90	10.1	19.1	10.5	15.9	10.1	13.3	21.0
Tm	2.28	3.14	1.81	1.33	1.59	0.93	1.41	1.44	2.65	1.49	2.20	1.40	1.88	0.30
Yb	15.7	21.8	12.5	9.19	11.1	6.46	9.85	10.2	18.1	10.4	15.2	9.72	13.1	1.90
Lu	2.34	3.30	1.86	1.37	1.69	0.99	1.53	1.61	2.71	1.56	2.29	1.46	1.99	0.30
Total	915	1216	624	437	528	335	523	572	1173	542	1032	564	728	144
Total LREE	717	945	467	318	383	251	396	443	940	409	828	436	562	92.9
Total HREY	198	272	157	120	146	84.0	127	129	233	133	204	127	167	51.2
% LREE	78.4	77.7	74.8	72.7	72.5	74.9	75.8	77.5	80.1	75.5	80.3	77.4	77.1	64.5
% HREY	21.6	22.3	25.2	27.3	27.5	25.1	24.2	22.6	19.9	24.5	19.8	22.6	22.9	35.5

Table 3.3. REY content in the individual layers of nodule sample AB01 BC07 N1. The columns are coloured to show the different layer types, yellow = hydrogenetic, blue = diagenetic, orange = mixed. The SEM image showing the different layers (1 – 10) sampled is shown in Figure 3.22. Note: LREE = Light REE, HREE = Heavy REE, LOD = Limit of detection, n/a = measurement not carried out. The bulk nodule REYs composition for this nodule sample and the crustal abundance (Rudnick & Gao, 2003) of the REYs are also shown. Note: the crustal abundance values for Co, Ni, Cu and Zn are in ppm. . Sample mass analysed depends on layer thickness and the amount of material that can be obtained from drilling the layer (typically 10 – 100 mg), approximate dilutions (500 – 4500x) were then carried out to determine final concentrations for each layer. The growth rate (GR) of individual layers determined for this sample is based on the Co, Fe and Mn content using the Co chronometry of Manheim and Lane-Bostwick (1988); $GR = 0.68/(Co_n)^{1.67}$ where $Co_n = Co \times 50/Fe + Mn$ with Co, Mn and Fe concentrations in wt%, note SD = standard deviation.

	1	2	3	4	5	6	7	8	9	10	Bulk nodule	Crustal abundance
Mn (wt%)	21.2	25.6	19.2	24.9	23.2	21.7	26.8	20.7	25.7	21.5	31.4	0.078
Fe	8.35	5.63	3.91	7.70	5.12	3.61	5.90	5.22	3.73	4.34	5.37	5.22
Co	0.21	0.12	0.08	0.18	0.12	0.07	0.16	0.11	0.06	0.06	0.15	26.6 ppm
Ni	1.21	1.31	1.54	1.11	1.55	1.15	1.61	1.19	1.29	1.14	1.42	59.0 ppm
Cu	0.78	1.04	1.15	0.85	1.09	0.90	1.27	1.01	1.05	0.79	1.02	27.0 ppm
Zn	0.12	0.16	0.20	0.16	0.17	0.19	0.16	0.15	0.17	0.19	0.19	72.0 ppm
Ba	0.34	0.56	0.61	0.40	0.32	0.65	0.29	0.47	0.77	0.63	0.42	456 ppm
Pb (ppm)	580	227	181	421	270	152	345	237	156	154	291	11.0
Mn/Fe	2.53	4.54	4.91	3.23	4.53	6.01	4.55	3.97	6.88	4.95	5.85	0.015
LREE												
La (ppm)	164	126	122	137	107	58.4	108	100	99.5	79.1	110	20.0
Ce	466	247	209	396	313	99.0	291	259	185	155	262	43.0
Pr	43.8	34.9	35.5	36.3	31.6	24.3	29.3	28.0	30.2	28.7	32.3	4.90
Nd	183	149	151	154	135	99.1	127	120	131	127	138	20.0
Sm	42.7	35.7	36.5	36.6	31.2	17.6	30.3	28.7	28.9	24.0	31.2	3.90
Eu	10.3	8.64	8.96	8.75	7.60	4.21	7.46	7.11	7.14	5.81	7.59	1.10
HREE												
Gd	31.0	27.9	29.0	27.2	24.0	14.8	23.6	22.4	23.7	21.7	24.5	3.70
Tb	5.80	4.82	4.99	4.97	4.48	2.61	4.30	3.95	3.85	3.00	4.28	0.60
Dy	33.4	28.1	28.6	29.2	26.3	14.6	25.6	23.9	23.4	20.7	25.4	3.60
Y	109	89.3	86.3	103	86.9	50.1	89.5	81.9	74.7	74.3	84.4	19.0
Ho	5.81	4.98	5.08	5.15	4.61	2.23	4.64	4.21	3.92	2.72	4.33	0.77
Er	16.3	13.9	14.1	14.7	13.4	7.23	13.4	12.4	11.5	10.2	12.7	21.0
Tm	1.93	1.71	1.86	1.64	1.52	n/a	1.60	1.30	1.09	n/a	1.23	0.30
Yb	15.4	13.6	13.9	13.9	13.2	6.91	13.0	11.9	11.3	9.57	12.3	1.90

Lu	1.93	1.68	1.85	1.69	1.57	n/a	1.65	1.37	1.11	n/a	1.28	0.30
Total	1131	788	748	971	801	401	770	706	636	561	751	144
Total LREE	910	602	563	769	625	303	593	543	482	420	581	92.9
Total HREY	221	186	186	201	175	99.0	177	163	155	141	170	51.2
% LREE	80.5	76.4	75.2	79.2	78.1	75.3	77.0	76.9	75.7	74.8	77.3	64.5
% HREY	19.5	23.6	24.8	20.8	21.9	24.7	23.0	23.1	24.3	25.2	22.7	35.5
GR (mm/Ma)	3.79	10.6	14.0	6.07	9.73	16.6	6.99	9.08	31.9	26.5	Mean GR = 13.5 SD = 9.15	

3.4 Discussion

3.4.1 Internal growth structures

Nodules from the CCFZ are mixed-type nodules: they exhibit both diagenetic and hydrogenetic characteristics in alternating concentric layers, with diagenetic layers making up the largest part of the nodules (by volume). Imaging analysis using SEM was able to delineate the hydrogenetic and diagenetic layers in the nodules as well as the different types of internal features present in these layers (Figure 3.23). The Fe-rich hydrogenetic layers (columnar, laminated, and compacted) have low reflectivity and appear as medium to dark grey in colour in the BSE images. They occur as finely laminated thin and wavy strips to radially oriented columns of laminated amorphous material which are more consolidated and dense with low Mn/Fe ratios of <3 . In contrast, the Mn-rich diagenetic layers ($\text{Mn/Fe} > 3$) appear brighter in the back scattered images, with mostly dendritic textures characterized by bulbous, globular morphologies. These textures are the most common in the nodules, particularly in large nodules while they occur in much lesser extent in the small nodules from the AB02 BC02 box core. Regions in the nodule with high volumes of dendritic textures are also associated with high proportions of pore spaces. The dense, compacted and laminated textures that dominate the hydrogenetic layers suggests that these layers formed from hydrogenetic processes where the slow precipitation from the bottom seawater resulted in the finely laminated dense and compacted structures.

This is in contrast to the dendritic structures in diagenetic layers where their morphology shows that they formed from the more rapid diagenetic precipitation from porewaters

in the underlying sediments. The rapid precipitation results in the bulbous and globular structures in dendritic layers with abundant pore spaces as precipitates do not have enough time to form laminated layers like in hydrogenetic layers where laminar seawater flows resulted in the stacking of the laminated and columnar structures.

All the morphologies discussed above were found in all the nodules with nodules from the same box cores showing very similar proportions in terms of their hydrogenetic versus diagenetic textures while some variations exist between box cores. In particular, nodules from box core AB02 BC02 showed a marked contrast in their internal structures compared to nodules from the other four box cores. These nodules, which are generally small in size (1 – 3 cm) are well rounded with smooth outer textures, dense and more consolidated, they do not disintegrate easily (which is a common physical feature in nodules) which is probably because they contain less pore spaces. Whilst their internal structures also consists of dendritic structures and pore spaces, they are less abundant compared to nodules from the other four box cores. Instead, they contain higher proportions of hydrogenetic (laminated, columnar and compacted) textures and fewer pore spaces. The variations in the internal structures between AB02 BC02 nodules and those from the other box cores is therefore largely controlled by their growth mechanism. The relative proportions made based on individual layer thicknesses show that nodules from the UK1 contain ~20% hydrogenetic, ~50% diagenetic and ~30% pore spaces and hiatus layers. Using the total REY compositions of hydrogenetic vs diagenetic layers for nodules AB02 BC06 N4 and AB02 BC07 N1, total REYs in hydrogenetic layers of nodules from the UK1 make up about 12 – 13% of the bulk composition by mass

Table 3.4).

Table 3.4. Percentage total REY by mass in hydrogenetic layers of nodules AB02 BC06 N4 and AB01 BC07 N1. The values were obtained based on the total REY in hydrogenetic layers as a percentage of the relative hydrogenetic layer thickness of 20%.

Nodule	Mean total REY composition in hydrogenetic layers (ppm)	Mean total REY composition in diagenetic layers (ppm)	% Total REY by mass in hydrogenetic layers
AB02 BC06 N4	908	481	13.1
AB01 BC07 N1	963	663	11.8

The variations in the proportions (based on layer thickness and elemental composition using REY) between diagenetic and hydrogenetic regions indicate that conditions under which hydrogenetic layers formed were not occurring often and that they were short lived, or (more likely) that the growth rates during hydrogenetic processes were lower. By comparing the growth rates of hydrogenetic versus diagenetic nodules; growth rates of hydrogenetic crusts from the Cook Islands are much lower (1 – 5 mm/Ma; Hein *et al.* (2015)) compared to diagenetic nodules from the Peru Basin [20 – 250mm/Ma; Von Stackelberg (1997)]. Nodules from the CCFZ are mixed type nodules, therefore, the individual layers grow at different rates depending on the growth mechanism where the hydrogenetic layers grow at much slower rates compared to diagenetic layers. The growth mechanisms that control nodule morphology are 1) rapid diagenetic precipitation producing large nodules with abundant dendritic textures and pore spaces, and 2) slow hydrogenetic precipitation results in small dense well rounded nodules with lower proportions of dendritic structures and pore spaces and higher proportions of hydrogenetic textures.

Another type of internal structures common in the nodules studied are 'hiatuses' (also known as unconformities, discontinuities), they have low reflectivity in BSE images and

are mostly composed of detrital and amorphous material where the laminae shows a chaotic and discontinuous pattern. Two types of hiatuses were observed in the nodules studied, the first type is where the hiatus is parallel to the layers (or sandwiched between two layers), this is the most common type and can be observed in nearly all nodules (e.g. Figure 3.23). The second type is where the hiatus cuts off an existing layer at an angle forming a 'discontinuity' (e.g. Figure 3.6e). Both types of hiatuses show periods of non-deposition of Fe and Mn (oxyhydr)oxides, and during these periods, detrital materials from the underlying sediments can be deposited. The length of these periods of non-deposition is not known and probably vary from a few hundreds to thousands of years and even up to a few million years. The thickness of the hiatus does not give any indication about the length of the period of non-deposition as layers that were not in contact with sediments will not have detrital materials in them. The presence of the hiatuses indicate that the growth of nodules in the deep-sea is not continuous and this can be interpreted as periods where nodules stopped growing or when there was no (or limited) supply of materials for nodule growth. Nodule abundance in the CCFZ decreases with sediment depth (see Table 2.5, chapter 2), most of the nodules are found on the top 2 cm of the sediment column, nodule abundance then decreases down the sediment layer. This indicates that nodules stop growing or become (partly) dissolved once they are buried, this is a possible scenario where a hiatus cuts off an existing layer or layers (e.g. Figure 3.6e). Anoxic conditions increase with sediment depth, this means that as nodules become buried with increasing depths, Mn(IV) in MnO₂ (which is the main Mn oxide in nodules) is reduced to Mn(II) and nodule dissolution starts as Mn(II) is soluble compared to the Mn(IV). Some of the nodules may be partly dissolved at depth in the sediment but then return to the top surface of the

sediment due to either changing oceanographic conditions or reworking by benthic organisms. Once they reach the oxic top sediment zone, MnO_2 is deposited again and a 'crosscutting' hiatus is observed.

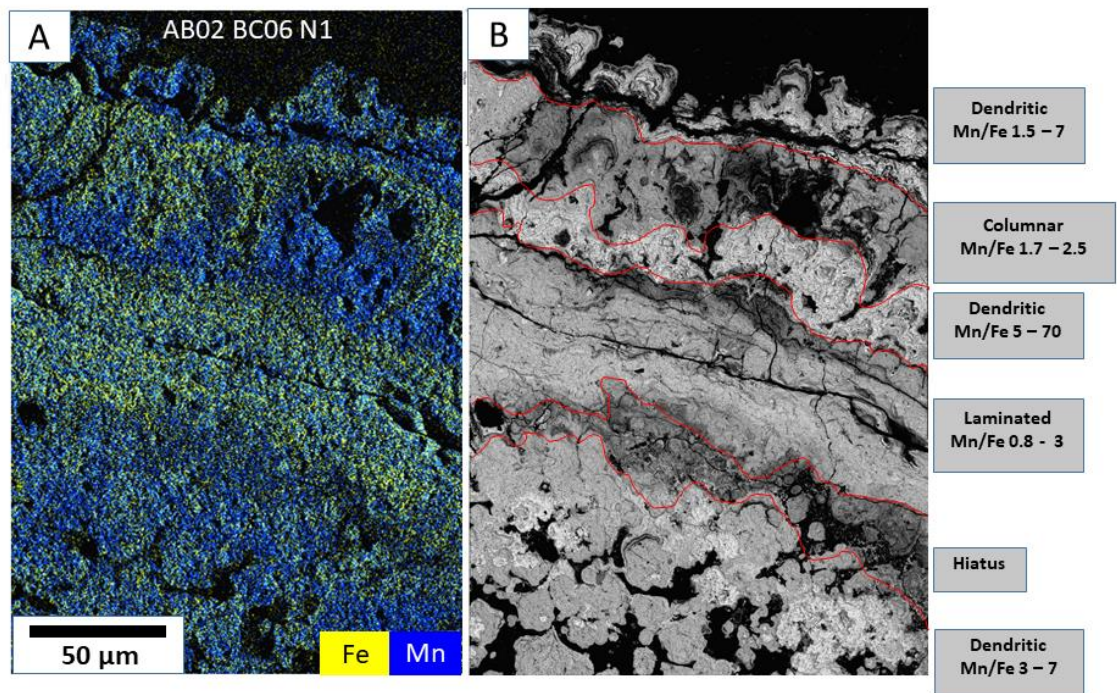


Figure 3.23. Typical nodule morphologies of mixed type nodules from the UK claim area (nodule sample: AB02 BC06 N1). The EDS image (A) shows the distribution of the Fe-rich hydrogenetic and Mn-rich diagenetic layers, BSE image (B) shows the morphologies associated with the individual layers as well as their Mn/Fe ratios. Diagenetic layers typically have Mn/Fe values of more than 3 while hydrogenetic layers have values less than 3.

Another type of structures found in the inner regions (~10 mm from rim) of one nodule sample (AB02 BC06 N1; Figure 3.24) are distinctly different from typical nodule internal structures. These structures have brick-like morphology and are systematically uniform in their arrangements with hollow structures ranging in diameter from <10 – 100 µm. The mats are flat and are oriented in all directions with visible edges in some cases, but in others the edges were not visible as they extend into Mn oxides. Some of the holes

are filled with rosette-like overgrowths of while some holes are empty. In some regions the Mn oxide overgrowths are so extensive that the biogenic structures are completely covered by Mn oxides. In other cases, a second layer of the biogenic structures can be seen over an existing layer, which indicates that they are growth structures where new layers grow over older layers. The structures observed in the nodule sample studied have a systematic arrangement of hollow structures, some of which are filled while others are empty. Compositional analysis using SEM-EDS (Figure 3.25) revealed that they are made up of Ca, Si, Mg and Na. This suggests that they are probably calcareous siliceous material of biogenic origin that become incorporated during nodule growth and undergo secondary mineralization. SEM EDS analysis shows that the fibrous material that fills up the holes are not Mn-oxides (Figure 3.26), their composition is siliceous which suggests they are probably amorphous silica that form by bio-mineralization (Weiner & Dove, 2003). Similarly, the material overgrown on the biogenic structures are not Mn-oxides (Figure 3.26, spectrum 41) and are likely organic in origin. The sample was coated with carbon prior to SEM imaging analysis, therefore, the carbon concentration in the EDS spectrum is not reliable. However, SEM imaging by Wang *et al.* (2009) on same type of structures revealed that the structures are comprised of carbon. The presence of these structures indicates that bio-minerals are present in the nodules, however, their role in nodule growth is unknown. It is likely that they were incorporated during nodule growth and eventually overgrown by phylломanganates. Whilst this is an interesting aspect in understanding the role of bio-minerals in nodules, the focus of this work is on rare metals and the physio-chemical processes associated with their incorporation in nodule mineral phases. Our work involving synthesis of phylломanganates (chapter 5) shows that nodules can grow by physio-chemical

processes. Therefore, the role of bio-mineralization in nodule growth is not the main mechanism for Mn deposition.

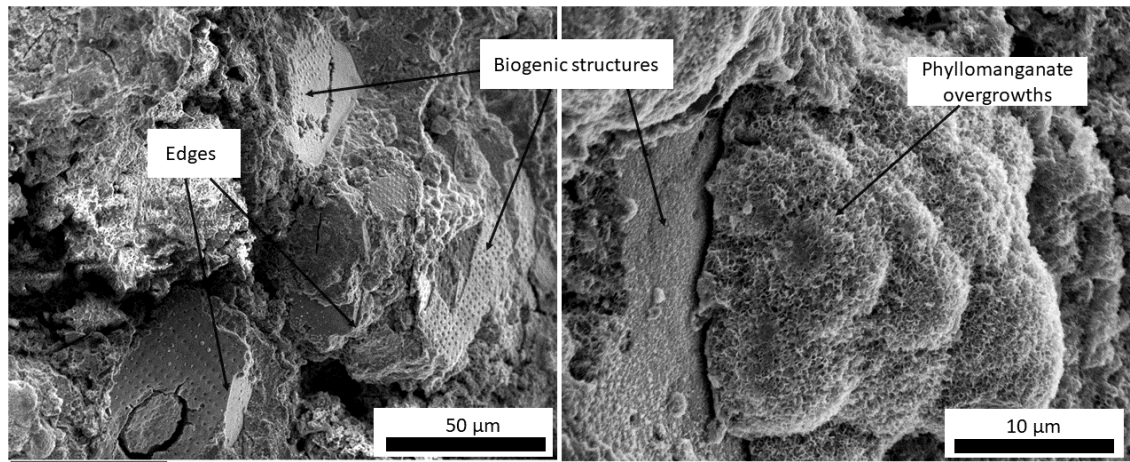


Figure 3.24. SEM secondary electron images (nodule sample AB02 BC06 N1) of biogenic structures with holes filled by fibrous rosette-like structures. The structures are overgrown by platy phyllophosphates.

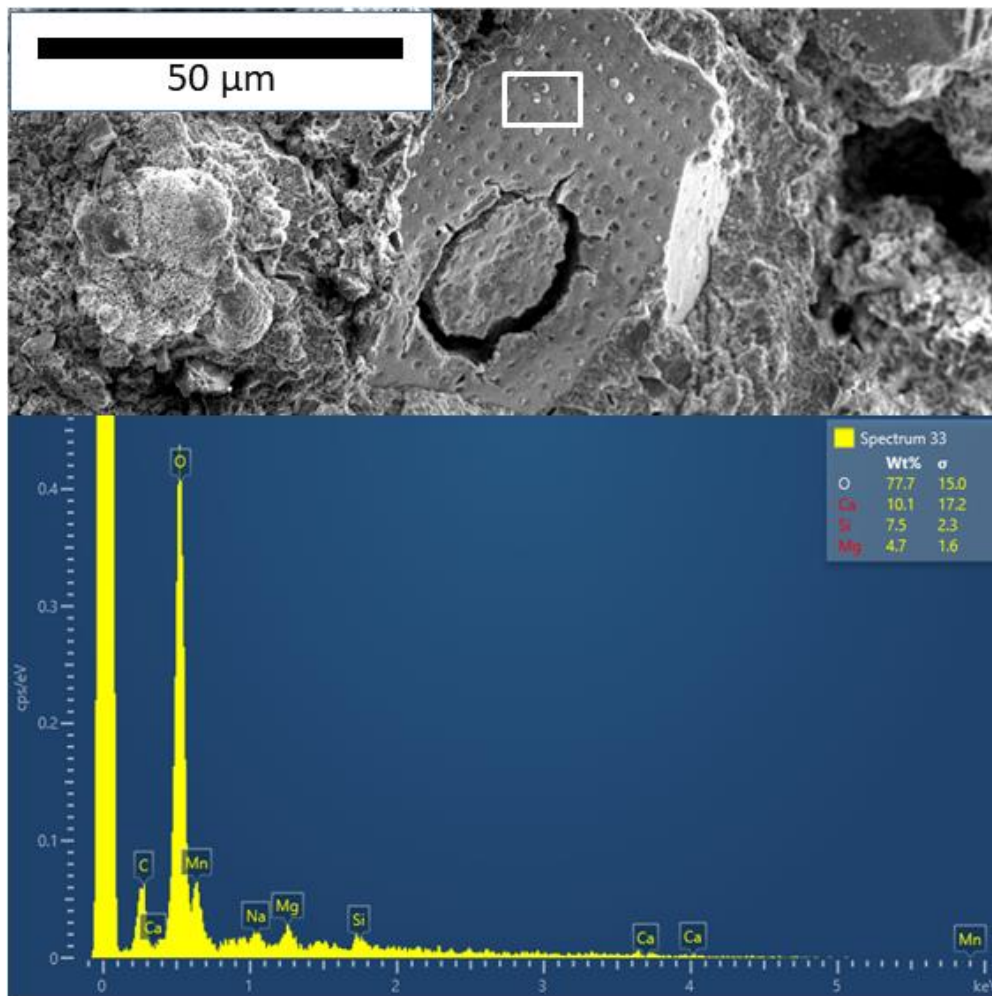


Figure 3.25. Composition of biogenic material based on SEM-EDS which shows that they are comprised of calcareous and siliceous material.

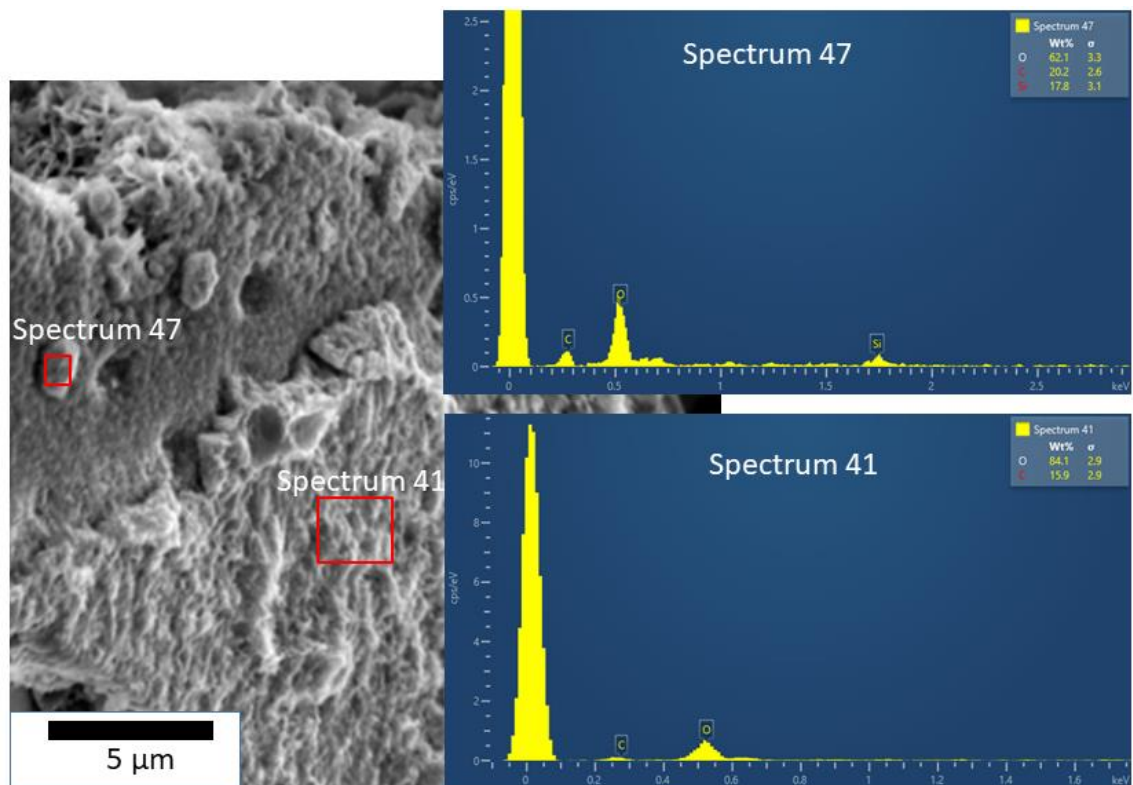


Figure 3.26. SEM-EDS composition of Mn oxides overgrowth (spectrum 44) and rosette-like spheres (spectrum 47) infilling holes on the surface of the biogenic structures. The compositions show that the rosette-like structures and the overgrowths are not Mn-oxides.

3.4.2 Composition and elemental distribution

Note that the discussion in this section attempts to provide some interpretations about the distributions of different metals between the diagenetic and hydrogenetic layers, however, further discussions with mineral phases are presented in the next chapter (chapter 4).

The chemical composition of polymetallic nodules is largely determined by the type of fluids that metals precipitate from and get adsorbed to Mn oxides and Fe oxyhydroxides. The trace metal compositional differences between nodules of different genetic types are becoming better understood. Hydrogenetic nodules such as those from the Cook Islands are enriched in trace metals such as Co, Ti, REY, Mo, Nb, V, W and Zr (Hein *et al.*,

2015). Diagenetic nodules such as those from the Peru Basin are enriched in Cu and Ni (Hein *et al.*, 2013). Nodules of mixed-type origin, such as those from the CCFZ scavenge metals from both pore water and seawater, and therefore their bulk composition falls between that of hydrogenetic and diagenetic nodules (Hein *et al.*, 2013; Wegorzewski & Kuhn, 2014). Since these nodules form from both mechanisms, their internal structure is made up of discrete diagenetic and hydrogenetic layers, each with a composition characteristic of the mechanism of formation. Geochemical analyses on two nodules using wet chemistry and SEM imaging on individual layers of several nodules show that their chemical compositions and distributions vary. The REYs are enriched by two to three times in hydrogenetic layers (~1200 ppm) compared to diagenetic layers (~600 ppm). Other metals that showed similar distribution to REYs are Co and Pb while Ni and Cu are more enriched in the diagenetic layers. The variations in the distribution of different metals between the two layer types can be due to mineralogical control and physiochemical processes (growth rate) associated with individual layers. The growth rate and metal enrichment relationship in mixed-type nodules is tabulated in Table 3.5.

Table 3.5. Growth rate and metal enrichment relationship between hydrogenetic and diagenetic layers in mixed-type nodules. The growth rates presented are for nodule sample AB01 BC07 N1 (Table 3.3).

Layer type	Growth rate (mm/Ma)	Enrichment
Diagenetic	9.08 – 31.9	Ni, Cu
Hydrogenetic	3.79 – 10.6	Co, REY, Pb

The enrichment of Ni and Cu in the diagenetic layers indicate that this could be due to their association with phyllophanates which is the dominant mineral phase in the

diagenetic layers. Mineralogical analysis using XRD and chemical leaching (chapter 4) shows that this is due to their association with the 10Å phyllo-manganates. The dominant mineral phase in the hydrogenetic layers is Fe-vernadite which is essentially a phyllo-manganate that is intergrown with Fe-oxyhydroxide nanoparticles. The enrichment of REYs, Co and Pb in the hydrogenetic layers shows that this can be due to their association with these phyllo-manganates. Another explanation for their enrichment in hydrogenetic layers can be also due to physiochemical processes, where the slower growth rates of this layer type allows time for these metals to become passively enriched. Therefore, considering a slow steady supply of these metals from seawater, the slow-accreting hydrogenetic layer will accumulate more of Co, REYs and Pb than the faster growing diagenetic layers.

The results also showed that diagenetic layers are more enriched in HREYs than hydrogenetic layers while the hydrogenetic layers are more enriched in LREEs than diagenetic layers (see Table 3.2 and 3.3). This is likely because the LREE form less stable carbonate complexes in seawater (hydrogenetic source) than the HREY which results in the LREY being more easily scavenged by marine particulates such as the (oxyhydr)oxides compared to the HREY (Elderfield & Greaves, 1982). The REYs exist as carbonate complexes in seawater where the LREEs bind to a single carbonate molecule (or a monodentate ligand) to form a $[\text{LREECO}_3^+]$ complex while the HREYs bind to two carbonate molecules (therefore, a bidentate ligand) to form a $[\text{HREY}(\text{CO}_3)_2^-]$ complex. In seawater, the stability of the REY carbonate complexes increases with increasing atomic number (Cantrell & Byrne, 1987; Piper & Bau, 2013).

The differences in the percentage HREY between diagenetic and hydrogenetic layers is in agreement with bulk nodule data from other ocean basins whereby the percentage

HREY is higher in diagenetic nodules (e.g. Peru Basin nodules – 32%) compared to hydrogenetic nodules (e.g. Cook Islands nodules – 16%) while those of mixed-type nodules such as CCFZ nodules are in moderate ratios (24%) (Hein *et al.*, 2013) (see Table 2.8, chapter 2). These differences as well as those of hydrogenetic versus diagenetic layers are important points to consider in terms of their resource potentials. The HREY enrichment in the diagenetic layers also suggests that the phylломanganates (main Mn oxide host mineral phase in diagenetic layers) have much greater preference for HREY over LREE. This can be due to how REYs are accommodated in the phylломanganate structure (see chapter 5).

Barium is distributed as discrete phases of barite in the diagenetic regions of nodules and shows that it is incorporated directly from the underlying sediments. SEM maps of Ca and P using peak deconvolution shows that the Ca-phosphate phase is more enriched in the hydrogenetic regions (Figure 3.15g) although discrete Ca-phosphate phases are also present in the diagenetic regions (Figure 3.27). This could suggest that it is sourced from both hydrogenetic and diagenetic sources. Using SEM-EDS point analysis, the discrete Ca-phosphate phases in the diagenetic layers are probably biogenic apatite from fish debris. Many studies have reported the occurrence of biogenic apatite from fish debris in deep-sea sediments in the CCFZ (Menendez *et al.*, 2019; Paul *et al.*, 2019b; Takebe, 2005; Toyoda & Tokonami, 1990). These Ca-phosphate phases might be also the same phases that are found in the nodules which gets deposited from the underlying sediments onto the nodule surface during nodule growth. Their presence as discrete phases in the diagenetic regions and sometimes on the edges of pore spaces, as well as in sediment-rich regions of the nodule supports the inference that they are directly deposited from the underlying sediments. The imaged Ca-phosphate phases are also

likely to be material from the underlying sediment incorporated in nodules during growth. However, the Ca-phosphate phases located in hydrogenetic layers are associated with phylломanganates and precipitated in the same way from bottom seawater. The association of Ca with phylломanganates is further discussed in chapter 5 using mineral synthesis approaches.

The distribution of Al-silicates shows that they are mostly found infilling pore spaces in both layer types which shows that they are derived from the underlying siliceous ooze and pelagic clay that is common in the eastern CCFZ. The composition of the hiatus layers are also rich in Al and Si which again shows that they are derived from the underlying sediments during periods of discontinuity in growth.

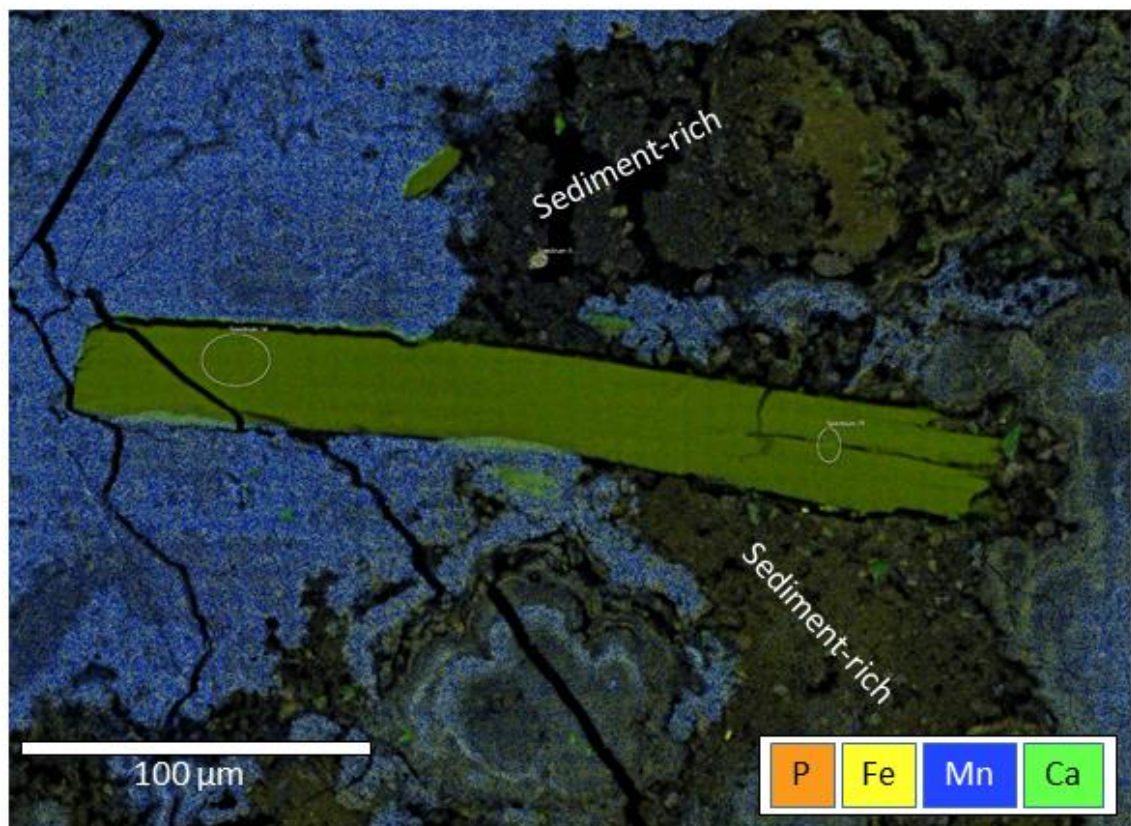


Figure 3.27. SEM-EDS map of an area of nodule AB02 BC19 N3 showing discrete CaP phases in the diagenetic and sediment-rich regions.

3.4.3 REY patterns

The Mn/Fe ratios of individual layers are clearly variable in nodule samples. Hydrogenetic layers have low ratios (2.53 – 4.54) while diagenetic layers show higher values (3.97 – 6.88). The high Fe concentrations in the hydrogenetic layers are due to the enrichment of FeOOH in these layers. The bottom seawater conditions are oxic, under these conditions both Fe and Mn exist in their oxidized forms as colloidal Fe³⁺OOH and Mn⁴⁺O₂. Both phases then precipitate onto the already forming nodule layers and form the Fe-rich hydrogenetic layers. The high Mn concentrations in the diagenetic layers are due to the precipitation of MnO₂ from suboxic sediment porewaters. The MnO₂ is the product of diagenetic mobilization in the porewater where organic matter that reaches the seafloor is oxidized by MnO₂ and thereby resulting in the reduction of Mn(IV) to Mn(II). The latter is soluble which therefore diffuses upward in the porewater and becomes oxidized once it reaches the oxic surface forming MnO₂ which precipitates onto the nodule surface to form the Mn-rich diagenetic layers. According to Kuhn *et al.* (2017) the normal Eh-pH conditions of the bottom seawater (Eh > 0.5, pH ~8) allows the oxidation of both Mn and Fe to Mn⁴⁺O₂ and Fe³⁺OOH which exist as insoluble colloidal particles. On the other hand, diagenetic mobilization is controlled by the oxidation of organic matter through a sequence of redox reactions starting with aerobic respiration by bacteria using dissolved oxygen from overlying water or interstitial waters. When oxygen is used up, the decomposition of organic matter can continue under anaerobic conditions (suboxic diagenesis) using secondary oxidants such as nitrate and MnO₂. Oxidation using MnO₂ results in the reduction of Mn(IV) to the soluble Mn(II) which then diffuses upward and becomes oxidized back to Mn(IV) as MnO₂ which then precipitates onto the nodule surface forming the diagenetic layers (Chesters & Jickells, 2012). The

primary source of Fe in the oceans is marine organisms with calcareous skeletons, when they die the skeletons dissolve and Fe is released to the water column and eventually supplied to nodule growth sites (ISA, 2010). The primary source of Mn for nodule growth could be from continental runoff, volcanic (seamounts) and atmospheric sources (ISA, 2010).

The REY patterns normalised to PAAS abundances are shown in Figure 3.28 and Figure 3.29 for the two nodule samples studied. The plots show variations in the Ce anomaly; hydrogenetic layers tend to show positive Ce anomalies while diagenetic layers tend to show a slightly negative Ce anomaly when normalised to PAAS abundances. The differences in the Ce anomalies can be due to the redox-sensitive nature of Ce where it can exist in the reduced (+3) and oxidized (+4) forms in marine systems, which makes it a useful proxy to characterise redox conditions (Bau & Koschinsky, 2009). The bottom seawater conditions where metal are precipitated hydrogenetically are oxic in character, while the porewater conditions are sub-oxic to oxic. The negative Ce anomalies in the diagenetic layers therefore, suggests that the sub-oxic (reducing) conditions in porewaters were not able to mobilize Ce by reducing it from the insoluble Ce(IV) which probably remain fixed in discrete phases making it less available in the porewater to supply to nodules. In contrast, positive Ce anomalies in the hydrogenetic layers are due to the oxidative scavenging of Ce(III) on ferromanganese oxides (also discussed in chapter 2; section 2.4.1).

The REY patterns of FeMn crusts, pore/sea waters and diagenetic/hydrogenetic nodules from other ocean basins are shown in Figure 3.30 for comparison purposes. The REY patterns of the hydrogenetic layers are similar to those of hydrogenetic nodules and hydrogenetic crusts that have well established formation processes. This shows that

these layers formed from the same processes as these deposit types, i.e. by surface sorption processes of trace metals onto colloids of hydrated Mn and Fe oxides in seawater (Hein *et al.*, 2013). In contrast, the REY pattern of the diagenetic layers are similar to those of the diagenetic nodules from the Peru Basin which confirms that they form from the same process of diagenetic remobilization in porewaters within the sediment column (Von Stackelberg, 1997). Since, diagenetic layers form from precipitation from porewaters, it is worth comparing their REY patterns as well. In the nodule diagenetic layers the Ce anomaly is negative, which is similar to porewaters from the CCFZ as reported by Paul *et al.* (2019a). However, the magnitude of the negative anomaly is much greater in the porewaters and increases with depth. The greater Ce anomaly in porewaters compared to the weak negative to nearly absent Ce anomaly in diagenetic nodule layers supports the explanation that porewaters supply nodules, in particular the diagenetic layers with metals precipitating from the pore fluids. The increasing Ce negative anomaly in sediments supports the inference that porewaters supply Ce to particulates including nodules.

In contrast to Ce, the nodule layers regardless of their dominant genetic origin show a strong negative Y anomaly which is also observed in bulk nodules (Figure 2.11, chapter 2; section 2.4.1) as well as FeMn deposits from other ocean deposits (Bau *et al.*, 1996; Hein *et al.*, 2015). This Y anomaly behaviour in nodules is markedly different from those of seawater and porewaters from the Central Pacific Ocean. Both North Pacific seawater and CCFZ porewater showed similar REY patterns, with strong negative Ce anomalies which is said to be due to the oxidative removal of the soluble Ce(III) from seawater by ferromanganese phases (Takahashi *et al.*, 2007; Takahashi *et al.*, 2000). Both displayed positive Y anomalies but the magnitude is far greater in seawater than in the

porewaters. The marked contrast in Y anomaly between porewater and seawater is due to the decoupling of Y and Ho as discussed by Bau *et al.* (2014). Yttrium and Ho are considered as geochemical twins because of their very similar ionic radii. This results in the preferential scavenging of Ho relative to Y on metal (oxyhydr)oxide surfaces due to lower stabilities of Y surface complexes (Bau *et al.*, 1996). The magnitude of this anomaly is greater in seawater compared to porewaters which shows that this behaviour is more prominent in seawater than in porewaters, i.e. more Ho is scavenged (relative to Y) in seawater than in porewaters.

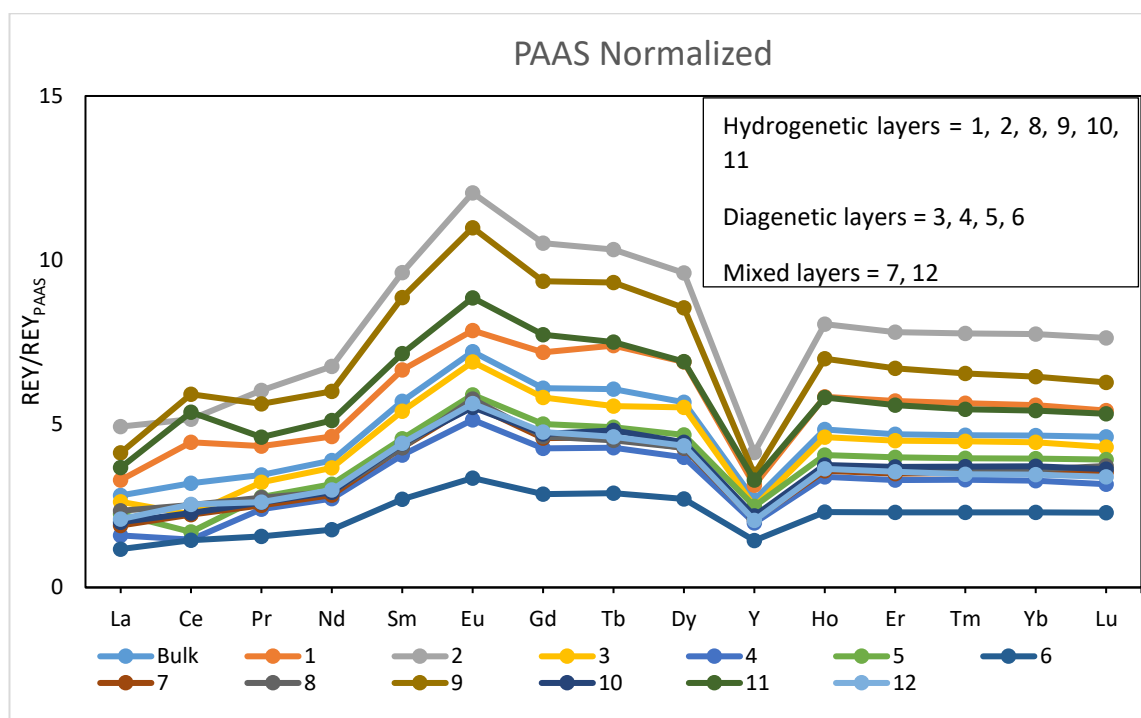


Figure 3.28. REY patterns normalised to PAAS abundances of the twelve individual layers of nodule sample AB02 BC06 N4. The growth layer type for each individual layer are shown inset.

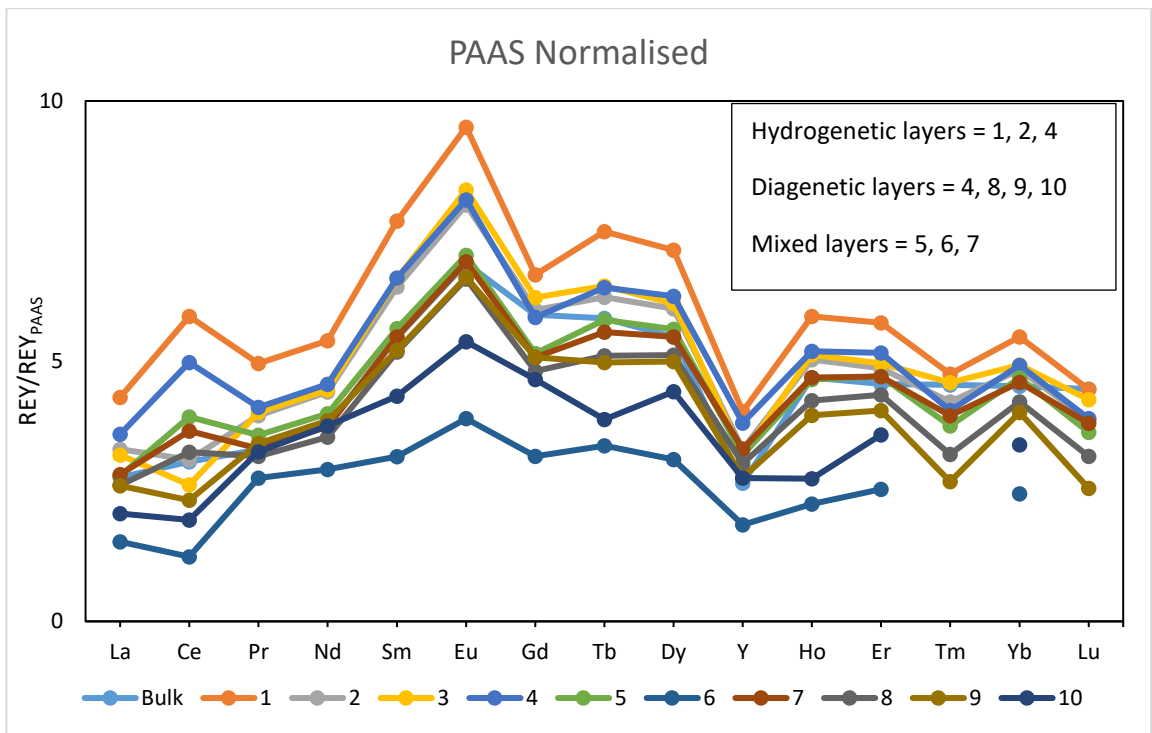


Figure 3.29. REY patterns normalised to PAAS abundances of the twelve individual layers of nodule sample AB01 BC07 N1. The growth layer type for each individual layer are shown inset.

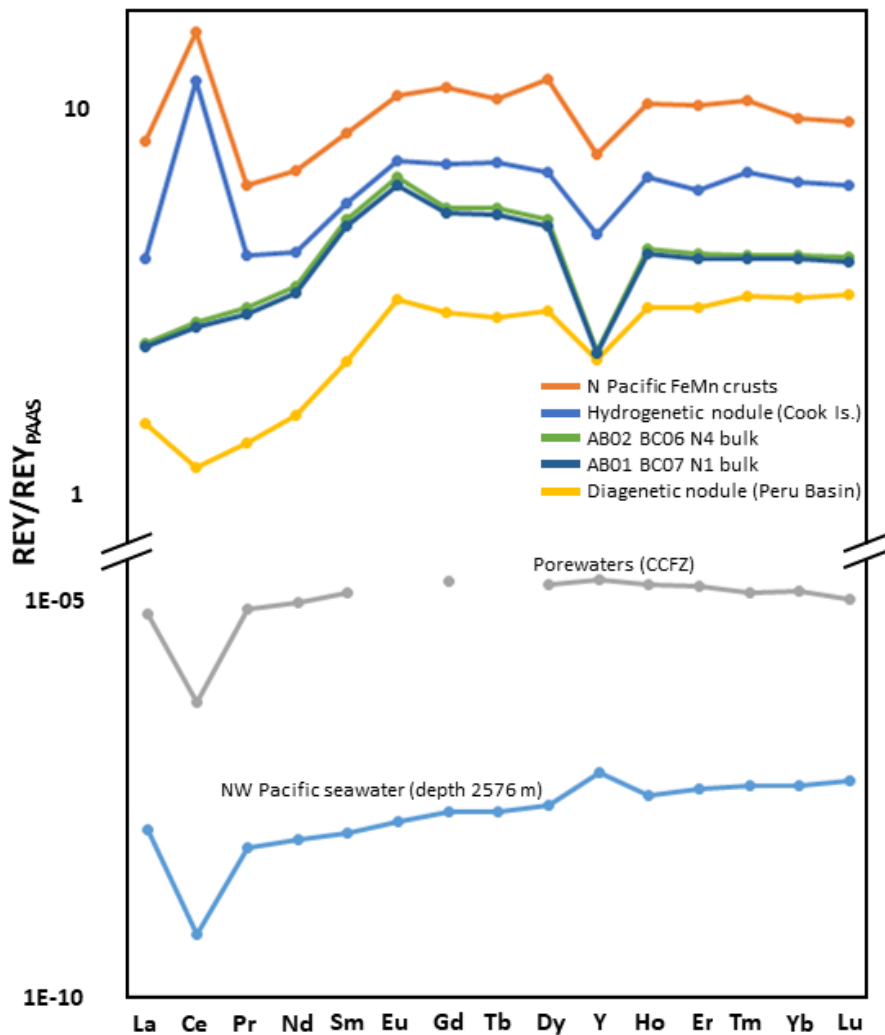


Figure 3.30. REY distribution patterns of North Pacific (NW) seawater (Alibo & Nozaki, 1999), North Pacific crusts, diagenetic nodules of Peru Basin and hydrogenetic nodules from Cook Islands (Hein et al., 2013), porewaters from CCFZ (Paul et al., 2019b) and bulk nodules: AB02 BC06 N4 and AB01 BC07 N1 from this study which were used for the layer chemical analyses. The REY patterns are normalised to PAAS abundances.

3.5 Conclusion

The nodule samples from the UK Claim Area in the Eastern Equatorial Pacific are mixed type nodules and are made up of both hydrogenetic and diagenetic layers. These layers are composed of different growth structures and elemental compositions. Diagenetic layers are characterized by dendritic to massive type structures that formed due to rapid precipitation from underlying pore fluids with high Mn/Fe ratios of >3 while

hydrogenetic layers are made up of laminated and columnar structures that formed from the slow precipitation from seawater with low Mn/Fe ratios of <3 . All the morphologies associated with each growth mechanism (diagenetic and hydrogenetic) were observed in nodules from all five box cores with few variations. In particular, small nodules (1 – 3 cm diameter) from AB02 BC02 showed distinct differences from the rest. The nodules have fewer pore spaces and dendritic structures and more laminated and columnar structures compared to nodules from the other box cores. In contrast, nodules from the other four box cores are generally large (<3 cm) and have similar internal growth structure compositions with more pore spaces and dendritic structures. Nodules from the CCFZ are mixed-type nodules with more diagenetic influence which results in the dendritic structures found in the nodules. AB02 BC02 nodules, however, showed the least diagenetic features and showed some hydrogenetic features compared to the nodules from the other box cores. These differences arose due to the seafloor topography where the samples were collected from. The AB02 BC02 site was located at a site where the presence of seamounts results in fast flowing bottom water currents which keeps the nodules exposed on the seafloor for most of their growth periods and thereby resulting in slightly more hydrogenetic precipitation from the bottom seawater compared to the nodules from the other four box core sites where only the surface of the nodules were exposed resulting in less hydrogenetic precipitation. Hiatus layers are common in the nodules where they are frequently observed to occur parallel to existing growth layers or where they crosscut existing growth layers. They are composed of detrital Al-silicates deposited from the underlying sediments and mark periods of discontinuity in nodule growth. Distribution of some elements using SEM-EDS chemical maps shows that Ni and Cu are concentrated in the diagenetic layers while Pb is

concentrated in the hydrogenetic layers. Using SEM-EDS peak deconvolution, Co is also enriched in the hydrogenetic layers. Discrete phases of Al-silicates are mostly found around pore spaces as well as in hiatus layers which shows that they are sourced from the underlying sediments. Barite discrete phases are found in diagenetic regions which indicates that they are also sourced from the underlying sediments. Ca-phosphate was observed to be enriched in the hydrogenetic layers as well as discrete phases in diagenetic and sediment-rich regions which suggests that it is sourced from both seawater and the underlying sediments. Wet chemistry was used to determine REY concentrations in the individual layers of two nodule samples. The results showed that REYs are more enriched in the hydrogenetic layers with concentrations up to 1200 ppm while their concentrations in the diagenetic layers range from 300 – 700 ppm. Similarly, Co concentrations (using nodule sample AB01 BC07 N1) in the hydrogenetic layers range from 0.1 – 0.2% while concentrations in diagenetic layers range from 0.06 – 0.08%. The enrichment of Ni and Cu in the diagenetic layers is due to the association of these metals with the phylломanganates phase where they are mostly sourced from the suboxic porewaters. Similarly, Pb, REY and Co found enriched in the hydrogenetic layers can be also due to their association with the phylломanganate phase however, their predominant source is bottom seawater.

Chapter 4

4 Determination of the host phases of rare earth elements in deep-sea nodules from the Eastern Equatorial Pacific using sequential leaching experiments and x-ray diffraction analyses

4.1 Introduction

The mineralogy of polymetallic nodules determines most of the physical and chemical properties of this type of resources. Their mineralogical composition is largely made up of Mn oxides and the Fe oxyhydroxides (Kuhn *et al.*, 2017; Wegorzewski *et al.*, 2015). These mineral phases, plus the redox conditions at the sediment-water interface, primarily control the concentrations of minor and trace elements in deep-sea nodules (Wegorzewski & Kuhn, 2014). The Mn oxides consist of two different groups: phylломanganates and the tectomanganates (Figure 4.1) (Bodeï *et al.*, 2007; Chukhrov *et al.*, 1985). While they are both made up of $[\text{MnO}_6]$ octahedral layers, in phylломanganates the layers are separated by an interlayer containing hydrated cations whereas in tectomanganates the layers are organized in a three-dimensional tunnel structure (Bodeï *et al.*, 2007; Burns, Burns & Stockman, 1983; Post & Bish, 1988). The phylломanganates can be subdivided into two groups: the ordered and the disordered group. The ordered group with an interlayer spacing of $\sim 7 \text{ \AA}$ and containing one plane of water molecules is called birnessite; the ordered phylломanganate with an interlayer spacing of $\sim 10 \text{ \AA}$ is named busserite and contains two planes of water molecules (Hao-Jie *et al.*, 2011). The general formula of both phylломanganates is $\text{M}_x\text{MnO}_2 \cdot 1.5\text{H}_2\text{O}$. Their

disordered (or turbostratic) equivalents are known as 7 Å vernadite and 10 Å vernadite (Drits *et al.*, 1997; Manceau, Lanson & Takahashi, 2014; Wegorzewski *et al.*, 2015). Their turbostratic nature arises from the random rotation of the [MnO₆] octahedral layers around the c axis, or the translation of the [MnO₆] octahedral layers in the a-b plane (Giovanoli, 1980; Manceau, Lanson & Takahashi, 2014). These phyllosulfates are commonly associated with some of the important metals found in polymetallic nodules. Metals can be accommodated in their crystal lattice by isomorphic substitution of Mn(IV) (for example by Mn(III), Ni(II), Cu(II), Co(III)) within octahedra, or in occupying vacant sites in the octahedral layer (Burns, 1976; Lanson *et al.*, 2002; Manceau *et al.*, 2007; Peacock & Sherman, 2007a). In both cases, charge deficits are created, these are balanced by the incorporation of hydrated cations in the interlayers or directly above/below layer vacancies (Manceau, Lanson & Takahashi, 2014; Manceau *et al.*, 1997; Post & Bish, 1988; Villalobos *et al.*, 2006).

Birnessite occurs in various geological environments and can form under different physiochemical conditions. It was first described by Jones and Milne (1956) after they discovered it in a fluvio-glacial deposit of gravels in the Birness region of Scotland. The chemical formula deduced following their discovery was Na_{0.7}Ca_{0.3}Mn₇O₁₄·2.8H₂O. It is the main Mn-bearing phase in deep sea ferromanganese precipitates as well as in soils (Chukhrov & Gorshkov, 1981; McLaren, Lawson & Swift, 1986) and in some Mn-rich ore deposits (Usui & Mita, 1995). Buserite however, is more commonly found in diagenetic ferromanganese nodules in the marine environment although they are also found in some terrestrial manganese oxide deposits (Choi, Kim & Kim, 2004).

The commonly occurring tectomanganate is todorokite with a [3 x 3] tunnel structure, transformed from buserite (Burns & Burns, 1978). It is most commonly found in

hydrothermal ferromanganese deposits and in late diagenetic nodules, while in early diagenetic nodules it can be found together with buserite or it may be absent altogether (Ito *et al.*, 1998; Manceau, Lanson & Takahashi, 2014; Usui *et al.*, 1986; Wegorzewski *et al.*, 2015). Some workers suggested that todorokite is the major 10 Å in nodules from the CCFZ (Calvert & Piper, 1984; Halbach *et al.*, 1981; Turner, Siegel & Buseck, 1982). It precipitates in less oxidizing environments from seawater or interstitial waters enriched in Mn(II) (Takematsu, Sato & Okabe, 1989). In diagenetic nodules, Cu and Ni are enriched in todorokite-rich nodules where they stabilize the tunnel structure, though they are not essential for its formation (Burns, Burns & Stockman, 1983; Calvert & Price, 1977).

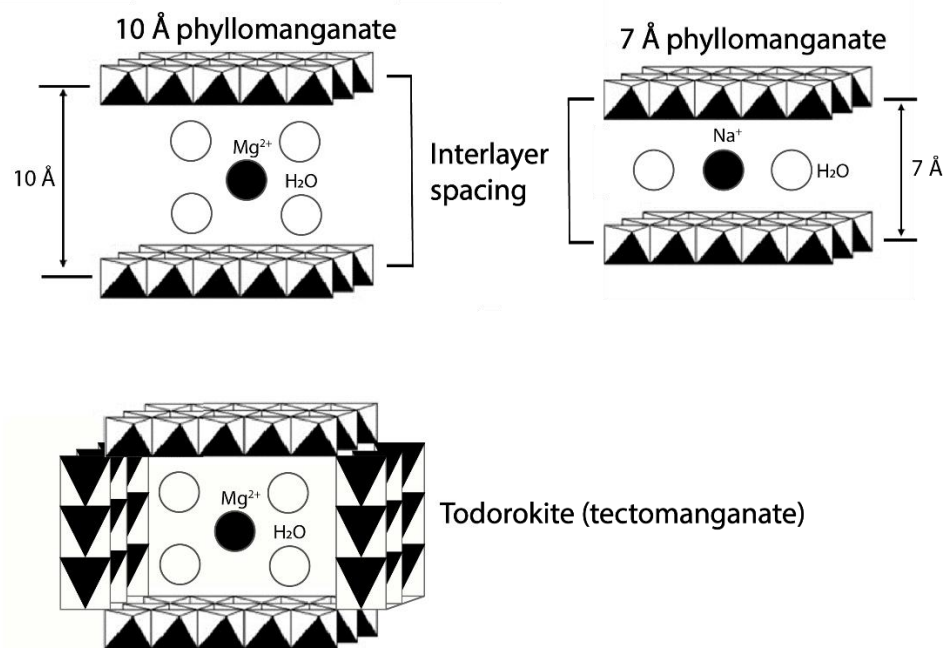


Figure 4.1. Schematic representations of the microstructures of the phyllosulfates: 7 Å phyllosulfate (Na-birnessite) and 10 Å phyllosulfate (Mg-buserite), and the tectomanganate todorokite, modified after Hao-Jie *et al.* (2011).

The commonly used analytical approach for the determination of the mineralogical composition of polymetallic nodules is XRD. This technique can differentiate between the types of phyllosulfates in the nodules. Differentiating between the 10 Å

phylломanganate and todorokite is possible using XRD but both have very similar patterns. Therefore, this can be difficult due to their nanometer size, poor crystallinity and fibrous platy structures (Giovanoli, 1988; Wegorzewski *et al.*, 2015). Hence, some workers now use special methods to differentiate between todorokite and phylломanganates, such as heating and cation exchange experiments (Marino *et al.*, 2018; Wegorzewski *et al.*, 2015). The bulk concentration of Mg in nodules has also been used to provide support for the presence/absence of todorokite as Mg is the common interlayer cation needed to stabilize the tectomanganate tunnel. A concentration of $\geq 2\%$ Mg suggests the possible presence of todorokite while a concentration of $\leq 2\%$ shows that it is absent (Bodeř *et al.*, 2007; Manceau, Lanson & Takahashi, 2014).

The elements present in nodules are associated with the different mineralogical phases present. One useful analytical approach to determine these associations is using wet chemical leaching techniques whereby individual phases are selectively dissolved by different acids. This results in the release of elements associated with the phases which are then measured for their elemental concentration. The sequential leaching procedures developed and modified by Koschinsky and Halbach (1995) from previous authors (e.g. Förstner & Stoffers, 1981; Miller, Martens & Zelazny, 1986) is the most commonly used method for ferromanganese deposits and applied in crust and nodule samples as well as in sediment samples (Konstantinova *et al.*, 2018; Marino *et al.*, 2018; Takahashi *et al.*, 2007). Using this method, the following phases are selectively dissolved sequentially; (1) surface-sorbed exchangeable cations and Ca carbonates using 1 M acetic acid; (2) easily reducible fraction where the elements associated with the Mn oxides are released with 0.1 M HCl or hydroxylamine hydrochloride; and (3) moderately reducible fraction where the elements associated with the FeOOH phase are released

with 0.2 M oxalic acid. The residual fraction that remained consists of the detrital component that consists mostly of (alumino)silicates. Some workers use simple leaching approaches where specific phases are targeted for their elemental associations. For example, leaching work by Elderfield *et al.* (1981a) on nodules from the CCFZ targeted only the Mn oxide phase using dilute HCl whilst work by Menendez (2017) also includes the FeOOH phase using dilute oxalic acid. Element-mineral phase associations vary between sample types (i.e. crust vs nodules vs sediments) and their geographic locations. In polymetallic nodules from the CCFZ, most of the REYs (>60%) are released with dilute HCl along with 40% P and >60% Ca (Elderfield *et al.*, 1981a; Menendez, 2017). The workers hence suggested the association of REYs with the CaP phase in the nodules with supporting data from inter-element correlation relationships (Menendez, 2017).

In this study, the mineralogical composition of the diagenetic and the hydrogenetic layers of a nodule sample was determined using XRD before and after heating. This was used to identify the types of phylломanganates present and also to differentiate between the 10 Å phylломanganate and todorokite. The mineral host phase of different metals in the nodules was investigated using wet chemical leaching methods where different leaching agents were used to attack specific mineral phases. Expanding on from the work carried out by previous workers (Koschinsky & Halbach, 1995; Menendez, 2017), the mineralogical composition before and after leaching was carried out to determine any change in mineralogy and to identify the host phases of different elements with a particular focus on the REYs.

4.2 Materials and method

4.2.1 Reagents

All reagents used for leaching experiments were of analytical grade and used without further purification. Ultra-pure water (Elga purelab, with resistivity >18.2 M Ω .cm) was used for preparing acid solutions. A leaching solution of 0.1 M acetic acid (pH 5)/Na acetate buffer was prepared by combining solutions of 0.1 M acetic acid (Sigma Aldrich, analytical grade) and 0.1 Na acetate (Fisher Scientific, 99% purity) and the pH adjusted using a pH meter. The Na acetate used is in granular form which was dissolved in ultra-pure water to prepare the 0.2 M required for the buffer solution. A leaching solution of 0.5 M HCl was prepared from a 37% HCl stock solution of trace analytical grade (Fisher Scientific) and diluted using ultra-pure water. The leaching solution of 0.2 M oxalic acid/ammonium oxalate pH 3.5 was prepared by combining solutions 0.2 M oxalic acid (Fisher Scientific, 99% purity) and 0.2 M ammonium oxalate (Fisher Scientific, 99% purity) and the pH adjusted using a pH meter. Concentrated nitric acid (70%) used for leaching was acquired from Fisher Scientific (analytical grade).

4.2.2 Simple leaching experiments

Elemental associations with mineral phases in the nodules were studied using wet chemical leaching approaches following methods reported by (Koschinsky & Halbach, 1995; Menendez, 2017) with some modifications. Firstly, simple leaching experiments using three acid leaching agents were carried out for method development purposes. Using this approach, 0.5 g of powdered samples of a polymetallic nodule sample from the UK1 (AB02 BC06 N4) were leached with 10 ml of 0.1 M acetic acid, 0.5 M HCl, 0.2 M

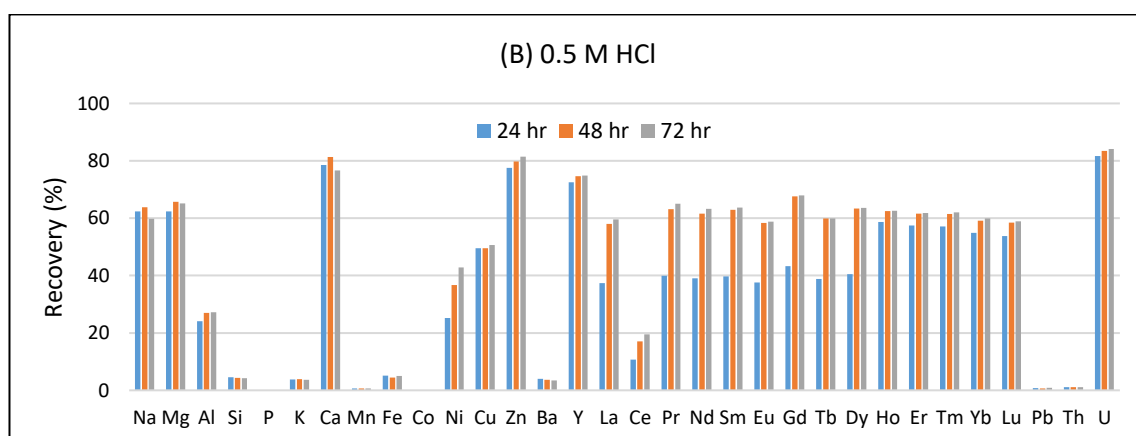
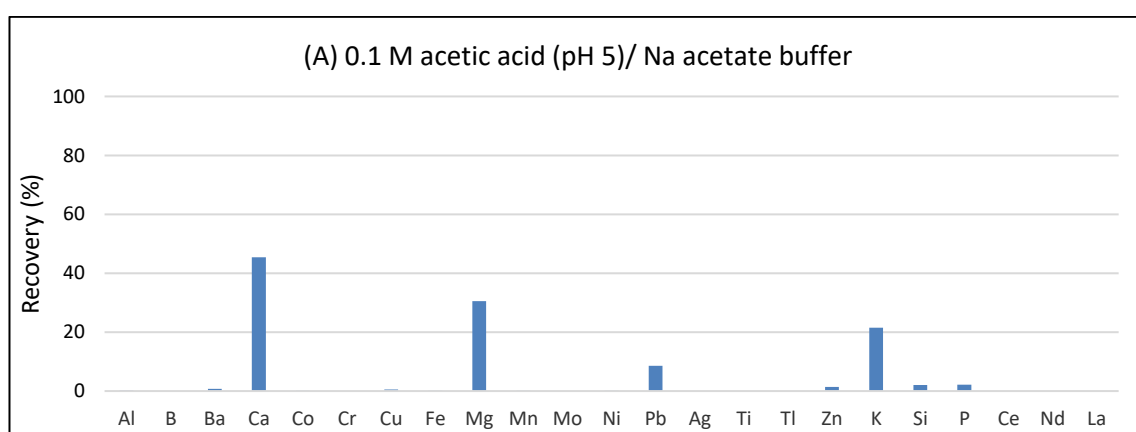
oxalic acid. Briefly, 0.5 g of sample powder was poured into a 13 mL polypropylene (PP) vial and 10 mL leaching agent was added. The vial was then closed and placed on a mechanical shaker for mixing. The shaking time for acetic acid was 3 hours, while shaking times for 0.5 M HCl were 24, 48 and 72 hours. Leaching with 0.2 M oxalic acid was performed at two shaking times of 8 and 24 hours.

Analyses were carried out in triplicates and mean values were used for recovery calculations. The bulk composition of nodule sample AB02 BC06 N4 was determined prior to leaching experiments (chapter 2), these values are considered as the 'known concentrations' which were used to determine the recoveries of each element. Elemental measurements for Na, Mg, Al, Si, P, K, Ca, Mn, Co, Ni, Cu, Zn, and Ba were carried out on an iCAP 7400 ICP-OES, whilst trace element measurements of REYs, Pb, Th and U were performed on an iCAP RQ ICP-MS at the Trace Elements laboratory at the University of Plymouth (see section 2.3.2 – 2.3.5 in chapter 2 for details about calibration standards, blanks, detection limits, precision and accuracy).

The results of the simple leaching experiments are presented in Figure 4.2. The simple leaching experiments shows that the first leaching step (A) which targets the exchangeable cations and carbonates releases moderate to low amounts of Ca, Mg and K and Pb. Note that for this fraction, only three REYs were measured (Ce, Nd and La). The recoveries of these showed that the REYs are not released in this step. The second leaching step (B) using 0.5 M HCl was carried out at three different shaking times of 24, 48 and 72 hours to see the effect of leaching time. The results show that leaching increases with time and plateaus off at 48 – 72 hours for most elements, and in particular the REYs. Bulk (>50%) of Na, Mg, Ca, Zn and the REYs (excluding Ce) and U were released in this step. While moderate (25 – 50%) of Al, Ni, Cu to low (<25%) of Si, P, K, Mn, Fe, Co,

Ba, Ce, Pb and Th were released. The third leaching step (C) using 0.2 M oxalic acid was carried out at two shaking times of 8 and 24 hours and targets the moderately reducible fraction. The recoveries of elements in this leaching step were all below 30% with K and U as the only two with highest recoveries exceeding 20% followed by Fe and then Cu and Mg. The recoveries of the REY were all below 10% and shows that there is a steady increase in recovery from the LREE to the HREY.

This approach of simple leaching was then used to develop the sequential leaching experiments in the following section (section 4.2.3), which are used to study the partitioning of various metals including the REYs with the mineral phases in the nodules.



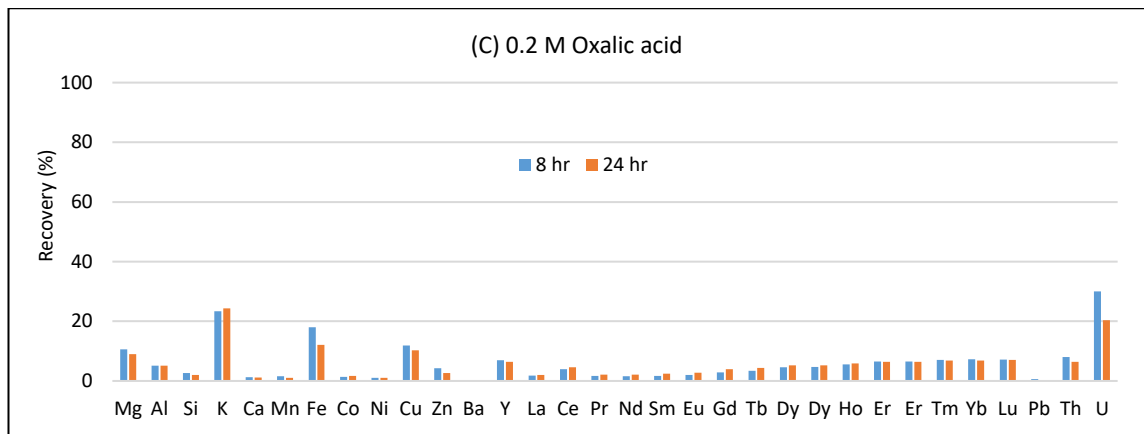


Figure 4.2. Simple leaching recoveries of major and trace metals carried out on nodule sample AB02 BC06 N4 for method development purposes. Leaching was carried out using three leaching agents; (A) 0.1 M acetic acid buffered to pH 5 using Na acetate targets the exchangeable cations and the carbonates; (B) 0.5 M HCl dissolves the easily reducible fraction; (C) 0.2 M oxalic acid (pH3)/ammonium oxalate attacks the moderately reducible fraction. The leaching experiments were carried out at room temperature at various leaching times, (A) was done at 5 hours while (B) and (C) were performed at the times shown inset in the respective graphs.

4.2.3 Sequential leaching experiments

Following on from the simple leaching experiments, three bulk nodule samples were chosen for sequential leaching experiments, each from different box cores. The samples are mixed-type nodules with small variations in their Mn/Fe ratios. Sample AB02 BC06 N5 and AB02 BC19 are mixed-type nodules consisting of alternating growth layers with hydrogenetic and diagenetic characteristics (see chapter 3) with Mn/Fe ratios of 4.95 and 4.78 respectively. Sample AB02 BC02 is a mix of nodules from this box core and has a Mn/Fe ratio of 2.91; as shown in chapter 2 and 3, nodules from this box core have unusual morphological and chemical characteristics which suggest a formation dominated by hydrogenetic processes. All samples were ground in an agate mortar prior to leaching. For comparison, a powdered GeoPT23 FeMn-1 Certified Reference Material (Bundesanstalt für Geowissenschaften und Rohstoffe, Hannover), which is representative for polymetallic nodules from the Peru Basin, was also included in the

experiments. Leaching experiments were adapted from the methods reported by Koschinsky and Halbach (1995) and Menendez (2017) with some modifications. Each of the following sequential leaching experiments was carried out in triplicate at room temperature.

The composition of the bulk samples were determined prior to leaching, for details see section 2.2 in chapter 2. These are considered as the 'known concentrations', the percentage of recovery obtained thus were based on these.

Step 1 (Leach 1): Exchangeable cations and Ca carbonates

1 g of sample powder was washed 3 times with ultra-pure water and shaken with 20 ml 0.1 M acetic acid/Na acetate buffer (pH 5) for 5 hours in a 50 ml (PP) vial. The residues were collected on the bottom of the vials by centrifugation after three times washing with ultra-pure water (Elga purelab, >18.2 M Ω .cm). The supernatants were combined and transferred to clean vials and stored for elemental determinations.

Step 2 (Leach 2): Easily reducible fraction

Twenty millilitres of 0.5 M HCl was added to the residues of leach 1 and the vials were placed on a shaker for 32 hours. The residues were collected on the bottom of the vials by centrifugation after three times washing with ultra-pure water. The supernatants were combined and transferred to clean vials and stored for elemental determinations.

Step 3 (Leach 3): Moderately reducible fraction

Twenty millilitres of 0.2 M oxalic acid/ ammonium oxalate pH 3.5 was added to the residues of leach 2 and placed on a shaker for 18 hours. The residues were collected on the bottom of the vials by centrifugation after three times washing with ultra-pure

water. The supernatants were combined and transferred to clean vials and stored for elemental determinations.

Step 4 (Leach 4): Strongly reducible fraction

The residues of leach 3 were soaked in 20 ml concentrated nitric acid with occasional shaking for 24 hours. After soaking, the residues were collected on the bottom of the vials by centrifugation after three times washing with ultra-pure. The supernatants were combined and transferred to clean vials and stored for elemental determinations.

Elemental measurements for Na, Mg, Al, Si, P, K, Ca, Mn, Co, Ni, Cu, Zn, and Ba were carried out on an iCAP 7400 ICP-OES, whilst trace element measurements of REYs, Pb, Th and U were performed on an iCAP RQ ICP-MS at the Trace Elements laboratory at the University of Plymouth (see section 2.3.2 – 2.3.5 in chapter 2 for details about calibration standards, blanks, detection limits, precision and accuracy).

4.2.4 Mineralogical analysis of nodules

4.2.4.1 Mineralogy of diagenetic vs hydrogenetic layers

Individual diagenetic and hydrogenetic layers of nodule sample AB02 BC06 N3 were sampled using a micro-drill for X-ray powder diffraction analysis for the identification of crystalline mineral phases. Layers of the same type (diagenetic versus hydrogenetic) were combined in order to obtain a sufficiently large sample mass (c. 100 mg) for each type and ground to a fine powder (<50 μm) using an agate mortar and pestle. In order to test the thermal stability of the mineral phases, one sample aliquot from each type was oven dried at 40°C while another aliquot from each type was dried at 105°C, in both

cases for 48 hours. In addition, a bulk sample from the same nodule (i.e., comprising a mixture of hydrogenetic and diagenetic material) was acid-leached before XRD analysis, to investigate the mineralogical changes in the samples that may result from leaching.

4.2.4.2 Mineralogy before and after sequential leaching

Mineralogical analysis before and after leaching was carried out on nodule sample AB02 BC06 N4.

1. Preparation of 'before leaching' samples

Two sample aliquots of each type (hydrogenetic layers versus diagenetic layers) weighing around 50 mg were oven dried, one at 40°C and the other at 105°C for 48 hours and then stored for XRD analysis.

2. Preparation of 'after leaching' samples

Two 50 mg aliquots of a bulk sample were leached with 0.1 M acetic acid/Na acetate buffer (pH 5) with occasional shaking for 3 hours in a 13 ml centrifuge vial. The residues were then separated from the supernatant by centrifugation. Residues were washed 3 times with ultra-pure water before shaken with 0.5 M HCl for 24 hours. After leaching in 0.5 M HCl, residues were separated from the supernatant by centrifugation and washed three times with ultra-pure water. One sample residue was dried at 40°C and the other was dried at 105°C. The dried residues were then stored for XRD analysis.

4.2.5 X-ray diffraction analysis for mineralogy

All samples were finely ground (< c. 10 μm) using an agate mortar and pestle, prior to random orientation of the sample on a silicon disc and subsequent examination by means of X-ray powder diffraction (XRD), using a Philips X'Pert pro XRD instrument at the National Oceanography Centre, University of Southampton; the sample loading and analysis were carried out by Dr. Richard B. Pearce (<https://www.southampton.ac.uk>). Samples were run using a Cu X-ray source and the following setup conditions: 35kV, 40mA, automatic slits and an angular step size of 0.02° 2θ at 3 seconds/step. The automatic slits maintain the size of the irradiated area on the sample, as compared with fixed slits, in which the irradiated area reduces progressively with higher X-ray incidence angles, as does total X-ray counts.

4.3 Results

4.3.1 Sequential leaching

The results of the different leaching experiments are shown in Figure 4.3, where the data is shown in the form of the 'recovery' of the element in each step, i.e., the measured concentration as a fraction of the bulk concentration for that sample, as determined by complete digestion (chapter 2). The concentrations of the elements in the leachates are shown in Appendix II for each of the four samples studied. The first leaching step (1) using 0.1 M acetic acid/Na acetate pH 5 dissolved up to 18% Mg, 20% Ca and 15% K. In addition, up to 16% of Y was also leached in this fraction along with trace amounts of Si, P, Mn, Fe, Co, Ni, Cu, Zn, Ba, REEs, Pb and U in some of the samples.

Leaching step 2 is designed to attack the Mn oxide phase, without fully dissolving it. Low to moderate amounts of some major metals (1 – 2% of the available Mn and P, 4% Si,

up to 25% Na, 59% Mg, 28 % Al and K, 68% Ca) were leached in this fraction. Only traces of Co was leached in this step while other minor metals showed moderate to high recoveries (41% Ni, 72 % Cu, 83% Zn and 36 % Ba. Except for Ce (26 – 40% leached), most of the REEs were dissolved in this fraction (66 – 78%), while Y showed a lower recovery of 40 – 65%. In addition most of the U was also leached in this fraction (58 – 99%) while only traces of Pb was dissolved.

Leach 3 (step 3) partly dissolved the moderately reducible Fe and Mn (oxyhydr)oxides (up to 15% of the available Fe) as well as 5 – 9% Co, 4% Ni, 7 – 10 % Cu and up to 4% Zn. For trace metals, up to 13% Th, low amounts of Y (up to 5%) were leached while trace to low amounts of REEs and U were dissolved in this fraction. For the REEs leached in this step, low but appreciable amounts of the heavy REEs (2 – 6%) were released compared to trace amounts of the light REEs (0.2 – 2%).

The final leaching step (4) using concentrated nitric acid dissolved the strongly reducible Fe oxyhydroxide. Up to 23% Fe and Mn along with 27 – 40% Co, 16% Ni, 5 – 7% Cu and Zn, 10 – 31% Ba were released. Moderate amounts of Y 17 – 24% and Ce 15 – 55% were leached while the recoveries of the rest of the REEs ranged from 3 – 16% with the Light REEs showing slightly more amounts being leached compared to the heavy REEs. Most of the Th (64 – 100%) in the CCFZ samples was leached in this step while for the Peru Basin sample, only trace amounts was released. Moderate amounts of Pb (21 – 59%) was leached while only traces of U was recovered in some of the samples.

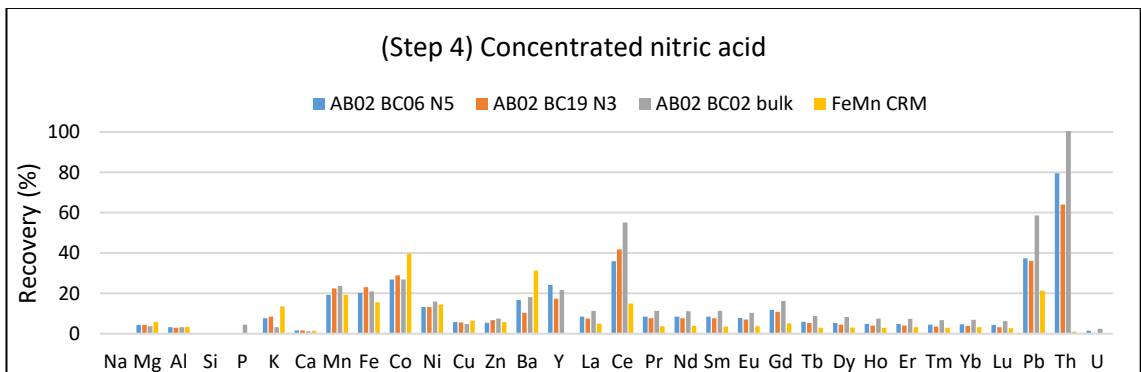
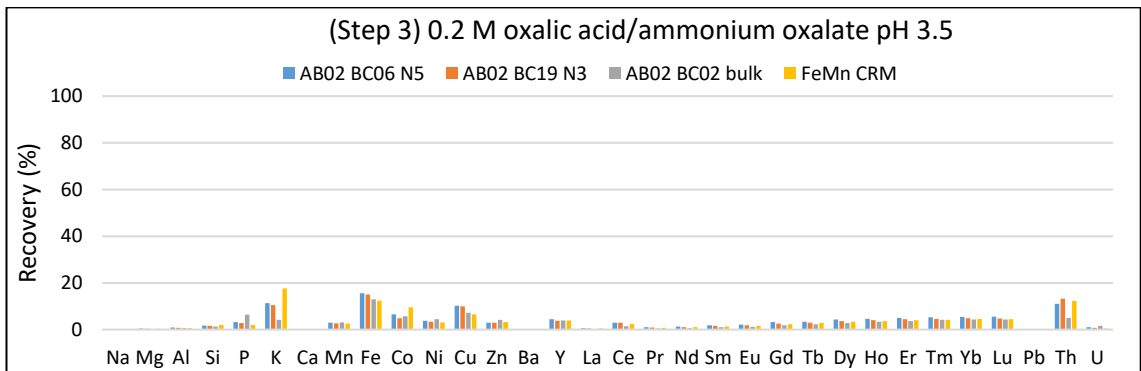
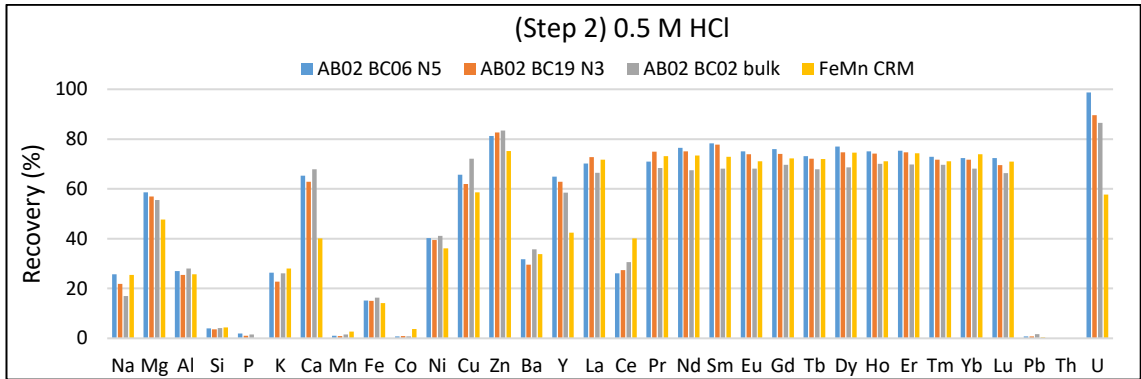
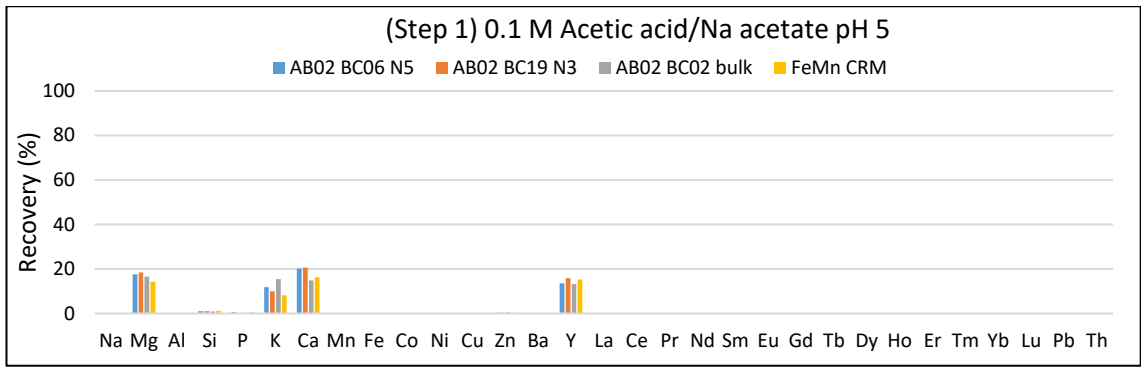


Figure 4.3. Major and trace metal leaching recoveries of three nodules from the Eastern Equatorial Pacific and one from the Peru Basin (FeMn CRM) with (1) 0.1 M acetic acid/Na acetate pH 5, (2) 0.5 M HCl, (3) 0.2 M oxalic acid/ammonium oxalate pH 3.5 and (4) concentrated nitric acid.

Figure 4.4 shows the balance, i.e., the fraction of the elements available that was not recovered in the four leaching steps. It can be seen that most of the Si and P (90 – 95%) were not leached and remained in the residues after the four leaching steps. Similarly, high fraction of Na, Al and Mn (~20 – 30%) also remained in the residues which are slightly lower than that of Co (~34%). For K, Fe and Ni, the amount that remained in the residues range from 40 - 50% while low levels of Mg, Ca, Cu and Zn (10 – 30%) remained in the residues. The amount that remained after leaching was relatively low for all the REYs ranging 10 – 20%, almost all of Y was leached while the amount remaining for Ce range from 20 – 40%. Significant levels of Pb were also not released 60 – 80%. The amount not leached for Th and U were variable between the samples. For Th, only low levels remained (0 – 20%) in the UK1 samples while for the Peru Basin CRM sample, most of it (87%) was not leached. Similarly, only low levels of U also remained for the UK1 samples (0 – 10%) compared to a higher percentage for the Peru Basin CRM of 41%.

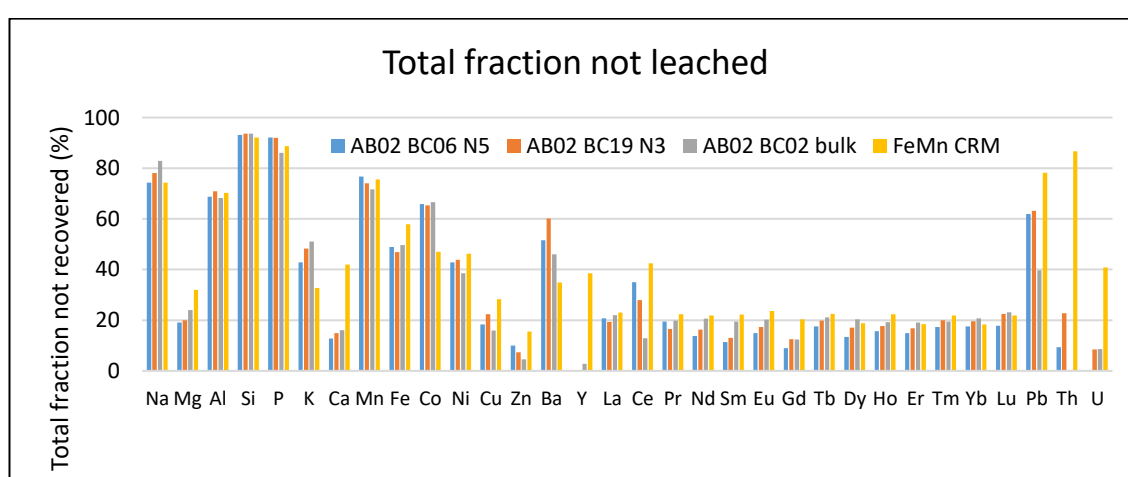


Figure 4.4. Total fraction not recovered by sequential leaching with the four leaching agents, expressed in percentage for each element in the four samples studied. The values were obtained by subtracting the combined recovery (of the four leaching steps – Figure 4.3) from 100%.

The residues that were left after the four leaching steps were not analysed further for their chemical composition except for the measurement of Ca and P on the three UK1 samples by SEM-EDS. The Ca and P compositions obtained were compared with the concentrations before leach. This was done to verify the low recovery of P from the leaching experiments as the Ca-phosphate phase is said to be the main host phase for the REYs in nodules from the Pacific according to some authors (Elderfield *et al.*, 1981a; Menendez, 2017). The compositions based on SEM-EDS are shown in Table 4.1 and shows that the concentrations before leaching are consistent with the compositions obtained for the samples using XRF. The compositions after leaching shows that, most of the Ca was leached while almost all the P remained in the residues.

Table 4.1. Compositions of Ca and P in wt% and converted to atomic proportions, before and after sequential leaching with 0.1 M acetic acid, 0.5 M HCl, 0.2 M oxalic acid and concentrated nitric acid of three samples. The before-compositions were obtained by XRF while the after-compositions were determined by SEM-EDS.

Sample		Before leaching	After leaching
AB02 BC06 N5	Ca (wt%)	1.62	0.24
	P (wt%)	0.16	0.19
	Atomic proportions		
	Ca	0.041	0.006
	P	0.005	0.006
	Ca:P	8.2	1
AB02 BC19 N3	Ca (wt%)	1.70	0.15
	P(wt%)	0.16	0.18
	Atomic proportions		
	Ca	0.043	0.004
	P	0.005	0.006
	Ca:P	8.6	0.7
AB02 BC02 rubbles	Ca (wt%)	2.24	0.14
	P(wt%)	0.39	0.52
	Atomic proportions		
	Ca	0.06	0.004
	P	0.012	0.017
	Ca:P	5	0.23

4.3.2 Mineralogy

4.3.2.1 Mineralogy of diagenetic versus hydrogenetic layers

The XRD patterns of the hydrogenetic versus diagenetic layers after drying at 40 and 105°C of a typical mixed type nodule (AB02 BC06 N3) are shown in Figure 4.5.

The XRD patterns of the diagenetic layer at 40°C shows broad but distinct peaks at 9.69 Å and 4.82 Å which can be attributed to the (001) and the (002) basal reflections of a

10Å phyllosulfates (Manceau, Lanson & Takahashi, 2014; Wegorzewski *et al.*, 2015). These peaks decrease in intensity and shifted slightly to smaller d-spacing after drying at 105°C. The broad low-intensity peak at 7.17 Å can be attributed to the (001) reflection of the 7Å phyllosulfates. This peak shows an increase in intensity after drying at 105°C. The peak at 3.35 Å that did not change in intensity upon heating is a quartz reference peak. Broad reflections can be observed at ~2.4 and 1.4 Å that did not change in intensity and position upon heating.

The XRD pattern of the hydrogenetic layer at 40°C showed low-intensity broad peaks at 9.7 and 4.8 Å which almost disappeared after drying at 105°C. The (001) reflection of the 7 Å phyllosulfate is visible but very weak, and its intensity increased slightly after heating at 105°C. In general, the 10 and 7 Å reflections showed only broad, low-intensity peaks in the hydrogenetic layer compared to the diagenetic layer, and only the peaks at 2.45 and 1.42 Å showed distinct but broad asymmetric peaks. This can be seen more clearly in Figure 4.6 where the peaks were plotted without background correction. The XRD peaks of diagenetic versus hydrogenetic layers shows that the peak locations of both layer types are the same which shows that same amount of material is present in both layer types. However, the weak reflections in hydrogenetic layers shows that it is mostly made up of amorphous phases. As the nodules are known to have Fe concentrations, and since the weak peaks identified are Mn phases, the amorphous phases are Fe-rich phases, probably FeOOH. The absence of typical todorokite diffraction peaks in the XRD patterns between 2.2 and 1.7 Å (Atkins, Shaw & Peacock, 2014; Manceau, Lanson & Takahashi, 2014) indicates that none of the samples analysed showed clear evidence for the presence of todorokite.

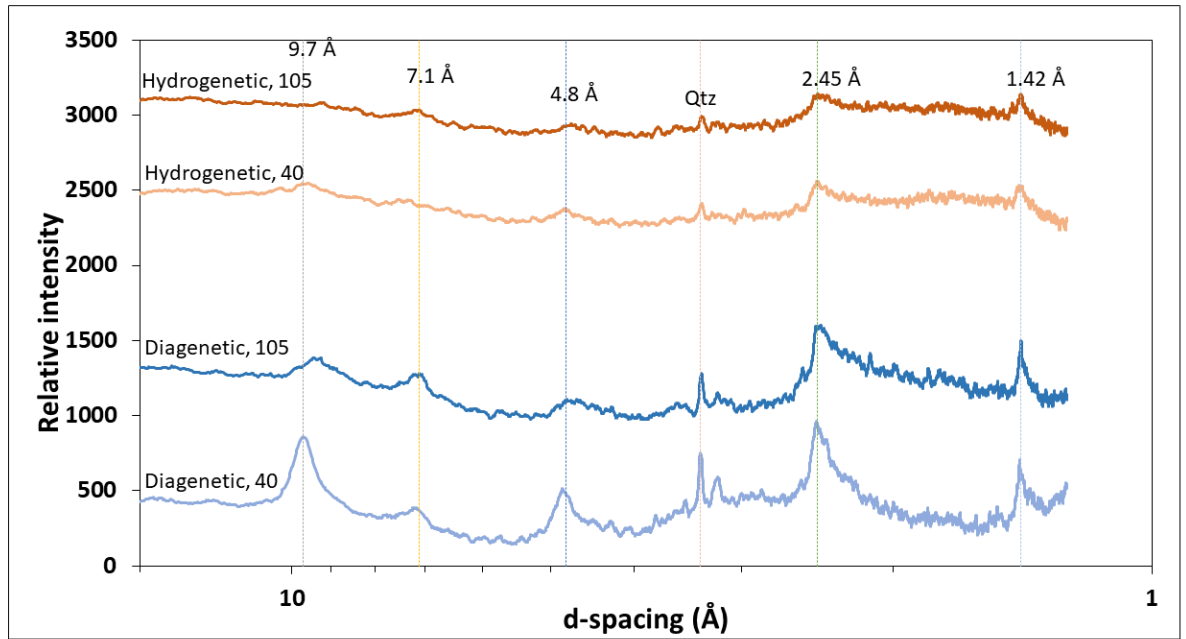


Figure 4.5. XRD patterns of the diagenetic versus hydrogenetic layers of nodule sample AB02 BC06 N4 before (40°C) and after heating (105°C). The d-spacing on the x-axis were obtained by converting from 2 theta using Bragg's law ($\sin \theta = n\lambda/2d$; where $n = 1$ and λ for a Cu source = 1.5418 Å). Corrections were done on the curves to remove background signal and plotted using the same intensity scale, but the scale only applies to the lower curve, and the curves are stacked by using a y-axis off-set for the upper three patterns. XRD plots of the same samples without background subtraction are shown in the next figure (Figure 4.6).

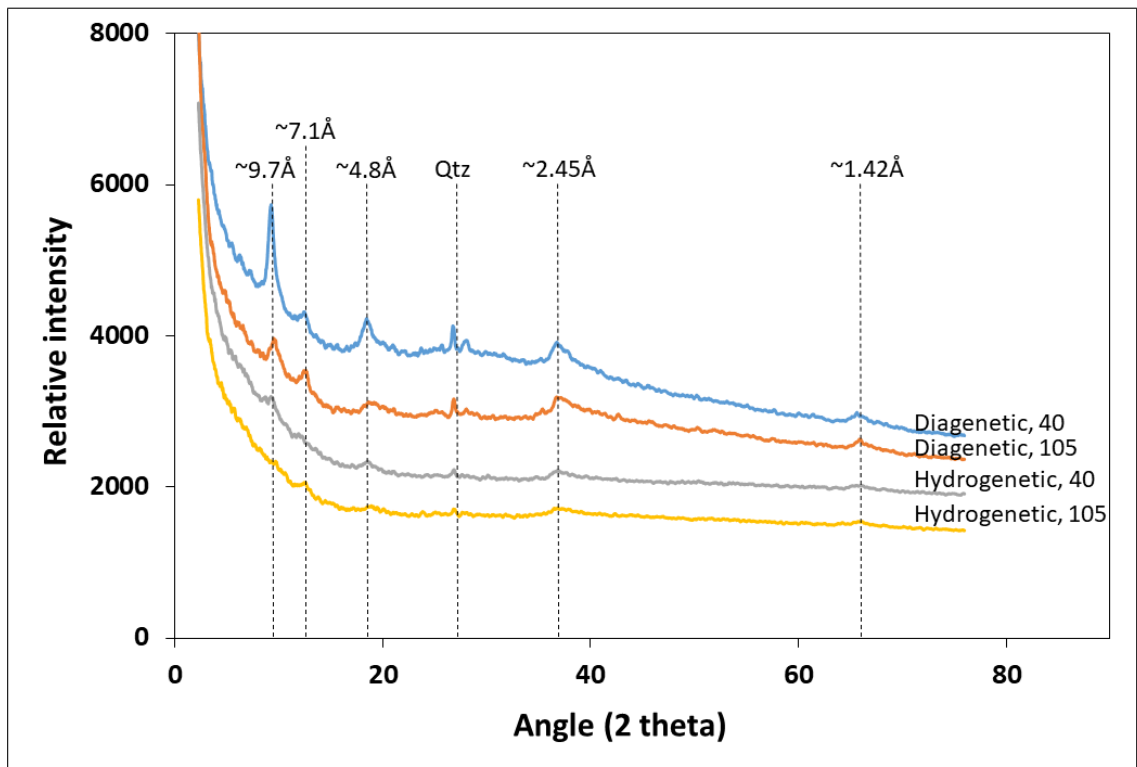


Figure 4.6. XRD patterns of the diagenetic versus hydrogenetic layers of nodule sample AB02 BC06 N4 before (40°C) and after heating (105°C) without background subtraction. All four patterns were plotted using the same intensity scale, but the scale only applies to the lower curve, and the curves are stacked by using a y-axis off-set for the upper three patterns. A comparison between the hydrogenetic versus diagenetic layers' patterns shows that the former have weaker intensity peaks compared to the latter.

4.3.2.2 Mineralogy before and after leaching

The XRD patterns of a bulk nodule sample (AB02 BC06 N3) before and after sequential leaching with 0.1 M acetic acid/Na acetate pH 5 and 0.5 M HCl and dried at 40°C and 105°C are shown in Figure 4.7 and Figure 4.8. For the 40°C dried sample before leaching, the pattern is similar to the one shown in Figure 4.5 for the sample made up of diagenetic layers dried at 40°C. It shows broad but distinct peaks at 9.64 and 4.83 Å, which can be attributed to the (001) and the (002) basal reflections of a 10 Å phyllosilicates, and a peak at 7.18, which can be attributed to the 001 reflection of the 7 Å phyllosilicate. After leaching the 10 Å (9.64 Å) peak decreased in intensity

while the 7 Å peak increased in intensity and shifts slightly to larger d-spacing of 7.24 Å. Similarly, the sample before leaching that was dried at 105°C showed a (001) reflection of the 10 Å phyllosilicate at 9.18 and a (002) broad reflection at 4.6 Å. The 10 Å peak decreased in intensity and almost disappeared after leaching while the 7 Å peak increased in intensity and shifts slightly to smaller d-spacing of 7.13 Å.

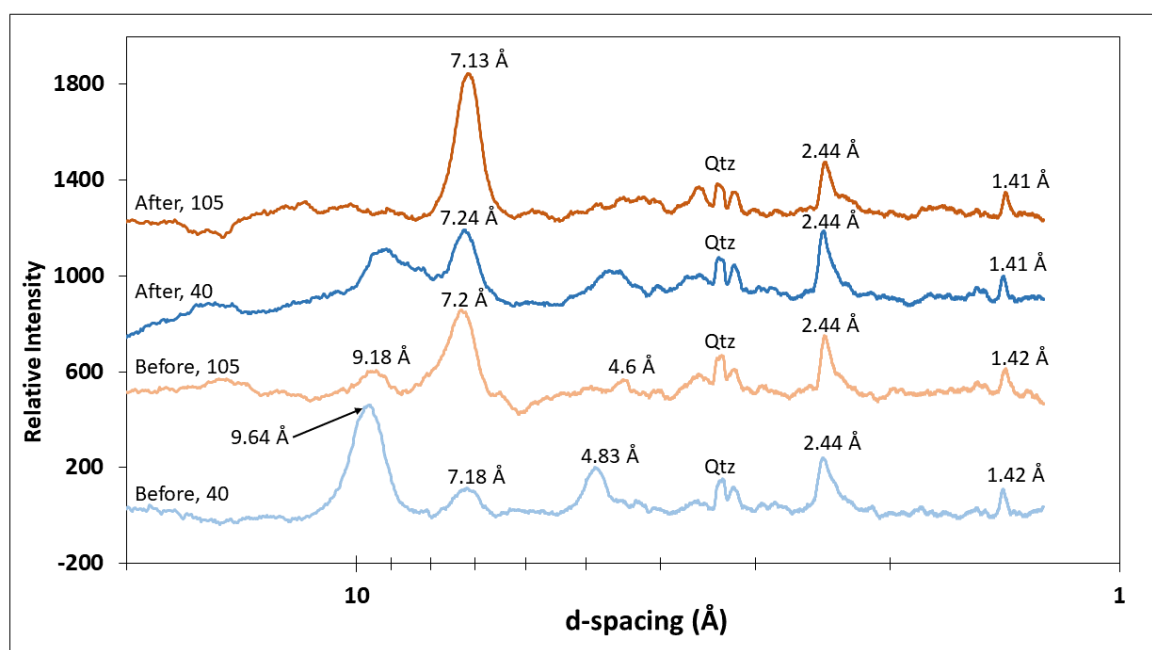


Figure 4.7. XRD patterns of nodule sample AB02 BC06 N4 before and after sequential leaching with 0.1 M acetic acid/Na acetate pH 5 and 0.5 M HCl, before (40°C) and after heating (105°C). The d-spacings on the x-axis were obtained by converting from 2θ using Bragg's law ($\sin \theta = n\lambda/2d$; where $n = 1$ and λ for a Cu source = 1.5418 Å). Corrections were done on the curves to remove the background signal and plotted using the same intensity scale, but the scale only applies to the lower curve, and the curves are stacked by using a y-axis off-set for the upper three patterns. XRD plots of the same samples without background subtraction are shown in the next figure (Figure 4.8).

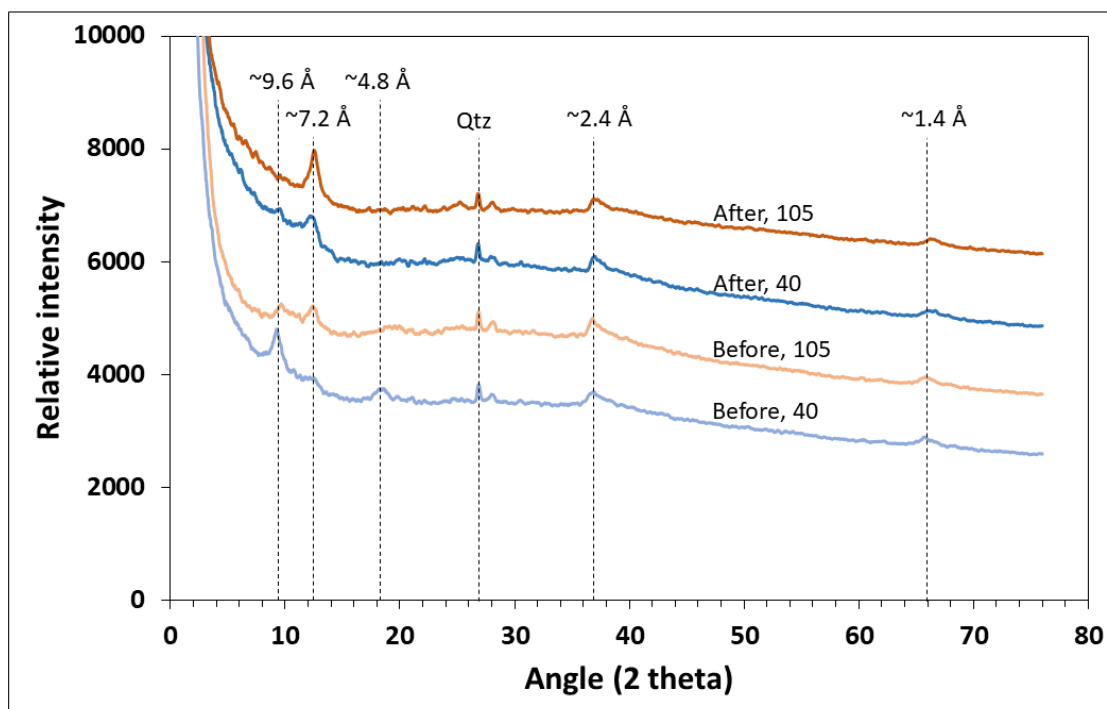


Figure 4.8. XRD patterns (without background correction and plotted against angle 2 theta) of nodule sample AB02 BC06 N4 before and after sequential leaching with 0.1 M acetic acid/Na acetate pH 5 and 0.5 M HCl, before (40°C) and after heating (105°C). The curves are plotted using the same intensity scale, but the scale only applies to the lower curve, and the curves are stacked by using a y-axis off-set for the upper three patterns.

4.4 Discussion

4.4.1 Metal associations with different mineral phases

The *first leaching step* releases the exchangeable plus carbonate-bound metals: in marine Fe-Mn deposits, these metals are incorporated in Ca carbonates and surface-sorbed onto oxides and clay fractions (Koschinsky & Halbach, 1995). These are weakly bound metals which can be easily released using weak acids such as acetic acid.

The *second leaching step* using 0.5 M HCl released most of the cations (40% Ni, 60% Cu, 80% Zn, 70% REY, and 90% U) but essentially no Mn. This suggests that the octahedral manganate layers are not destroyed during this leaching step. Results from the XRD showed the disappearance of the 10 Å phase and an increase in intensity of the 7 Å phase, which suggests the collapse of the 10 Å phase to the 7Å. Thus the second leaching step affects the hydrated interlayer of the phylломanganates. Therefore, elements released in this step (Mg, Ca, Ni, Cu, Zn, REY, U) are interpreted as being hosted in the interlayers as hydrated cations, predominantly in the 10 Å phylломanganate (10 Å vernadite). However, Co and Pb not released in this step can be interpreted to be hosted in different site and/or phase (i.e., in octahedral manganate layer and/or in a FeOOH phase).

In addition, the leaching recovery of Ce is markedly low (~30%) compared to the rest of the REYs. The proportion of Ce leached in step 2 is interpreted as that associated with the phylломanganates where it was hosted in easily leachable interlayers. Most of the Ce was released in step 4 with a strong oxidizer (nitric acid) and is interpreted to be released from the FeOOH phase. These results show that Ce is partitioned between both oxide phases with most of it hosted in the FeOOH phase. Low amounts of Fe released in

step 2 can be from; (i) Fe associated with the phylломanganates as hydrated cations (ii) Fe associated with the FeOOH nanoparticles that are intergrown with the phylломanganates (also known as Fe-vernadite). Another possibility is that the low pH of the dilute HCl (pH ~2) might have resulted in the FeOOH phase having previously been attacked in step 2.

Moderate amounts of Na released in step 2 are hosted in the phylломanganates where Na commonly occupies the interlayer spaces as single and double layer hydrated Na cations (Giovanoli, 1985; Golden, 1987). Similarly, high amounts of Mg released from the Mn oxide phase in step 2 is consistent with the presence of the phylломanganate, 10 Å vernadite where hydrated Mg cations occupy the interlayer spacing (Manceau, Lanson & Takahashi, 2014).

Almost all the U was released in this step (90%), bulk nodule composition (chapter 2) showed a linear relationship of U with Fe which suggests that U is associated with Fe-vernadite (vernadite epitaxially intergrown with amorphous δ -FeOOH). Furthermore, the results show that U is most probably co-precipitated with Fe in the nodules from bottom seawater. Uranium is a redox sensitive element, and its precipitation from the oxic bottom seawater suggests that it is present in the oxidized form as U(VI). At bottom seawater (pH 8.2), U exists as a tricarbonate complex $\text{UO}_2(\text{CO})_3^{4-}$ (Djogić, Sipos & Branica, 1986). Based on the colloidal-chemical sorption model of Koschinsky and Halbach (1995), this anionic species will be sorbed onto the slightly positively charged hydrous δ -FeOOH in the water column, which then co-precipitates on the nodule surface along with the negatively charged vernadite. The co-precipitation of both phases results in the fine-grained epitaxial intergrowth of amorphous Fe-vernadite (δ -MnO₂) which is predominant in the hydrogenetic layers of nodules.

The **third leaching step** using 0.2 M oxalic acid which targets the moderately reducible FeOOH phase dissolves up to 14% of the available Fe as well as 2% Mn, 15% K, 6% Co, 3% Ni, 10% Cu and 10% Th. The REY recovery shows an increase from the LREE to the HREY (0.2 – 5%). The low recovery of Fe (14%) shows that the FeOOH phase was attacked but it was only partly dissolved, and that this part of the phase was leached in the next leaching step (step 4) using concentrated nitric acid (next paragraph). Minor amounts of Mn released in step 3 are probably those that are part of the Mn-bearing FeOOH (Mn-feroxyhyte), which is common in hydrogenetic deposits (Hein *et al.*, 2000; Marino *et al.*, 2018; Varentsov *et al.*, 1991).

The **final leaching step (4)** using nitric acid (a strong oxidizer), targets the strongly reducible FeOOH phase and releases the cations that were not leached by oxalic acid or that were not able to be reduced and leached in the previous steps. Whilst the recoveries of cations are generally low in this step, a few cations showed higher recoveries, particularly Ce, Pb (40%) and Th (80%). Apart from Ce, the minor amounts of REYs released in concentrated nitric acid, as well as in the previous step (3) with 0.2 M oxalic acid, are those that are associated with the FeOOH phase. This shows that the REYs are partitioned between the two oxide phases with the phylломanganate phase as the predominant host phase. More than 60% of the Th was released in step 4 compared to ~10% in oxalic acid (step 3), both are interpreted as being associated with the FeOOH phase which is consistent with the linear relationship of the bulk compositions of Th and Fe noted in chapter 2. These results are consistent with literature indicating that Th exists in the oxidized tetravalent form as Th(OH)₂ in seawater and then is sorbed on the FeOOH phase (Koschinsky & Halbach, 1995), which then precipitates on the nodule surface. As previously mentioned, most of the Ce were released in step 4 which

therefore led to the conclusion that most of Ce is hosted in the FeOOH phase. Ce is a redox sensitive element and can exist in both Ce(III) and Ce(IV) in natural systems. In seawater it can be easily oxidized even with dissolved oxygen (de Baar *et al.*, 1988). Ce(III) in seawater can be scavenged by both MnO₂ and FeOOH, once on the hydro(oxide) surface it is oxidized to Ce(IV). Therefore, the Ce leached in steps 2 and 4 is interpreted as Ce(IV). Another possible interpretation of the Ce host phase in this study is that Ce is associated with the phyllosilicates and were all leached step 2 but re-adsorbed onto the FeOOH as suggested by Takahashi *et al.* (2007) which was then released in the nitric acid step (step 4). However, we cannot provide evidence to support this inference, but we can demonstrate that Ce is hosted in both oxide phases.

The residues left after the final leaching step (4) were not analysed further in this study, however, the fraction of cations not leachable by this method is shown in Figure 4.4. The residues that remained mostly consist of Al-silicate phases (70% Al, 90% Si). Cations that remained such as Na, K and Ca can be from Al-silicate detrital phases such as phillipsite and montmorillonite which are common in deep-sea sediments in the Pacific (Piper, 1974). These Al-silicate phases are also known REY host phases in deep-sea sediments (Bischoff, Piper & Leong, 1981; Piper, 1974), which may account for some of the REYs that remained in the residues. The leaching results showed that Al and Si are not only present in the refractory detrital phases, but are also present in the leachable fraction as observed in the HCl leaching step (2) where 25% Al and 4% Si were released. These proportions of Al and Si may be from colloidal phases that precipitated from seawater (e.g. opal; Moorby and Cronan (1981)). Variable amounts of Al and Si can be also leached from some Al-silicates such as phillipsite in North Pacific Mn nodules using 1 M hydroxylamine hydrochloride as reported by Bischoff, Piper and Leong (1981).

The leaching results showed that 50% of Fe in the nodules was not leachable and remained in the residues. This can either represent Fe associated with refractory FeOOH phases such as goethite (Moorby & Cronan, 1981) or Fe-bearing oxide minerals and Al-silicates such as magnetite, spinel, smectite, amphibole, and pyroxene (Hein, Schulz & Gein, 1992; Koschinsky & Halbach, 1995). Similarly, the high Mn fraction (70%) that remained is from the manganate layers after the interlayer cations were released in 0.5 M HCl (step 2). Based on the XRD pattern after leaching with 0.5 M HCl (step 2), these manganate layers are predominantly that of the 7Å phyllomanganate transformed from the 10 Å phyllomanganate phase. Therefore, some of the cations that remained are associated with the un-leachable FeOOH and the 7Å phyllomanganate. This indicates that some of the cations that remained such as Ni, Cu, Co are those that occupy sites within the manganate octahedral layers of the 7Å phyllomanganate. This interpretation for Ni and Cu are in agreement with the SEM results in chapter 3 which shows that they are enriched in the Mn-rich diagenetic layers. The leaching results show that ~65% of Co remained in the residues which led to the suggestion that this Co is probably hosted in the non-leachable octahedral layers of the phyllomanganates. Variable amounts of Co released in steps 3 (~6%) and 4 (~28%) are interpreted as Co associated with the FeOOH phase. This proportion of Co is consistent with the SEM chemical maps for Co (chapter 3) which show that it is enriched in the Fe-rich hydrogenetic layers.

Most of the Ba (50%) that remained in the residues is interpreted as a component of authigenic barite as it is not dissolvable with the acids used in these leaching experiments. It is therefore possible that some proportion of the remaining REYs is that which is associated with this barite phase and is consistent with studies such as Guichard *et al.* (1979) and Piper (1974). The release of Ba in 0.5 M HCl and 0.2 oxalic acid (steps 2

and 3) shows that Ba is also present in other phases. The leaching results showed that up to 90% of P remained in the final residues while most of Ca (~70%) was leached, the results are also consistent with the composition obtained using the SEM-EDS. The results using SEM-EDS (Table 4.1) shows that Ca:P ratio before the leach was ~5 - 8 whereas the ratio in apatite is 1.7, so there are other Ca minerals which clearly breakdown or are leached. But in the after-leach residues, there was an 'excess' of P (not enough Ca, $\text{Ca:P} \leq 1$) for it all to be in some apatite. This presence of excess P is interpreted as probably due to some Fe-phosphates and/or Mn-phosphates which were either already present from the start (before leaching) or formed during the leaching process when some apatite was destroyed and now exist as Fe-phosphate (and/or Mn-phosphate). However, the leaching process did not show in which step most of the apatite was broken down although some workers have reported both Ca and P (interpreted to be from apatite) are released in the HCl step (Elderfield *et al.*, 1981a; Menendez, 2017).

The leaching results for Pb shows that it was only released (40%) in concentrated nitric acid (step 4) and the rest of it remained in the residues. The proportion of Pb released in nitric acid is interpreted as that which is associated with the amorphous FeOOH phase while the rest of the Pb is hosted in the octahedral manganese layers which were not leached in step 2. These results are consistent with the colloidal-chemical sorption model of Koschinsky and Halbach (1995) where they showed that Pb can exist as cationic Pb(II) and anionic $\text{Pb}(\text{CO})_3$ in seawater where the cationic Pb(II) is sorbed onto the negatively charged Mn-oxide while the anionic $\text{Pb}(\text{CO})_3$ is sorbed onto the slightly positively charged FeOOH. These then precipitate onto the nodule surface and are incorporated into their respective oxide phases which are reflected in the leaching results. Thus, it follows that some of the Pb that remained in the residues may be part

of the MnO₂ component that is hosted in the octahedral layers of the phyllosulfates. However, the association of Pb with the FeOOH phase is consistent with SEM-EDS chemical maps for Pb in chapter 3 and shows that it is enriched in the hydrogenetic layers.

The REY distribution patterns for the samples studied in the sequential leaching experiments normalised to PAAS are shown in Figure 4.9. REY distribution patterns of the three nodule samples plus the FeMn CRM from the Peru Basin normalised to PAAS for their HCl, buffered oxalic acid and concentrated nitric acid leaches. The REY distribution pattern for North Pacific (NW) seawater (Alibo & Nozaki, 1999) and North Pacific crusts (Hein et al., 2013) are included in the plots for AB02 BC06 N5. The distribution patterns for North West Pacific seawater, North Pacific ferromanganese crusts and bulk FeMn CRM from the Peru Basin are also included in Figure 4.9. Leach stage 2, 3 and 4 showed very similar REY patterns in all four samples. All the three leaches showed very similar patterns in all the four samples. Note that REY pattern for step 1 (acetic acid leach) was not included as the low recoveries of REY in that step are considered negligible. The REY pattern for the dilute HCl leach (stage 2) matches that of diagenetic nodules (e.g., Fe-Mn CRM - from the Peru Basin analysed here alongside the Pacific nodules from the study area) which shows that the phyllosulfate phase is formed during early suboxic diagenesis in the upper top layer of the sediments. This is then followed by different post-depositional processes that may lead to the release or uptake of metals and eventually to the stabilization of the phyllosulfate structure (Kuhn *et al.*, 2017).

The oxalic acid leach (stage 3) REY pattern closely matches that of North Pacific ferromanganese crusts. This is because the mineralogy of both is controlled by the Fe-

oxyhydroxides and shows that the minor amounts of REYs in this phase are incorporated into the Fe-oxyhydroxides by scavenging from the oxic seawater. This is also the same mechanism proposed for the incorporation of trace metals in ferromanganese crusts (Koschinsky & Halbach, 1995).

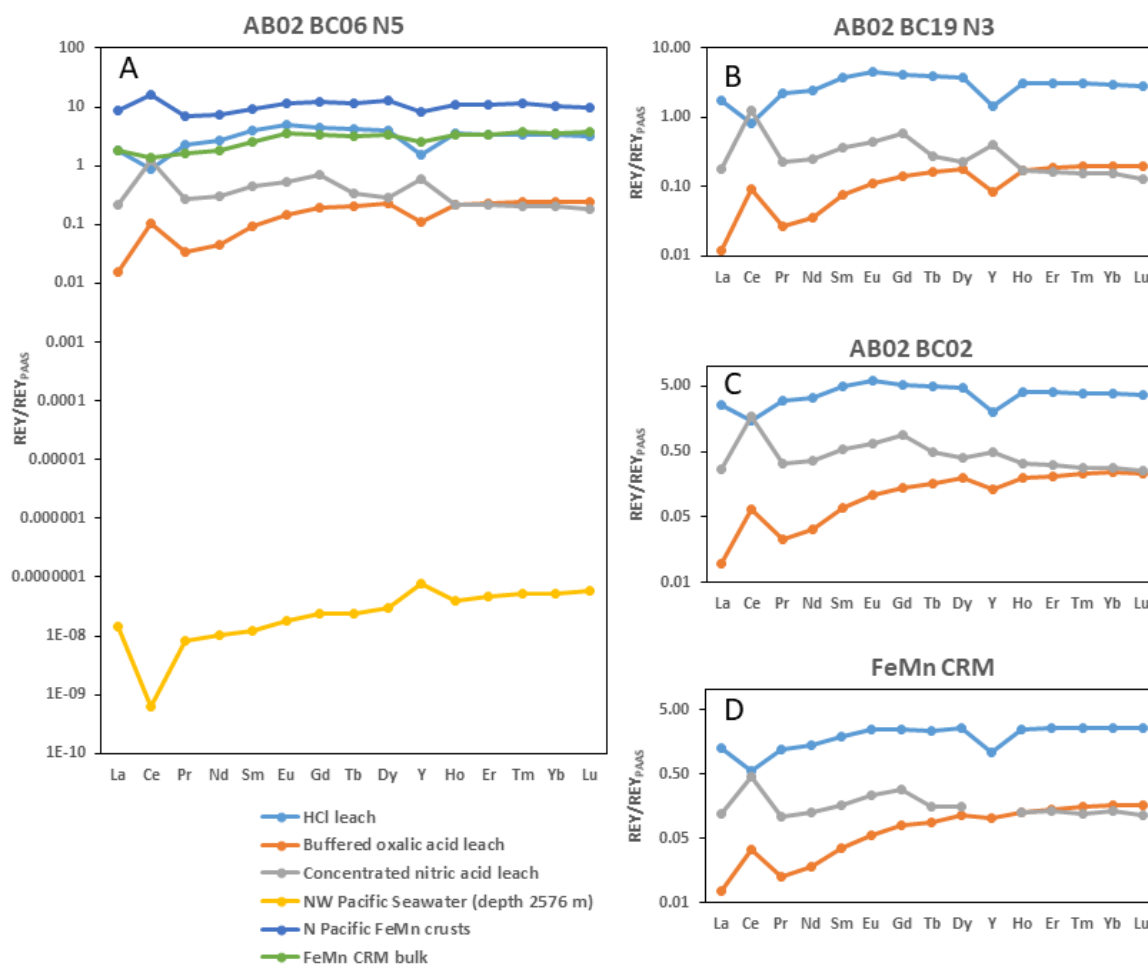


Figure 4.9. REY distribution patterns of the three nodule samples plus the FeMn CRM from the Peru Basin normalised to PAAS for their HCl, buffered oxalic acid and concentrated nitric acid leaches. The REY distribution pattern for North Pacific (NW) seawater (Alibo & Nozaki, 1999) and North Pacific crusts (Hein et al., 2013) are included in the plots for AB02 BC06 N5.

The LREEs and HREEs show distinct behaviours, with a relative enrichment of HREEs compared to the LREEs, which is also consistent with previous studies (e.g. Menendez (2017)). This can be explained by the scavenging behaviour of REEs from seawater by

phylломanganates and Fe oxyhydroxides. In seawater, REEs occur mainly as carbonate complexes (Ohta & Kawabe, 2001), with the LREEs forming monocarbonate complexes $[\text{LREECO}_3^{3+}(\text{aq})]$ and the HREEs forming bicarbonate complexes $[\text{HREE}(\text{CO}_3)_2^-]$. Halbach, Jahn and Cherkashov (2017a) proposed that due to the nature of these complexes the phylломanganate phases prefer to scavenge the LREEs, while the Fe-oxyhydroxides phases scavenge the HREEs from seawater. This behaviour is likely responsible for the REE leaching pattern observed in the oxalic acid leaching step (3), which attacks the Fe-oxyhydroxides phases, in which relatively more HREE are released compared to LREE. However, this is not the only cause for relative HREE enrichment in polymetallic nodules compared to most land-based REE deposits: results in chapter 5 show that laboratory-synthesized phylломanganates strongly fractionate between HREE and LREE, with a strong preference for HREE.

4.4.2 Mineralogy

Based on the XRD results, the collapse of the 10 Å Mn phase (to 7 Å) upon heating confirms the presence of the 10 Å phylломanganate in this study. In addition, the absence of typical todorokite diffraction peaks in the XRD pattern between 2.2 and 1.7 Å (Atkins, Shaw & Peacock, 2014; Manceau, Lanson & Takahashi, 2014) strongly suggests the absence of todorokite as the main Mn-phase in the nodules. Furthermore, bulk Mg concentrations of 1.6 – 1.9% determined in the nodules studied here are likely too low for the transformation of 10 Å vernadite to todorokite (Bodeï *et al.*, 2007; Manceau, Lanson & Takahashi, 2014). These observations indicate that todorokite is not the main Mn-phase in the nodules. Instead the 10 Å Mn phase is a phylломanganate, which is

present along with the 7 Å turbostratic phyllomanganate phase and are the two main Mn-phases in the nodules.

The collapse upon heating is due to the release of interlayer water molecules from the phyllomanganate structure (Mellin & Lei, 1993). The presence of broad asymmetric reflections at ~2.45 and 1.42 Å (before and after heating) compared to those of ordered phyllomanganates (birnessite and buserite) from XRD spectral libraries indicate that the phyllomanganates are turbostratically disordered 10 and 7 Å phyllomanganates (also known as vernadites) with a hexagonal symmetry (Drits *et al.*, 1997; Manceau, Lanson & Takahashi, 2014).

The mineralogy of the diagenetic versus hydrogenetic layers based on their XRD patterns shows that the hydrogenetic layers are dominated by Fe-rich amorphous phases (Fe-vernadite, a disordered phyllomanganate intergrown with Fe nanoparticles characterized by the two broad reflections at 2.42 and 1.42 Å (Manceau, Lanson & Takahashi, 2014). The basal reflections at 9.7 Å (001) and 4.8 Å (002) from the vernadite component are only weakly showing due to the intergrowth of the FeOOH nanoparticles (Golden *et al.*, 1988).

The XRD patterns before and after sequential leaching shows the 7 and 10 Å as the dominant phyllomanganate mineral phases. After leaching, the 10 Å phase collapses to the 7 Å phase. This collapse is due to the removal of the hydrated cations that occupy the interlayer spaces in the phyllomanganates. The change in the phyllomanganate structure is likely only in the c direction as all the peaks remained the same after leaching. Since the 7 Å phyllomanganate cannot collapse further, it is also assumed that the hydrated cations in the interlayers of the 7 Å phase were also mostly released during

leaching with weak HCl. Based on results from sequential leaching, most of the REYs (up to 70%) were released after leaching with weak HCl. This shows that the REYs released after leaching with weak HCl likely occupied the interlayers of the 10 and 7 Å phylломanganates which can be easily released with weak HCl.

4.5 Conclusion

Whilst the mineralogy of polymetallic nodules is relatively well known now, the association of various trace metals including the REYs with different host phases in nodules can be complex. Although the interpretation of chemical leaching results can be equivocal, it is useful in studying the trace metal mineralogy in nodules. An approach of combining leaching experiments with XRD analysis that is presented here shows that REYs are predominantly hosted in phylломanganate phases, from which they are easily and efficiently leached by weak hydrochloric acid, with minor amounts hosted in the amorphous Fe-oxyhydroxides phases and in the non-leachable detrital fraction. The results from the mineralogical analysis using XRD show that the REE are likely hosted within the interlayers of the phylломanganate layers, instead of being absorbed onto the surface of phylломanganates, and that they stabilize the 10 Å phylломanganate phase, which almost completely collapses to a 7 Å phase as a result of leaching. The same is probably true for Ni, Cu and Zn, which are also relatively easily leached from phylломanganate interlayers, in contrast to Co, which is most likely hosted within octahedral sites within the octahedral phylломanganate layers as well as in the FeOOH phase.

Chapter 5

5 Interlayer cationic exchange of Mg(II), Ca(II), Cu(II), Co(II), La(III), Nd(III) and Yb(III) for Na in synthetic birnessite

5.1 Introduction

The trace metal chemistry of deep sea Mn oxides such as birnessite and buserite can be controlled by both structural (e.g., the presence of vacancies and the chemical species in the interlayer), and physiochemical factors (e.g., pH) (Manceau *et al.*, 2007; Peacock & Sherman, 2007a). The incorporation of transition metals into Mn oxides results in changes to their structural and physiochemical properties. Transition metals can be incorporated into the interlayers and adsorbed on vacancies, edge sites or they can isomorphically substitute for Mn in the octahedral layers (Burns, 1976; Lanson *et al.*, 2002; Manceau *et al.*, 2007; Peacock & Sherman, 2007a).

Mineral synthesis is a useful approach in modelling the association of trace metals and mineral phases in the natural environment. Birnessite and buserite can be synthesised under laboratory conditions, which is useful in understanding the sorption behaviours of trace metals in phylломanganates as has been shown in the previous works (Drits *et al.*, 1997; Golden, 1987; Kuma *et al.*, 1994; Yin *et al.*, 2014).

In the previous chapter (chapter 4), the host phases of metals in (natural) nodule samples were investigated by sequential leaching. The results show that some of the metals such as the REYs occupy the interlayers of the phylломanganates. In this chapter the association of interlayer cations including the REYs with the phylломanganates is

investigated using mineral synthesis approaches. Based on this, a 7 Å phyllomanganate (Na-birnessite) was synthesised under laboratory conditions and sorbed with different cations. The ability of the cations to replace Na and occupy the interlayers was then investigated. Based on the leaching results in the previous chapter, some of the metals leached with dilute HCl which are therefore associated with the phyllomanganates, should be able to replace Na and hence occupy the interlayer space. Furthermore, the cation experiments using REYs (La, Nd and Yb) were used to study the sorption preferences of phyllomanganates for LREE and HREE.

5.2 Materials and method

5.2.1 Synthesis of Na-birnessite

Na-Birnessite was prepared following the method by Golden (1987) with some modifications. A 50 ml 0.5 M MnSO_4 solution was prepared in a 600 ml beaker and O_2 gas was bubbled through the solution at a rate of ≥ 1.5 L/min on a glass frit. Chilled (7 °C) 100 ml of 5.5 M NaOH was added quickly to the MnSO_4 solution, with subsequent continued oxygenation for 5 hours. The suspension was then let to sit overnight before the precipitates were washed three times with ultra-pure water. The washed residues were then separated into three fractions, these are: (1) oven dried at 40°C (48 hrs); (2) oven dried at 105°C (48 hrs), and (3) freeze dried. The thus-produced Na-birnessite was characterized by SEM and XRD. A schematic of this method can be found in Appendix III.

5.2.2 Cation hydration experiments

Thirty milligrams of the synthesised freeze dried Na-birnessite was soaked in 20 ml each of 1 M of MgCl_2 , CaCl_2 , CoCl_2 , CuCl_2 , LaCl_3 , NdCl_3 , YbCl_3 and a combination of LaCl_3 , NdCl_3 , YbCl_3 ($\text{La}+\text{Nd}+\text{Yb}$), where REE = a solution containing 4 ml each of 1 M LaCl_3 , NdCl_3 , YbCl_3 . Cation hydration was carried out for 44 hours at room temperature with occasional shaking. Hydrated residues were then washed three times with ultra-pure water and dried at 40°C for 48 hours. The dried cation-hydrated birnessites were characterized by XRD and SEM.

5.2.3 Analytical techniques

5.2.3.1 XRD

All samples were finely ground using an agate mortar and pestle, prior to random orientation of the sample on a silicon disc and subsequent examination using XRD, using a Philips X'Pert pro XRD machine at the National Oceanography Centre, University of Southampton (<https://www.southampton.ac.uk/>), operated by Dr. Richard Pearce. Samples were run using a Cu X-ray tube and the following setup conditions; 35kV, 40mA, automatic slits and a step size of $0.02^\circ 2\theta$ at 3 seconds/step. The background counts of the pattern traces are typical for automatic slits, which maintain the size of the irradiated area, as compared with fixed slits, in which the irradiated area reduces progressively with higher X-ray incidence angles, as does total X-ray counts.

5.2.3.2 SEM

Detailed analysis for morphological and chemical composition was performed on a JEOL 7001 FEG SEM instrument at the Plymouth University Electron Microscopy Centre. The microstructures were imaged using both a secondary detector and a backscatter electron detector. Elemental compositions were determined using Energy Dispersive X-ray Spectroscopy (EDS; Oxford Instruments, Abington, UK) combined with Aztec Energy software. Sample grains were scanned using a focussed electron beam produced by a Schottky field emission gun at accelerating voltage of 5 – 20 kV, a probe current of 10 nA and a working distance of 10 mm.

5.3 Results

5.3.1 Na-birnessite

The synthesised Na-birnessite has a platy morphology with rosettes of hexagon-shaped flakes aggregated together, which are oriented in different directions (Figure 5.1a). Chemical compositions obtained before and after substitution shows that exchanges were successful, the spectrum of REE-doped phyllosilicate is shown as an example (Figure 5.2). Using EDS analysis of four sample points, a mean value of 89% of Na cations were exchanged by La+Nd+Yb cations with their exchange capacity in the order Yb>Nd>La. A value of 89% was also obtained for Nd exchanged birnessite using EDS composition analysis of five points.

SEM-EDS images obtained before and after cation exchange shows that the platy birnessites appear less crystalline after cation exchange. The platy morphology is still present in the exchanged-phyllosilicates but some of the plates aggregate as lumps

and become merged together, and the edges are not very clear in some cases, for example after-exchange images with Cu and La+Nd+Yb (Figure 5.3). The straight hexagonal edges of the platy crystals is lost in some cases after cation exchange and the edges are slightly rounded and twisted, this can be observed in the zoomed-in image of the exchanged La+Nd+Yb birnessite (Figure 5.4).

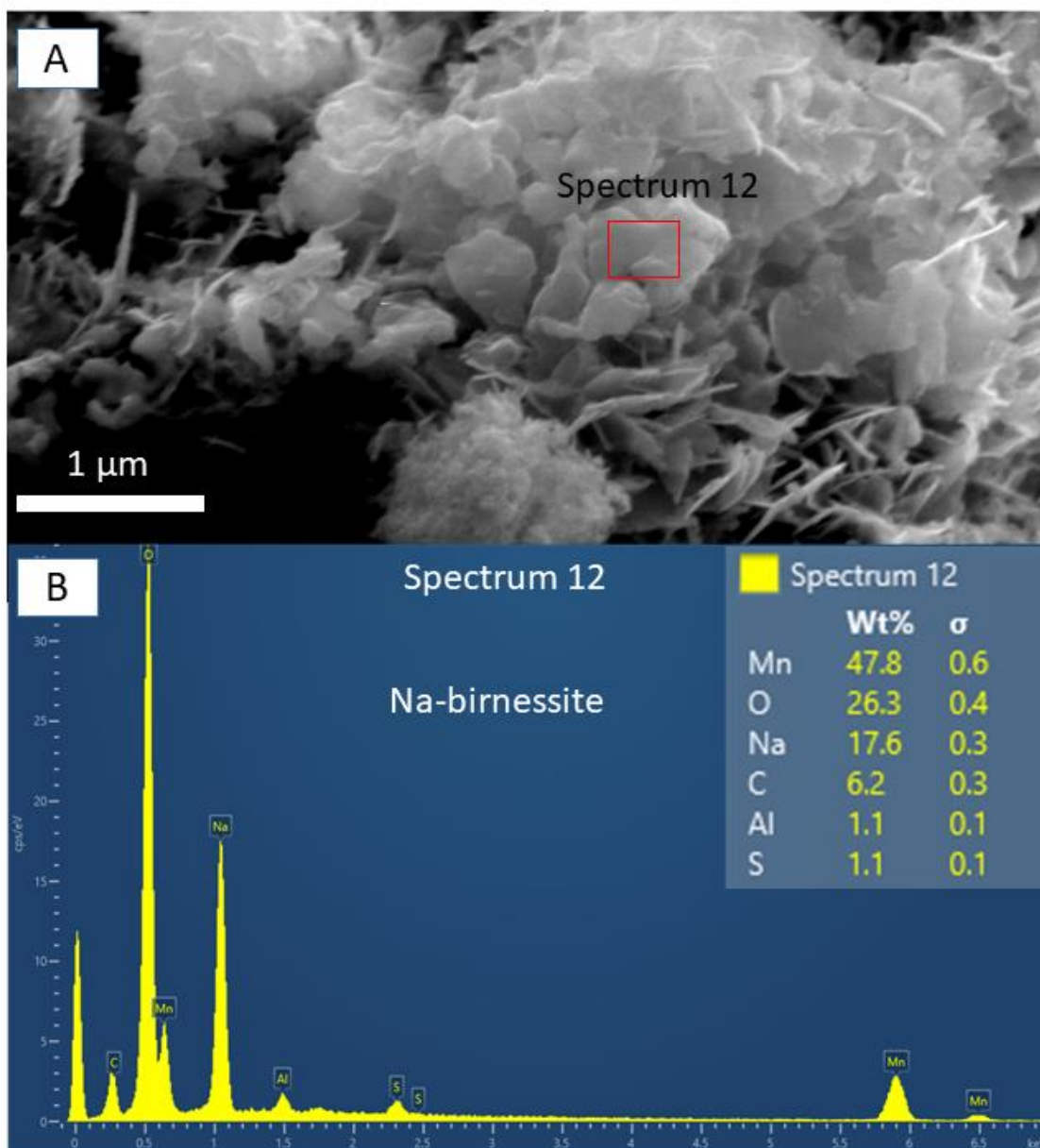


Figure 5.1. SEM-EDS image of synthetic Na-birnessite (image a). The synthesised phyllo manganese is crystalline and has platy morphology with rosettes of hexagonal shaped crystals. The composition of the Na-birnessite is confirmed by SEM-EDS point analysis (area shown inset in image a), spectrum is shown in image b.

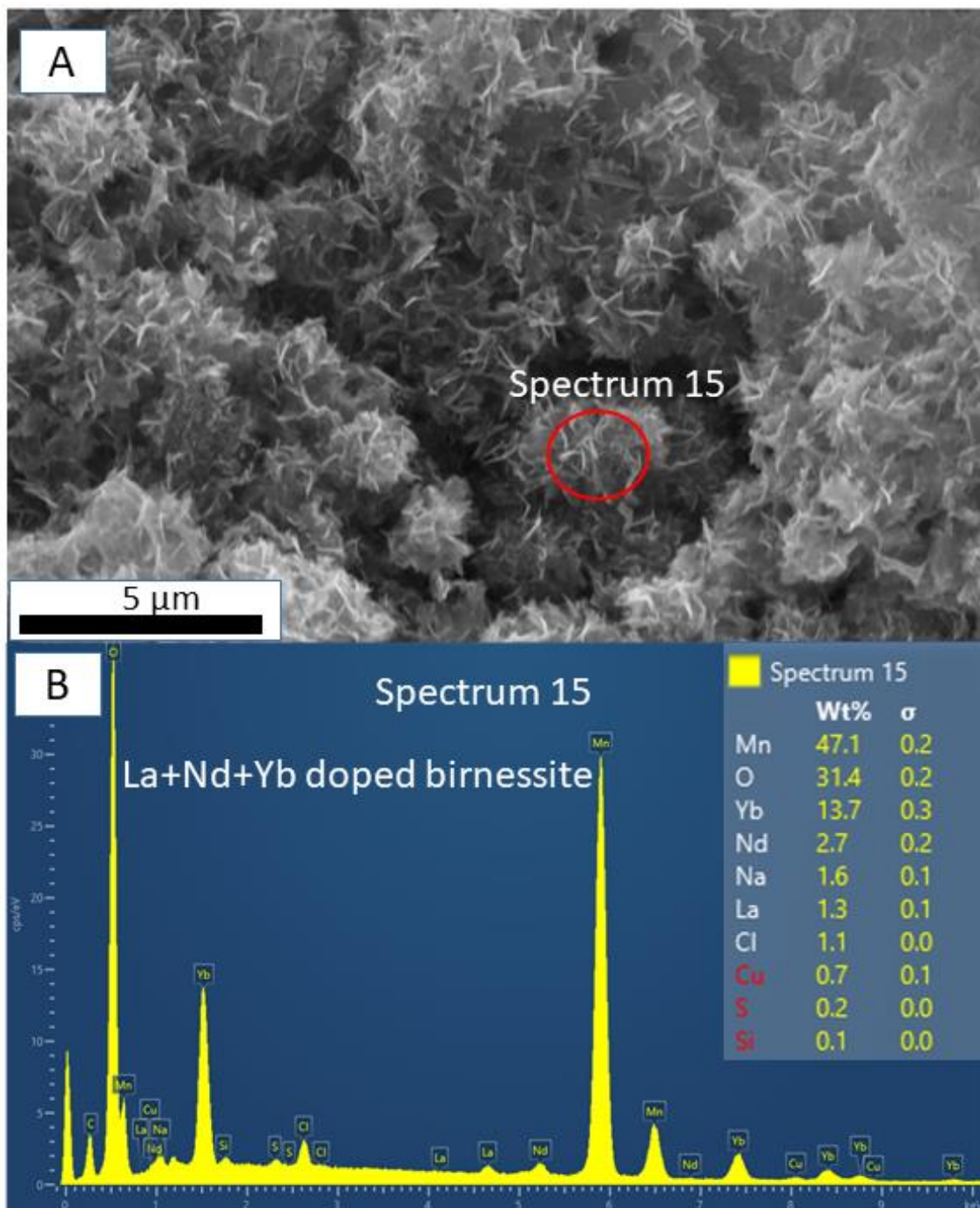


Figure 5.2. SEM-EDS image of synthetic La+Nd+Yb doped birnessite (image a). The synthesised phyllo-manganate is crystalline and has platy morphology with rosettes of hexagonal shaped crystals. The composition of the REY-birnessite is confirmed by SEM-EDS point analysis (area shown inset in image a), spectrum is shown in image b. The EDS spectrum shows that some of the Na still remain after the exchange and the La+Nd+Yb exchanged birnessite shows exchange capacity in the order: Yb>Nd>La.

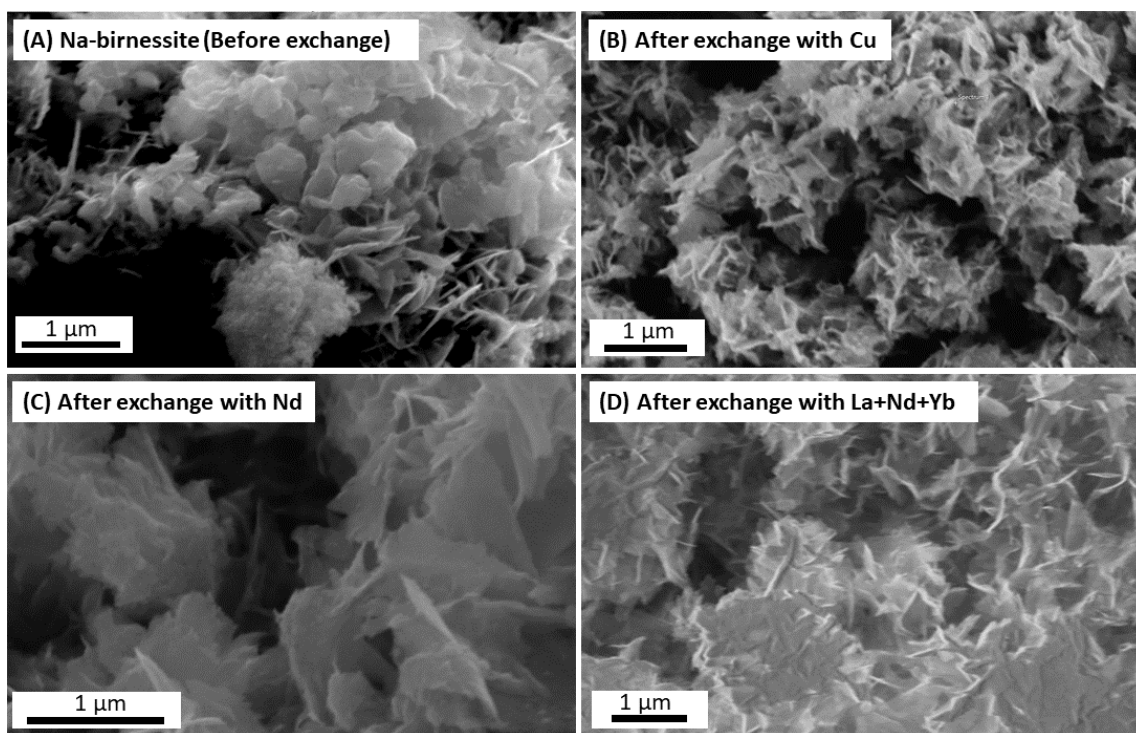


Figure 5.3. EDS images and spectra of Na-birnessite before cation exchange (a) and after exchange with Cu (b), Nd and La+Nd+Yb cations (c and d). Note that the platy birnessites are less crystalline after the exchanges compared to the Na-birnessite precursor mineral.

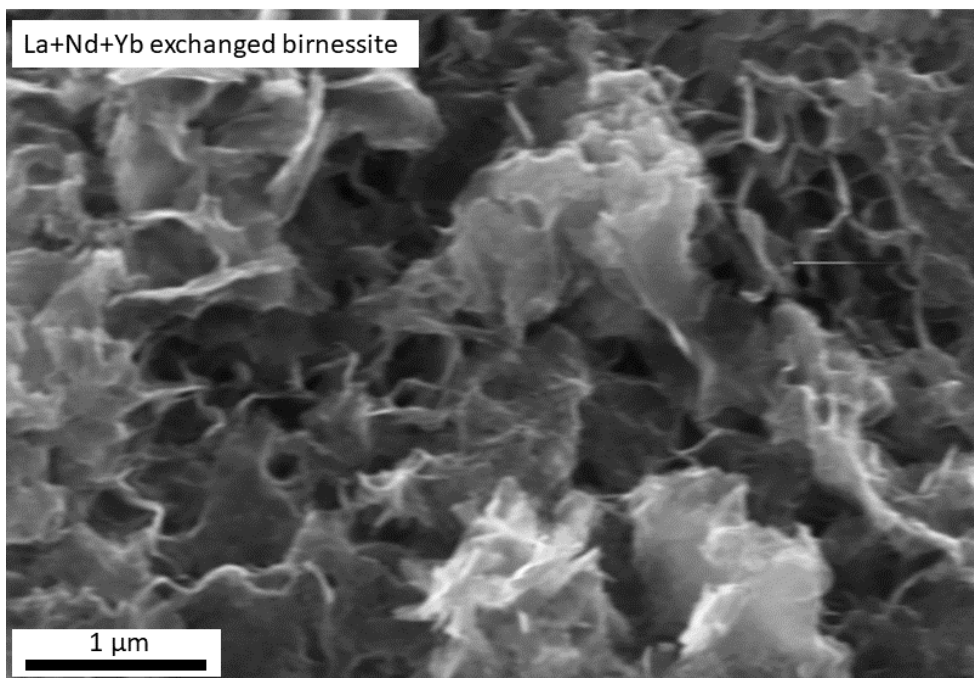


Figure 5.4. La+Nd+Yb birnessite after cation exchange. Note that the platy birnessite crystals are slightly rounded and twisted on the edges compared to the original Na-birnessite (Figure 5.1).

The interlayer basal spacings (001) of the cation-exchanged birnessites are shown in Table 5.1. The XRD patterns of the synthesised Na-birnessite before and after cation exchange are shown in Figure 5.5 and Figure 5.6. The changes in the patterns in terms of the intensity, broadness/sharpness and position of peaks after the cation exchange compared to before exchange shows that the Na birnessites were modified to some degree during cation exchange with Na being substituted by the cations. The Na-birnessite gave basal spacings characteristic of a 7 Å phyllomanganate (typical for birnessite) with sharp peaks at 7.09 Å and 3.56 Å and broad peaks at 2.50, 2.43 and 2.15 Å. With the exception of Mg, all the cation exchanged birnessites gave basal interlayer spacing of ~7 Å. The REE exchanged birnessites gave broad peaks at ~7 Å with reduced intensities compared to the Na birnessite. The peak reflections of the Co exchanged birnessite are weak possibly due to precipitate formation (CoO) during the substitution reaction. Another possibility is that Co destroyed the crystallinity, making it more turbostratic or even amorphous. The XRD pattern, however, clearly shows a basal interlayer spacing of ~7 Å. The Mg-doped birnessite showed sharp peaks at 9.66 and 4.84 Å; these peaks are the first and second order basal reflections of 10 Å phyllomanganates such as buserite (Arrhenius, 1981).

Table 5.1. The interlayer spacings of the exchanged phyllosulfates. (Note: nd = not determined)

Cation exchanged	EDS remaining Na after exchange	Percentage exchange (%)	Interlayer spacing d (001) (Å)
Ca	nd	nd	7.10
Mg	nd	nd	9.66
Cu	nd	nd	7.13
Co	nd	nd	7.25
La	nd	nd	7.13
Nd	Yes	89	7.13
Yb	nd	nd	7.22
La+Nd+Yb	Yes	89	7.24

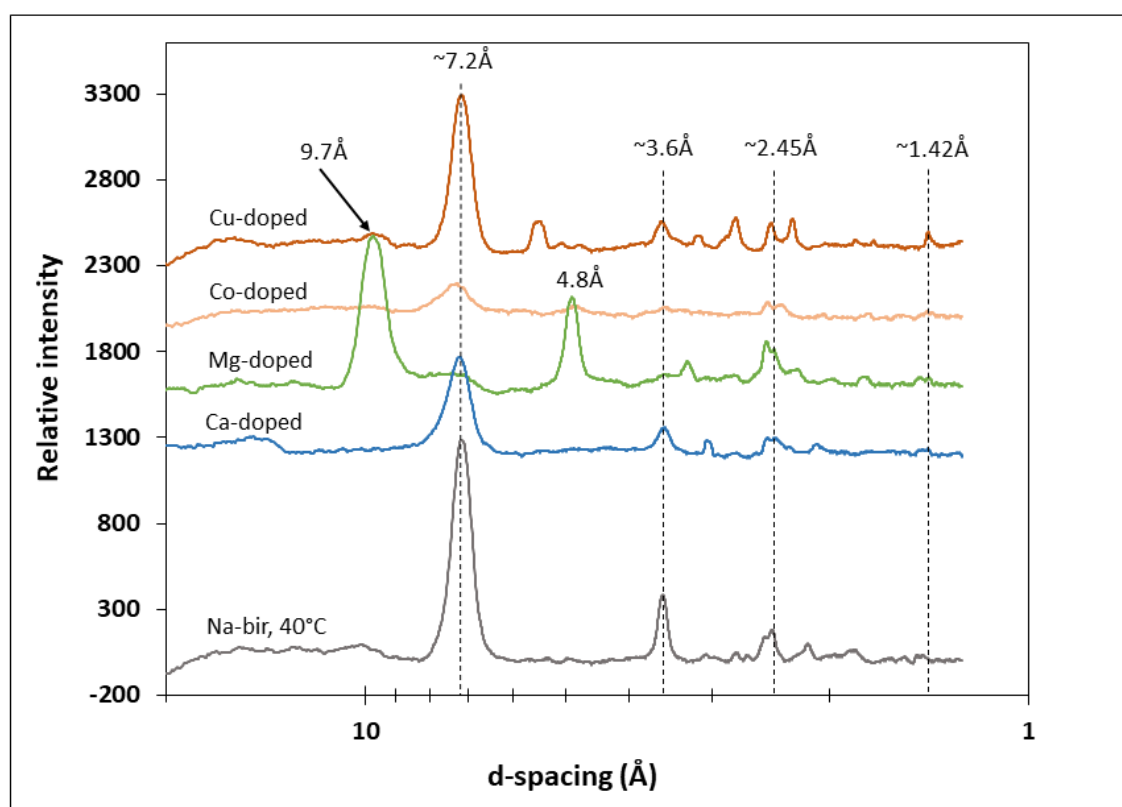


Figure 5.5. XRD patterns for Na-birnessite before cation exchange and after exchange with Ca, Mg, Cu and Co. Patterns shown with background subtracted and with regular vertical offsets for clarity.

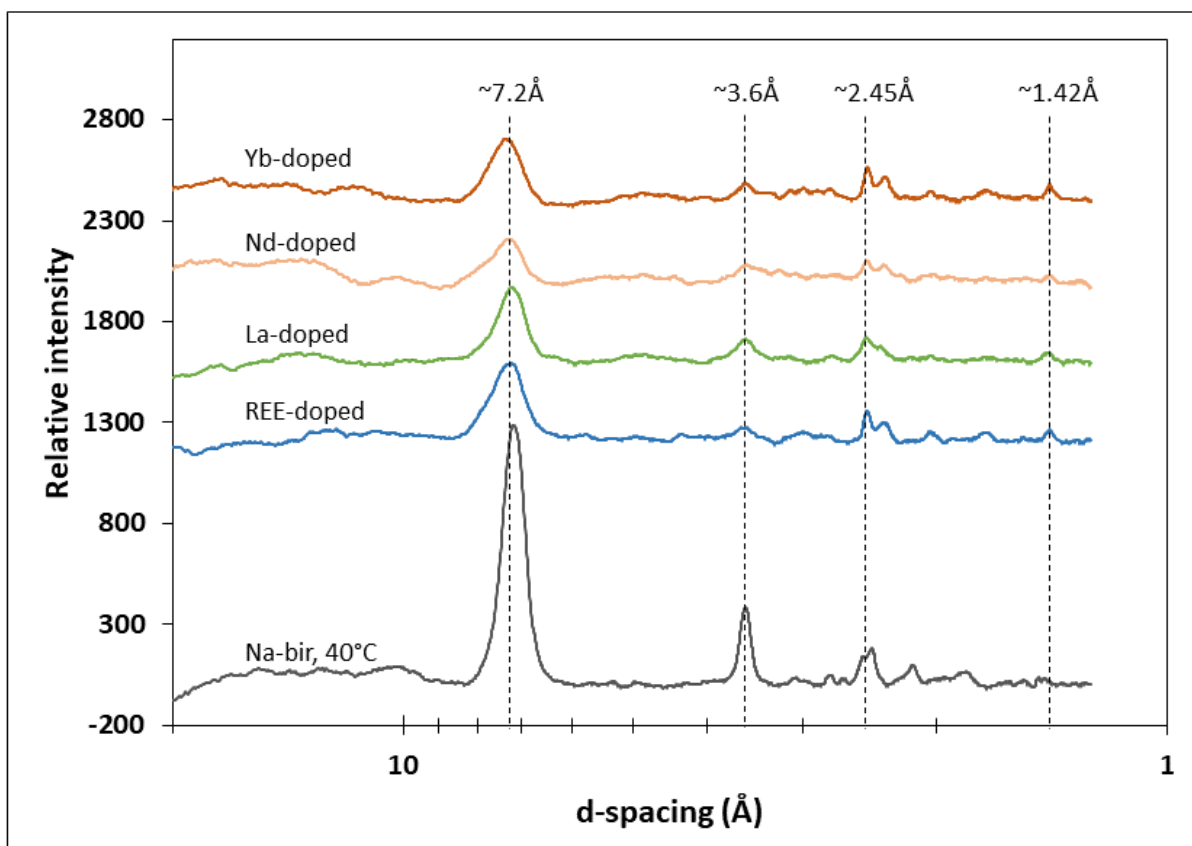


Figure 5.6. XRD patterns for Na birnessite before cation exchange and after exchange with the rare earth elements (Note: REE-doped = La+Nd+Yb combined). Patterns shown with background subtracted and with regular vertical offsets for clarity.

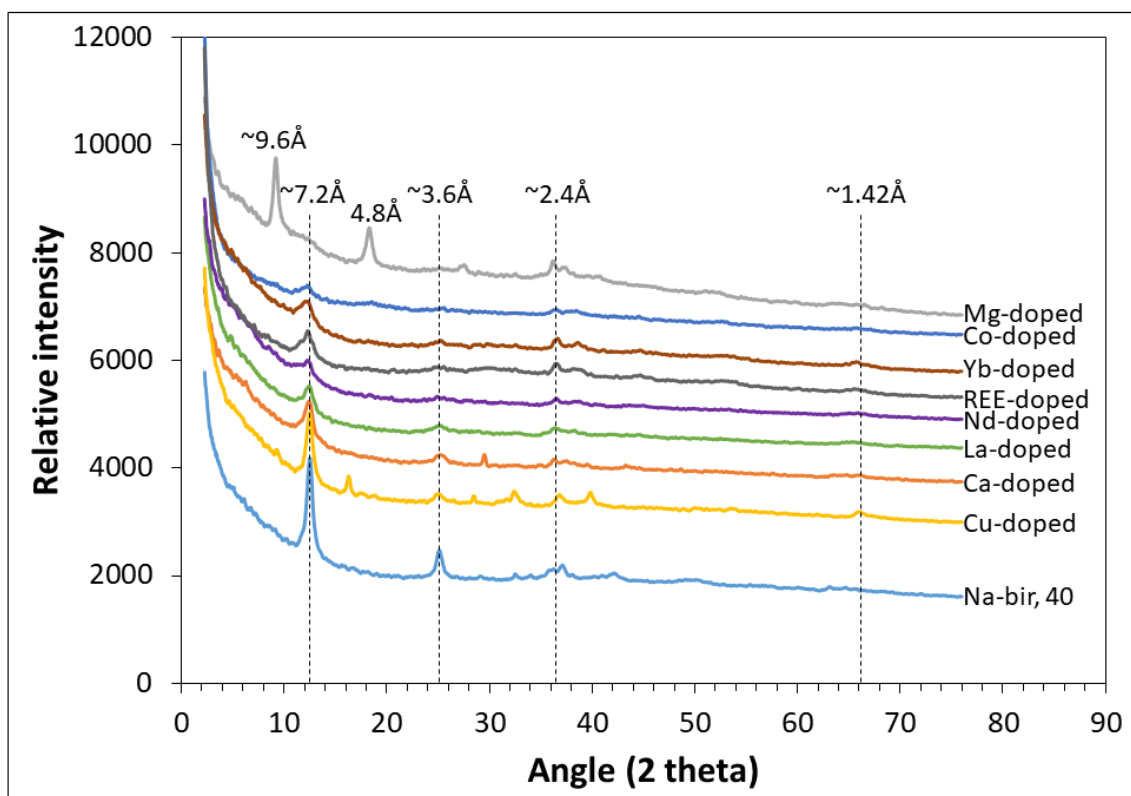


Figure 5.7. XRD patterns (without background correction) for Na birnessite before and after cation exchange and plotted against 2 theta angle. The curves are plotted using the same intensity scale, but the scale only applies to the lower curve, and the curves are stacked by using a y-axis off-set for the upper spectra.

5.4 Discussion

The interlayer water in phyllosulfates is said to be strongly bound to the interlayer cations, and therefore, plays an important role in their stability (Johnson & Post, 2006). The interlayer spacing of phyllosulfates can either accommodate a single or a double layer of water molecules and thus enables phyllosulfates to go back and forth; swelling and collapsing between the two phases. The interlayer spacing in phyllosulfates is related to the hydration energy of the cations in the interlayer spaces, which itself, depends on the size and charge of the cation. These parameters are also said to control the bonding strength between the cations and the water molecules in the interlayer spacings, which is directly related to the temperature at which a 10 Å phyllosulfate can become dehydrated and collapse to the 7 Å phase (Johnson & Post, 2006). The ionic radii and hydration energies of the cations studied in this work are shown in Table 5.2. Cations with high hydration energies tend to be associated with the expanded 10 Å phyllosulfate while cations with lower hydration energies are associated with the 7 Å phase. Few metals have been used in cation substitution experiments of the phyllosulfates by previous workers. In most cases the alkali, alkali earth, and some transition metals (Mn, Co, Ni, Cu, Zn, La, Pb) have been studied in these experiments (Drits *et al.*, 2002; Golden, 1987; Johnson & Post, 2006; Kuma *et al.*, 1994; Paterson, Bunch & Clark, 1986; Yin *et al.*, 2014). These studies have shown that most of the cation-exchanged product exist in the 10 Å phase when in suspension or when moist, and some collapse to the 7 Å phase after drying in air or elevated temperatures. Some cations have been reported to be able to exist in the 7 Å phase in both suspension and in air (K, Cs, Ba) (Paterson, Bunch & Clark, 1986).

Table 5.2. Ionic radii and hydration energy values for REE and other cations [values for monovalent and divalent cations are obtained from Rosseinsky (1965), values for REEs are obtained from Moldoveanu and Papangelakis (2013)]. The interlayer spacings by previous workers from cation exchange experiments of air-dried exchanged synthetic birnessite/buserite are also included for comparison. (Note: nd = means no data).

Substituent cation (charge)	Ionic radius Å	Hydration energy kcal./mol	Interlayer spacing (Å) (Kuma <i>et al.</i> , 1994)	Interlayer spacing (Å) (Golden, 1987)	Interlayer spacing (Å) (Johnson & Post, 2006)	Interlayer spacing (Å) (Paterson, Bunch & Clark, 1986)	Interlayer spacing (Å) (This work)
Na(+1)	0.95	98	7.13	7.1	7.24	7.1	7.09
Ca(+2)	0.99	381	9.98	~10	9.96, 7.31	9.9	7.10
Mg(+2)	0.65	456	9.61	~10	9.49, 7.04	9.6	9.66
Cu(+2)	0.82	499	nd	nd	nd	7.1	7.13
Co(+2)	0.74	478	nd	nd	nd	9.5	7.25
La(+3)	1.15	758	nd	~10	nd	nd	7.13
Nd(+3)	0.99	817	nd	nd	nd	nd	7.13
Yb(+3)	0.86	888	nd	nd	nd	nd	7.22

The XRD patterns of the cation-exchanged birnessites at ambient atmospheric water vapour pressure showed that only the Mg-exchanged phylломanganate has an interlayer spacing of ~10 Å. This result is consistent with previous reports, which has been attributed to the small ionic size of Mg (Golden, 1987; Johnson & Post, 2006; Kuma *et al.*, 1994). The fact that the Mg-exchanged product was able to retain the 10 Å phase after drying at 40°C shows that it forms the most stable exchanged product. In contrast, the Ca-exchanged product gave a basal spacing characteristic of the 7 Å phase. Previous reports show that both the Mg- and Ca-exchanged phylломanganates are able to retain the 10 Å phase after drying in air (Golden, 1987; Johnson & Post, 2006; Kuma *et al.*, 1994; Paterson, Bunch & Clark, 1986). They demonstrated that the 10 Å phase only collapses to the 7 Å phase after drying at temperatures greater than 50°C or under vacuum or in some cases both phases are present, which also happens if the products

are partially moist. In this study, however, the Ca-substituted phyllomanganate gave a basal spacing characteristic of a 7 Å phyllomanganate. This contrasting behaviour to previous reports shows that the Ca-exchanged phyllomanganate obtained in this study is less stable in terms of its bonding with the interlayer water molecules. It is likely that the exchanged product initially formed a 10 Å phyllomanganate and then collapsed to the 7 Å phase when dried at 40°C. In marine ferromanganese nodules Mg is associated with the 10 Å vernadite and todorokite. Its hydrated diameter of 8.6 Å fits the interlayer spacing, which stabilizes the phyllomanganate structure. This later undergoes a topotactic transformation to the tectomanganate todorokite with the Mg ions acting as spacers between the pillars of the transformed octahedral sheets, thereby stabilizing it (Manceau, Lanson & Takahashi, 2014). On the other hand, Ca can be associated with both phyllomanganate phases occurring as interlayer cations (Drits *et al.*, 1997; Usui & Mita, 1995). Terrestrial busserites which generally contain high proportion of Ca in the interlayers, collapsing to the 7 Å phase upon dehydration, have also been reported by Usui and Mita (1995). The Co-exchanged birnessite gave a basal spacing characteristic of the 7 Å phase. The hydration energy of Co is much higher than that of Mg and therefore, might preferentially be associated with the interlayers of the 10 Å phase as reported by Paterson, Bunch and Clark (1986). The study by Paterson, Bunch and Clark (1986), however, reported that the Co-exchanged busserite collapsed to the 7 Å phase in a vacuum. This shows that the (likely) transformation of the Co-exchanged busserite to Co-birnessite in this study has to do with the stability of the interlayer Co and water molecules.

The other exchanged products, Cu, La, Nd, Yb and La+Nd+Yb (combined) birnessites, gave interlayer spacings of the ~7 Å phase. The hydration energies of these cations are

all higher than that of Mg, and therefore, theoretically should be associated with the 10 Å phase. Previous work by Paterson, Bunch and Clark (1986) showed that the wet Cu-exchanged product initially formed both the 10 and 7 Å phyllosulfates and only the 7 Å phase when air-dried. Similarly, (Golden, 1987) demonstrated that La-exchanged birnessite exists in the 10 Å phase after being air-dried (measurements of wet products were not carried out in this study). It is likely that in this study, the exchanged products initially formed the 10 Å phase and collapsed to the 7 Å phase after drying, losing a layer of interlayer water in the process (similar case to Ca). Another possibility is that the layer structures were not completely expanded during exchange as suggested by Johnson and Post (2006). However, this explanation can be ruled out because for this to happen the XRD patterns should show the presence of both phases (Johnson & Post, 2006), which was not the case in this study. Therefore, it seems that the rare earth exchanged birnessites in this study are unstable at temperatures up to 40°C, resulting in their collapse to the 7 Å phase. The EDS composition analysis also showed that La, Nd and Yb are also not fully effective in replacing Na; the exchange capacity obtained for Nd and La+Nd+Yb was 89%. The order of exchange capacity of these rare earths decreases in the order Yb>Nd>La. This is in agreement with a previous report by Golden (1987) that La is not effective in replacing Na and the exchange capacity obtained for La in that work was 45%. The trend for these rare earths therefore, indicates that the smaller cations are more easily hydrated (hence higher hydration energies) and they are more effective in substituting Na in the interlayers compared to the larger cations with lower hydration energies.

By comparing the past results with the ones obtained from this study, it seems that whether a dried cation-exchanged phyllosulfate product exists in the 10 or the 7 Å

phase depends on its interlayer stability, which is controlled by the bonding between the interlayer cation and the water molecules. Exchanged products with the most stability are able to retain the 10 Å interlayer spacing upon drying in air, up to 105°C and in a vacuum, while the less stable products collapse to the 7 Å phase. Some authors consider that there are two forms of the 10 Å vernadite (disordered buserite): the first is thermally unstable 10 Å vernadite which collapses between room temperature and 100°C, the second is thermally stable 10 Å vernadite which collapses between 100 and 300°C (Manceau, Lanson & Takahashi, 2014; Pal'chik, Grigor'eva & Moroz, 2013; Wegorzewski *et al.*, 2015). The structural models of the buserites are shown in Figure 5.8. The thermally unstable buserite transforms to 7 Å upon dehydration while the thermally stable buserite contains a high amount of interlayer cations above vacancy sites which prevent it from collapsing to the 7 Å phase. Cation experiments by Wegorzewski *et al.* (2015) using natural samples showed that nodules with higher interlayer cation exchange ability seem to contain higher proportions of thermally unstable phylломanganates compared to nodules with low exchange capacity. Following on from that, it is likely that the REE cation exchanged phylломanganates obtained in this study initially formed the thermally unstable buserite, which then collapsed to the 7 Å birnessite. This makes sense considering the fact that under laboratory conditions only low proportions of cations are probably exchanged compared to under natural conditions where the proportions are much higher and more than one type of cation exists in the interlayers which prevent the collapse. Wegorzewski *et al.* (2015) suggested that the different thermal stability and cation exchange ability of phylломanganates is probably due to different amounts and types of cations and how they are incorporated

in the structure, possibly as inner or as outer sphere complexes or being incorporated within vacancies of the MnO_6 octahedra.

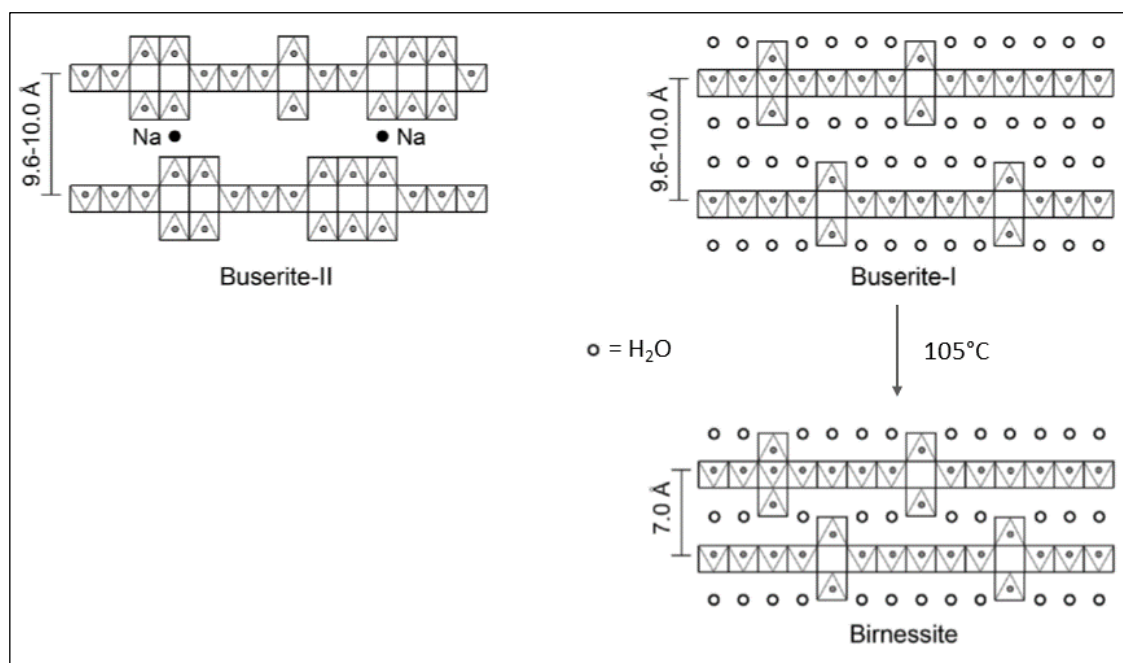


Figure 5.8. Schematic of the structural models of the two types of 10 Å buserite. The thermally unstable buserite-I loses one layer of water and collapses to 7 Å birnessite in air, upon heating to 105°C or in vacuum. The thermally stable buserite-II contains high proportions of interlayer cations above vacancy sites which prevent it from collapsing to birnessite. The models are adapted from Pal'chik, Grigor'eva and Moroz (2013).

The cation exchanged phylломanganates obtained in this study are comparable to their natural analogues. The broadening of peak reflections and reduction in peak intensities of the exchanged products indicate that the products are less crystalline (e.g., more turbostratic) after the exchange, due to disordering of the phylломanganate structures. A composite XRD pattern created by (mathematically) combining the individual patterns of the Mg and Ca exchanged phylломanganates in the ratio of 5.1 (based on the Mg/Ca ratio of modern open ocean water which ranges from 4.9 to 5.3 mol:mol; Lebrato *et al.*

(2020)) closely matches that of the natural nodule samples from the study area (Figure 5.9). This indicates that the cation-exchanged phyllomanganates are similar in mineralogy to the natural samples, and that the exchanged products are essentially vernadites, with their broad and somewhat subdued peaks compared to the Na-birnessite precursor mineral.

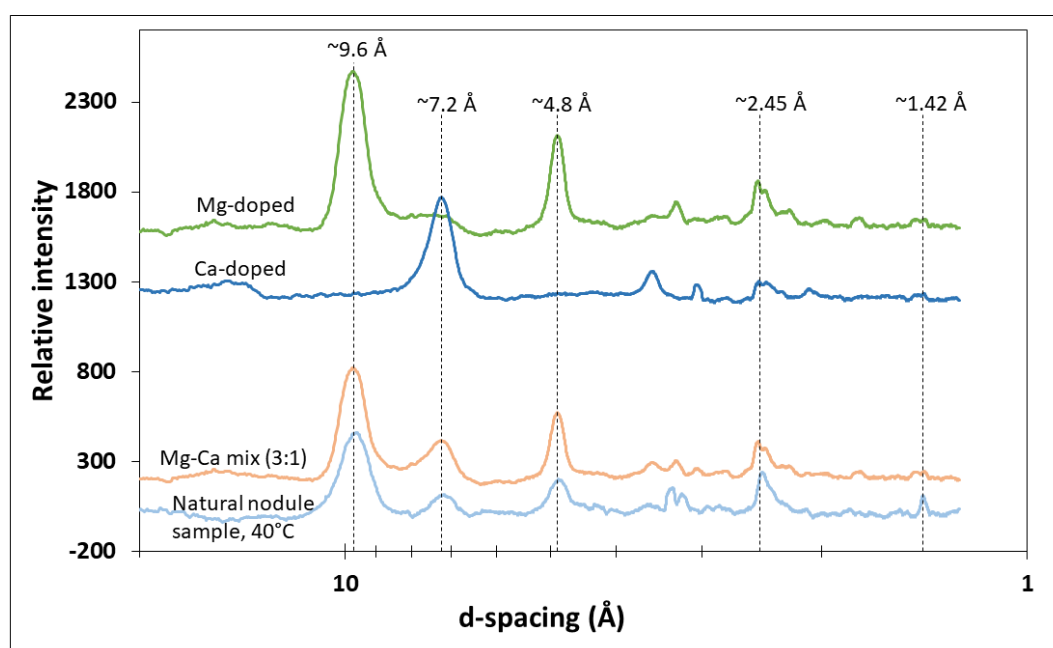


Figure 5.9. Comparison between the XRD patterns of a natural nodule sample (dried at 40°C) and that of a combined Mg-doped and Ca-doped synthetic phyllomanganate (Mg-Ca mix). The individual patterns of both Mg- and Ca-doped phyllomanganates (shown in graph) were combined in the ratio 5:1 based on their ratio in seawater. Note that the samples (natural and synthetic) were dried in the same way (40°C for 48 hours) so that they are directly comparable. The curves are plotted using the same intensity scale, but the scale only applies to the lower curve, and the curves are stacked by using a y-axis off-set for the upper three patterns.

5.5 Conclusion

The results from this study shows that the thermal stability of phyllomanganates, which is related to the size and hydration energy of the interlayer cation and the structure of the phyllomanganate, controls whether a cation-exchanged phyllomanganate exists in the 7 or the 10 Å phase. Only the Mg-exchanged product gave basal spacings characteristic of the 10 Å phase which shows that it formed that most stable product after dehydration at 40°C. The rest of the cation (Ca, Cu, Co, La, Nd, Yb) exchanged products gave interlayer spacings of the 7 Å phase. The exchange capacity of the La, Nd and Yb increases with decreasing cationic size (and increasing hydration energy) with Yb more effective in replacing Na than La. The replacement of interlayer Na by REEs in synthetic birnessite is fully consistent with the results from leaching experiments discussed in the previous chapter, which showed that REE were not adsorbed onto manganese surfaces, but were nonetheless easily leached with 0.5 M HCl, which led to the suggestion that they were hosted in the interlayers. Importantly, the experiments also provide an explanation as to how phyllomanganates can efficiently fractionate LREE from HREE, and why they have a greater affinity for the smaller HREE than for the larger LREE cations. This in turn explains why polymetallic nodules have a much higher proportion of valuable HREE compared to most land-based REE-deposits.

The phyllomanganates synthesised in this work are generally thermally unstable (Pal'chik, Grigor'eva & Moroz, 2013); in natural samples, the thermally stable phases with higher proportions of interlayer cations may be more abundant. Therefore, it is possible that in natural phases, the REEs can exist in the interlayers of the 7 Å phase or the thermally stable 10 Å phase or in both. The XRD patterns of the cation-exchanged phyllomanganates are very similar to those of the natural samples. The broad and

reduced intensity peak reflections are similar to that of the vernadites in natural samples and indicates that the products underwent some degree of structural disordering during cation exchange. The peaks are however, less broadened compared to the natural phases which is probably because in natural samples there are more than one type, as well as different proportions of interlayer cations compared to the synthetic phases from this study.

Chapter 6

6 Nd and Sr isotopic composition in the individual layers of a nodule sample

6.1 Introduction

Deep-sea polymetallic nodules are important archives for trace metal isotopes such as Nd and Sr, which are powerful tracers for past and present ocean processes such as seawater mixing and circulation patterns (Freslon *et al.*, 2014; Ito & Komuro, 2006; Tachikawa, Piotrowski & Bayon, 2014). In nodules, these tracers can be used to study nodule genesis as well as the source of the metals enriched in the nodules. Nd hosted in solid authigenic phases such as ferromanganese deposits are immobile and therefore, can provide a moderately long-term (c. 1-10 Ma) record of regional oceanographic parameters (Amakawa *et al.*, 2017). Nodules from the Clarion-Clipperton Fracture Zone (CCFZ) are mixed-type nodules that are made up of individual hydrogenetic and diagenetic layers. These two layer types are from two different sources; oxic bottom seawater (hydrogenetic) and suboxic/oxic pore waters. Therefore, the metals enriched in these individual nodule layers are expected to reflect the type of fluid they were sourced from (seawater or pore water).

Sr has an intermediately long residence time in the oceans (in the order of several millions of years) and is well mixed. The main sources are continental weathering material, release by hydrothermal sources, and dissolution of marine carbonates; Sr isotope ratios of water and marine precipitates are used to constrain paleo-circulation

and inputs of weathered material into the ocean (Frank, 2002). The $^{87}\text{Sr}/^{86}\text{Sr}$ isotope ratio of the oceans has steadily increased over the last 35 Ma, possibly due to the rise of the Alpine-Himalayan mountain belt shedding continental material enriched in radiogenic ^{87}Sr (riverine input has typical high $^{87}\text{Sr}/^{86}\text{Sr}$ of 0.7119), and the present-day value of seawater is well constrained at 0.709175 (McArthur, Howarth & Shields, 2012). In contrast, Nd has a shorter oceanic residence time (600-2000 years), shorter than the global mixing time of the ocean, and is mainly derived from weathering and erosion of continental crust (Frank, 2002). Nd isotope ratios are often considered as showing conservative behaviour in seawater, i.e., oceanic water masses acquire distinctive isotopic signatures, which are then only modified by mixing (Piepgras and Jacobsen, 1988; Frank, 2002; Abbott et al., 2015; Haley et al., 2017). The Nd isotopic signature of water masses is mainly controlled by riverine and aeolian input into the oceans, and hydrothermal input (e.g., from mid-ocean ridges and seamounts) is considered much less significant because of precipitation of Nd very close to these hydrothermal sources (Frank, 2002). Nd isotopic ratios are generally expressed in epsilon notation: The Nd isotopic value (ϵ_{Nd}) is defined as $[(^{143}\text{Nd}_{\text{sample}}/^{144}\text{Nd}_{\text{sample}})/(^{143}\text{Nd}_{\text{CHUR}}/^{144}\text{Nd}_{\text{CHUR}}) - 1] \times 10^4$, where CHUR is the chondritic uniform reservoir, used as an average Earth value ($^{143}\text{Nd}/^{144}\text{Nd} = 0.512638$) (Jacobsen & Wasserburg, 1980).

Relevant for the present study is the mean ϵ_{Nd} for North Pacific seawater of -3.9; values are generally higher (c. -3.0) for shallower water, and lower (down to -5) for the deepest parts of the Western Pacific (Lacan et al., 2012). Piepgras and Jacobsen (1988) found ϵ_{Nd} -3.3 to -3.8 for deep bottom waters in the Eastern North Pacific. Abbott et al. (2015) after Haley et al. (2014) distinguished two distinct water masses in the Northern Pacific:

North Pacific Deep Water (NPDW, 3000 m depth, $\epsilon_{Nd}=-3.5$) and North Pacific Intermediate Water (NPIW, 240 m depth, $\epsilon_{Nd}=-3.0$).

The assumption of strictly conservative behaviour of Nd has been challenged by some studies which found evidence for a significant 'benthic flow' of Nd in parts of the oceans close to continental margins (e.g., Abbott et al., 2015). Abbott et al. (2015) showed that Nd isotope ratios of deep bottom waters in an area in the Northern Pacific at 44°N differed from the expected value of NPDW, and approached those of the underlying sediments at the seafloor, and pore-fluids within those, suggesting release of Nd from the pore-fluids modifying the Nd isotope ratio of the water mass.

Seafloor sediments in relevant parts of the Clarion-Clipperton Fault Zone (CCFZ) are probably mostly derived from the North American Continent. Stancin et al. (2006) presented maps with contoured ϵ_{Nd} values for clay fractions from seafloor sediments, showing values in the range -4 to -6 for the UK claim area of the CCFZ, and they concluded that these sediments are indeed mainly derived from the North American Continent. Similarly, older maps by Jones et al. (1994) show values around -6 for the clays in the area of interest, and concluded that these sediments were mainly derived as aeolian dust from North America. Jihua et al. (2005) found that clay minerals in the eastern part of their study area in the CCFZ (their study area extended from 138° to 154° W, and is therefore situated west of the UK claim areas) were predominantly derived from riverine input from North America, had ϵ_{Nd} values with a typical range of -6 to -8. Based on these studies it can be concluded that seafloor sediments of the study area can be expected to have significantly lower (more radiogenic) ϵ_{Nd} values (<-4, probably around -6) than North Pacific Deep Water (c. -3.5). Eolian dust derived from the Asian continent, which dominates the Nd isotopic composition in the western and central

northern Pacific, has an even more radiogenic isotopic signature, with ϵ_{Nd} values of -9 to -13 (Jihua et al., 2005; Stancin et al., 2006).

Given the close proximity of several volcanic seamounts, assumed to be of basaltic composition, and the thin nature of the sedimentary layer on top of Pacific basaltic ocean crust (noting that sea stacks of basalt are often exposed at the seafloor in the area (personal observation (March, 2020))), a potential Nd contribution from these basaltic rocks should also be considered, either via weathering of basaltic rock or via a hydrothermal flux. Fresh basaltic glasses from the nearest part of the East Pacific Rise between 11°45 and 15°N have ϵ_{Nd} values of +8.5 to +11.0, with compositions in off-axis seamounts extending to lower values, down to +6.0 (Castillo et al., 2000).

The question, therefore, arises whether Rare Earth Elements (such as Nd) in nodules from the study area are mainly derived from bulk oceanic water masses (e.g., NPDW, with $\epsilon_{Nd}=-3.5$) or from sedimentary pore-fluids. The Nd in sedimentary pore fluids may be derived from clay minerals with a North America provenance ($\epsilon_{Nd}<-4$), or from basaltic rocks ($\epsilon_{Nd}>+6$). Moreover, it can be hypothesised that the source of the Nd and other REE varies throughout the growth history of the nodules, especially between periods of hydrogenetic and diagenetic growth.

Previous work on the bulk Nd isotopic composition of polymetallic nodules found at the water-sediment surface from the Pacific Ocean shows that their ϵ_{Nd} values resemble that of the ambient bottom seawater and mimics distribution of abyssal water masses (Amakawa *et al.*, 2017; Goldstein & O'Nions, 1981; Mantyla & Reid, 1983). Changes in their Nd isotopic signature over time have been interpreted as resulting from shifts in the global ocean circulation with time (Abbott, Haley & McManus, 2016; Abouchami *et*

al., 1997). However, the Nd isotopic composition of nodules can be also altered by processes during early diagenesis (Abbott, Haley & McManus, 2016; Elderfield *et al.*, 1981b; Elderfield & Sholkovitz, 1987; Haley & Klinkhammer, 2003). Moreover, polymetallic nodules not only contain authigenic minerals, but also detrital minerals captured during growth, and their bulk isotopic composition is not expected to reflect the pure ambient seawater or porewater composition at the time of formation. In addition to Nd isotope ratios, Sr isotope ratios are also expected to yield information about seawater chemistry; Sr isotopic signatures in Pacific nodules are found to be very similar to present-day seawater and therefore, pointing to a seawater origin (Courtois & Clauer, 1980; Goldstein & O'Nions, 1981; Ingram, Hein & Farmer, 1990; Ito *et al.*, 1998).

In this study, the Nd and Sr isotopic compositions ($^{143}\text{Nd}/^{144}\text{Nd}$ and $^{87}\text{Sr}/^{86}\text{Sr}$ ratios) in the individual growth layers of nodule sample (AB02 BC06 N3) were measured, using a unique and novel approach developed here based on the results of the leaching experiments described in previous chapters. Instead of a conventional bulk digestion of the sample material, the method used here specifically targeted Nd and Sr within primary authigenic phyllosilicate minerals without a contribution from trapped detrital materials and or loosely adsorbed Nd and Sr from present-day seawater. This approach should therefore provide the best estimate of Sr and Nd isotope ratios within the layers at their time of formation. These are used to interpret the fluid origin of the isotopes and their ultimate provenance in the individual nodules as well as the processes associated with nodule growth.

6.2 Method

Prior to isotopic measurements, most of the Nd and Sr were isolated by several separation steps ranging from leaching to column separation. The first step is leaching which was developed from the work in chapter 4 where more than 60% of Nd (plus the rest of the REYs) are expected to be released. The second separation step is specific for Nd and Sr and was done by column separation.

6.2.1 Sample preparation

Individual nodule layers were sampled using a steel razor blade, sampling was carried out under a light microscope to aid in identifying the individual layers. Varying sample masses were obtained ranging from 20 – 200 mg. The sampled material was then pulverized using a pestle and mortar and pre-weighed prior to leaching.

6.2.2 Sequential leaching

Sample powders were rinsed with ultra-pure water by centrifuging three times, with the leachate discarded after the leaching. Sequential leaching for the separation of the REYs from the matrix was carried out on the residues in the following steps

- I. Leach 1: Exchangeable cations and Ca carbonates

3 mL of 0.1 M acetic acid/Na acetate buffered (pH 5 at 25°C) was added to a 10 mL vial containing the residues and shaken for 3 – 5 hours. The residues were separated from the leachate by centrifugation. This was repeated two more times with ultra-pure rinsing between the steps. The leachate was discarded as

it most likely contains Nd and Sr from secondary carbonate minerals, and Nd and Sr weakly adsorbed onto clay minerals and phyllosilicate minerals, which are expected to be influenced by present-day seawater rather than seawater at the time of formation of the layers.

II. Leach 2: Easily reducible fraction

0.5 mL of 0.5 M HCl was added to the residues from leach 1 and shaken for 15 minutes, the leachate was then separated from the residues by centrifugation. The leachate was transferred to a 5 mL savillex vial and dried down on a hot plate at 120°C and prepared for column separation and isotopic measurements. The Nd and Sr thus leached is most likely derived from the hydrated interlayers between octahedral manganese sheets within the phyllosilicate minerals, but not from detrital minerals trapped within nodules, as concluded in chapter 4. It is this fraction that was used for subsequent isotope analysis.

6.2.3 Scanning Electron Microscopy

Detailed analysis for morphological, textural and elemental composition was carried out using a Scanning Electron Microscopy (SEM) and performed on a JEOL 7001 Field Emission Gun (FEG) SEM instrument at the Plymouth University Electron Microscopy Centre. The polished nodule section was imaged using both secondary detector and a backscatter electron detector. Major element concentrations were determined using Energy Dispersive X-ray Spectroscopy (EDS; Oxford Instruments, Abington, UK) combined with Aztec Energy software.

6.2.4 Nd and Sr isotope analysis

Dried-down Nd and Sr leachates were sent off to Southampton University (<https://www.southampton.ac.uk/>) for analysis, and the following purification and analytical steps were carried out by local laboratory staff under the overall supervision of Dr. Andy Milton.

Nd isotope measurements were carried out using a multi-core inductively coupled plasma mass spectrometer (MC-ICP-MS, Thermo Scientific Neptune) at the University of Southampton, National oceanography Centre, Southampton. Prior to measurement, the dried down residue from the final leaching step was diluted in sub boiled 3% HNO₃, and the Nd fraction was purified from the bulk digest via ion exchange column chemistry. Nd isotopic compositions were obtained following corrections made by adjusting to a $^{146}\text{Nd}/^{144}\text{Nd} = 0.7219$ and a secondary normalization to $^{142}\text{Nd}/^{144}\text{Nd} = 1.141876$ (Vance & Thirlwall, 2002). Replicate measurements (six over 2 years) of the JNdi-1 reference standard (Tanaka *et al.*, 2000) as an unknown gave reproducible results with a mean value of 0.51211 ± 0.000006 (2 SD).

Sr separation for isotopic analysis was carried out by column chemistry using Sr-sec resin. Measurement of Sr isotopes was performed on a Thermo Scientific Triton Thermal Ionization Mass Spectrometer at the University of Southampton, National Oceanography Centre, Southampton, using a static procedure with amplifier rotation (on an ^{88}Sr beam of $> 2\text{V}$). Fractionation was corrected using an exponential correction normalized to $^{86}\text{Sr}/^{88}\text{Sr} = 0.1194$. A long-term value of 0.710249 ± 0.000022 (2 SD) was obtained for the instrument accuracy measurements on a NIST 987 reference standard (334).

6.3 Results

6.3.1 Sample description

Details of sampling location and descriptions of nodule sample AB02 BC06 N3 are given in Table 6.1. The original image of nodule sample AB02 BC06 N3 is shown in Figure 6.1. Part of the sample was chipped off and the individual layers sampled while part of it was imaged using SEM.

Table 6.1. Location and description of nodule sample (AB02 BC06 N3) used in this study. Note, the bathymetry map of the box core location for this nodule sample can be seen in Figure 2.3 in chapter 2.

Nodule sample	Position	Water depth (m)	Sample description
AB02 BC06 N3	12° 34.73770 N 116° 41.21773 W	4237	Nodule has a 7 cm diameter and has a smooth top and a rough bottom with a botryoidal rim.



Figure 6.1. Image of nodule sample AB02 BC06 N3 before cutting and sampling of the individual layers.

6.3.2 Nd and Sr Isotopic composition

The SEM backscatter and EDS images of the nodule sample AB02 BC06 N3 are shown in Figure 6.2. Layers were sampled from the outer rim to the inner regions (layers 1 to 11). The individual Fe-rich hydrogenetic layers can be distinguished from the Mn-rich diagenetic layers. Sampling was carried out in a manner whereby the individual hydrogenetic and diagenetic layers were individually sampled and mixing of samples was minimised as much as possible.

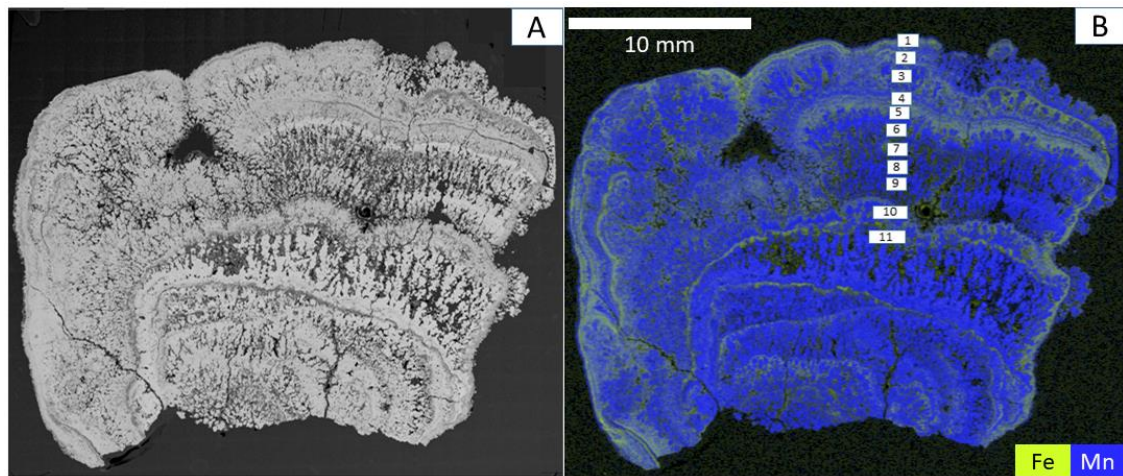


Figure 6.2. Mosaics of SEM backscatter images (A) and EDS chemical maps for Fe and Mn (B) of nodule sample ABO2 BC06 N3. The individual layers sampled shown by their sample numbers.

The ϵ_{Nd} and $^{87}Sr/^{86}Sr$ ratios are shown in Table 6.2. The Nd isotopic composition of the individual layers show little spread ranging from ϵ_{Nd} values -3.26 to -3.46; the values are similar to that of the North Pacific Deep Water ($\epsilon_{Nd} = -3.5$) (Jones *et al.*, 1994). Similarly, The Sr isotopic composition values for all the layers are within-error identical to the present day global seawater value ($^{87}Sr/^{86}Sr = 0.709175$) (McArthur, Howarth & Shields, 2012).

Table 6.2. Results table showing the Nd and Sr isotope ratios of the individual nodule layers.

Nodule layer	Nd ($\mu\text{g/g}$)	$^{143}\text{Nd}/^{144}\text{Nd}$	$\pm 2\sigma$	ϵ_{Nd}	$\pm 2\sigma$	Sr ($\mu\text{g/g}$)	$^{87}\text{Sr}/^{86}\text{Sr}$	$\pm 2\sigma$
1	82.7	0.512461	0.0000058	-3.46	0.11	179	0.709169	0.000013
2	72.1	0.512463	0.0000057	-3.42	0.11	176	0.709182	0.000014
3	61.3	0.512466	0.0000052	-3.35	0.10	172	0.709171	0.000013
4	67.3	0.512461	0.0000056	-3.46	0.11	227	0.709171	0.000013
5	99.0	0.512464	0.0000051	-3.39	0.10	298	0.709175	0.000015
6	61.5	0.512464	0.0000045	-3.39	0.09	136	0.709161	0.000014
7	45.6	0.512467	0.0000058	-3.33	0.11	120	0.709174	0.000014
8	31.5	0.512471	0.0000056	-3.26	0.11	85.2	0.709150	0.000014
9	37.5	0.512468	0.0000055	-3.33	0.11	91.6	0.709163	0.000014
10	58.8	0.512471	0.0000063	-3.26	0.12	132	0.709170	0.000014
11	42.5	0.512468	0.0000057	-3.32	0.11	119	0.709170	0.000013

The graphical representation of the Nd concentrations and ϵ_{Nd} values plotted against the vertical profile of the nodule sample from the outer rim to the inner regions is shown in Figure 6.3. Following on from the work in chapter 3 where hydrogenetic layers are enriched in REYs, the hydrogenetic regions are marked by elevated Nd concentrations compared to diagenetic regions. From layer 1 (rim, which is a hydrogenetic layer) to layer 3, there is a gradual decrease in Nd concentration. The concentrations then increase in layers 4 and 5 (hydrogenetic layers), after which the concentrations decreased again until layer 9 where they started to increase to layer 10 and then decreased in layer 11. The trend observed for Nd is also the same as that observed for Sr. Note that a clear hiatus exists between layers 9 and 10, which marks the boundary between the diagenetic regions (layers 6 – 9) and the hydrogenetic layer just before layer 10.

The results show that the ϵ_{Nd} values in the layers are generally similar as they are within the error bars plotted, however, variations in the ϵ_{Nd} values can be noted. While the ϵ_{Nd} values show a general increasing trend from the outer rim to the inner layers, the values are generally lower (more negative) in the hydrogenetic layers and are higher (more positive) in the diagenetic layers. Comparison of the ϵ_{Nd} values of the individual layers and that of the North Pacific Deep Water (NPDW) (Abbott, Haley & McManus, 2015; Piepgras & Jacobsen, 1988) shows that the ϵ_{Nd} values in the diagenetic layers deviate most in the positive direction away from the (NPDW) values while the values in the hydrogenetic layers deviate (to more negative direction) towards the NPDW values.

In terms of the Sr isotopic composition of the layers, the $^{87}\text{Sr}/^{86}\text{Sr}$ ratios in both layer types are also similar and their error bars are within the range of present day seawater. However, it can be observed that the $^{87}\text{Sr}/^{86}\text{Sr}$ ratios of the hydrogenetic layers are closest to the present day $^{87}\text{Sr}/^{86}\text{Sr}$ ratio of seawater while the values for the diagenetic layers are the farthest away from the seawater value. The $^{87}\text{Sr}/^{86}\text{Sr}$ ratios deviate to a higher (more positive) value for the diagenetic layer closest to the rim (layer 2) and deviate to more lower (more negative) values for the rest of the inner-located diagenetic layers.

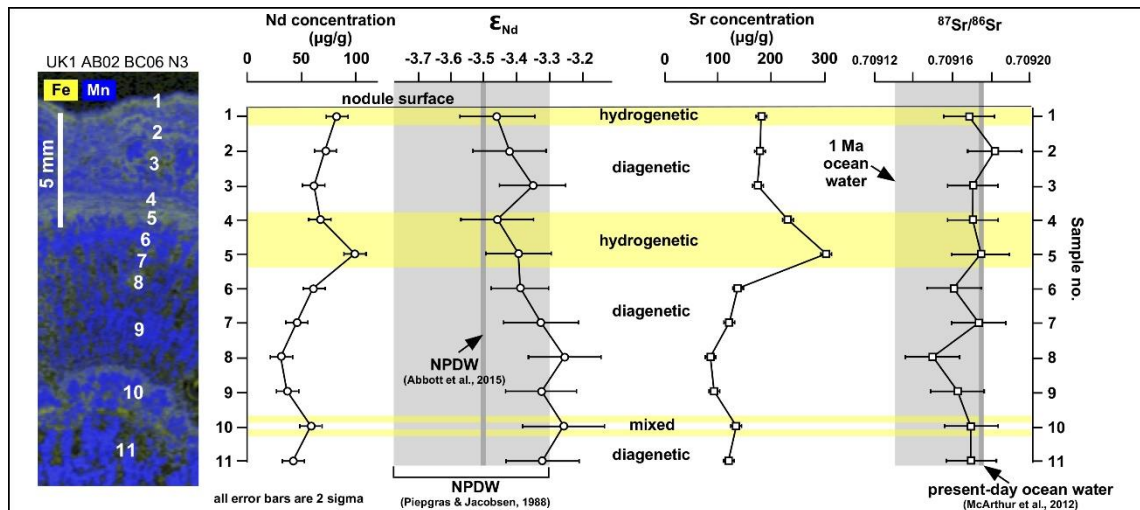


Figure 6.3. SEM-EDS image of nodule sample showing the predominantly Fe-rich hydrogenetic (yellow) and Mn-rich diagenetic (blue) layers and the vertical profile with the individual layers sampled. The Nd and Sr concentrations and isotopic compositions based on ϵ_{Nd} values and $^{87}\text{Sr}/^{86}\text{Sr}$ ratios for the eleven layers sampled are also shown as well as the ϵ_{Nd} values of the North Pacific Deep Water (Abbott, Haley & McManus, 2015; Piepgras & Jacobsen, 1988) and the $^{87}\text{Sr}/^{86}\text{Sr}$ value of the present-day seawater (McArthur, Howarth & Shields, 2012) (both marked in grey). In the graphical diagram, the hydrogenetic layers are colour-coded yellow while the diagenetic layers are colourless.

6.4 Discussion

Polymetallic nodules from the CCFZ are mixed-type nodules and are made up of Fe-rich hydrogenetic layers which formed from precipitation from the ambient oxic bottom seawater, and diagenetic layers which formed from precipitation from suboxic/oxic porewaters within the underlying sediments. SEM-EDS imaging shows that layers 1, 4 and 5 have a strongly hydrogenetic character, while layer 10 is classified as a mixed-type layer. Analysis of Nd concentration in the individual layers shows that Nd is enriched in these layers compared to the diagenetic layers which is consistent with the results for two nodules in chapter 3. The fact that mixed-type nodules are made up of hydrogenetic and diagenetic layers, one would expect that their isotopic signature would be different: hydrogenetic layers should theoretically show seawater isotopic signatures, while diagenetic layers should give values that are similar to that of the pore-waters within the underlying sediments. In many places in the modern oceans it has been shown that sedimentary pore-fluids and seawater are not isotopically identical, particularly with regards to Nd isotopic ratios.

The Nd and Sr isotopic compositions obtained for the nodule sample studied shows that the isotopic values are similar to that of bottom seawater but there are variations between the values for the hydrogenetic layers and that of the diagenetic layers. Based on the ϵ_{Nd} values, growth from sedimentary pore waters is not consistent with the isotopic Nd signature found, as isotopic signatures of pore fluids should approach those of the sediments, and the measured values are very different from those of the seafloor sediments from the region ($\epsilon_{Nd} < -4$, most likely around -6; (Jones *et al.*, 1994).

Geochemical and mineralogical analyses using sequential leaching and X-ray Diffraction (XRD) (chapter 4) have shown that most of the Nd in the nodules (60 – 70%) occupy the interlayers of the phyllophanates. In this work, the same leaching protocol was used and therefore, the Nd isotopes analysed are essentially those that occupy the interlayers of the phyllophanates. The isotopic compositions obtained in this work shows that they have two sources: a bottom seawater origin (NPDW) for the hydrogenetic layers and a porefluid origin for the diagenetic layers, although the mechanism of their incorporation into the interlayers are yet to be fully known. The possibility of Nd exchange with seawater due to the porous morphology of nodules could be suspected to have some influence on the Nd isotopic composition of the nodules. However, this can almost certainly be ruled out as surface-sorbed Nd in nodules, which could be influenced by post-growth seawater exchange, are absent or at least below the detection limit, as the first leaching step using acetic acid would have released these. Note that results from weak acetic acid leaching in section 4.3.1 have shown that surface-sorbed Nd are not present or are present at least below detection in the nodules. Also, the Nd concentration in nodules is so high (~140 ppm) compared to that of the bottom Pacific seawater ($\sim 3.5 \times 10^{-7}$ ppm) (Alibo & Nozaki, 1999) making it almost impossible to significantly change them by seawater exchange. Nd from detrital phases such as clay minerals is also not present as these are too tightly held to be released by weak acetic acid and HCl, and where therefore not included in the isotope analysis.

The Nd isotopic composition of the North Pacific Deep Water (NPDW) is well established as reported in the literature and presented in the introduction section of this chapter. The ϵ_{Nd} values reported by Abbott, Haley and McManus (2015) and Piepgras and

Jacobsen (1988) are used here to compare the values obtained in this study to that of the bottom seawater in the North Pacific Ocean (Figure 6.4).

The results show that the ϵ_{Nd} values in all the layers sampled deviate slightly from the seawater values to higher values. More importantly, the values for the diagenetic layers deviate the most away from the NPDW values to higher (more positive values) while the ϵ_{Nd} values for the hydrogenetic layers are lower and deviate the least, and are more closer to the ϵ_{Nd} value of NPDW. Based on the ϵ_{Nd} values of seafloor sediments in the CCFZ and the UK claim area which ranges from -4 to -6, the sediments are mostly derived from the North American Continent as eolian dust and riverine input (Jones *et al.*, 1994; Liu *et al.*, 2005; Stancin *et al.*, 2006). The ϵ_{Nd} values for the sediments are therefore expected to be radiogenic and lower than the ϵ_{Nd} value of NPDW (c. -3.5). This is also the case for eolian dust from the Asian continent but the ϵ_{Nd} values are more radiogenic, ranging from -9 to -13. Based on these observations, the Nd and the REYs in hydrogenetic layers are interpreted to be from the NPDW where it is primarily sourced from North American-derived sediments as eolian dust and riverine input as well as some possible contributions from the East Asian dust.

The ϵ_{Nd} values in the diagenetic layers are generally higher and therefore less radiogenic than the values for the hydrogenetic layers. The only 'source' that has higher ϵ_{Nd} values are seafloor basalts and/or seamounts. For example, fresh basaltic glasses from the nearest part of the East Pacific Rise between 11°45 and 15°N have ϵ_{Nd} values of +8.5 to +11.0, with the compositions in off-axis seamounts extending to lower values, down to +6.0 (Castillo *et al.*, 2000). The bathymetry map of the AB02 area in the UK Claim area (Figure 2.3, chapter 2) shows that seamounts are abundant in that area. Furthermore, visual observations of the bottom profile of the same area re-visited in March 2020

shows that rock outcrops (presumably basaltic crust) are common in the area. Therefore, some of the local sediments in the area are expected to be derived from basaltic detrital material weathered from the basaltic seamounts and outcrops and hence are interpreted to be the primary source of Nd and the REYs in the porewaters and subsequently in the diagenetic layers of nodules in the UK claim area. Hydrothermal release of Nd from seamounts can be also considered, however, some workers argued that hydrothermal fluxes do not contribute to seawater Nd due to removal by precipitates at vent sites (Frank, 2002; German *et al.*, 1990; Halliday *et al.*, 1992). Therefore, hydrothermal sources are not considered key sources of Nd and REY in polymetallic nodules.

Another contrasting pattern is the differences in Nd isotopic composition between the older and the younger diagenetic layers, which are separated by the hydrogenetic region (layers 4 and 5). The hydrogenetic layers 4 and 5 seem to mark the boundary in terms of Nd isotopic composition, values before these layers are slightly different from the ones after these layers. Two predominantly diagenetic regions can be observed on the EDS image that are separated by the hydrogenetic region consisting of layers 4 and 5, these are; older diagenetic region (layers 6 – 11) and younger diagenetic region (layers 2 and 3). The older diagenetic region have slightly higher ϵ_{Nd} values compared to the younger region. This 'jump' shows that there was a change in the chemistry of the pore fluids over time which resulted in the two isotopically different diagenetic regions. This change could either be a sudden jump that is associated with an event that is marked by the hydrogenetic layer. Alternatively, the change was gradual with time, but looks sudden because time is very much condensed in the hydrogenetic layers as they grow at considerably slow rates compared to diagenetic layers.

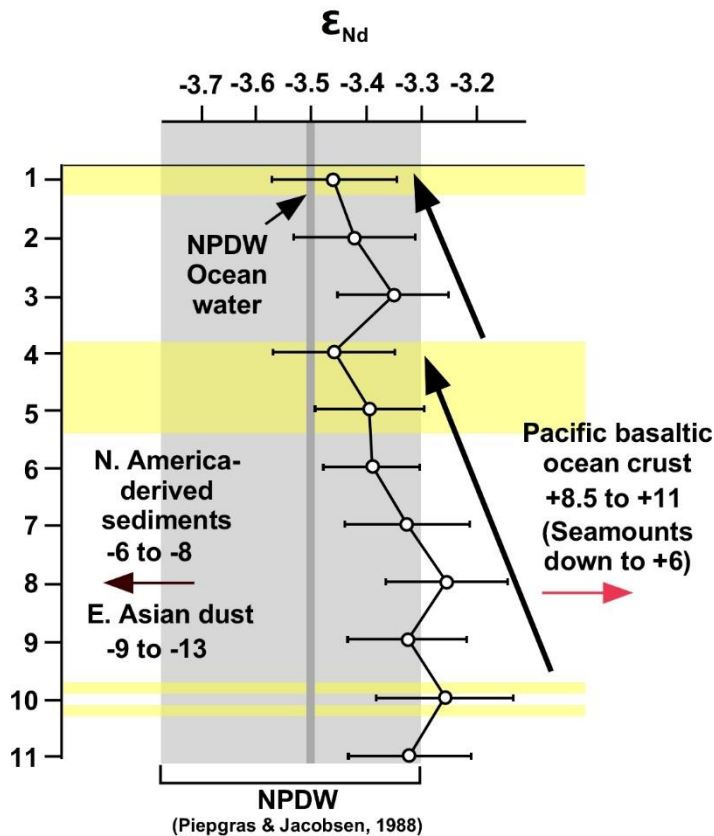


Figure 6.4. Nd isotopic composition based on ϵ_{Nd} values of the individual layers and compared to that of NPDW. Also included are the ϵ_{Nd} values of the North American-derived sediments and East Asian dust (both have lower ϵ_{Nd} values compared to NPDW) and sediments derived from basaltic Pacific Ocean crust and seamounts which have higher ϵ_{Nd} values when compared to NPDW. The two arrows show the younger region of the nodule (layers 1 -3) with generally lower ϵ_{Nd} values and the older regions (layers 4 -11) with higher ϵ_{Nd} values.

The Sr isotopic ratio is much less marked compared to that of Nd and the $^{87}\text{Sr}/^{86}\text{Sr}$ ratios are generally all within error. In deep sea sediments and precipitates including, nodules, Sr associated with poorly ordered oxyhydroxide phases can undergo isotopic exchange with that of seawater, as a result they can have a modified seawater isotopic signature (Dymond *et al.*, 1973; Elderfield, 1986). However, the seemingly slight increasing trend in Sr isotopic ratio towards the rim with time fits the seawater curve which has been increasing over the last 40 Ma reflecting the increased input of Sr enriched in ^{87}Sr (derived from weathering and erosion of continental rocks in mountain belts) coupled

with the relative decrease of ^{86}Sr from hydrothermal input (Dubinin *et al.*, 2017; McArthur, Howarth & Shields, 2012). The changes in seawater Sr isotopic ratio have been rapid over the last 30 Ma, so the very minor increase would fit with the idea that the outer part of the nodules are <1 Ma old. Comparison of the $^{87}\text{Sr}/^{86}\text{Sr}$ ratios obtained in this work with recent seawater values based on planktonic foraminifera in sediment cores from the southwest Pacific (Hodell, Mead & Mueller, 1990), correspond with recent seawater values up to 230 ka (Figure 6.5). The Sr results therefore show that the Sr present in the outer regions of the nodule (from rim to layer 11) resemble that of the bottom seawater which suggests that there is considerable exchange with the younger seawater in terms of Sr, at least in the outer nodule layers.

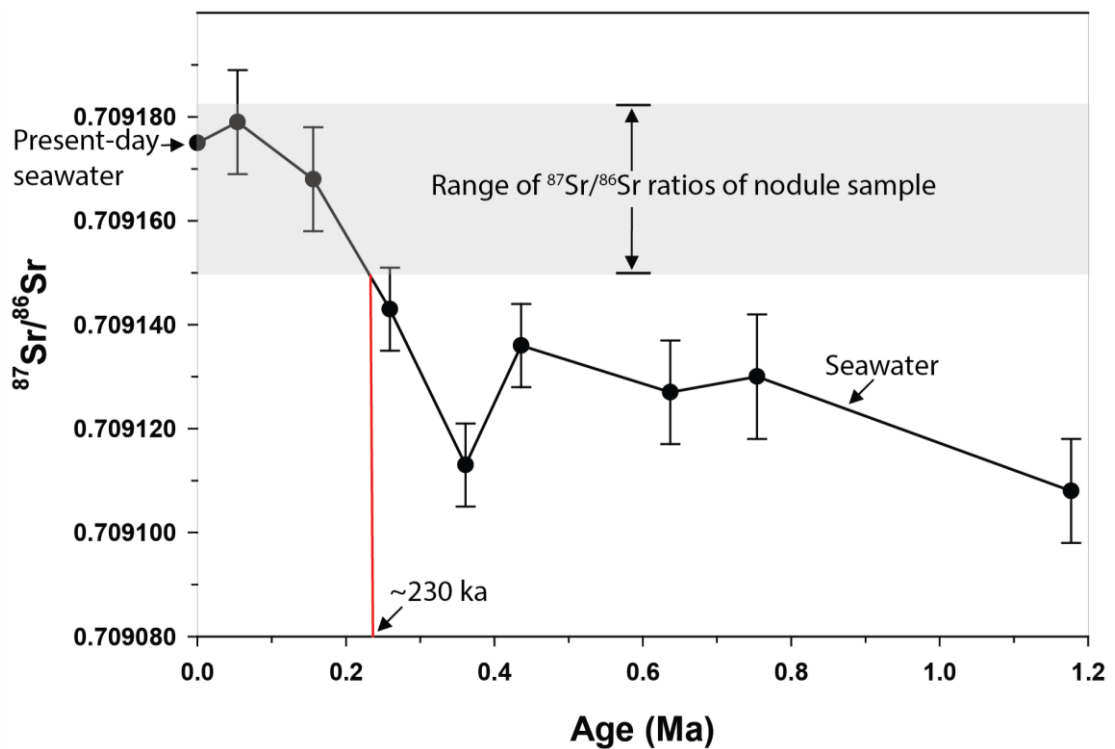


Figure 6.5. Seawater Sr evolution in the past ~1.2 Ma based on data from Hodell, Mead and Mueller (1990) of $^{87}\text{Sr}/^{86}\text{Sr}$ ratios measured in planktonic foraminifera in sediment cores from the southwest Pacific. The grey region shows the range of $^{87}\text{Sr}/^{86}\text{Sr}$ ratios measured in the nodule sample studied which corresponds to seawater values up to 230 ka.

6.5 Conclusion

The novel approach applied here for the determination of the Nd and Sr isotopic compositions on a nodule sample showed that the ϵ_{Nd} and $^{87}Sr/^{86}Sr$ ratios are similar in the individual layers and are also similar to seawater values for North Pacific Deep Water. However, some interesting variations between hydrogenetic and diagenetic layers were observed particularly for Nd. The ϵ_{Nd} values for hydrogenetic layers were lower (therefore more radiogenic) and are closer to the North Pacific Deep Water value (c. -3.5) and hence the Nd in this layer type is interpreted to be derived from the North Pacific Deep Water where most of the Nd is sourced from the North American continent as riverine input and eolian dust. In contrast, ϵ_{Nd} values for the diagenetic layers deviate the most away from that of the North Pacific Deep Water to higher (and therefore less radiogenic) values. Nd in diagenetic layers is therefore interpreted to be sourced from within porewaters in which most of the Nd is from weathered basaltic material from exposed seamounts and sea stacks, or from the ocean crusts just below the sediments. The results from this chapter therefore provide useful insights into the sources of the REYs in polymetallic nodules from the UK claim area in the Clarion-Clipperton Fracture Zone.

7 Final conclusions and future work

7.1 Final conclusions

Deep-sea polymetallic nodules are considered potential sources for valuable metals such as Ni, Cu, Mn and critical metals such as Rare Earth Elements plus Yttrium (REY) and Co. The Clarion-Clipperton Fracture Zone (CCFZ) is currently the area of greatest interest in terms of nodule mining where sixteen contractors are currently carrying out exploration activities. The increasing interest in deep-sea minerals is largely driven by the increasing demand of metals such as Ni, Co and REY, and the decreasing grade of terrestrial ore bodies. This is coupled with other issues associated with terrestrial mining such as environmental, human rights and geopolitical issues. These challenges led to the setting up of this project with the aim of enhancing our understanding of the geochemistry and mineralogy of critical metals particularly REY and Co in nodules from the UK Claim Area in the CCFZ.

There is now growing understanding on the bulk chemical and mineralogical composition of CCFZ nodules, particularly as part of the International Seabed Authority's (ISA) efforts to develop a framework for deep sea mining (ISA, 2010). The nodules are of mixed-type origin, and therefore diagenetic and hydrogenetic processes are considered to be the major formation mechanisms, whilst other processes such as the roles of micro and benthic organisms in nodule formation and growth are largely unknown at present. The nodules are made up of individual diagenetic and hydrogenetic layers, and with recent advances in analytical techniques such as electron microscopy, La-ICP-MS and μ XRF, the distribution of some elements within these layers are now known in more detail (Manceau, Lanson & Takahashi, 2014; Menendez *et al.*, 2019; Wegorzewski *et al.*, 2015). It is now generally accepted that elements enriched in the hydrogenetic layers

are primarily sourced from ambient seawater (hydrogenetic) while elements enriched in the diagenetic layers are sourced from the porewaters within the underlying sediments (diagenetic). Based on this, hydrogenetic precipitation occurs via sorption of cationic and anionic species onto colloidal MnO_2 and FeOOH in seawater and their subsequent precipitation onto a hard substrate. This is also the same mechanism proposed for the formation of ferromanganese crusts (Koschinsky & Halbach, 1995). Diagenetic precipitation occurs via a sequence of reactions within the sediment column, resulting in the upward flux of Mn to the sediment surface where it forms crystallized phylломanganates, in contrast to hydrogenetic precipitates which are composed of vernadite (Wegorzewski *et al.*, 2015).

The 10 Å phylломanganate (which includes busserite and todorokite) is the main mineralogical component in diagenetic nodules, this occurs with vernadite if nodules have a hydrogenetic component which is the case in mixed-type nodules.

In Pacific nodules elemental-mineral phase associations are largely controlled by the Mn and Fe oxides. Cobalt is associated with the Mn oxide component (vernadite) where it is incorporated as Co(III) in the vernadite layer by replacement of Mn (Manceau, Lanson & Takahashi, 2014). Similarly, Ce is also associated with vernadite as Ce(IV) but its incorporation in the structure is unknown (Manceau, Lanson & Takahashi, 2014; Takahashi *et al.*, 2000). The host phases of the rest of the REYs is largely unknown although recent work by Menendez (2017) suggested that it is associated with the phosphate phase such as apatite, similar to associated sediments in the CCFZ (Paul *et al.*, 2019b). Nickel is also associated with the Mn oxide component and is partitioned between vernadite and todorokite where it is hosted inside the MnO_2 layers (Bodeï *et al.*, 2007; Peacock & Sherman, 2007b).

Metals including REYS in CCFZ nodules are acquired from two major sources: seawater and sediment porewaters, where their primary sources are considered to be terrigenous and volcanic, as riverine input, continental weathering products and aeolian dust from the North and Central American Continents (ISA, 2010). Other sources considered include volcanic sources from the East Pacific Rise (ISA, 2010; Shimizu *et al.*, 1994). In Pacific nodules, the growing body of evidence shows that their Nd isotopic composition correspond to bottom seawater values. This therefore suggests a predominantly radiogenic seawater source where the REYs are largely derived from the North American Continent as riverine runoff (Elderfield *et al.*, 1981a; Piegras & Jacobsen, 1988; Stancin *et al.*, 2006).

Nodules from five box core locations within the UK Claim Area in the CCFZ were studied in this project. The general physical features of the nodules shows that they are of mixed-type origin, with a smooth top where they were recently in contact with seawater and a rough underside where they were in contact with the sediments. The nodules are generally variable in size (1 – 12 cm), the large ones (6 – 12 cm) have more botryoidal morphologies which shows more diagenetic-type precipitation. In contrast, nodules from one box core (AB02 BC02) are physically small in size (1 – 3 cm), they are smooth and well-rounded which shows that they were mostly sitting on the surface of sediments where the growth mechanism shifts slightly to a hydrogenetic-type precipitation.

In terms of the analytical measurement of trace metals, the sodium peroxide sintering method proved to be a reliable and effective method for sample decomposition that can be applied to the measurement of REY in nodules. The mean concentrations for the UK1 nodules are as follows: Mn = 28.4%, Ni = 1.3%, Cu = 1%, Co = 0.2% and REYs = 770 ppm. In terms of resource potential, the CCFZ nodules can be classified as large tonnage and

low grade deposits for REY, and large tonnage and medium grade deposits for Co, Ni and Cu. Small nodules from AB02 BC02 are enriched in REY and Co and are least enriched in Ni and Cu compared to nodules from the other box cores. This shows that REY and Co are predominantly sourced from the bottom seawater while Ni and Cu are sourced from within sediment porewaters. The differences in the morphologies of the nodules studied are due to differences in seafloor topography that affects the bottom water current flow. At sites close to seamounts, outcrops and on slopes, faster movement of bottom water currents are expected. This prevents nodule burial and nodules remain exposed on the sediment surface for most of their growth history. As a result, nodule growth is slightly more of a hydrogenetic-type and nodules are small in size, smooth and well rounded due to slow hydrogenetic precipitation. In contrast, at sites where there is slow bottom current flow, such as in plain flat areas and in valleys, nodules are only partly exposed and some are even buried. Under these conditions, the predominant growth mechanism is diagenetic, and nodules are generally large in size with more pore spaces and dendritic structures due to rapid diagenetic precipitation.

The nodules grow by both diagenetic and hydrogenetic precipitation where both growth mechanisms largely control the elemental enrichment in each layer type. Based on individual layer-type relative proportion estimations of 50% diagenetic layers and 20% hydrogenetic layers, diagenetic precipitation is the predominant mechanism of nodule growth compared to hydrogenetic precipitation. The internal structures of the nodules are made up of alternating layers of Fe-rich hydrogenetic and Mn-rich diagenetic layers. The hydrogenetic layers are thin (~20 – 500 µm in diameter) dense and compacted with laminated to columnar structures with low Mn/Fe ratios (<3). These structures formed from the hydrogenetic precipitation from the ambient seawater, where the slow laminar

flow of seawater is responsible for their morphologies. Growth rate calculations show that this layer type grow at rates of 3 – 10 mm/Ma. This slow accretion rate allows more time for REY and Co to precipitate on this-layer type from seawater which results in their enrichment in hydrogenetic layers.

The internal structures in the diagenetic layers are mostly dendritic with high Mn/Fe ratios (>3), the layers are thicker (up to 5 mm) due to faster growth rates (10 – 32 mm/Ma) but porous due to rapid diagenetic precipitation. Diagenetic layers are enriched in Ni and Cu and shows that they are predominantly sourced from the sediment pore waters as previously mentioned. The presence of growth discontinuities in the internal structures of nodules shows that nodule growth is not continuous and there are periods of non-growth as well as periods where nodules dissolve. Nodule dissolution occurs when nodules are buried in the sediments for enough time that reducing conditions prevail. This results in the reduction of Mn(IV) to Mn(II), the latter being soluble is mobilised in porewaters and diffuses upward to the oxic layer where it is re-oxidised to Mn(IV) and hence precipitates and participates in nodule formation. Nodule dissolution also results in the release of other cations into porewaters, which are mobilized and diffuse upward to nodule formation site where they are incorporated into an actively growing nodule.

Elemental distribution using SEM shows that Ni and Cu are enriched in diagenetic layers while REY and Co are enriched in hydrogenetic layers. The SEM results for Ni and Cu are consistent with the sequential leaching experiments and shows that they are predominantly associated with the phylломanganates where they are hosted in the interlayer spacings. Similarly, the REY are also associated with the phylломanganates where they are hosted in the interlayer spacings. The leaching results contradict the SEM

results for REY distribution. The conclusion drawn from these observations therefore is, REYs are predominantly hosted in the interlayers of the phyllosulfates. XRD results showed that the phyllosulfates are present in both layer types. Therefore, it is interpreted that most of the REYs are hosted in the phyllosulfates that are distributed in the hydrogenetic layers. Their enrichment in the hydrogenetic layers is due to the slower growth of this layer-type compared to the diagenetic layer. Therefore, if we consider a constant (very low) supply of REY from the water column a higher concentration of REY will be deposited in the slowly accreting hydrogenetic layers as opposed to the faster accreting diagenetic layers. The results for Co, however, shows that it is partitioned between FeOOH and the phyllosulfates phases.

Cationic exchange experiments of REY with synthetic Na-birnessite shows that the REYs can occupy the interlayer spacings of the phyllosulfates which supports the inference that REYs are hosted in the interlayers of the phyllosulfates. The synthesis experiments also show that the growth of polymetallic nodules in the deep sea can be wholly or predominantly by physiochemical processes and not by bio-mineralization as has been suggested by some workers (Dugolinsky, Margolis & Dudley, 1977; Wang & Müller, 2009; Wang *et al.*, 2009).

In chapter 6, and building on from the leaching work in chapter 4, interlayer Nd was isolated and isotopic measurements were carried out to determine its likely source. The results show slight variations in Nd isotopic signatures between the hydrogenetic and the diagenetic layers and therefore points to possibly two different sources. Based on comparisons between Nd isotopic composition in the nodule layers to those of the bottom seawater in the North Pacific Ocean and that of basaltic crust in the Eastern Pacific Ocean, it is proposed that Nd enriched in the hydrogenetic layers is derived from

North Pacific Deep Water while the Nd in diagenetic layers is likely from sediment pore fluids in which most of the Nd is derived from weathered basaltic material from exposed seamounts and sea stacks, or from the ocean crusts just below the sediments.

Based on the results obtained from this work and the conclusions discussed above, the growth model proposed for abyssal nodules from the CCFZ UK1 Claim Area is summarised in Figure 7.1.

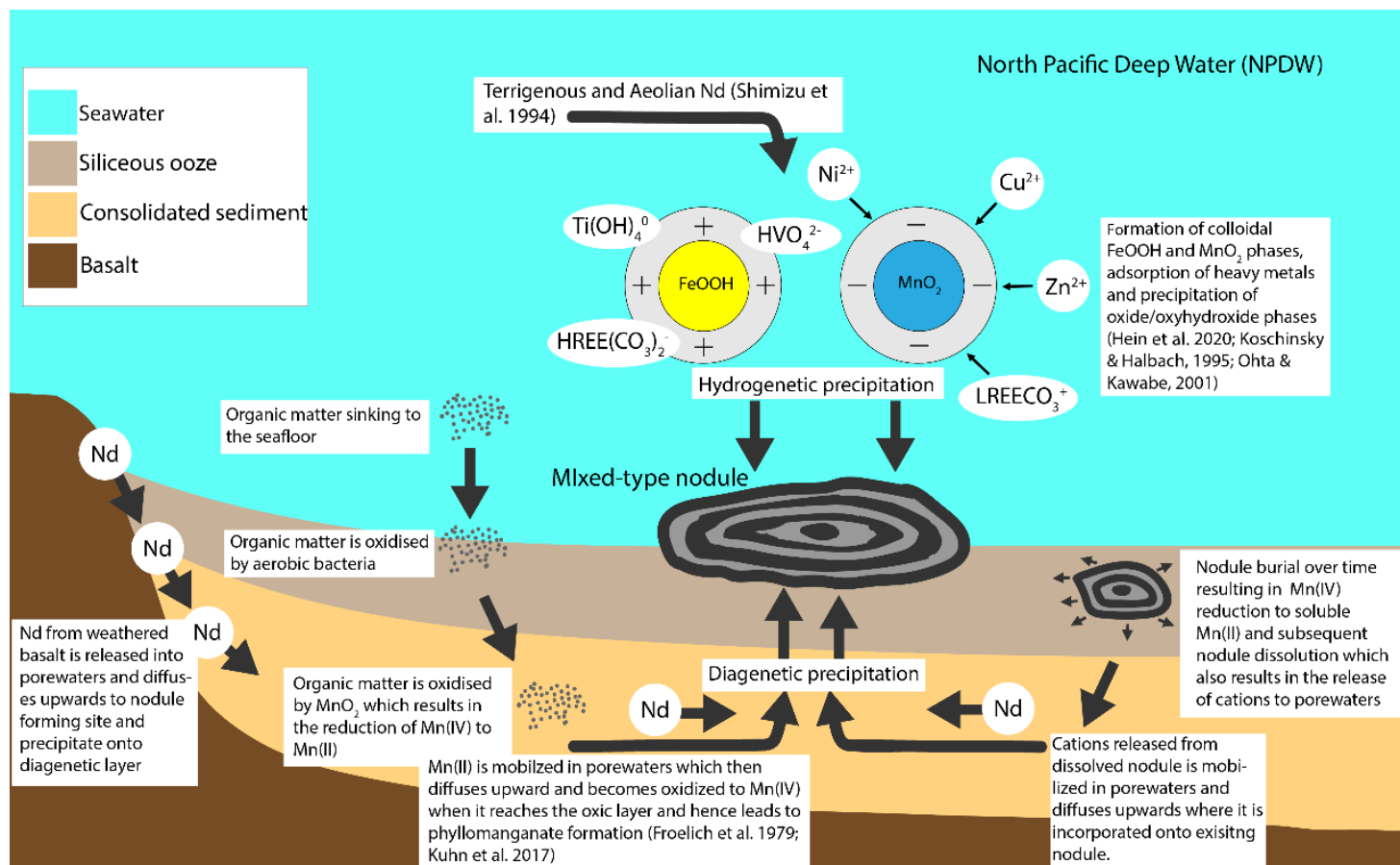


Figure 7.1. Schematic of the proposed growth model of mixed-type nodules from the CCFZ. Nodules grow by both diagenetic and hydrogenetic precipitation. Hydrogenetic growth begins with the formation of colloidal FeOOH and MnO₂ phases in oxic seawater, these phases possess surface charges, thereby enabling the adsorption of dissolved cations and anionic complexes. The colloidal oxide/oxyhydroxide phases then precipitate onto a hard rock substrate or an existing nodule and hence forming a hydrogenetic growth layer. In contrast, diagenetic reactions in porewaters starting with the oxidation of organic matter by aerobic bacteria and then by MnO₂ results in the mobilization and upward diffusion of Mn to the sediment where it precipitates as MnO₂ and hence forming a diagenetic growth layer.

Both growth processes are associated with metal enrichment with MnO₂ as vernadite intergrown with FeOOH as the main host phases in hydrogenetic layers and MnO₂ as 10 Å phyllomanganate in diagenetic layers. Another source of cations for diagenetic growth is from dissolved nodules, cations released are mobilized in porewaters and diffuse to the oxic layer where they are incorporated into the phyllomanganate structure. Neodymium in the nodules is sourced from two different sources, with Nd in hydrogenetic layers from terrigenous and aeolian sources while basaltic crust as the main source for diagenetic layers.

7.2 Future work

Building on the results obtained from this study, the following suggestions are made for future work:

1. The conclusion drawn from this study that REYs are associated with the phylломanganates can be improved and/or tested with high resolution spectroscopy methods such as X-ray near edge spectroscopy (XANES). In this PhD project, a pilot test study was performed for Ce distribution on a nodule sample using μ XRF, which suggests that it is possible to further this analysis to the molecular level to investigate the association of REYs with the phylломanganates. The association of Ce with the phylломanganates has been investigated by some workers (Takahashi *et al.*, 2007; Takahashi *et al.*, 2000), which suggests that this can be applied to the other REYs as well.
2. Imaging analysis in this project, performed using SEM shows that the nodules contain high amounts of discrete phases of apatite and barite (XRF bulk results in wt%: P = 0.19%, Ca = 1.65, Ba = 0.46). Detailed analysis such as imaging and chemical leaching (on extracted apatite and barite samples) on these phases will improve the understanding of the elements enriched in them, particularly as some workers have reported that apatite is the major host phase of REY in marine authigenic deposits including nodules (Elderfield *et al.*, 1981a; Menendez, 2017).
3. The Co chronometry method was applied in this study to determine growth rates of the individual layers of a nodule sample. This method does not account for growth hiatuses, therefore, other quantitative methods such using Be isotopes

can be used to improve growth calculations of individual layers as well as to determine the age of polymetallic nodules from the UK1.

4. The reconnaissance Nd and Sr isotopic work demonstrated in chapter 6 yielded very interesting and somewhat unexpected results. Further investigation can be carried out to build on the results obtained in this study and to further validate them. This include determining the isotopic composition of sediments and porewaters. This will further our understanding of the sources of metals in the individual growth layers of nodules and the overall processes associated with the growth of nodules on the seafloor. In addition, analysis of Mn, Fe and REY in sediments and porewaters will greatly enhance our understanding of their cycling in the sediments as well as redox boundaries, and their implications on the diagenetic growth of nodules within sediments.

References

Abbott, A. N., Haley, B. A. & McManus, J. (2015) 'Bottoms up: Sedimentary control of the deep North Pacific Ocean's ϵ Nd signature'. *Geology*, 43 (11), pp. 1035-1035.

Abbott, A. N., Haley, B. A. & McManus, J. (2016) 'The impact of sedimentary coatings on the diagenetic Nd flux'. *Earth and Planetary Science Letters*, 449 pp. 217-227.

Abouchami, W., Goldstein, S. L., Gazer, S. J. G., Eisenhauer, A. & Mangini, A. (1997) 'Secular changes of lead and neodymium in central Pacific seawater recorded by a FeMn crust'. *Geochimica et Cosmochimica Acta*, 61 (18), pp. 3957-3974.

Alibo, D. S. & Nozaki, Y. (1999) 'Rare earth elements in seawater: particle association, shale-normalization, and Ce oxidation'. *Geochimica et Cosmochimica Acta*, 63 (3-4), pp. 363-372.

Amakawa, H., Usui, A., Iijima, K. & Suzuki, K. (2017) 'Surface layer Nd isotopic composition of ferromanganese crusts collected from the Takuyo-Daigo Seamount reflects ambient seawater'. *Geochemical Journal*, 51 (1), pp. e1-e7.

Arrhenius, G. (1981) 'Structure, phase transformation and prebiotic catalysis in marine manganate minerals'. *Scripps Institution of Oceanography Reference Series*, pp. 1-19.

Atkins, A. L., Shaw, S. & Peacock, C. L. (2014) 'Nucleation and growth of todorokite from birnessite: Implications for trace-metal cycling in marine sediments'. *Geochimica et Cosmochimica Acta*, 144 pp. 109-125.

Axelsson, M. D., Rodushkin, I., Ingri, J. & Ohlander, B. (2002) 'Multielemental analysis of Mn-Fe nodules by ICP-MS: Optimisation of analytical method'. *Analyst*, 127 (1), pp. 76-82.

Balaram, V. (1999) 'Determination of precious metal concentrations in a polymetallic nodule reference sample from the Indian Ocean by ICP-MS'. *Marine Georesources & Geotechnology*, 17 (1), pp. 17-26.

Battery University (2018) 'How does cobalt work in Li-ion?'. [Online]. Available at: https://batteryuniversity.com/learn/article/bu_310_cobalt (Accessed: 19/04/2020).

Baturin, G. & Dubinchuk, V. (2010) 'On the composition of ferromanganese nodules of the Indian Ocean', *Doklady Earth Sciences*. Springer Science & Business Media, pp. 1179.

Bau, M. & Koschinsky, A. (2009) 'Oxidative scavenging of cerium on hydrous Fe oxide: Evidence from the distribution of rare earth elements and yttrium between Fe oxides and Mn oxides in hydrogenetic ferromanganese crusts'. *Geochemical Journal*, 43 (1), pp. 37-47.

Bau, M., Koschinsky, A., Dulski, P. & Hein, J. R. (1996) 'Comparison of the partitioning behaviours of yttrium, rare earth elements, and titanium between hydrogenetic marine ferromanganese crusts and seawater'. *Geochimica et Cosmochimica Acta*, 60 (10), pp. 1709-1725.

Bau, M., Schmidt, K., Koschinsky, A., Hein, J., Kuhn, T. & Usui, A. (2014) 'Discriminating between different genetic types of marine ferro-manganese crusts and nodules based on rare earth elements and yttrium'. *Chemical Geology*, 381 pp. 1-9.

Benites, M., Millo, C., Hein, J., Nath, B., Murton, B., Galante, D. & Jovane, L. (2018) 'Integrated geochemical and morphological data provide insights into the genesis of ferromanganese nodules'. *Minerals*, 8 (11), pp. 488.

Bischoff, J. L., Piper, D. Z. & Leong, K. (1981) 'The aluminosilicate fraction of North Pacific manganese nodules'. *Geochimica et Cosmochimica Acta*, 45 (11), pp. 2047-2063.

Bodeř, S., Manceau, A., Geoffroy, N., Baronnet, A. & Buatier, M. (2007) 'Formation of todorokite from vernadite in Ni-rich hemipelagic sediments'. *Geochimica et Cosmochimica Acta*, 71 (23), pp. 5698-5716.

Bokhari, S. N. H. & Meisel, T. C. (2017) 'Method development and optimisation of sodium peroxide sintering for geological samples'. *Geostandards and Geoanalytical Research*, 41 (2), pp. 181-195.

Bonatti, E. (1981) 'Metal deposits in the oceanic lithosphere'. *The sea*, 7 pp. 639-686.

Bonatti, E., Kraemer, T. & Rydell, H. (1972) 'Classification and genesis of submarine iron-manganese deposits. In: Horn, D.R. (Ed.), Papers from a conference on ferromanganese deposits on the ocean floor'. *National Science Foundation*, pp. 149-166.

Bruneau, L., Jerlov, N. G. & Koczy, F. (1953) 'Physical and chemical methods, Rep. Swedish deep-sea expedition 3'. *Physics and Chemistry*, (4), pp. 100-112.

Burns, R. G. (1976) 'The uptake of cobalt into ferromanganese nodules, soils, and synthetic manganese (IV) oxides'. *Geochimica et Cosmochimica Acta*, 40 (1), pp. 95-102.

Burns, R. G., Burns, V. M. & Stockman, H. W. (1983) 'A review of the todorokite-buserite problem; implications to the mineralogy of marine manganese nodules'. *American Mineralogist*, 68 (9-10), pp. 972-980.

Burns, V. & Burns, R. (1978) 'Authigenic todorokite and phillipsite inside deep-sea manganese nodules'. *American Mineralogist*, 63 (9-10), pp. 827-831.

Calvert, S. & Piper, D. (1984) 'Geochemistry of ferromanganese nodules from DOMES Site A, Northern Equatorial Pacific: Multiple diagenetic metal sources in the deep sea'. *Geochimica et Cosmochimica Acta*, 48 (10), pp. 1913-1928.

Calvert, S. E., Cousens, B. L. & Soon, M. Y. S. (1985) 'An X-ray fluorescence spectrometric method for the determination of major and minor elements in ferromanganese nodules'. *Chemical Geology*, 51 (1), pp. 9-18.

Calvert, S. E. & Price, N. B. (1977) 'Geochemical variation in ferromanganese nodules and associated sediments from the Pacific Ocean'. *Marine Chemistry*, 5 (1), pp. 43-74.

Cantrell, K. J. & Byrne, R. H. (1987) 'Rare earth element complexation by carbonate and oxalate ions'. *Geochimica et Cosmochimica Acta*, 51 (3), pp. 597-605.

Charette, M. A. & Smith, W. H. (2010) 'The volume of Earth's ocean'. *Oceanography*, 23 (2), pp. 112-114.

Chester, R. & Jickells, T. (2012) *Marine geochemistry*. 3rd edn. Oxford: Wiley-Blackwell.

Chesters, R. & Jickells, T. (2012) *Marine geochemistry*. 3rd edition edn. Oxford: Wiley-Blackwell.

Choi, H. S., Kim, S. J. & Kim, J. J. (2004) 'Dehydration behaviors of interlayer water in synthetic buserites'. *Geosciences Journal*, 8 (3), pp. 273-279.

Chubarov, V., Amosova, A. & Finkelshtein, A. (2020) 'X-ray fluorescence determination of major elements in ferromanganese nodules'. *X-Ray Spectrometry*, 49 (5), pp. 615-621.

Chukhrov, F. & Gorshkov, A. (1981) 'Iron and manganese oxide minerals in soils'. *Earth and Environmental Science Transactions of The Royal Society of Edinburgh*, 72 (3), pp. 195-200.

Chukhrov, F., Sakharov, B., Gorshkov, A., Drits, V. & Dikov, Y. P. (1985) 'Crystal structure of birnessite from the Pacific Ocean'. *International Geology Review*, 27 (9), pp. 1082-1088.

Corliss, J. B., Dymond, J., Gordon, L. I., Edmond, J. M., von Herzen, R. P., Ballard, R. D., Green, K., Williams, D., Bainbridge, A. & Crane, K. (1979) 'Submarine thermal springs on the Galapagos Rift'. *Science*, 203 (4385), pp. 1073-1083.

Cotta, A. J. B. & Enzweiler, J. (2012) 'Classical and new procedures of whole rock dissolution for trace element determination by ICP-MS'. *Geostandards and Geoanalytical Research*, 36 (1), pp. 27-50.

Courtois, C. & Clauer, N. (1980) 'Rare earth elements and strontium isotopes of polymetallic nodules from southeastern Pacific Ocean'. *Sedimentology*, 27 (6), pp. 687-695.

Cronan, D. (1975) 'Manganese nodules and other ferromanganese oxide deposits from the Atlantic Ocean'. *Journal of Geophysical Research*, 80 (27), pp. 3831-3837.

Cronan, D. (1977) 'Deep-sea nodules: Distribution and geochemistry', *Elsevier Oceanography Series*. Elsevier, pp. 11-44.

Cronan, D. & Hodkinson, R. (1993) 'An evaluation of manganese nodules and cobalt-rich crusts in South Pacific exclusive economic zones. Part III. Nodules and crusts in the EEZ of Tuvalu (Ellice Islands)'. *Marine Georesources & Geotechnology*, 11 (2), pp. 153-174.

Danielsson, L.-G., Dyrssen, D. & Granéli, A. (1980) 'Chemical investigations of Atlantis II and Discovery brines in the Red Sea'. *Geochimica et Cosmochimica Acta*, 44 (12), pp. 2051-2065.

de Baar, H. J., German, C. R., Elderfield, H. & Van Gaans, P. (1988) 'Rare earth element distributions in anoxic waters of the Cariaco Trench'. *Geochimica et Cosmochimica Acta*, 52 (5), pp. 1203-1219.

Degens, E. T. & Ross, D. A. (2013) *Hot brines and recent heavy metal deposits in the Red Sea: a geochemical and geophysical account*. Springer.

Djogić, R., Sipos, L. & Branica, M. (1986) 'Characterization of uranium (VI) in seawater 1'. *Limnology and Oceanography*, 31 (5), pp. 1122-1131.

Drits, V. A., Lanson, B., Bougerol-Chaillout, C., Gorshkov, A. I. & Manceau, A. (2002) 'Structure of heavy-metal sorbed birnessite: Part 2. Results from electron diffraction'. *American Mineralogist*, 87 (11-12), pp. 1646-1661.

Drits, V. A., Silvester, E., Gorshkov, A. I. & Manceau, A. (1997) 'Structure of synthetic monoclinic Na-rich birnessite and hexagonal birnessite: I. Results from X-ray diffraction and selected-area electron diffraction'. *American Mineralogist*, 82 (9-10), pp. 946-961.

Dubinina, A., Yu. Uspenskaya, T., Rimszkaya-Korsakova, M. & P. Demidova, T. (2017) *Rare elements and Nd and Sr isotopic composition in micronodules from the Brazil Basin, Atlantic Ocean*. vol. 52.

Dugolinsky, B. K., Margolis, S. V. & Dudley, W. C. (1977) 'Biogenic influence on growth of manganese nodules'. *Journal of Sedimentary Research*, 47 (1), pp. 428-445.

Dymond, J., Corliss, J. B., Heath, G. R., Field, C. W., Dasch, E. J. & Veeh, H. H. (1973) 'Origin of metalliferous sediments from the Pacific Ocean'. *Geological Society of America Bulletin*, 84 (10), pp. 3355-3372.

Eggins, S. M., Woodhead, J. D., Kinsley, L. P. J., Mortimer, G. E., Sylvester, P., McCulloch, M. T., Hergt, J. M. & Handler, M. R. (1997) 'A simple method for the precise determination of ≥ 40 trace elements in geological samples by ICP-MS using enriched isotope internal standardisation'. *Chemical Geology*, 134 (4), pp. 311-326.

Elderfield, H. (1986) 'Strontium isotope stratigraphy'. *Palaeogeography, palaeoclimatology, palaeoecology*, 57 (1), pp. 71-90.

Elderfield, H. & Greaves, M. J. (1982) 'The rare earth elements in seawater'. *Nature*, 296 pp. 214-219.

Elderfield, H., Hawkesworth, C., Greaves, M. & Calvert, S. (1981a) 'Rare earth element geochemistry of oceanic ferromanganese nodules and associated sediments'. *Geochimica et Cosmochimica Acta*, 45 (4), pp. 513-528.

Elderfield, H., Hawkesworth, C. J., Greaves, M. J. & Calvert, S. E. (1981b) 'Rare earth element geochemistry of oceanic ferromanganese nodules and associated sediments'. *Geochimica et Cosmochimica Acta*, 45 (4), pp. 513-528.

Elderfield, H. & Sholkovitz, E. R. (1987) 'Rare earth elements in the pore waters of reducing nearshore sediments'. *Earth and Planetary Science Letters*, 82 (3), pp. 280-288.

Ero Copper (2019) 'Ero Copper: This Brazilian copper producer will continue to deliver'. [Online]. Available at: <https://seekingalpha.com/article/4309454-ero-copper-this-brazilian-copper-producer-will-continue-to-deliver> (Accessed: 19/04/2020).

- Förstner, U. & Stoffers, P. (1981) 'Chemical fractionation of transition elements in Pacific pelagic sediments'. *Geochimica et Cosmochimica Acta*, 45 (7), pp. 1141-1146.
- Francheteau, J., Needham, H., Choukroune, P., Juteau, T., Seguret, M., Ballard, R. D., Fox, P., Normark, W., Carranza, A. & Cordoba, D. (1979) 'Massive deep-sea sulphide ore deposits discovered on the East Pacific Rise'. *Nature*, 277 (5697), pp. 523.
- Frank, M. (2002) 'Radiogenic isotopes: tracers of past ocean circulation and erosional input'. *Reviews of geophysics*, 40 (1),
- Freslon, N., Bayon, G., Toucanne, S., Bermell, S., Bollinger, C., Chéron, S., Etoubleau, J., Germain, Y., Khripounoff, A. & Ponzevera, E. (2014) 'Rare earth elements and neodymium isotopes in sedimentary organic matter'. *Geochimica et Cosmochimica Acta*, 140 pp. 177-198.
- Froelich, P. N., Klinkhammer, G. P., Bender, M. L., Luedtke, N. A., Heath, G. R., Cullen, D., Dauphin, P., Hammond, D., Hartman, B. & Maynard, V. (1979) 'Early oxidation of organic matter in pelagic sediments of the eastern equatorial Atlantic: suboxic diagenesis'. *Geochimica et Cosmochimica Acta*, 43 (7), pp. 1075-1090.
- German, C., Klinkhammer, G., Edmond, J., Mura, A. & Elderfield, H. (1990) 'Hydrothermal scavenging of rare-earth elements in the ocean'. *Nature*, 345 (6275), pp. 516-518.
- Giovanoli, R. (1980) 'Vernadite is random-stacked birnessite'. *Mineralium Deposita*, 15 (2), pp. 251-253.
- Giovanoli, R. (1985) 'A review of the todorokite–buserite problem: Implications to the mineralogy of marine manganese nodules: Discussion'. *American Mineralogist*, 70 (1-2), pp. 202-204.
- Giovanoli, R. (1988) 'Morphology and composition of manganese nodules: Structural chemistry of marine manganese and iron minerals and synthetic model compounds'. *The Manganese Nodule Belt of the Pacific Ocean*, pp. 20-37.
- Glasby, G. (1986) 'Marine minerals in the Pacific'. *Oceanography and Marine Biology An Annual Review*, 24 pp. 11-64.
- Glasby, G. P. (ed.) (1977) *Marine manganese deposits*. Rates of accretion. New York: Elsevier Scientific Publishing Company. 249 pp.
- Golden, D. (1987) 'Transformation of birnessite to buserite, todorokite, and manganite under mild hydrothermal treatment'. *Clays and Clay Minerals*, 35 pp. 271-280.

Golden, D., Chen, C., Dixon, J. & Tokashiki, Y. (1988) 'Pseudomorphic replacement of manganese oxides by iron oxide minerals'. *Geoderma*, 42 (3-4), pp. 199-211.

Goldstein, S. & O'Nions, R. (1981) 'Nd and Sr isotopic relationships in pelagic clays and ferromanganese deposits'. *Nature*, 292 (5821), pp. 324-327.

González, F. J., Somoza, L., Lunar, R., Martínez-Frías, J., Rubí, J. A. M., Torres, T., Ortiz, J. E. & Díaz-del-Río, V. (2010) 'Internal features, mineralogy and geochemistry of ferromanganese nodules from the Gulf of Cadiz: The role of the Mediterranean outflow water undercurrent'. *Journal of Marine Systems*, 80 (3-4), pp. 203-218.

Goodenough, K. M., Wall, F. & Merriman, D. (2018) 'The rare earth elements: demand, global resources, and challenges for resourcing future generations'. *Natural Resources Research*, 27 (2), pp. 201-216.

Graedel, T. E., Harper, E. M., Nassar, N. T., Nuss, P. & Reck, B. K. (2015) 'Criticality of metals and metalloids'. *Proceedings of the National Academy of Sciences*, 112 (14), pp. 4257-4262.

Grandell, L., Lehtilä, A., Kivinen, M., Koljonen, T., Kihlman, S. & Lauri, L. S. (2016) 'Role of critical metals in the future markets of clean energy technologies'. *Renewable Energy*, 95 pp. 53-62.

Guichard, F., Church, T. M., Treuil, M. & Jaffrezic, H. (1979) 'Rare earths in barites: Distribution and effects on aqueous partitioning'. *Geochimica et Cosmochimica Acta*, 43 (7), pp. 983-997.

Halbach, P. (1984) 'Deep-sea metallic deposits'. *Ocean Management*, 9 (1), pp. 35-60.

Halbach, P., Friedrich, G. & von Stackelberg, U. (1988) *The manganese nodule belt of the Pacific Ocean: Geological environment, nodule formation, and mining aspects*. Stuttgart: F. Enke.

Halbach, P., Scherhag, C., Hebisch, U. & Marchig, V. (1981) 'Geochemical and mineralogical control of different genetic types of deep-sea nodules from the Pacific Ocean'. *Mineralium Deposita*, 16 (1), pp. 59-84.

Halbach, P. E., Jahn, A. & Cherkashov, G. (2017a) 'Marine Co-rich ferromanganese crust deposits: Description and formation, occurrences and distribution, estimated world-wide resources', *Deep-Sea Mining*. Springer, pp. 65-141.

Halbach, P. E., Jahn, A. & Cherkashov, G. (2017b) 'Marine Co-rich ferromanganese crust deposits: Description and formation, occurrences and distribution, estimated world-wide resources', in

- Sharma, R. (ed.) *Deep-Sea Mining: Resource Potential, Technical and Environmental Considerations*. Cham: Springer International Publishing, pp. 65-141.
- Haley, B. A. & Klinkhammer, G. P. (2003) 'Complete separation of rare earth elements from small volume seawater samples by automated ion chromatography: method development and application to benthic flux'. *Marine Chemistry*, 82 (3-4), pp. 197-220.
- Halliday, A. N., Davidson, J. P., Holden, P., Owen, R. M. & Olivarez, A. M. (1992) 'Metalliferous sediments and the scavenging residence time of Nd near hydrothermal vents'. *Geophysical Research Letters*, 19 (8), pp. 761-764.
- Hao-Jie, C., Fan, L., Wen-Feng, T. & Xiong-Han, F. (2011) 'Effect of cobalt-doped framework on formation of todorokite from layered manganese oxides with Mg²⁺/Co²⁺ ions as template'. *Pedosphere*, 21 (6), pp. 730-737.
- Haque, N., Hughes, A., Lim, S. & Vernon, C. (2014) 'Rare earth elements: Overview of mining, mineralogy, uses, sustainability and environmental impact'. *Resources*, 3 (4), pp. 614-635.
- Hawkins, L. K. (1969) 'Visual observations of manganese deposits on the Blake Plateau'. *Journal of Geophysical Research*, 74 (28), pp. 7009-7017.
- Hein, J. R., Konstantinova, N., Mikesell, M., Mizell, K., Fitzsimmons, J. N., Lam, P. J., Jensen, L. T., Xiang, Y., Gartman, A. & Cherkashov, G. (2017) 'Arctic deep water ferromanganese-oxide deposits reflect the unique characteristics of the Arctic Ocean'. *Geochemistry, Geophysics, Geosystems*, 18 (11), pp. 3771-3800.
- Hein, J. R. & Koschinsky, A. (2014a) 'Deep-ocean ferromanganese crusts and nodules ', in Turekian, K.K. and Holland, H. (eds.) *Treatise on Geochemistry (Second Edition)*. Oxford: Elsevier, pp. 273-291.
- Hein, J. R. & Koschinsky, A. (2014b) 'Deep-ocean ferromanganese crusts and nodules', in Turekian, K.K. and Holland, H. (eds.) *Treatise on geochemistry (second edition)*. Oxford: Elsevier, pp. 273-291.
- Hein, J. R., Koschinsky, A., Bau, M., Manheim, F. T., Kang, J.-K. & Roberts, L. (2000) 'Cobalt-rich ferromanganese crusts in the Pacific'. *Handbook of marine mineral deposits*, 18 pp. 239-273.
- Hein, J. R., Koschinsky, A., Halbach, P., Manheim, F. T., Bau, M., Kang, J.-K. & Lubick, N. (1997) 'Iron and manganese oxide mineralization in the Pacific'. *Geological Society, London, Special Publications*, 119 (1), pp. 123-138.

Hein, J. R., Mizell, K., Koschinsky, A. & Conrad, T. A. (2013) 'Deep-ocean mineral deposits as a source of critical metals for high- and green-technology applications: Comparison with land-based resources'. *Ore Geology Reviews*, 51 pp. 1-14.

Hein, J. R. & Petersen, S. (2013) *The geology of manganese nodules*. Secretariat of the Pacific Community.

Hein, J. R., Schulz, M. S. & Gein, L. M. (1992) 'Central Pacific cobalt-rich ferromanganese crusts: Historical perspective and regional variability', *Geology and offshore mineral resources of the Central Pacific Basin*. Springer, pp. 261-283.

Hein, J. R., Spinardi, F., Okamoto, N., Mizell, K., Thorburn, D. & Tawake, A. (2015) 'Critical metals in manganese nodules from the Cook Islands EEZ, abundances and distributions'. *Ore Geology Reviews*, 68 pp. 97-116.

Heller, C., Kuhn, T., Versteegh, G. J. M., Wegorzewski, A. V. & Kasten, S. (2018) 'The geochemical behavior of metals during early diagenetic alteration of buried manganese nodules'. *Deep Sea Research Part I: Oceanographic Research Papers*, 142 pp. 16-33.

Herrington, R. (2013) 'Road map to mineral supply'. *Nature Geoscience*, 6 (11), pp. 892.

Herzig, P. M., Petersen, S. & Hannington, M. (2002) 'Polymetallic massive sulphide deposits at the modern seafloor and their resource potential', *Polymetallic massive sulphides and cobalt-rich ferromanganese crusts: Status and prospects*. International Seabed Authority, pp. 7-35.

Hodell, D. A., Mead, G. A. & Mueller, P. A. (1990) 'Variation in the strontium isotopic composition of seawater (8 Ma to present): Implications for chemical weathering rates and dissolved fluxes to the oceans'. *Chemical Geology: Isotope Geoscience section*, 80 (4), pp. 291-307.

Hund, K., La Porta, D., Fabregas, P. T., Laing, T. & Drexhage, J. (2020) *Minerals for climate action: The mineral intensity of the clean energy transition*. Washington: Climate-Smart Mining Facility, World Bank. Available.

Iijima, K., Yasukawa, K., Fujinaga, K., Nakamura, K., Machida, S., Takaya, Y., Ohta, J., Haraguchi, S., Nishio, Y. & Usui, Y. (2016) 'Discovery of extremely REY-rich mud in the western North Pacific Ocean'. *Geochemical Journal*, 50 (6), pp. 557-573.

Ingram, B. L., Hein, J. & Farmer, G. (1990) 'Age determinations and growth rates of Pacific ferromanganese deposits using strontium isotopes'. *Geochimica et Cosmochimica Acta*, 54 (6), pp. 1709-1721.

ISA (2010) *A geological model of polymetallic nodule deposits in the Clarion Clipperton Fracture Zone (No. 6)*. Kingston, Jamaica: International Seabed Authority. Available at: <https://www.isa.org.jm/documents/geological-model-polymetallic-nodule-deposits-clarion-clipperton-fracture-zone>.

ISA (2015). Available at: <https://www.isa.org.jm/> (Accessed: 12/04/2020).

ISA (2016) *International Seabed Authority News*, Issue 6, Kingston.

Ito, T. & Komuro, K. (2006) 'Paleoceanographic setting and preservation of buried manganese deposits in DSDP/ODP cores'. *Resource geology*, 56 (4), pp. 457-470.

Ito, T., Usui, A., Kajiwara, Y. & Nakano, T. (1998) 'Strontium isotopic compositions and paleoceanographic implication of fossil manganese nodules in DSDP/ODP cores, Leg 1–126'. *Geochimica et Cosmochimica Acta*, 62 (9), pp. 1545-1554.

Jacobsen, S. B. & Wasserburg, G. (1980) 'Sm-Nd isotopic evolution of chondrites'. *Earth and Planetary Science Letters*, 50 (1), pp. 139-155.

Jauhari, P. J. (1987) 'Classification and inter-element relationships of ferromanganese nodules from the Indian Ocean Basin'. *Marine Mining*, 6 pp. 419-429.

Johnson, E. A. & Post, J. E. (2006) 'Water in the interlayer region of birnessite: Importance in cation exchange and structural stability'. *American Mineralogist*, 91 (4), pp. 609-618.

Jones, C. E., Halliday, A. N., Rea, D. K. & Owen, R. M. (1994) 'Neodymium isotopic variations in North Pacific modern silicate sediment and the insignificance of detrital REE contributions to seawater'. *Earth and Planetary Science Letters*, 127 (1-4), pp. 55-66.

Jones, L. & Milne, A. A. (1956) 'Birnessite, a new manganese oxide mineral from Aberdeenshire, Scotland'. *Mineralogical Magazine and Journal of the Mineralogical Society*, 31 (235), pp. 283-288.

Jones, M. T., Pearce, C. R., Jeandel, C., Gislason, S. R., Eiriksdottir, E. S., Mavromatis, V. & Oelkers, E. H. (2012) 'Riverine particulate material dissolution as a significant flux of strontium to the oceans'. *Earth and Planetary Science Letters*, 355 pp. 51-59.

Kanazawa, Y. & Kamitani, M. (2006) 'Rare earth minerals and resources in the world'. *Journal of alloys and compounds*, 408 pp. 1339-1343.

Kato, Y., Fujinaga, K., Nakamura, K., Takaya, Y., Kitamura, K., Ohta, J., Toda, R., Nakashima, T. & Iwamori, H. (2011) 'Deep-sea mud in the Pacific Ocean as a potential resource for rare-earth elements'. *Nature Geoscience*, 4 (8), pp. 535-539.

Kerr, R. A. (1984) 'Manganese nodules grow by rain from above'. *Science*, 223 (4636), pp. 576-577.

Kon, Y., Hoshino, M., Sanematsu, K., Morita, S., Tsunematsu, M., Okamoto, N., Yano, N., Tanaka, M. & Takagi, T. (2014) 'Geochemical characteristics of apatite in heavy REE-rich deep-sea mud from Minami-Torishima Area, Southeastern Japan'. *Resource geology*, 64 (1), pp. 47-57.

Konstantinova, N., Hein, J. R., Gartman, A., Mizell, K., Barrulas, P., Cherkashov, G., Mikhailik, P. & Khanchuk, A. (2018) 'Mineral phase-element associations based on sequential leaching of ferromanganese crusts, Amerasia Basin Arctic Ocean'. *Minerals*, 8 (10), pp. 1-21.

Koschinsky, A. & Halbach, P. (1995) 'Sequential leaching of marine ferromanganese precipitates: Genetic implications'. *Geochimica et Cosmochimica Acta*, 59 (24), pp. 5113-5132.

Koschinsky, A. & Hein, J. R. (2003) 'Uptake of elements from seawater by ferromanganese crusts: solid-phase associations and seawater speciation'. *Marine Geology*, 198 (3), pp. 331-351.

Ku, T. (1977) 'Rates of accretion', *Elsevier Oceanography Series*. Elsevier, pp. 249-267.

Kuhn, T., Bau, M., Blum, N. & Halbach, P. (1998) 'Origin of negative Ce anomalies in mixed hydrothermal–hydrogenetic Fe–Mn crusts from the Central Indian Ridge'. *Earth and Planetary Science Letters*, 163 (1), pp. 207-220.

Kuhn, T., Wegorzewski, A., Ruhlemann, C. & Vink, A. (2017) *Composition, formation and occurrence of polymetallic nodules*. ed. Sharma, R., Deep Sea Mining. Springer, Cham.

Kuma, K., Usui, A., Paplawsky, W., Gedulin, B. & Arrhenius, G. (1994) 'Crystal structures of synthetic 7 Å and 10 Å manganates substituted by mono- and divalent cations'. *Mineralogical Magazine*, 58 (392), pp. 425-447.

Lanson, B., Drits, V. A., Gaillot, A.-C., Silvester, E., Plançon, A. & Manceau, A. (2002) 'Structure of heavy-metal sorbed birnessite: Part 1. Results from X-ray diffraction'. *American Mineralogist*, 87 (11-12), pp. 1631-1645.

Lebrato, M., Garbe-Schönberg, D., Müller, M. N., Blanco-Ameijeiras, S., Feely, R. A., Lorenzoni, L., Molinero, J.-C., Bremer, K., Jones, D. O. B., Iglesias-Rodríguez, D., Greeley, D., Lamare, M. D., Paulmier, A., Graco, M., Cartes, J., Barcelos e Ramos, J., de Lara, A., Sanchez-Leal, R., Jimenez,

P., Paparazzo, F. E., Hartman, S. E., Westernströer, U., Küter, M., Benavides, R., da Silva, A. F., Bell, S., Payne, C., Olafsdottir, S., Robinson, K., Jantunen, L. M., Korablev, A., Webster, R. J., Jones, E. M., Gilg, O., Bailly du Bois, P., Beldowski, J., Ashjian, C., Yahia, N. D., Twining, B., Chen, X.-G., Tseng, L.-C., Hwang, J.-S., Dahms, H.-U. & Oschlies, A. (2020) 'Global variability in seawater Mg:Ca and Sr:Ca ratios in the modern ocean'. *Proceedings of the National Academy of Sciences*, 117 (36), pp. 22281.

Li, J., Fang, N., Qu, W., Ding, X., Gao, L., Wu, C. & Zhang, Z. (2008) 'Os isotope dating and growth hiatuses of Co-rich crust from central Pacific'. *Science in China Series D: Earth Sciences*, 51 (10), pp. 1452.

Liu, J., Shi, X., Chen, L., Huang, Y., Wang, Y., Cui, Y. & Bu, W. (2005) 'REE and ϵNd of clay fractions in sediments from the eastern Pacific Ocean: Evidence for clay sources'. *Science in China Series D: Earth Sciences*, 48 pp. 701-712.

Longerich, H. P., Jenner, G. A., Fryer, B. J. & Jackson, S. E. (1990) 'Inductively coupled plasma-mass spectrometric analysis of geological samples: A critical evaluation based on case studies'. *Chemical Geology*, 83 (1), pp. 105-118.

Lowenstam, H. A. & Weiner, S. (1989) *On biomineralization*. Oxford University Press on Demand.

Lu, Y., Leshner, C. M. & Deng, J. (2019) 'Geochemistry and genesis of magmatic Ni-Cu-(PGE) and PGE-(Cu)-(Ni) deposits in China'. *Ore Geology Reviews*, 107 pp. 863-887.

Lusty, P. A. J. & Murton, B. J. (2018) 'Deep-ocean mineral deposits: Metal resources and windows into earth processes'. *Elements*, 14 (5), pp. 301-306.

Macholdt, D. S., Jochum, K. P., Wilson, S. A., Otter, L. M., Stoll, B., Weis, U. & Andreae, M. O. (2016) 'Suitability of Mn- and Fe-rich reference materials for microanalytical research'. *Geostandards and Geoanalytical Research*, 40 (4), pp. 493-504.

Manceau, A., Kersten, M., Marcus, M. A., Geoffroy, N. & Granina, L. (2007) 'Ba and Ni speciation in a nodule of binary Mn oxide phase composition from Lake Baikal'. *Geochimica et Cosmochimica Acta*, 71 (8), pp. 1967-1981.

Manceau, A., Lanson, M. & Takahashi, Y. (2014) 'Mineralogy and crystal chemistry of Mn, Fe, Co, Ni, and Cu in a deep-sea Pacific polymetallic nodule'. *American Mineralogist*, 99 pp. 2068-2083.

Manceau, A., Silvester, E., Bartoli, C., Lanson, B. & Drits, V. A. (1997) 'Structural mechanism of Co^{2+} oxidation by the phylломanganate buserite'. *American Mineralogist*, 82 (11-12), pp. 1150-1175.

Manheim, F. & Lane-Bostwick, C. (1988) 'Cobalt in ferromanganese crusts as a monitor of hydrothermal discharge on the Pacific sea floor'.

Mantyla, A. W. & Reid, J. L. (1983) 'Abyssal characteristics of the World Ocean waters'. *Deep Sea Research Part A. Oceanographic Research Papers*, 30 (8), pp. 805-833.

Marino, E., González, F., Lunar, R., Carrión, M., Bellido, E. & Somoza, L. (2018) *High-resolution analysis of critical minerals and elements in Fe–Mn Crusts from the Canary Island Seamount Province (Atlantic Ocean)*. vol. 8.

May, T. W. & Wiedmeyer, R. H. (1998) 'A table of polyatomic interferences in ICP-MS'. *ATOMIC SPECTROSCOPY-NORWALK CONNECTICUT-*, 19 pp. 150-155.

McArthur, J., Howarth, R. & Shields, G. (2012) 'Strontium isotope stratigraphy', *The geologic time scale*. Elsevier, pp. 127-144.

McLaren, R., Lawson, D. & Swift, R. (1986) 'Sorption and desorption of cobalt by soils and soil components'. *Journal of Soil Science*, 37 (3), pp. 413-426.

Meisel, T., Schöner, N., Paliulionyte, V. & Kahr, E. (2002) 'Determination of rare earth elements, Y, Th, Zr, Hf, Nb and Ta in geological reference materials G-2, G-3, SCo-1 and WGB-1 by sodium peroxide sintering and inductively coupled plasma-mass spectrometry'. *Geostandards and Geoanalytical Research*, 26 (1), pp. 53-61.

Mellin, T. A. & Lei, G. (1993) 'Stabilization of 10Å-manganates by interlayer cations and hydrothermal treatment: Implications for the mineralogy of marine manganese concretions'. *Marine Geology*, 115 (1-2), pp. 67-83.

Menendez, A. (2017) *Controls on the composition and extraction of rare earth elements and yttrium (REY) in deep sea polymetallic nodules and sediments*. University of Southampton.

Menendez, A., James, R., Shulga, N., Connelly, D. & Roberts, S. (2018) 'Linkages between the genesis and resource potential of ferromanganese deposits in the Atlantic, Pacific, and Arctic Oceans'. *Minerals*, 8 (5), pp. 197.

Menendez, A., James, R. H., Lichtschlag, A., Connelly, D. & Peel, K. (2019) 'Controls on the chemical composition of ferromanganese nodules in the Clarion-Clipperton Fracture Zone, eastern equatorial Pacific'. *Marine Geology*, 409 pp. 1-14.

Mero, J. L. (1962) 'Ocean-floor manganese nodules'. *Economic Geology*, 57 (5), pp. 747-767.

Mero, J. L. (1965) *The mineral resources of the sea*. vol. 1. Amsterdam: Elsevier.

Mewes, K., Mogollón, J. M., Picard, A., Rühlemann, C., Kuhn, T., Nöthen, K. & Kasten, S. (2014) 'Impact of depositional and biogeochemical processes on small scale variations in nodule abundance in the Clarion-Clipperton Fracture Zone'. *Deep Sea Research Part I: Oceanographic Research Papers*, 91 pp. 125-141.

Miller, W., Martens, D. & Zelazny, L. (1986) 'Effect of Sequence in Extraction of Trace Metals from Soils 1'. *Soil Science Society of America Journal*, 50 (3), pp. 598-601.

Mining Data Solutions (2018) 'Sorowako Mine'. [Online]. Available at: <https://miningdataonline.com/property/1494/Sorowako-Mine.aspx#Reserves> (Accessed: 18/04/2020).

Mining Technology (2005) 'Anaconda Nickel Ltd Nickel and Cobalt Mine'. [Online]. Available at: <https://www.mining-technology.com/projects/murrin/> (Accessed: 18/04/2020).

Mining Technology (2009) 'Goro Nickel Project, South Pacific Island of New Caledonia'. [Online]. Available at: <https://www.mining-technology.com/projects/goro-nickel/> (Accessed: 18/04/2020).

Mogollón, J. M., Mewes, K. & Kasten, S. (2016) 'Quantifying manganese and nitrogen cycle coupling in manganese-rich, organic carbon-starved marine sediments: Examples from the Clarion-Clipperton fracture zone'. *Geophysical Research Letters*, 43 (13), pp. 7114-7123.

Moldoveanu, G. & Papangelakis, V. (2013) 'Leaching of lanthanides from various weathered elution deposited ores'. *Canadian Metallurgical Quarterly*, 52 (3), pp. 257-264.

Moorby, S. A. & Cronan, D. S. (1981) 'The distribution of elements between co-existing phases in some marine ferromanganese-oxide deposits'. *Geochimica et Cosmochimica Acta*, 45 (10), pp. 1855-1877.

Mukhopadhyay, R. & Ghosh, A. K. (2010) 'Dynamics of formation of ferromanganese nodules in the Indian Ocean'. *Journal of Asian Earth Sciences*, 37 (4), pp. 394-398.

Murray, J. & Renard, A. (1891a) *Report on deep sea deposits based on the specimens collected during the voyage of HMS Challenger in the years 1872-1876*. ed. nodules, O.o.t.m.a.m., Report on deep sea deposits based on the specimens collected during the voyage of HMS Challenger in the years 1872-1876'.

Murray, J. & Renard, A. F. (1891b) *Report on deep-sea deposits based on the specimens collected during the voyage of HMS Challenger in the years 1872 to 1876*. HM Stationery Office.

Ohta, A., Ishii, S., Sakakibara, M., Mizuno, A. & Kawabe, I. (1999) 'Systematic correlation of the Ce anomaly with the Co/(Ni+ Cu) ratio and Y fractionation from Ho in distinct types of Pacific deep-sea nodules'. *Geochemical Journal*, 33 (6), pp. 399-417.

Ohta, A. & Kawabe, I. (2001) 'REE (III) adsorption onto Mn dioxide (δ -MnO₂) and Fe oxyhydroxide: Ce (III) oxidation by δ -MnO₂'. *Geochimica et Cosmochimica Acta*, 65 (5), pp. 695-703.

Pak, S.-J., Seo, I., Lee, K.-Y. & Hyeong, K. (2019) 'Rare earth elements and other critical metals in deep seabed mineral deposits: Composition and implications for resource potential'. *Minerals*, 9 (1), pp. 3.

Pal'chik, N., Grigor'eva, T. & Moroz, T. (2013) 'Natural and synthetic manganese minerals'. *Russian Journal of Inorganic Chemistry*, 58 (2), pp. 138-143.

Paterson, E., Bunch, J. & Clark, D. (1986) 'Cation exchange in synthetic manganates: I. Alkylammonium exchange in a synthetic phyllo-manganate'. *Clay Minerals*, 21 (5), pp. 949-955.

Pattan, J. & Banakar, V. (1993) 'Rare earth element distribution and behaviour in buried manganese nodules from the Central Indian Basin'. *Marine Geology*, 112 (1-4), pp. 303-312.

Pattan, J. N. & Parthiban, G. (2007) 'Do manganese nodules grow or dissolve after burial? Results from the Central Indian Ocean Basin'. *Journal of Asian Earth Sciences*, 30 (5-6), pp. 696-705.

Pattan, J. N. & Parthiban, G. (2011) 'Geochemistry of ferromanganese nodule-sediment pairs from Central Indian Ocean Basin'. *Journal of Asian Earth Sciences*, 40 (2), pp. 569-580.

Pattan, J. N., Rao, C. M., Migdisov, A. A., Colley, S., Higgs, N. C. & Demidenko, L. (2001) 'Ferromanganese nodules and their associated sediments from the Central Indian Ocean Basin: Rare Earth Element Geochemistry'. *Marine Georesources & Geotechnology*, 19 (3), pp. 155-165.

Paul, S., Haeckel, M., Bau, M., Bajracharya, R. & Koschinsky, A. (2019a) 'Small-scale heterogeneity of trace metals including REY in deep-sea sediments and pore waters of the Peru Basin, SE equatorial Pacific'. *Biogeosciences Discussions*, pp. 1-29.

Paul, S. A., Volz, J. B., Bau, M., Köster, M., Kasten, S. & Koschinsky, A. (2019b) 'Calcium phosphate control of REY patterns of siliceous-ooze-rich deep-sea sediments from the central equatorial Pacific'. *Geochimica et Cosmochimica Acta*, 251 pp. 56-72.

Peacock, C. L. & Sherman, D. M. (2007a) 'Sorption of Ni by birnessite: Equilibrium controls on Ni in seawater'. *Chemical Geology*, 238 (1-2), pp. 94-106.

Peacock, C. L. & Sherman, D. M. (2007b) 'Crystal-chemistry of Ni in marine ferromanganese crusts and nodules'. *American Mineralogist*, 92 (7), pp. 1087-1092.

Pelleter, E., Fouquet, Y., Etoubleau, J., Cheron, S., Labanieh, S., Josso, P., Bollinger, C. & Langlade, J. (2017) 'Ni-Cu-Co-rich hydrothermal manganese mineralization in the Wallis and Futuna back-arc environment (SW Pacific)'. *Ore Geology Reviews*, 87 pp. 126-146.

Petavratzi, E., Gunn, G. & Kresse, C. (2019) *BGS Commodity review: Cobalt*.

Petersen, S., Krätschell, A., Augustin, N., Jamieson, J., Hein, J. R. & Hannington, M. D. (2016) 'News from the seabed – Geological characteristics and resource potential of deep-sea mineral resources'. *Marine Policy*, 70 pp. 175-187.

Piegras, D. J. & Jacobsen, S. B. (1988) 'The isotopic composition of neodymium in the North Pacific'. *Geochimica et Cosmochimica Acta*, 52 (6), pp. 1373-1381.

Piper, D. Z. (1974) 'Rare earth elements in the sedimentary cycle: A summary'. *Chemical Geology*, 14 (4), pp. 285-304.

Piper, D. Z. & Bau, M. (2013) 'Normalized rare earth elements in water, sediments, and wine: identifying sources and environmental redox conditions'. *American Journal of Analytical Chemistry*, 2013

Post, J. E. & Bish, D. L. (1988) 'Rietveld refinement of the todorokite structure'. *American Mineralogist*, 73 (7-8), pp. 861-869.

Potts, P. J. (2012) 'A proposal for the publication of geochemical data in the scientific literature'. *Geostandards and Geoanalytical Research*, 36 (3), pp. 225-230.

Pratt, R. M. & McFarlin, P. F. (1966) 'Manganese Pavements on the Blake Plateau'. *Science*, 151 (3714), pp. 1080-1082.

Reykhard, L. Y. & Shulga, N. (2019) 'Fe-Mn nodule morphotypes from the NE Clarion-Clipperton Fracture Zone, Pacific Ocean: comparison of mineralogy, geochemistry and genesis'. *Ore Geology Reviews*, 110 pp. 102933.

Reyss, J. L., Lemaitre, N., Ku, T. L., Marchig, V., Southon, J. R., Nelson, D. E. & Vogel, J. S. (1985) 'Growth of a manganese nodule from Peru Basin: A radiochemical anatomy'. *Geochimica et Cosmochimica Acta*, 49 (11), pp. 2401-2408.

Rosseinsky, D. (1965) 'Electrode potentials and hydration energies. Theories and correlations'. *Chemical Reviews*, 65 (4), pp. 467-490.

Rudnick, R. & Gao, S. (2003) 'Composition of the continental crust'. *Treatise on geochemistry*, 3 pp. 659.

Rühlemann, C., Kuhn, T., Wiedicke, M., Kasten, S., Mewes, K. & Picard, A. (2011) 'Current status of manganese nodule exploration in the German license area', *Ninth ISOPE Ocean Mining Symposium*. International Society of Offshore and Polar Engineers.

Shimizu, H., Tachikawa, K., Masuda, A. & Nozaki, Y. (1994) 'Cerium and neodymium isotope ratios and REE patterns in seawater from the North Pacific Ocean'. *Geochimica et Cosmochimica Acta*, 58 (1), pp. 323-333.

Slack, J., Kimball, B. & Shedd, K. (2017) *Cobalt* U.S. Geological Survey (Report No. Professional Paper 1802-F.53). Available at: <https://pubs.er.usgs.gov/publication/pp1802F>.

Somayajulu, B. (1967) 'Beryllium-10 in a manganese nodule'. *Science*, 156 (3779), pp. 1219-1220.

Somayajulu, B. (2000) 'Growth rates of oceanic manganese nodules: Implications to their genesis, palaeo-earth'. *Current Science*, 78 (3), pp. 10.

Somayajulu, B., Heath, G., Moore Jr, T. & Cronan, D. (1971) 'Rates of accumulation of manganese nodules and associated sediment from the equatorial Pacific'. *Geochimica et Cosmochimica Acta*, 35 (6), pp. 621-624.

Spickermann, R. (2012) 'Rare Earth content of Manganese nodules in the Lockheed Martin Clarion-Clipperton Zone exploration areas', *Offshore Technology Conference*. Offshore Technology Conference.

Spiess, F. N., Macdonald, K. C., Atwater, T., Ballard, R., Carranza, A., Cordoba, D., Cox, C., Garcia, V. D., Francheteau, J. & Guerrero, J. (1980) 'East Pacific Rise: Hot springs and geophysical experiments'. *Science*, 207 (4438), pp. 1421-1433.

Stancin, A., Gleason, J., Rea, D., Owen, R., Moore Jr, T., Blum, J. & Hovan, S. (2006) 'Radiogenic isotopic mapping of late Cenozoic eolian and hemipelagic sediment distribution in the east-central Pacific'. *Earth and Planetary Science Letters*, 248 (3-4), pp. 840-850.

Tachikawa, K., Piotrowski, A. M. & Bayon, G. (2014) 'Neodymium associated with foraminiferal carbonate as a recorder of seawater isotopic signatures'. *Quaternary Science Reviews*, 88 pp. 1-13.

Takahashi, Y., Manceau, A., Geoffroy, N., Marcus, M. A. & Usui, A. (2007) 'Chemical and structural control of the partitioning of Co, Ce, and Pb in marine ferromanganese oxides'. *Geochimica et Cosmochimica Acta*, 71 (4), pp. 984-1008.

Takahashi, Y., Shimizu, H., Usui, A., Kagi, H. & Nomura, M. (2000) 'Direct observation of tetravalent cerium in ferromanganese nodules and crusts by X-ray-absorption near-edge structure (XANES)'. *Geochimica et Cosmochimica Acta*, 64 (17), pp. 2929-2935.

Takaya, Y., Yasukawa, K., Kawasaki, T., Fujinaga, K., Ohta, J., Usui, Y., Nakamura, K., Kimura, J.-I., Chang, Q. & Hamada, M. (2018) 'The tremendous potential of deep-sea mud as a source of rare-earth elements'. *Scientific Reports*, 8 (1), pp. 5763.

Takebe, M. (2005) 'Carriers of Rare Earth Elements in Pacific Deep-Sea Sediments'. *Journal of Geology*, 113 (2), pp. 201-215.

Takematsu, N., Sato, Y. & Okabe, S. (1989) 'Factors controlling the chemical composition of marine manganese nodules and crusts: A review and synthesis'. *Marine Chemistry*, 26 (1), pp. 41-56.

Tanaka, T., Togashi, S., Kamioka, H., Amakawa, H., Kagami, H., Hamamoto, T., Yuhara, M., Orihashi, Y., Yoneda, S. & Shimizu, H. (2000) 'JNdi-1: A neodymium isotopic reference in consistency with LaJolla neodymium'. *Chemical Geology*, 168 (3-4), pp. 279-281.

Thermo Fisher Scientific (2017) 'Robust ICP-MS with ease of use and high productivity for routine laboratories'.

Toyoda, K. & Tokonami, M. (1990) 'Diffusion of rare-earth elements in fish teeth from deep-sea sediments'.

Turner, S., Siegel, M. D. & Buseck, P. R. (1982) 'Structural features of todorokite intergrowths in manganese nodules'. *Nature*, 296 (5860), pp. 841.

UKSR (2015) *UK1-AB01 (2013) and UK1-AB02 (2015) polymetallic nodule collection data*. UK Seabed Resources Ltd. Available.

UN (2016) 'Sustainable development goals'. [Online]. Available at: <https://www.un.org/sustainabledevelopment/> (Accessed: 27/05/2019).

USGS (2020a) *Rare earths*. Available at: <https://pubs.usgs.gov/periodicals/mcs2020/mcs2020-rare-earths.pdf>.

USGS (2020b) *Cobalt*. Available at: <https://pubs.usgs.gov/periodicals/mcs2020/mcs2020-cobalt.pdf>.

Usui, A. & Mita, N. (1995) 'Geochemistry and mineralogy of a modern buserite deposit from a hot spring in Hokkaido, Japan'. *Clays and Clay Minerals*, 43 (1), pp. 116-127.

Usui, A., Yuasa, M., Yokota, S., Nohara, M., Nishimura, A. & Murakami, F. (1986) 'Submarine hydrothermal manganese deposits from the Ogasawara (Bonin) Arc, off the Japan Islands'. *Marine Geology*, 73 (3-4), pp. 311-322.

Valsangkar, A. B. & Rebello, J. M. S. (2015) 'Significance of size in occurrence, distribution, morphological characteristics, abundance, and resource evaluation of polymetallic nodules'. *Marine Georesources & Geotechnology*, 33 (2), pp. 135-149.

Van Gosen, B. S., Verplanck L, P., Seal R, R., Long R, K. & Joseph, G. (2017) *Rare earth elements*. Reston, VA: USGS. Available at: <https://pubs.er.usgs.gov/publication/pp1802O>.

Vance, D. & Thirlwall, M. (2002) 'An assessment of mass discrimination in MC-ICPMS using Nd isotopes'. *Chemical Geology*, 185 (3-4), pp. 227-240.

Varentsov, I., Drits, V., Gorshkov, A., Sivtsov, A. t. & Sakharov, B. (1991) 'Mn-Fe oxyhydroxide crusts from Krylov Seamount (eastern Atlantic): Mineralogy, geochemistry and genesis'. *Marine Geology*, 96 (1-2), pp. 53-70.

Villalobos, M., Lanson, B., Manceau, A., Toner, B. & Sposito, G. (2006) 'Structural model for the biogenic Mn oxide produced by *Pseudomonas putida*'. *American Mineralogist*, 91 (4), pp. 489-502.

Vineesh, T. C., Nagender Nath, B., Banerjee, R., Jaisankar, S. & Lekshmi, V. (2009) 'Manganese nodule morphology as indicators for oceanic processes in the Central Indian Basin'. *International Geology Review*, 51 (1), pp. 27-44.

Visbeck, M., Kronfeld-Goharani, U., Neumann, B., Rickels, W., Schmidt, J., van Doorn, E., Matz-Lück, N. & Proelss, A. (2014) 'A sustainable development goal for the ocean and coasts: global ocean challenges benefit from regional initiatives supporting globally coordinated solutions'. *Marine Policy*, 49 pp. 87-89.

Vlasova, I. E. (1995) 'Growth rates of the ferromanganese nodules from the pacific subequatorial belt by the alpha-radiographic technique'. *Radiation Measurements*, 25 (1), pp. 503-506.

Volz, J., Haffert, L., Haeckel, M., Koschinsky, A. & Kasten, S. (2020) 'Impact of small-scale disturbances on geochemical conditions, biogeochemical processes and element fluxes in surface sediments of the eastern Clarion-Clipperton Zone, Pacific Ocean'. *Biogeosciences*, 17 pp. 1113-1131.

Volz, J. B., Mogollón, J. M., Geibert, W., Arbizu, P. M., Koschinsky, A. & Kasten, S. (2018) 'Natural spatial variability of depositional conditions, biogeochemical processes and element fluxes in sediments of the eastern Clarion-Clipperton Zone, Pacific Ocean'. *Deep Sea Research Part I: Oceanographic Research Papers*, 140 pp. 159-172.

Von Stackelberg, U. (1997) 'Growth history of manganese nodules and crusts of the Peru Basin'. *Geological Society, London, Special Publications*, 119 (1), pp. 153-176.

Von Stackelberg, U. (2000) 'Manganese nodules of the Peru Basin'. *Handbook of marine mineral deposits*, pp. 197-238.

von Stackelberg, U. & Beiersdorf, H. (1988) 'Manganese nodules and sediments in the equatorial-North Pacific Ocean'. *Geologisches Jahrbuch Reihe D*, 500 pp. 87.

von Stackelberg, U. & Marchig, V. (1987) 'Manganese nodule from the equatorial North Pacific Ocean'. *Geol Jahrb*, D87 pp. 123-227.

Wang, X. & Müller, W. E. G. (2009) 'Marine biominerals: perspectives and challenges for polymetallic nodules and crusts'. *Trends in Biotechnology*, 27 (6), pp. 375-383.

Wang, X., Schröder, H. C., Wiens, M., Schloßmacher, U. & Müller, W. E. G. (2009) 'Manganese/polymetallic nodules: Micro-structural characterization of exolithobiontic- and endolithobiontic microbial biofilms by scanning electron microscopy'. *Micron*, 40 (3), pp. 350-358.

Wegorzewski, A., Köpcke, M., Kuhn, T., Sitnikova, M. & Wotruba, H. (2018) 'Thermal Pre-Treatment of Polymetallic Nodules to Create Metal (Ni, Cu, Co)-Rich Individual Particles for Further Processing'. *Minerals*, 8 (11), pp. 523.

Wegorzewski, A., Kuhn, T., Dohrmann, R., Wirth, R. & Grangeon, S. (2015) 'Mineralogical characterization of individual growth structures of Mn nodules with different Ni+Cu content from the Pacific Ocean'. *American Mineralogist*, 100 pp. 2497-2508.

Wegorzewski, A. V. & Kuhn, T. (2014) 'The influence of suboxic diagenesis on the formation of manganese nodules in the Clarion Clipperton nodule belt of the Pacific Ocean'. *Marine Geology*, 357 pp. 123-138.

Weiner, S. & Dove, P. M. (2003) 'An overview of biomineralization processes and the problem of the vital effect'. *Reviews in mineralogy and geochemistry*, 54 (1), pp. 1-29.

Yang, K.-F., Fan, H.-R., Santosh, M., Hu, F.-F. & Wang, K.-Y. (2011) 'Mesoproterozoic carbonatitic magmatism in the Bayan Obo deposit, Inner Mongolia, North China: constraints for the mechanism of super accumulation of rare earth elements'. *Ore Geology Reviews*, 40 (1), pp. 122-131.

Yang, Y., Walton, A., Sheridan, R., Güth, K., Gauss, R., Gutfleisch, O., Buchert, M., Steenari, B.-M., Van Gerven, T., Jones, P. & Binnemans, K. (2017) 'REE recovery from end-of-life NdFeB permanent magnet scrap: A critical review'. *Journal of Sustainable Metallurgy*, 3

Yin, H., Li, H., Wang, Y., Ginder-Vogel, M., Qiu, G., Feng, X., Zheng, L. & Liu, F. (2014) 'Effects of Co and Ni co-doping on the structure and reactivity of hexagonal birnessite'. *Chemical Geology*, 381 pp. 10-20.

Yu, H. & Leadbetter, J. R. (2020) 'Bacterial chemolithoautotrophy via manganese oxidation'. *Nature*, 583 (7816), pp. 453-458.

Zhu, B., Yu, J., Qin, X., Rioual, P., Liu, Z., Zhang, Y., Jiang, F., Mu, Y., Li, H. & Ren, X. (2013) 'The significance of mid-latitude rivers for weathering rates and chemical fluxes: evidence from northern Xinjiang rivers'. *Journal of hydrology*, 486 pp. 151-174.

Appendix I. Sample preparation for SEM

Cutting of nodule samples was done using a diamond saw with much caution as most of them are not very hard and can easily disintegrate. The cut up nodules were then placed in an oven set at 105°C overnight to remove as much water or moisture as possible before resin impregnation.

Before impregnation with the resin mixture, a releasing agent was applied to the inner parts of the moulds to enable removal of cured block later. Nitrile gloves were worn during handling of these chemicals. During impregnation, the nodule sample was placed in the mould and the resin mixture was slowly poured over it until completely covered. Nodules are highly porous, which can result in the formation of bubbles in the resin. To minimise this, the mould was placed in a closed vacuum compartment for up to an hour to release air from the pores. The mould was then removed from vacuum and left to cure at 60°C for at least 3 hrs. After it has cured, the polished block was taken out of the mould and the surface was ground using a diamond grinder or a coarse polishing surface until the nodules sample was exposed.

Subsequent grinding and polishing of the surface was carried out using a slurry of alumina with water starting from larger grain sizes to smaller sizes (29 µm, 14 µm and 9 µm). Much finer polishing steps with grain sizes of 6 µm, 3 µm and 1 µm were performed using diamond paste slurry on mechanical polishers. Polished blocks were carefully rinsed in tap water and sonicated when going from a larger grain size to a smaller one to avoid any large grains that might scratch the surface during later polishing. A low power microscope was used each time to view the surface of polished sections to look for any surface deformities or scratches, if present, the polishing has to be repeated

from the coarser polishers again. Once complete, the block was dried and stored in a desiccator to minimise moisture absorption since nodules are highly hygroscopic. Prior to analysis, the polished resin block was oven dried overnight at 105°C to remove moisture; it was found that this step was critical for SEM analysis, as it was impossible to achieve the necessary high vacuum in the SEM without it.

Appendix II. Sequential leachate concentrations for nodule samples: AB02 BC06 N5, AB02 BC19 N3, AB02 BC02 rubbles and FeMn CRM. All measurements for each element carried out in triplicates.

AB02 BC06 N5									
		0.1 M Acetic acid		HCl		0.2 M Oxalic acid		Concentrated nitric acid	
	Bulk composition (ppm)	Conc. (ppm)	RSD (%)	Conc. (ppm)	RSD (%)	Conc. (ppm)	RSD (%)	Conc. (ppm)	RSD (%)
Na	21640	<LOD		5553	15.8	<LOD		17.5	58.0
Mg	16957	2976	10.4	9939	2.90	72.4	12.6	738	3.06
Al	21555	5.01	56.8	5830	3.37	204	4.63	685	6.88
Si	79462	848	3.03	3168	4.93	1345	6.57	89.6	26.4
P	1571	8.96	4.37	30.8	61.2	51.7	62.4	<LOD	
K	9275	1093	15.7	2446	5.94	1056	5.74	704	15.7
Ca	16231	3271	2.58	10609	2.82	18.94	89.9	259	4.79
Mn	297968	42.0	82.2	3243	9.39	8686	3.13	57308	5.15
Fe	60152	14.4	89.4	9161	5.89	9404	3.27	12173	0.72
Co	1814	0.24	87.9	14.7	41.1	119	5.50	486	2.95
Ni	14741	2.36	76.5	5936	2.18	548	2.45	1936	8.24
Cu	11181	2.54	51.2	7344	2.06	1140	4.60	642	4.75
Zn	1649	5.77	10.2	1340	2.86	47.7	41.8	90.5	12.0
Ba	4613	2.83	11.0	1462	3.16	<LOD		770	42.1
Y	65.4	8.91	60.0	42.4	4.84	2.95	34.0	15.8	84.2
La	98.9	0.03	35.7	69.4	11.5	0.59	5.19	8.38	1.5
Ce	274	0.04	77.6	71.5	13.0	8.23	8.74	98.2	9.28
Pr	28.2	0.01	41.5	20.0	10.9	0.30	4.90	2.40	1.77
Nd	121	0.04	44.0	92.5	4.00	1.57	4.35	10.2	2.07
Sm	28.9	0.01	34.0	22.6	3.64	0.53	3.72	2.44	1.23
Eu	7.29	<LOD		5.48	3.97	0.15	4.47	0.57	3.94
Gd	27.6	0.01	36.5	22.4	4.60	0.90	4.88	3.24	2.49
Tb	4.53	<LOD		3.32	3.94	0.15	3.36	0.27	2.33

Dy	24.8	0.01	38.7	19.1	4.81	1.06	2.80	1.32	4.33
Ho	4.63	<LOD		3.48	4.57	0.21	3.09	0.22	3.81
Er	13.0	<LOD		9.77	4.59	0.65	2.93	0.61	3.29
Tm	1.87	<LOD		1.37	4.65	0.10	3.81	0.08	7.04
Yb	12.8	<LOD		9.25	5.03	0.70	3.16	0.58	3.96
Lu	1.90	<LOD		1.38	5.55	0.10	2.89	0.08	12.8
Pb	289	0.03	59.5	2.33	7.85	0.12	31.4	118	11.5
Th	12.2	<LOD		<LOD		1.53	22.0	11.1	57.7
U	2.98	0.04	5.31	2.78	3.72	0.03	4.92	0.04	315

AB02 BC19 N3									
		0.1 M Acetic acid		HCl		0.2 M Oxalic acid		Concentrated nitric acid	
	Bulk composition (ppm)	Conc. (ppm)	RSD (%)	Conc. (ppm)	RSD (%)	Conc. (ppm)	RSD (%)	Conc. (ppm)	RSD (%)
Na	22901	<LOD		5002	6.96	<LOD		15.7	46.7
Mg	16131	2971	4.17	9187	5.12	52.8	9.01	700	4.67
Al	22577	<LOD		5743	5.19	176	8.01	646	6.06
Si	84157	873	1.98	3029	7.08	1311	5.53	90.7	4.40
P	1558	3.58	105	17.0	86.2	44.8	51.1	<LOD	
K	8878	886	6.08	2022	5.77	933	9.79	751	9.87
Ca	17045	3510	0.69	10712	4.49	<LOD		278	9.33
Mn	290484	3.21	92.3	2724	6.24	7628	1.98	65080	4.25
Fe	60732	<LOD		9119	7.78	9157	1.77	13951	6.97
Co	1735	<LOD		15.9	8.15	85.5	4.34	500	5.12
Ni	15148	0.43	28.1	5972	4.74	517	6.13	2008	6.46
Cu	11440	1.65	23.0	7096	5.50	1139	3.82	639	5.00
Zn	1684	4.66	10.2	1392	3.30	50.8	19.4	112	2.06
Ba	5347	3.07	12.2	1580	6.69	<LOD		549	10.3
Y	61.0	9.70	69.0	38.3	10.4	2.28	50.1	10.6	84.2
La	91.4	0.03	21.8	66.6	0.57	0.45	5.77	6.78	4.51
Ce	244	0.03	44.9	66.6	2.21	7.14	9.18	102	4.27
Pr	25.9	0.01	26.7	19.4	0.66	0.23	5.48	1.99	5.26
Nd	112	0.03	28.7	83.9	0.70	1.20	5.17	8.53	5.17
Sm	26.6	0.01	31.0	20.6	0.51	0.41	4.76	2.04	5.36
Eu	6.78	<LOD		5.01	0.37	0.12	3.13	0.47	5.50
Gd	25.8	0.01	17.7	20.4	0.38	0.67	3.79	2.80	4.82
Tb	4.19	<LOD		3.02	0.50	0.12	2.97	0.22	6.62
Dy	23.2	0.01	21.8	17.4	0.50	0.85	2.95	1.06	6.65
Ho	4.24	<LOD		3.15	0.62	0.17	2.06	0.17	8.23
Er	11.8	<LOD		8.83	0.57	0.52	2.41	0.47	6.80
Tm	1.73	<LOD		1.24	0.64	0.08	2.46	0.06	8.27
Yb	11.7	<LOD		8.42	0.56	0.57	1.64	0.45	8.82

Lu	1.79	<LOD		1.24	0.61	0.09	3.03	0.06	11.1
Pb	289	0.02	68.2	2.29	3.53	0.02	27.6	104	3.03
Th	12.2	<LOD		<LOD		1.60	5.13	7.80	10.2
U	2.98	0.03	2.52	2.67	1.44	0.02	24.3	<LOD	

AB02 BC02 rubbles									
		0.1 M Acetic acid		HCl		0.2 M Oxalic acid		Concentrated nitric acid	
	Bulk composition (ppm)	Conc. (ppm)	RSD (%)	Conc. (ppm)	RSD (%)	Conc. (ppm)	RSD (%)	Conc. (ppm)	RSD (%)
Na	20466	<LOD		3475	5.64	<LOD		17.1	57.5
Mg	18103	3009	5.78	10046	1.92	45.5	22.5	668	3.01
Al	24644	<LOD		6894	1.66	169	12.3	770	3.48
Si	93193	784	5.23	3833	0.09	1258	7.90	82.1	9.57
P	3855	12.91	38.8	60.2	38.7	248	38.3	173	59.9
K	8578	1321	7.39	2238	3.36	357	17.2	281	24.8
Ca	22377	3329	3.78	15176	6.03	16.7	115	259	5.77
Mn	247456	2.10	74.0	3727	5.26	7735	4.52	58761	6.27
Fe	84996	0.58	253	13894	5.81	10991	3.62	17864	0.87
Co	2286	<LOD		17.4	64.8	131	5.32	615	4.65
Ni	12495	<LOD		5147	1.53	553	4.51	1983	2.09
Cu	8109	1.46	10.3	5846	2.91	589	3.31	384	8.20
Zn	1220	4.93	25.8	1019	3.44	50.6	5.53	90.7	15.4
Ba	3304	3.62	22.4	1182	5.70	<LOD		601	26.6
Y	91.1	12.10	21.8	53	3.76	3.56	45.9	13.2	25.1
La	148	0.02	17.7	98.2	3.42	0.37	9.49	10.3	7.65
Ce	375	0.02	102	115	7.02	5.32	10.0	134	4.66
Pr	39.2	0.01	41.4	26.8	3.61	0.20	9.25	2.94	8.34
Nd	168	0.03	24.2	114	3.26	1.10	8.21	12.5	8.47
Sm	39.1	0.01	40.4	26.6	2.92	0.39	8.63	3.00	8.37
Eu	9.45	<LOD		6.44	3.41	0.12	8.04	0.70	8.81
Gd	35.2	0.01	36.4	26.8	3.30	0.64	7.11	4.16	7.90
Tb	5.72	<LOD		3.88	3.71	0.13	5.73	0.37	9.35
Dy	32.3	0.01	40.9	22.1	3.14	0.90	3.83	1.91	9.36
Ho	5.76	<LOD		4.03	3.26	0.19	3.02	0.32	8.70
Er	16.2	<LOD		11.3	3.16	0.60	2.96	0.87	9.45
Tm	2.25	<LOD		1.57	3.17	0.09	2.49	0.12	11.7
Yb	15.6	<LOD		10.6	3.07	0.67	2.37	0.80	9.88

Lu	2.35	<LOD		1.56	2.44	0.10	2.52	0.11	9.31
Pb	432	<LOD		7.13	5.12	0.13	42.4	170	13.5
Th	16.3	<LOD		<LOD		0.82	14.8	13.2	22.0
U	3.70	0.04	7.27	3.20	4.51	0.06	18.8	0.07	24.4

FeMn CRM									
		0.1 M Acetic acid		HCl		0.2 M Oxalic acid		Concentrated nitric acid	
	Bulk composition (ppm)	Conc. (ppm)	RSD (%)	Conc. (ppm)	RSD (%)	Conc. (ppm)	RSD (%)	Conc. (ppm)	RSD (%)
Na	26500	<LOD		6762	3.51	<LOD		52.3	14.8
Mg	16897	2413	3.79	8060	3.63	63.5	4.73	964	5.51
Al	15506	0.73	213	3984	3.80	98.0	16.0	532	8.46
Si	66893	817	2.48	2968	2.28	1350	0.62	118	12.0
P	1536	7.99	26.0	<LOD		31.5	42.4	<LOD	
K	8100	669	5.22	2266	2.41	1423	3.82	1097	6.50
Ca	25005	4090	4.15	10036	3.98	12.2	82.3	382	0.94
Mn	343740	11.1	14.6	9144	4.22	8829	3.26	66184	6.45
Fe	86865	0.21	386	12262	2.16	10724	2.25	13566	6.20
Co	475	<LOD		17.9	35.5	45.0	13.4	189	5.84
Ni	13100	2.19	15.1	4738	4.87	410	3.31	1897	8.22
Cu	5957	0.93	52.8	3493	3.07	388	6.72	392	9.33
Zn	1845	6.90	14.6	1387	2.67	59.3	11.8	105	7.11
Ba	3158	0.72	13.9	1067	4.23	<LOD		987	9.52
Y	69.1	10.52	40.3	29.3	44.1	2.70	67.3	<LOD	
La	68.2	0.01	5.58	48.9	0.76	0.28	1.72	4.47	5.37
Ce	110	<LOD		44.2	2.92	2.61	4.26	36.5	5.21
Pr	14.1	<LOD		10.3	0.52	0.11	0.83	0.94	6.72
Nd	63.0	0.02	8.50	46.2	0.56	0.61	1.29	4.21	7.34
Sm	14.0	<LOD		10.2	0.74	0.19	1.07	0.92	5.64
Eu	3.80	<LOD		2.70	0.56	0.06	1.50	0.25	7.87
Gd	15.6	<LOD		12.2	1.59	0.36	0.54	1.30	6.62
Tb	2.52	<LOD		1.81	0.97	0.07	2.07	0.12	8.28
Dy	15.8	<LOD		11.8	1.30	0.54	1.08	0.72	6.75
Ho	3.42	<LOD		2.43	1.25	0.12	1.56	0.12	7.16
Er	9.80	<LOD		7.28	1.72	0.40	2.56	0.38	8.37
Tm	1.49	<LOD		1.06	1.42	0.06	2.29	0.05	8.95
Yb	10.0	<LOD		7.39	1.23	0.46	2.08	0.38	8.17

Lu	1.59	<LOD		1.13	1.88	0.07	2.83	0.05	11.3
Pb	127	<LOD		0.56	4.88	<LOD		61.74	4.55
Th	6.87	<LOD		<LOD		0.85	2.51	0.12	1472
U	4.39	0.04	1.83	2.53	1.28	0.02	5.79	<LOD	

Appendix III. Na-birnessite synthesis experimental set-up

